UNIVERSITY OF SOUTHAMPTON

Photovoltaic Applications of Si and Ge Thin Films Deposited by PECVD

by

M. Akhtar Rind

A thesis submitted in partial fulfillment for the
degree of Doctor of Philosophy

in the
Faculty of Engineering, Science and Mathematics
School of Electronics and Computer Science

July 2014

UNIVERSITY OF SOUTHAMPTON

ABSTRACT

FACULTY OF ENGINEERING, SCIENCE AND MATHEMATICS
SCHOOL OF ELECTRONICS AND COMPUTER SCIENCE

Doctor of Philosophy

by M. Akhtar Rind

This thesis represents a systematic study of amorphous silicon microcrystalline silicon and germanium thin films, and a-Si:H thin film solar cells fabricated using an OPT plasma lab 100 RF-PECVD system carried out with a view to studying novel light-trapping structures for thin film solar cells and novel IR photovoltaic cells. The work includes the optimisation of amorphous based single layers by optical and electrical characterisation, their doping and the fabrication and optimisation of single junction solar cells. These developments were extended to include deposition of microcrystalline and germanium films with the aim of developing a range of multijunction and single junction research devices.

The optical characterisation of intrinsic amorphous based layers shows that device-grade layer fabrications are achievable with more than 90% absorption in the 450 to 550 nm wavelength range which can be deposited at 4-5$\mathring{A}$/s with good thickness uniformity. The bandgap of intrinsic amorphous layers can be tuned from 1.4 to 1.7 eV. Secondary Ion Mass Spectroscopy (SIMS) depth profile characterisation has verified that doping levels in p-type and n-type are in the range of 10^{21} atoms/cm^3 which can maintain high open circuit voltage of 0.83V in the single junction device.

Systematic single layers well as in-device optimisations lead to the best single junction devices fabricated at a temperature of 250^{o}C and at a pressure of 350 mT and of initially 8.22% efficiency. Initial quantum efficiency (QE) measurements show 75% photon absorption at 550 nm wavelength. A novel technique of wavelength and angle resolved scattering (WARS) measurements have been used to analyse the effects of textured TCOs on light-trapping in single junction device. Showing *Asahi-U* to be the best substrate with regards to light-trapping, although thicker films benefited more from *TEC8*.

Deposition of microcrystalline silicon and germanium have also been reported. More focus has been given to optical characterisation of germanium films whose absorption has reached more than 70% in 400 to 1600 nm wavelength range with successful n-type and p-type doping. Ohmic contacts with a low resistivity of 0.029 Ω-cm for p-type Ge with the usage of Ni have been achieved. The overall working capacity of the OPT PECVD tool has been analysed and it was concluded that chamber design modification are essential for the system to work in a multidisciplinary field to avoid serious chamber contamination and 10% efficient a:Si:H benchmarks.

Declaration Of Authorship

I, **M. Akhtar Rind**, declare that the thesis entitled **Photovoltaic Applications of Si and Ge thin Films Deposited by PECVD** and the work presented in the thesis are both my own, and have been generated by me as the result of my own original research. I confirm that:

- this work was done wholly or mainly while in candidature for a research degree at this University;
- where any part of this thesis has previously been submitted for a degree or any other qualification at this University or any other institution, this has been clearly stated;
- where I have consulted the published work of others, this is always clearly attributed;
- where I have quoted from the work of others, the source is always given. With the exception of such quotations, this thesis is entirely my own work;
- I have acknowledged all main sources of help;
- where the thesis is based on work done by myself jointly with others, I have made clear exactly what was done by others and what I have contributed myself;
- parts of this work have been published as:

  M Akhtar Rind*, Owain D. Clark and Darren M. Bagnall. Amorphous and Microcrystalline Silicon Films for Thin Film Solar Cells. In PVSAT-7, Heriot-Watt University, 1-3 April 2011

  M.A. Rind*, D .N.R. Payne and D.M. Bagnall Thin Film Amorphous Silicon Solar Cells on Different Textured Transparent Conducting Oxides. In PVSAT-8, Northumbria University, 2-4 April 2012

  L. J. Crudgington , M. A. Rind , D. N. R. Payne , D. M. Bagnall. The Effects of Varied Deposition Conditions, Including the Use of Argon, on Thin-Film Silicon Solar Cells Prepared Using PECVD. In Molecular Crystals and Liquid Crystals Feb 14, 2014

Signed: ....

Date 22/07/2014

Contents

List of Figures

List of Tables

Acknowledgements

It gives me a great pleasure to express my warmest thanks to those people who helped me in this lengthy process of research and thesis. Firstly I would like to express my appreciation and gratitude Professor Darren Bagnall for valuable guidance and helpful encouragement during my Ph.D. Without Darrens support, arrangements and partial funding, I might never have finished the project.

I would also like to thank many colleagues at University of Southampton, who have helped me immeasurably in undertaking and understanding my work. My special thanks to Dr Owain Clark providing large amount of information. Thanks to my colleagues Lee Crudgington, David Payne, M. Banakar, and Carsten Gollasch for all the time spent both in and out of work. Every individual member of the Nano-Group really deserves a big thanks for making it a great department to be part of.

I would also like to thank many people for their friendship and help, which made living and working at Southampton a pleasure. I would like to thanks Gull and Altaf Nizamani for such help and support all the time. Lastly I would like to express my gratitude to my parents and family for their patience and understanding and making all of this possible.

Chapter 1

Introduction

Reliable energy supply has always been a core issue in human development. In todays modern world, it would be hard to imagine our lives without electricity and fuel. At present, main conventional energy resources are petroleum, coal, natural gas, hydropower and nuclear power. The world's total primary energy consumption in 2010 was estimated at 0.15 10^{15} kWh; an increase of 50% with respect to the energy consumption in 1990[11]. The declining oil, natural gas and coal extractions and the environmental impact of obtaining and using these conventional energy resources have changed our thinking towards future of energy supplies. A large proportion of resources have therefore been put forward in to the research, development and deployment of alternative energy.

A growth of interest in photovoltaics as a potential alternative source of energy has been established since the 1970s. After the oil crisis it was realized that significant electrical power could be obtained from sunlight as an alternative to burning fossil fuels or using nuclear fission. Photovoltaics has been perceived as a reliable source of electricity for a wide range of applications including remote area power sources, communications, peak load assistance, and powering satellites orbiting in space and small electronic devices. A key reason for implementing photovoltaic technology is the availability of solar power all over the world in varying levels of irradiance. It is believed that in the long run, photovoltaic technology could contribute to energy security and reductions in carbon dioxide emissions

The first observation of the photovoltaic effect is attributed to Edmund Becquerel in 1839. Becquerel discovered that an illuminated platinum electrode immersed in a liquid electrolyte produced an electric current. Although the magnitude of this effect was too small to be useful for energy generation, this discovery motivated more research into understanding the mechanism behind the illuminated current generation. The first functional large area (30 cm^2) PV device was made by Charles Fritts in 1883[12] using a thin film of selenium on a metal substrate. The selenium based solar cell is an example of a barrier layer cell, because it contains an electrical barrier that is highly resistive to current flow in one direction (a rectifying junction) while allowing free current flow in the other.

Two other barrier layer cells, the thallous sulphide cell(1920)[13], and the copper oxide cell (1927)[14], were developed during the 1920s. However, both types of cells had solar very low (less than 1%) solar conversion efficiencies.

The modern era of photovoltaic began in 1954 in Bell Laboratories, USA with the discovery of voltage generation under illumination of a p-n junction. Chapin et al[15] reported a *p-n* junction solar cell which achieved 6% energy conversion efficiency, and since then many researchers have contributed to photovoltaic development by investigating new materials and processes in order to enhance device understanding and improve the performance of solar cell.

The crystalline silicon cell can be made from either single (c-Si) or multi-crystalline (mc-Si) silicon material. These crystalline-based devices hold more than a 90% share of the PV industry. The best efficiencies of c-Si and multi c-Si cells have been recorded as 25% and 20%. Despite their longevity, reliability and environmental compatibility, crystalline silicon cells remain relatively complex and heavy devices with significant material and fabrication costs.

One drawback of c-Si devices is relatively poor light absorption, which means that cells must be relatively thick to absorb entire enough visible and near-IR light with reasonable efficiency. The thickness of the c-Si layer in a cell requires a substantial volume of very pure, high quality solar-grade silicon with long carrier lifetimes. Solar grade ingots are therefore expensive to produce, and the wafer sawing and and polishing consumes lot of time and energy. To achieve lower costs at the commercial scale, there is a need for different semiconductor technologies for photovoltaic applications like thin film technologies.

In principle, thin film technology has significant fabrication cost advantages over c-Si at large scale. Thin film solar cells are 100 times thinner than c-Si wafers and they are generally deposited onto relatively low cost substrates at lower temperatures.

This technology can tolerate higher impurity concentration and thus need less expensive purification of raw materials. Many materials are being investigated for thin film growth historically three particular semiconductor system have attracted most research effort thin film silicon, CdTe and $Cu(In,Ga)Se_2$.

Other materials, including Se, Cu_2S, Cu_2O, InP, CdSe and Zn_3P_2, have been studied, but because of disappointing results or high cost are no longer intensively investigated[16][17]. Only GaAs is being developed and used for special applications where very high efficiency is required in spite of high cost[18].

More recently Dye-Sensitised Solar Cell (DSSC) and organic photovoltaics (OPV) have been the subject of considerable research but DSSCs have yet to reach suitable module efficiencies for commercial production while OPV has yet to achieve suitable efficiencies or sufficient device lifetimes. Most recently perovskite solar cells have shown huge potential with lab device efficiencies rising from nowehere to 16% in a little over a year[19].

At this time, of all thin film technologies, it seems that only CdTe devices have any commercial possibilities, as a result of ongoing efforts by First Solar, while in the medium term it is perhaps the new perovskites devices that offer the most promise. Overall, in spite of the inherent cost advantages thin film technologies have largely failed to keep up with the continued efficiency enhancement and cost-reduction of wafer silicon technologies.

The main disadvantage of thin film solar cells is that they have lower efficiencies and are a less developed technology compared to c-Si. Thin film technologies are not fully matured and experience although, often in fits and starts large-area semiconductor growth for PV is developing constantly.

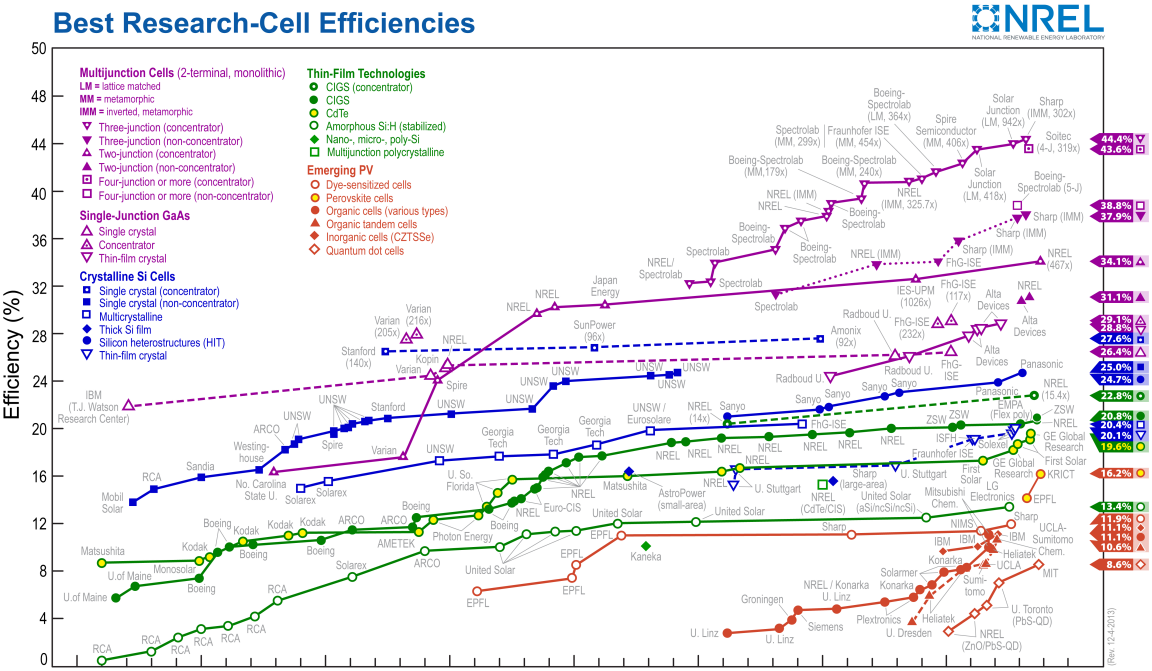

FIGURE 1.1: The NREL chart (2013) of on record cell efficiencies.

In the recent years, the photovoltaic world market has been increased by more than 60 % a year in terms of production. The estimated production in 2015 could be as much as at 100,000,0 MW, with a thin film share of 22,000 MW as shown in Figure 1.2. It is very likely that photovoltaic generation will become an important source of world electricity in the next half century. We will move from a time when the market for PV will go from being dependent on subsidy and global environmental concerns time when PV is the cheapest source of electrical energy for users and then producers.

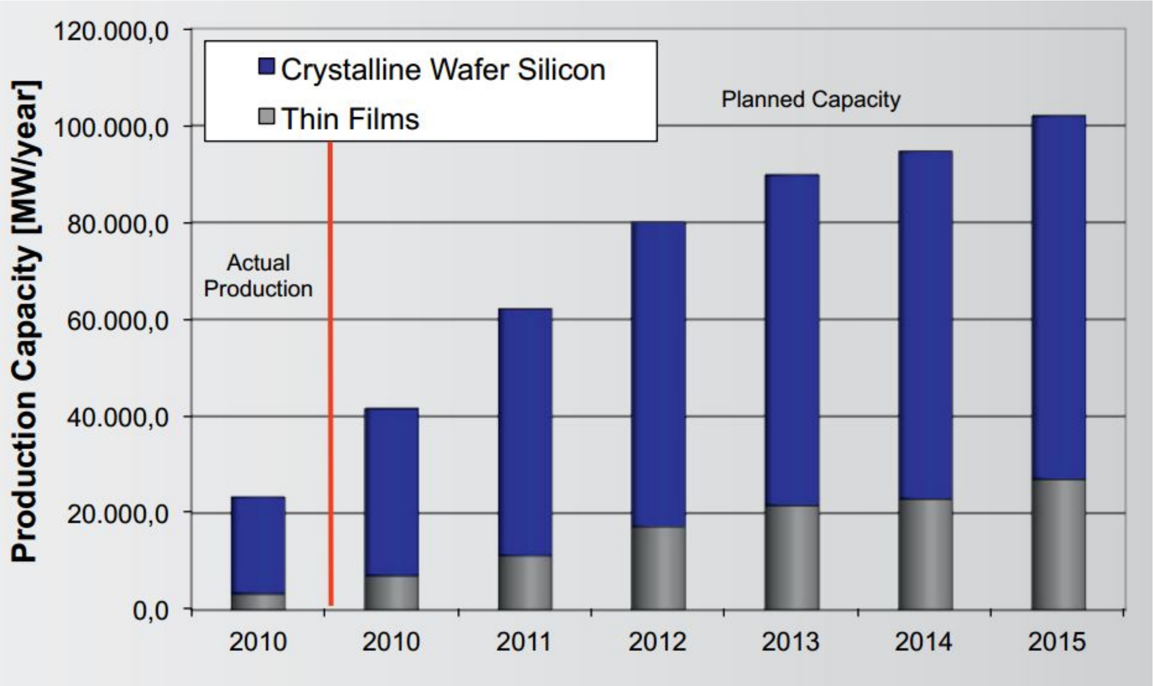

Figure 1.2: PV production capacities 2011/12 and planned production capacity increases[1]

This work has focused on thin film silicon based photovoltaic devices. Although it is clear that commercial thin film silicon PV manufacturers have suffered greatly in the last few years, it is our belief that thin silicon perhaps within tandem or triple-junction designs and with the deployment of advanced deposition techniques and sophisticated light-trapping techniques could yet be the system to realise promise of thin film PV technologies.

Unlike crystalline silicon (c-Si) which has a uniform crystal lattice structure, amorphous silicon lacks long-range atomic order. It is a material which possess random or disordered structure at atomic level but it also has similar short range order to single crystal silicon[20]. The lack of long range order within the atomic structure of unpassivated amorphous silicon has significant effects on the material properties and cannot conventionally be used in electronic applications. Hydrogen is therefore incorporated into the silicon material and electronic grade amorphous silicon is therefore called hydrogenated amorphous silicon (a-Si:H). Many authors simply use the term amorphous silicon to refer to the hydrogenated amorphous silicon for use in electronic applications.

The simplest form of a-Si:H solar cell *pin* junction structure is shown in Figure 1.3. In the *pin* configuration, the *p*-type a-Si:H is deposited on glass or other substrate followed by intrinsic layer a-Si:H and *n*-type a-Si:H. This *pin* structure of a-Si:H is sandwiched between a front transparent conducting oxide (TCO) and a back metal contact (such as Aluminium or silver).

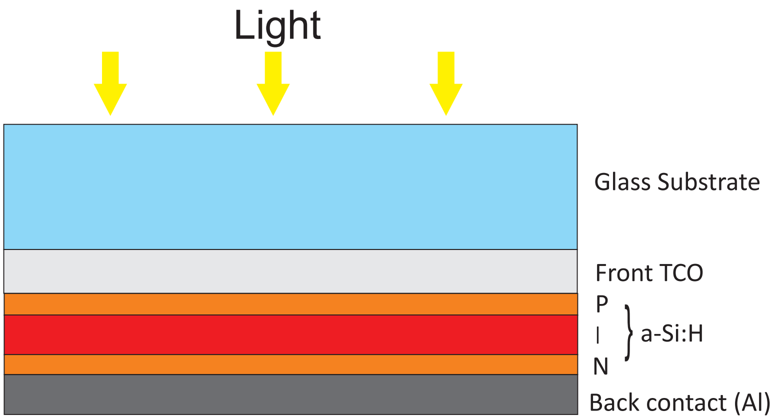

FIGURE 1.3: Sketch of single junction a-Si:H based PIN structure

The p-type and n-type layers along with an intrinsic (i-type) layer set up an electric field and also determine the voltage of the cell or device. The electric field separates the electron-hole pairs generated by the light. The most active layer in *pin* structure device is the intrinsic layer in which photons are absorbed and from which the current originates. The a-Si:H based solar cell can also be deposited by stacked *pin* structures (called tandem) or three *pin* structures (called triple junction) for better performance than single junction devices.

Amorphous based thin film solar cells can provide 11.9 % sub-module efficiencies on 1.227 cm^2 area and module efficiency of amorphous based tandem solar cells reached at 12.5 %[21]. Figure 1.4 shows IV-characteristics of a single junction a-Si:H with stabilized efficiencies of 9.47% by Neuchatel[2]. The thickness of intrinsic layer in this *pin* device is only 250 nm which is far less than the standard c-Si which can be as thick as 250 μm.

In the current era, to compete within the photovoltaic market, amorphous based thin film device technologies must address many important technology issues in order to remain active in industry. In the broadest sense, those issues include enhancement of conversion efficiency, elimination of light induced degradation, increased deposition rate of the active absorber layer, the correct choice of mass production technique and the reduction of the cost of materials used.

The first set of deliverable targets of this report is the enhancement of conversion efficiency in terms of improved light management schemes. Light management comprises of effective light trapping and reduction of absorption loses. Effective light trapping may simply be defined as a technique to capture incoming light in the absorber layer of thin film device and prevent it from escaping by transmission or reflection. By using light trapping techniques, it is possible to increase effective optical thickness to incoming light in the very thin absorber layer. The use of a thin absorber layer in the case of a-Si:H based devices allows the minimisation of the impact of light induced degradation

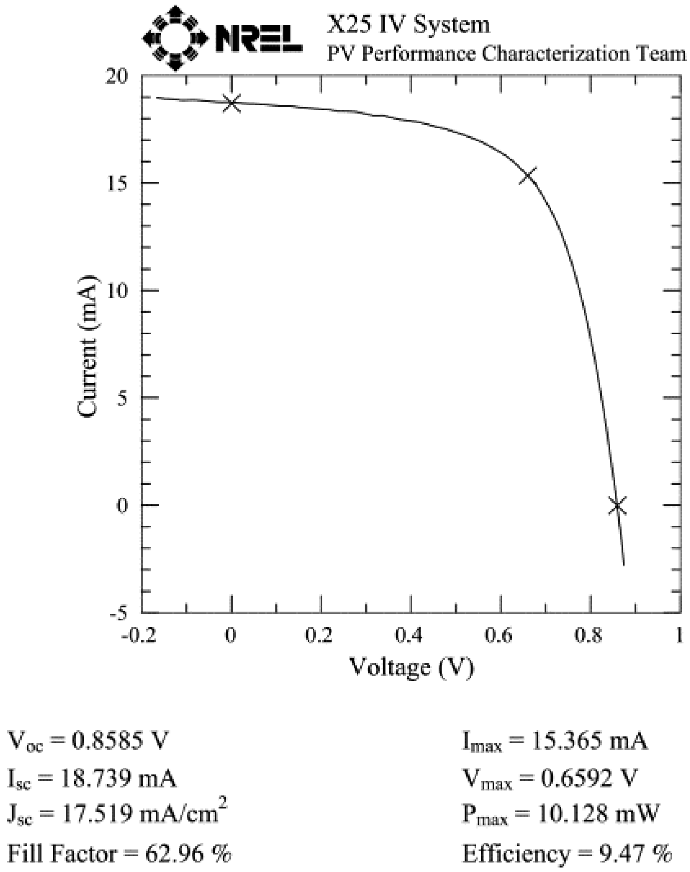

V_{oc} = 0.8585 V
I_{sc} = 18.739 mA
J_{sc} = 17.519 mA/cm^2
Fill Factor = 62.96 %
I_{max} = 15.365 mA
V_{max} = 0.6592 V
P_{max} = 10.128 mW
Efficiency = 9.47 %

FIGURE 1.4: IV characteristics as measured by NREL of an a-Si:H p-i-n solar cell[2].

The techniques used for light trapping are in-coupling of incident photons at the front side, reflection at the back side, intermediate reflectors in tandem solar cells, scattering at rough interfaces, and scattering at metal nano-particles (plasmonic effects)[22].

A further approach to increase the efficiencies of thin film solar cells is the use of multi-junction structures. The active absorber layers in multi-junction devices mostly based on a-Si:H, alloys of a-Si:H such as hydrogenated amorphous silicon germanium (a-SiGe:H) and hydrogenated microcrystalline silicon (μc-Si:H) as a stack of two structures[23] or more[24]. In two-junction device structures commonly known as *micromorph* tandem, μc-Si:H is the main material used as a bottom cell along with a-Si:H cell at the top.

Crystalline germanium (c-Ge) has a much narrower band gap of 0.67 eV compared to silicon, which makes it very useful to convert near infrared radiation into electrical energy[25].The growth of highly crystallized germanium thin films at low temperatures is attracting attention, because of its potential importance to reduce the contact resistance and increase the carrier mobility for large-area electronic devices such as thin film transistor and solar cells[26,27]. Along with this germanium has emerged out as a strong alternate candidate for complementary metal-oxide semiconductor (CMOS) technology, as it has larger carrier mobilities as compared to silicon[28], Ge p-MOSFETs[29] and for infrared detection applications[30]. All these Ge application to different technologies are closely tied with reliable Ohmic contact which remained a challenged due to Schottky behaviour and high contact resistance[31].

In the second set of deliverable targets, this report presents a systematic study of growth processes and characterisation of intrinsic layers of a-Si:H andμc-Si:H, microcrystalline germanium (mc-Ge:H) its Ohmic contact with metal and devices fabricated using plasma-enhanced chemical vapour deposition. For this study, and Oxford Instruments PlasmaLab System 100 PECVD tool is used. As the system was newly installed, initial growth is dedicated to achieve optimized method for thin film growth. The grown layers then characterised by various tools *including dark and photo conductivity, ellipsometry, Raman spectroscopy, SIMS measurement, AFM, SEM, and EQE* which are discussed in coming chapters.

The third set of deliverable target consist of optimized TCO for the application of a-Si:H on the bases of analysis done by novel WARS measurement with AFM and optical characterisation of commercially available TCOs.

Chapter 2

Background Theory and Literature Survey

This chapter introduces the solid state physics of amorphous silicon, and the structure and operation of thin film silicon photovoltaic devices. The chapter concludes with a detailed exploration of the techniques used to deposit silicon thin film and recent progress of thin film a-Si:H based solar cells.

2.1 Solar Irradiance

The sun has a surface temperature of 5762 K and emits light with a range of wavelengths covering the ultraviolet, visible and infrared segments of the electromagnetic spectrum. The Earths surface receives a continuous supply of over $12\text{x}10^{16}$J of energy from the sun in the form of electromagnetic radiation each second[32], which is sufficient to supply the world's entire annual energy requirement in less than one hour. Figure 2.1 shows the solar irradiance (energy per unit area per unit time) as a function of wavelength. Sunlight reaching the surface of the earth is assumed to be parallel as light has to cover a great distance (93 million miles) and only the light in the direction of the earth is considered. The extra-terrestrial spectrum can be approximated by a black body radiator at 5760 K which is also shown in Figure 2.1. The power density at the surface of the sun is 62 MWm^{-2} and at a point just outside the Earth's atmosphere, the power density reduces to 1353 Wm^{-2} because of the reduced angular range of the sun[33]. Solar irradiance is largest at visible wavelengths (300-800 nm), peaking in the blue green region. The spectrum that reaches Earth's surface is attenuated due to absorption and scattering by various atmospheric constituents such as atomic and molecular oxygen, ozone and nitrogen.The optical path length between the Sun and the Earth depends on the Sun's declination angle.This angle is described by specifying a zenith angle of the Sun, the angle between the Earth-Sun radius and the normal of the plane containing the horizon

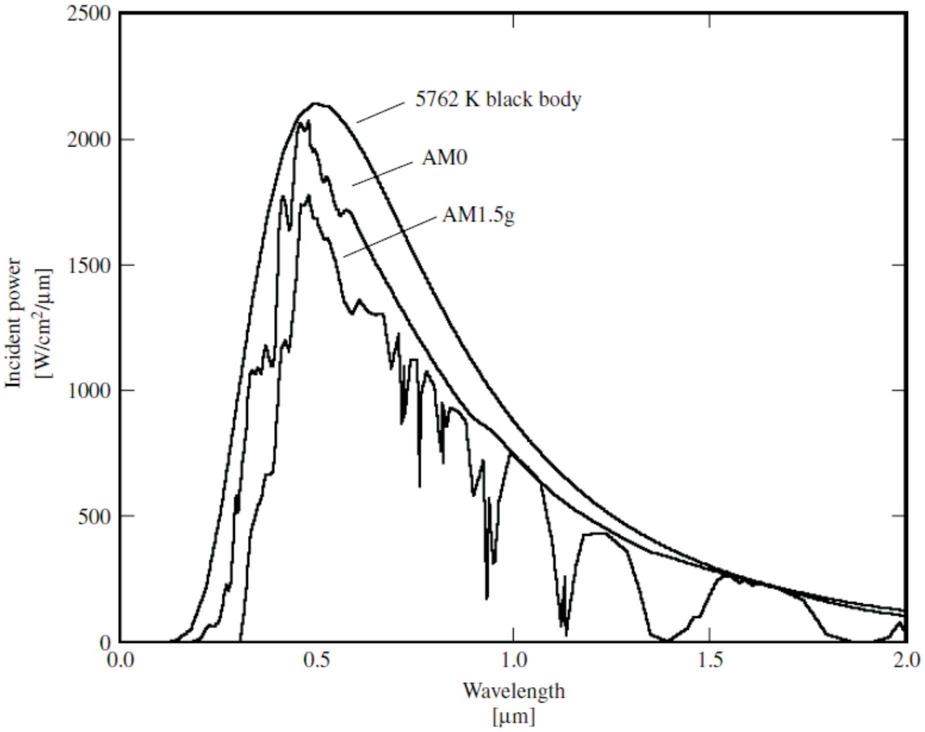

Figure 2.1: The radiation spectrum for a black body at 5762 K, the AMO spectrum, and the AM 1.5 global spectrum

circle[34]. Air Mass is a measure of atmospheric attenuation and is given by Equation 2.1

$$\text{Air Mass} = \frac{\text{optical path length to sun}}{\text{optical path length if Sun directly overhead}} \tag{2.1}$$

In outer space the solar spectral distribution is referred as air mass zero (AM0) radiation spectrum. At sea level on clear day at noon at a latitude when the sun is directly overhead, the radiation from the sun corresponds to airmass 1 (AM1). A typical spectrum at Earth's surface at angle of 48.19^o on clear day is called AM1.5 or airmass 1.5 which is the standard spectrum for solar cell operation comparison, normalized to a total power of 1000 Wm^{-2}. The real irradiance is always changing because of seasonal and daily variations in the position of the sun and orientation of the Earth.

2.2 Atomic structure amorphous silicon

In order to understand the design and operation of a-Si:H solar cells it is necessary to examine the differences between crystalline silicon and amorphous silicon. In order to understand the design and operation of a-Si:H solar cells it is necessary to examine the differences between crystalline silicon and amorphous silicon. In single crystal silicon each atom is covalently connected to four neighbouring atoms with equal bond length

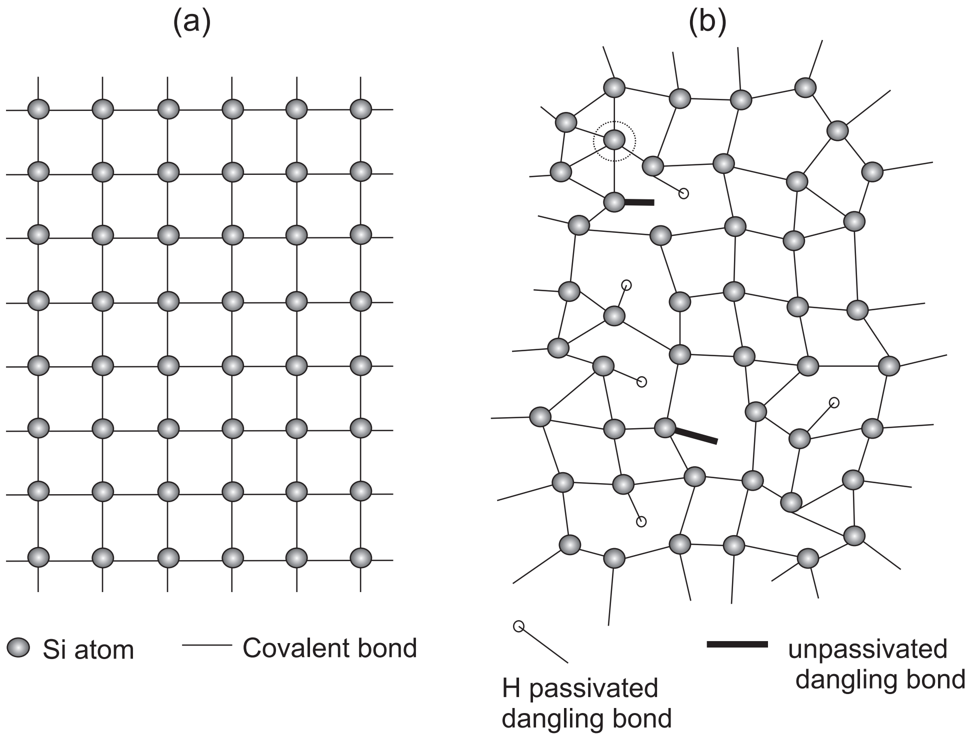

Figure 2.2: Schematic view of the atomic structure of (a) single crystal silicon, (b) hydrogenated amorphous silicon (reproduced[3])

and bond angle. This formation is called tetrahedral four-fold coordination as shown in Figure 2.2. This regular atomic arrangement is known as long range order which is present in c-Si. If there is no structural order over long range as compared to single crystal silicon, that material is amorphous silicon. The atomic structure of amorphous silicon is described as a continuous random network. However, there is similarity at the local atomic level as shown in Figure 2.2. Amorphous silicon always lacks long range order but it has similar short range order to single crystal silicon, therefore amorphous silicon also possesses some of same qualities as single crystal silicon, including similar energy state band configuration[3].

A five-fold coordination in which an extra bond is connected is called a *floating bond* the three-fold coordination in which there is an unpaired bond of silicon is called a *dangling bond* as shown in Figure 2.2(b). Both floating bonds and dangling bonds are considered defects in a crystal structure. Thermally deposited pure amorphous silicon contains about 10^{21} defects per cm^3, and this high defect density material cannot be used in any functional device[3]. However, hydrogen can play an important role in modifying the opto-electronic properties of amorphous materials[35]. During amorphous silicon deposition if hydrogen atoms interact with the dangling bonds and create Si-H bonds, the resulting material is called hydrogenated amorphous silicon (a-Si:H) and this material is of central interest in this thesis. The defect density of a-Si:H can be reduced to 10^{15} cm^{-3} after a hydrogen passivation that also leads to wider band gaps and improved optical absorption thus making the material suitable for electronic applications[3].

The bonding disorder caused by deviation in bond length and angle in a-Si:H broadens the electronic densities of states and causes electron and hole localization as well as strong scattering of charge carriers[36]. Dangling bonds lead to corresponding electronic states in the band gap while floating bonds lead to electronically induced metastable states[36]. The potential energy function arising from the amorphous silicon structure is not periodic, which causes perturbation in wave-functions and consequent scattering in electronic states, which in turn causes a large uncertainty in momentum. Therefore the energy bands are only described by the density of state distribution, and due to uncertainty in momentum, the distinction between a direct and indirect band gap is lost[36] and a-Si:H behave like a direct bandgap material.

2.3 Band structure and density of states

The concept of density of states (DOS), and their distribution is vital to understanding the electronic and optical properties of a semiconductor. The idea behind is a simple approximation that if a single electron is joined to a solid, it might be seen as occupying a well-defined state at some distinct energy level. In a range of energies, the number of such available states per unit volume per unit energy is referred to as the density of states. For an ideal intrinsic semiconductor crystal such as silicon, there is a well-defined gap between valence band and conduction band and there are no permitted energy levels within the band-gap. In a-Si:H, due to non-periodic structure and long range disorder, it is extremely difficult to determine complete density of state distributions. Due to the long random networks, potential fluctuations in a-Si:H create an exponential distribution of band **tail states** and the valence band and conduction band energy states are spread into the band-gap. These extensions are called *band tails.*

Additionally, defects in amorphous material also create allowed energy states within the region between valence band and conduction band states. These states are known as *localized states* and due to this localisation, there is no well-defined band-gap in a-Si:H. The regions where carriers are considered free are **non-localized states** or extended states.

The mobility that characterises the transport of carriers through localised states is strongly reduced. A sharp drop in mobility in localized state as compared to non-localized states where carriers are considered free is used to define band-gap in a-Si:H. The energy levels that separate the non-localized states from localized states are known as conduction and valence band **mobility edges**[37]. Therefore bandgap of a-Si:H is explained in terms of a **mobility gap**.

As discussed, there is no clear method is available to determine the band-gap of a-Si:H. There are various models developed to describe the optical properties related to band-gap but the most versatile methods used are the Cody-Lorentz model[38] and Tauc-Lorentz model[39]. In this report, the band-gap of a-Si:H determined by Cody-Lorentz model. Typically a mobility gap of 1.70 eV is assigned to the a-Si:H but this value varies substantially with the deposition conditions employed.

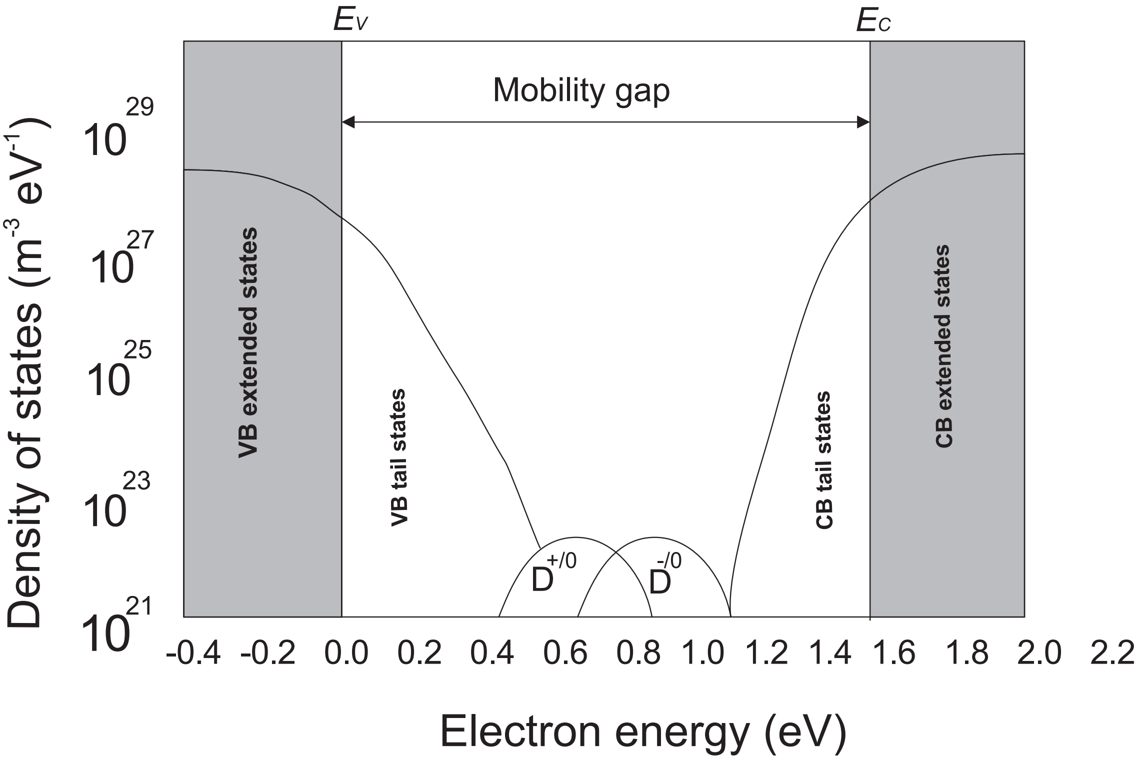

FIGURE 2.3: The standard model for density of states in a-Si:H. The shaded areas indicate extended states in the bands[3])

Figure 2.3 illustrates the standard model of the density of states for a-Si:H characterised by three regions including the non-localized states above the conduction band mobility edge, the non-localized states below the valence band mobility edge and localized states due to defects between two mobility edges. The charge state of deep lying dangling bonds in the mobility gap depends on the location of Fermi energy in the a-Si:H. If the Fermi energy is high in the mobility gap then the defect states are regarded as negatively charged dangling bond states (D^-); if the Fermi energy lies close to the valence band edge, defect states are considered as positively charged dangling bond states (D^+) and if Fermi energy lies close to the middle of mobility gap defect states are called neutral dangling bond states (D^o)[40].

These defect states are very crucial in the determination of the quality of material as they behave as trapping and recombination centres which influence the collection of photo generated carriers and the performance of a-Si:H solar cells. By optimising the growth conditions, device grade a-Si:H material can be deposited whose defect densities can be as low as 10^{15} cm^{-3} with carrier life times in the range of 10^{-8} to 10^{-6} s[41].

2.4 Doping

The conductivity of an intrinsic semiconductor can be altered by introducing specific impurities with energy levels close to the conduction or valence band edge. This process is called doping. The material is said to be n-type if it is doped to enhance the density of electrons. For example an element from group V is phosphorus, which has five valence electrons and in tetravalent silicon lattice configuration, the extra electron would be loosely bound and therefore becomes ionized easily. Such impurity atoms are called *donors*. A material is said to be p-type if it has been doped to enhance positive charge density. In p-type material, atoms with fewer valence electrons compared to silicon are added to the silicon lattice, causing a vacancy in the crystal. These impurity atoms are called *acceptors*. A vacancy is the absence of an electron and assumed to have positive charge, this is a hole. Atoms from group III such as boron are used in silicon for this purpose.

A-Si:H can be doped both n type and p type whereas un-doped a-Si:H is purely intrinsic or slightly n type in nature with Fermi energy level at mid of the mobility gap. In order to manipulate the electrical conductivity and its magnitude, a controlled amount of impurity atoms (from boron and phosphorus sources) are added in the a-Si:H during manufacture. The electrical properties can be varied by shifting of Fermi energy towards band edges, and this principal works differently in a-Si:H when compared to c-Si. By doping the conductivity of a- Si:H can be varied by a factor of up to 10^8 and the activation energy can be decreased to ~ 0.2 eV for n type film[3]. A phosphorus atom with five valence electrons can incorporate itself in the continuous random network by forming three covalent bonds with neighbouring atoms, as shown inFigure 2.4.The phosphorus

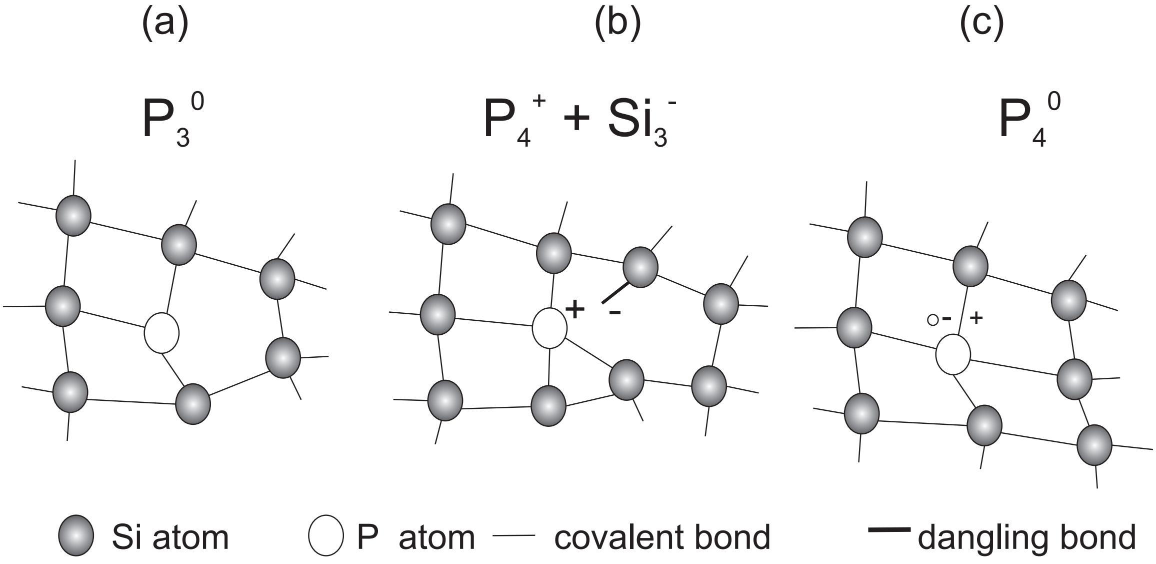

Figure 2.4: Possible configuration of phosphorous atom in a-Si:H network: (a) the non-doping state $P_3{}^0$ (b) the defect compensated donor state $P_4{}^+ + Si_3{}^-$, (c) the neutral donor $P_4{}^0$ (redrawn[3])

configuration involves the three valence electrons in the p atomic orbital, and the final two electrons are paired in the s atomic orbital which do not participate in bonding and remain tightly attached to the phosphorous atom. The notation ${T_z}^q$ is used here, where T is the atom, z is the coordination and q is the charge state.

Most phosphorous atoms are incorporated according to the **8-N rule** and adopt the optimal threefold coordination that represents the non-doping state and is thus electrically inactive. The phosphorous atom can also be incorporated in the network by forming ${P_4}^0$ (a neutral donor) but this configuration is characterized by a much higher energy than the optimal ${P_3}^0$ configuration and so is unstable in the continuous random network. Most atoms that contribute to doping are charged phosphorus atoms ${P_4}^+$ with the formation of a negatively charged dangling bond to preserve charge neutrality. This configuration is more energetically favourable and is known as a defect compensation donor. Excess doping in a-Si:H produces defect states near the mid-gap which limit the doping efficiency and reduce carrier life times thereby severely effect device performance[42] as a result doped a-Si:H layers can not be used as an active absorber layer in photovoltaic devices.

2.5 The Staebler-Wronski effect and metastability

A significant technological challenge in a-Si:H solar cell design is overcoming light induced variations in electronic properties commonly known as the *Staebler-Wronski effect* (SWE).[43]. It was found that dark and photo conductivity of a-Si:H films decrease when illuminated with sunlight over time. Moreover these light induced changes in the carrier transport of thin films are found to be metastable which means they are reversible and can be removed by annealing at a temperature of 150 ^{o}C. Figure 2.5(a) shows the decrease in photo and dark conductivity that occurs on illumination of a-Si:H. The reversible changes occur at an annealed state A and a light soaked state B. Changes in the absorption coefficient measured by the dual beam photoconductivity method are shown in Figure 2.5(b). Sub-band gap absorption increases with illumination time in the photon energy range between 0.8 and 1.40 eV, which represents an increase in mid gap defect density. The microstructure is also important in considering light induced changes, as an important aspect of light induced defect generation in a-Si:H is that defect density of dangling bond defects increases until reaching a saturation value after a long time of exposure as shown in Figure 2.6. The saturation value near room temperature is almost independent of illumination and also independent of the sample temperature up to 70^{o}C[44]. Therefore for commercial purpose, its vital that a-Si:H based devices always go for light soaking stabilization prior to shipment.

Despite being widely investigated, there is no definitive conclusion for the reason of the Staebler-Wronski effect (SWE). Most researchers agree that the principal cause of the

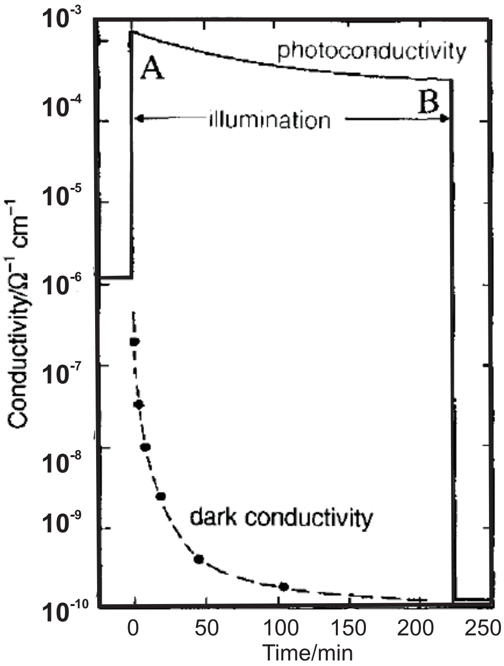

(a)

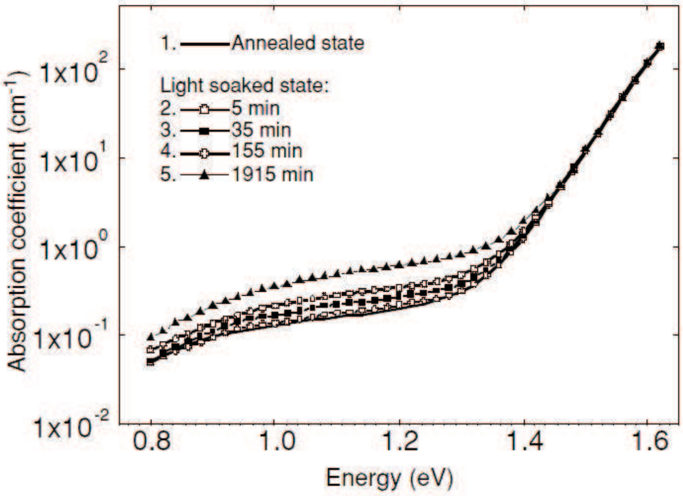

(b)

FIGURE 2.5: (a) Photoconductivity and dark conductivity of an a-Si:H thin film as a function of illumination time, (b) the changes in sub-band gap absorption coefficient of a-Si:H due to light soaking.[3,4]

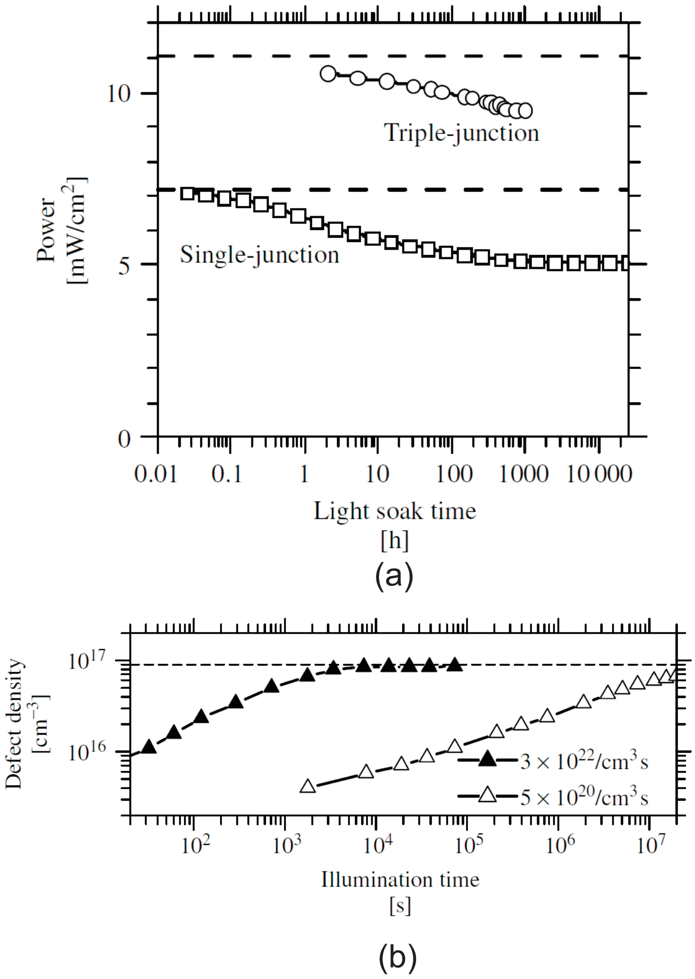

FIGURE 2.6: (a) The conversion efficiency decline under a solar simulator (100mW/cm^2) for a single junction cell and for a triple junction module; the dashed lines indicate the initial power measured for each device. (b) Plot of defect (dangling bond) density during extended illumination of an a-Si:H film.[5]

SWE is the increase in the dangling bond density after light soaking[5]. These changes or effects are a consequence of defect states created by the light and act as additional recombination canters which reduce carrier lifetimes. Hydrogen plays a key role in eliminating dangling bond defects as well as in SWE. The reasoning is that illumination provides the energy required to shift hydrogen atoms away from their dilute phase site and thus creating an additional dangling bond. There is no commonly accepted model for explaining all experimental observation of SWE as the exact role of hydrogen, weak Si-Si bonds and Si-H bonds in the creation of metastable defects are still under investigation.

2.6 Physics of the amorphous silicon solar cells

The basic solar cell structure in a-Si:H based devices is fundamentally different to standard crystalline silicon (c-Si) solar cells, which are based on p-n junctions. The carrier diffusion length of charge carriers in a-Si:H thin films are very short as compared to c-Si, as they inherently contain higher defect densities. The diffusion length of minority carriers in intrinsic a-Si:H is even shorter, and the majority of such carriers would recombine in doped regions before reaching in the depletion region of a p-n junction. Therefore p-n junction structure is found invalid for a-Si:H based solar cell devices which now require three major layers: a p-doped a-Si:H layer, an intrinsic a-Si:H and an n-doped a-Si:H layer. These three individual layers construct a *pin* junction, which in the form of solar cell device are shown in Figure 2.7.

In devices the doped layers need to be very thin, typically as p-type layers are ∼10nm and n type layer ∼20 - 30nm. The thickness of active intrinsic a-Si:H layers range between 300 - 400 nm. Thin doped layers not only establish an internal field but also arrange good ohmic contacts between a-Si:H and external electrodes which are added during later processing steps. The intrinsic a-Si:H layer in *pin* devices acts as an absorber layer, which generates electron-hole pairs when irradiated with sunlight and the internal electric field facilitates the separation of electrons and holes to the external contacts. The performance of a-Si:H solar cell is strongly dependent on the quality of the intrinsic material and the magnitude of the internal electric field, which in turn depends on several other interrelated factors which are discussed in this section.

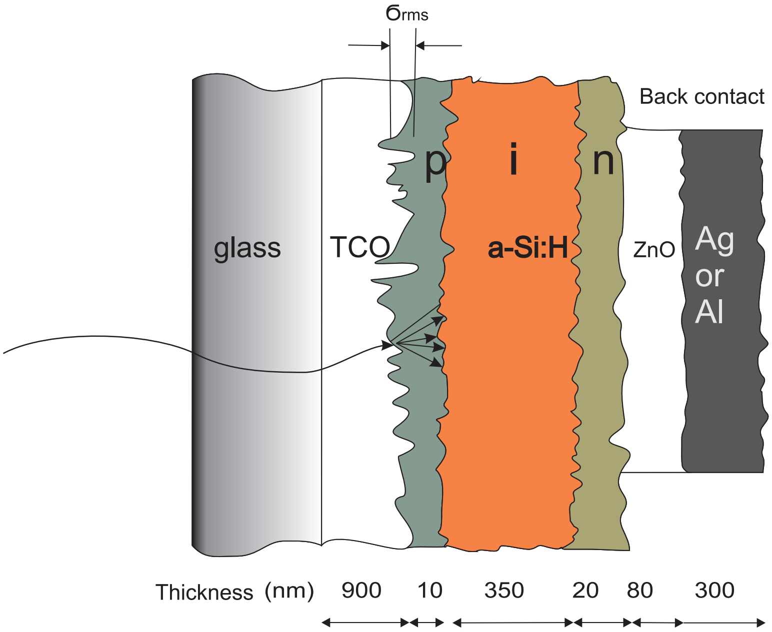

FIGURE 2.7: Band profile of *p, i* and *n*-type semiconductors in isolation.

We start from the internal electric fields, which also termed as built-in electric fields. In isolation, the Fermi energies of *p*-type, *n*-type and intrinsic materials are very different to each other as shown in Figure 2.8. In *p*-type layer, the Fermi energy (E_F) is close to the valence band edge (E_V) and in *n*-type it is close to the conduction band edge (E_C). When these individual layers are combined as a *pin* structure, their Fermi energies are aligned at create thermal equilibrium. Electrons migrate from the *n*-layer to the *p*-type

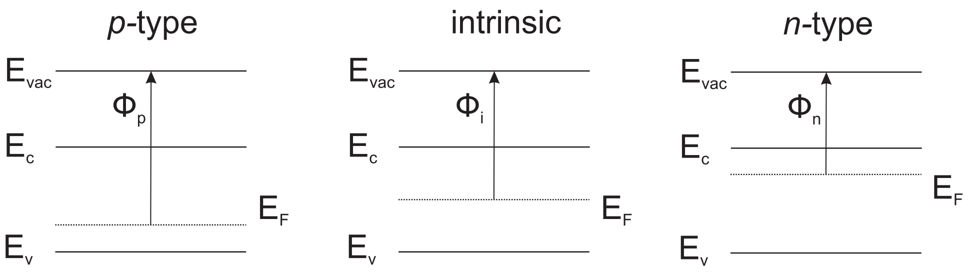

FIGURE 2.8: Schematic structure of single junction *p-i-n* a-Si:H solar cell.

layer, which creates an internal electric field. In this situation, band-edge energies vary in the device but the Fermi energy itself remains constant. The original difference in Fermi energies is converted into the *built-in potential* across the device as illustrated in Figure 2.9(a).

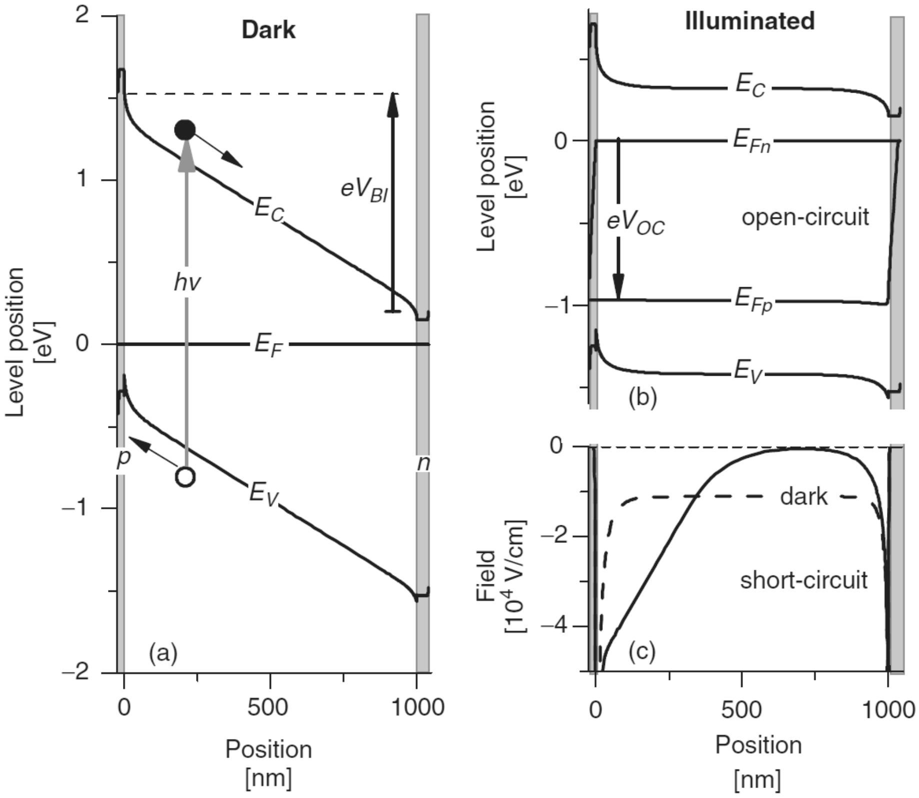

FIGURE 2.9: Calculated energy level profile position and electric field for a single junction *p-i-n* solar cell. (a) Profile level in dark. (b) Profile level under illumination. (c) Electric field in short circuit.[6]

The higher gradient of band banding creates higher a built-in potential, which is why higher doping levels in the n and p-type layers of a-Si:H solar cell are required to establish large built-in potential. The typical built-in field is illustrated in Figure 2.9(c) labelled as dark. A large built-in potential not only allows higher built-in electric fields but also helps to establish high open circuit voltages V_{OC} across cells when illuminated. Photo-generated carriers (electrons and holes) will drift due to the built-in electric field in their respective direction as shown in Figure 2.9(a). Figure 2.9(c) presents the calculated open circuit profile of band edge levels for uniformly absorbed illumination. Under illumination a cell is no longer in the state of thermal equilibrium therefore no Fermi energy profile is shown. Due to the photo-generated population of carriers, two separate *quasi-Fermi energies* of electrons E_{Fn} and holes E_{Fp} are now shown. The separation in two new quasi-Fermi energies looks constant in the middle but these energies combine with the p-layer and the n-layers at the edges. Thus in a-Si:H, V_{OC} is determined by the splitting of quasi-Fermi levels.

In a-Si:H, electron and hole mobilities and diffusion lengths are low as compare to c-Si. The higher built-in fields help photogenerated carriers to overcome such inherited limitations. The efficient collection of photo-generated carriers in the intrinsic layer purely depends on the drift current which is generally established to be the result of the magnitude of electric field across the intrinsic layer, mobility and the lifetime of the carriers. This field-assisted carrier collection is very sensitive to the thickness (L) of intrinsic layer of a-Si:H being approximately proportional to $1/\mathrm{L}^2$[45]. To determine the optimal thickness of intrinsic a:Si:H is vital part in solar cell design. This thickness is delicate trade-off between absorption which is higher in thicker layer and carrier collection which is more efficient in the thinner layer.

The electric field produced by the doped layer across the intrinsic layer is not uniform but greatly depends on the spreading of space charge. This space charge is produced when photo-generated carriers are trapped in the gap states. These gap states are the result of native and light induced defects in a-Si:H solar cells which severely affect their carrier collection. At first defects act as recombination centres which eliminate photo-generated carries and secondly these defects cover the electric field profiles produced by the doped layers make them non-uniform across the thickness of intrinsic layer.

The random network disorder in the a-Si:H atoms obstruct the electron motion and it is the reason that electrons in a-Si:H have mobility of about 2 $\mathrm{cm}^2/\mathrm{Vs}$, about 500 times smaller than for c-Si[6]. The holes in a-Si:H are slower still and only travel 200nm in 1 μs which is 1000 times longer than it takes electrons[46]. This slow motion of holes in a-Si:H is attributed to trapping by valence band states in bandtails[47]. In 1 μs a hole can be trapped and released by valence band states many times and this severely slows down its motion[46].

Under dark conditions, the electric field across an a-Si:H *pin* junction is near constant as illustrated in Figure 2.9(b) but this will change when cell is illuminated. At large photo-generation rate, slow moving holes accumulate and re-establishes the built-in electric field profile illustrated in Figure 2.9(c) where under illumination, the electric field profile is higher near the *p*-layer but very low near the *n*-layer. The combination of low hole drift mobility and the reduced field near the *n*-layer noticeably affects the functioning of a solar cell[48]

The photo-generated carrier collection in the intrinsic layer also determines the short circuit current densities J_{SC} in the solar cells, which depends on both the thickness of the intrinsic layer and the absorption of sunlight in that layer. A thicker intrinsic layer will absorb more sunlight but this has an adverse effect on carrier collection and J_{SC}. Another parameter which is most sensitive to thickness is the fill factor since during illumination internal electric fields are significantly reduced. In a-Si:H solar cells, it is customary to obtain higher optical absorption with efficient carrier collection without making thick intrinsic layer by using light-trapping techniques.

Doped layers specially at the p/i interface also have profound effects on the stability and performance of a-Si:H solar cells[49,50]. Defect densities at this interface are much higher than in the bulk intrinsic layer. Despite of the relatively thin region, these densities can have a large effect on both carrier recombination and electric field distribution of the device. As the p/i interface is located immediately next to the p-layer, it also has influence on the open circuit voltage and *fill factor* of the device[49]. This low open circuit voltage is a result of a low built-in potential arising from narrowing of the band-gap of the p layer[49]. Though light induces defects in the p/i interface have pronounced effects on the device. Optimized p/i interfaces with the correct boron profiles will raise the open circuit voltage and not degrade in sunlight[49,50].

Summarising, we can say that low mobility limitation of charge carriers in a-Si:H device can be compensated by increased optical absorption and low space-charge densities in the intrinsic layer. This will allow the generated electric field profile to collect free carriers before recombination occurs. Carrier lifetimes and electric field profiles mainly depend on the defect state types and their densities and these must be carefully controlled in an optimised device.

2.7 Deposition of amorphous silicon

Amorphous silicon can be deposited onto a number of different substrates using a variety of widely available techniques. The first film growth was reported in 1965 by silane growth in RF glow discharge[51]. In its un-hydrogenated form, amorphous silicon possesses a high defect density ($\backsim 10^{19}$ cm^{-3}) because of atomic departure from local tetrahedral *coordination* between four silicon atoms. These defects are called *dangling bonds* and serve as recombination centers which drastically reduce carrier lifetime and diffusion lengths. They also pin the Fermi energy so material can not be doped. Incorporation of hydrogen during amorphous silicon growth greatly reduces the defect density which was first discovered by Chittick in 1969[52].

The first a-Si:H solar cell was reported by Carlson and Wronski in 1976 with 2.4 % efficiency[53]. After that amorphous silicon solar cell technology showed considerable improvement and today it is a mature technology which is simpler and less expensive

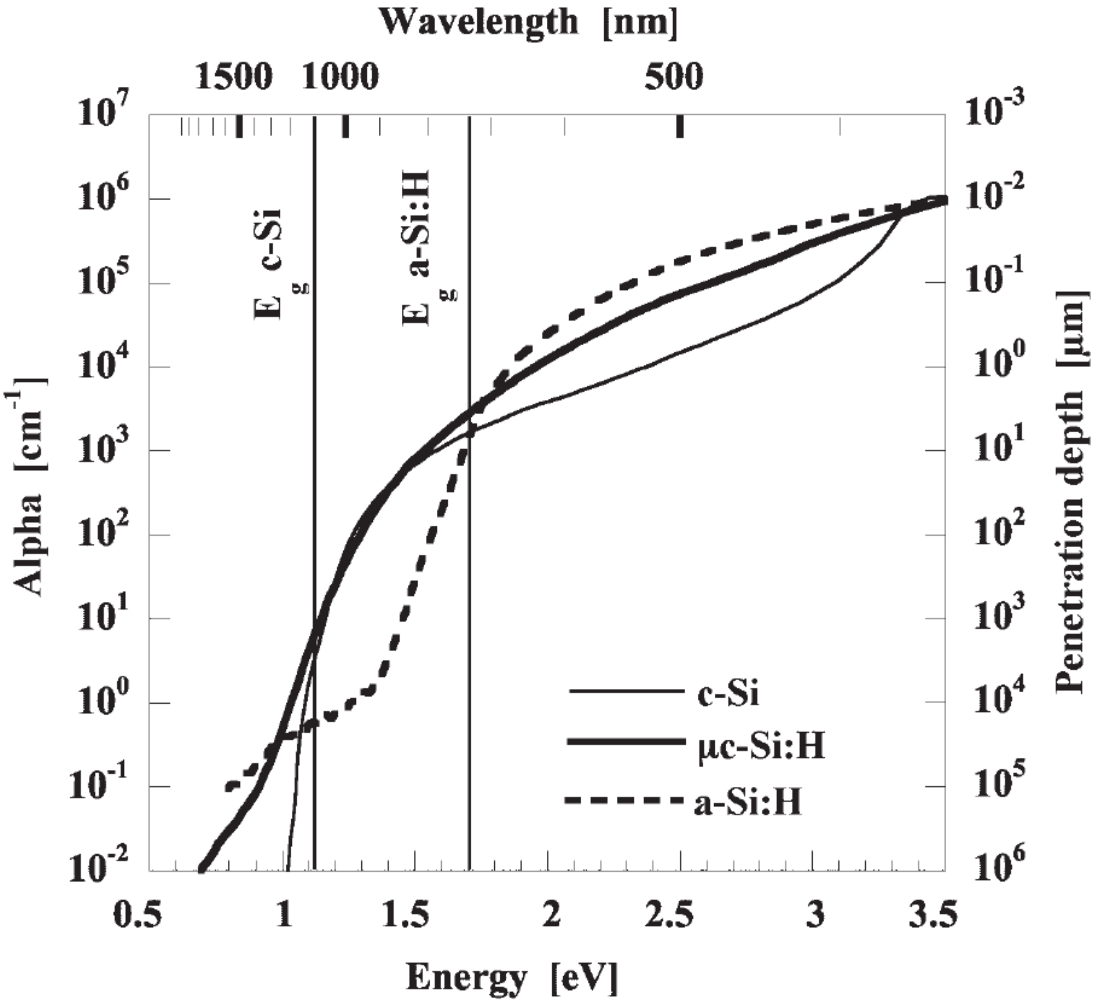

Figure 2.10: Optical absorption coefficient as a function of the photon energy for typical a-Si:H, c-Si and μc-Si. The vertical axis is calibrated in penetration depth, i.e., layer thickness within which 63% of the corresponding photons are absorbed[7]

when compared to silicon wafer technology. A-Si:H has a higher absorption edge and a larger optical absorption coefficient in the solar spectrum than crystalline silicon. Absorption depends simply upon the availability of photons and the density of states in the valence and conduction bands. The absorption coefficient is roughly an order of magnitude greater than c-Si at visible wavelengths. A-Si:H has a well defined band gap ($\sim$1.75 eV) and a thickness of only 0.5 to 1 μm is required for efficient absorption.

2.7.1 Growth mechanism of a-Si:H

Amorphous silicon is most commonly deposited by Plasma Enhnaced Chemical Vapour Deposition (PECVD) using silane (SiH_4) as the source gas. The deposition mechanism can be described as a four step process:[54].

1. The first stage is the dissociation of SiH_4 into a partly ionized reactive mixture. The SiH_4 molecules are decomposed by electron impact excitation by an RF glow discharge which generates neutral radicals and molecules, positive and negative ions, and electrons.
2. Secondary reactions in the plasma between molecules and ions and radicals result in the formation of reactive species and eventually large silicon hydrogen clusters as a powder or dust particles. Neutral species diffuse to the substrate, positive ions bombard the growing film and negative ions are trapped within the plasma.
3. Interaction of radicals with the surface of growing film. this results in radical diffusion, chemical bonding, hydrogen sticking to the surface or abstraction from the surface.
4. The sub-surface release of hydrogen and relaxation of the silicon network.

The low-temperature decomposition of silane using highly energetic RF plasma produces silicon thin films on the substrate whose optical and electrical properties depend heavily on growth parameters. The growth or deposition process is controlled by the chamber pressure, gas flow rate, substrate temperature and RF power. The gas pressure determines the mean free path for collisions of the gas molecules and influences whether the reactions are at the growing surface or in the gas[36]. The residence time of the gas species in the reactor chamber is determined by the gas flow rate and high flow rate will cause the chamber pressure to increase. The RF power controls the rate of dissociation of the gas and also the film growth rate and while substrate temperature controls the chemical reactions-nucleation and crystallinity on the growing surface[36,55].

In the deposition chamber, the first step is the electron-impact excitation, dissociation and ionization of silane source gas by the plasma. The plasma consists of neutral radicals, molecules, electrons, positive and negative ions which are sustained by an RF electric field. The dissociation mechanism in molecules takes place through the electronic excitation by inelastic collision of high energy electrons in the plasma[56]. The energy of electrons in plasma usually range from 10-30 eV. The high energy electrons cause gas ionization and release additional electrons that maintains the plasma during deposition[36]. The ionization energy of molecules are typically in the range of 10-20 eV.

Along with ionization, the other important process is the dissociation of the source gas molecules. For example, excitation of SiH_4 can lead to spontaneous dissociation to SiH_3, SiH_2, Si, H_2 and H[56]. In the same way hydrogen molecules also decomposed to atomic hydrogen. These dissociation reactions are[36]

$$\mathrm{SiH_4} \longrightarrow \mathrm{SiH_2} + \mathrm{H_2} \tag{2.2}$$

$$\mathrm{SiH_4} \longrightarrow \mathrm{SiH_3} + \mathrm{H} \tag{2.3}$$

$$SiH_4 \longrightarrow Si + H_2 \tag{2.4}$$

These generated radicals can be further modified when they undergo secondary reactions with parent SiH_4 and H_2. For a given set of conditions a plasma will find steady state conditions shortly after a deposition is initiated. The growth of a-Si:H film involves two further process after primary excitation and secondary reactions. The first process is the adsorption of silicon radicals on the growth surface and the second process is the release of the atoms or molecules from growing surface[36]. Many researchers believe that most dominant radical involved in the growth of a-Si:H film is SiH_3. It is proposed that during the growth of a-Si:H, when SiH_3 radicals arrive on the growth surface, they start to diffuse and adsorb onto the surface thereby covering the bonded hydrogen by forming SiH_4 and leaving a dangling bond on the growth-site, where other SiH_3 radical diffuses towards the dangling bong site on the growth surface and makes the Si-Si bond and thus film growth continues[57,58].

2.7.2 Radio frequency plasma enhanced chemical vapor deposition

Radio frequency plasma enhanced chemical vapor deposition (RF-PECVD) is the most widely used method for deposition of high quality hydrogenated amorphous silicon at both laboratory and industrial level. An RF (typically 13.56 MHz) electric field is used to excite the plasma. Energy transferred to silane molecules during collisions with electrons is radiated as visible light, causing the deposition method also referred as glow discharge deposition method. A schematic view of a typical RF-PECVD reactor is shown in Figure 2.11. The system consist of a gas delivery system which contains gas cylinders or lines, pressure regulators, mass flow controllers and several gas valves to handle gas flow. A stainless steel vacuum chamber with capacitatively coupled parallel electrodes, substrate holders, substrate heaters and the RF power feed through. A pumping system that usually consists of a turbo molecular pump backed with a mechanical rotary pump. An electronic and control system that consists of a DC or RF power generator with matching box and vacuum, pressure and temperature gauging and control. An exhaust system with a scrubber or a burn box to process the outlet gases.

The pressure range for a-Si:H deposition is normally between 200- 1000 mTorr. Low pressure is desirable for uniform deposition whereas higher pressure is more desirable for preparing microcrystalline silicon films[59]. The RF power should be set at between 10 and 100 mW/cm^2 for a capacitively coupled reactor. Below 10 mW/cm^2, it is difficult to maintain a plasma. Higher powers are required for high deposition rates but above 100 mW/cm^2, the reactions in the gas can create a silicon poly-hydride powder that can contaminate the growing film. This problem can be handled by using a low pressure or strong hydrogen dilution. The substrate temperature is usually set between 150 and 350 ^oC.

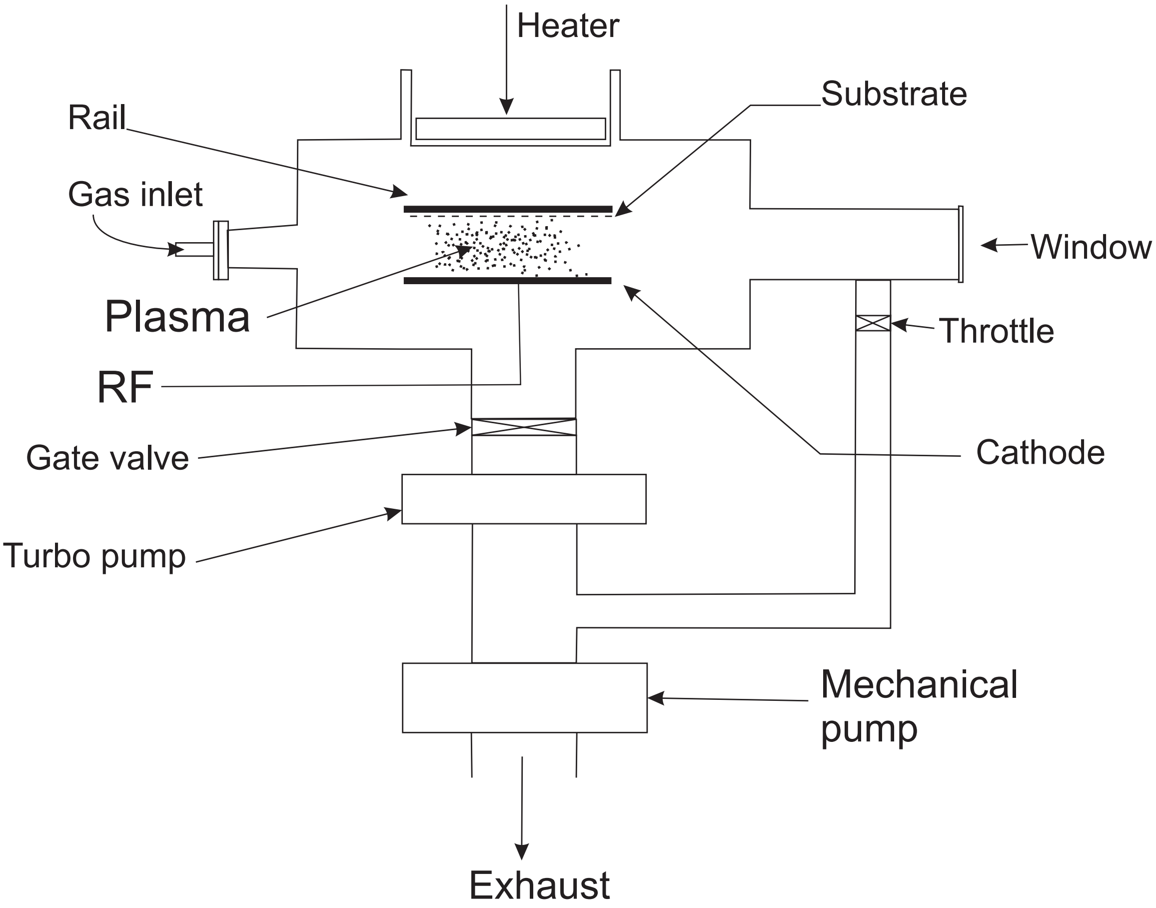

FIGURE 2.11: Schematic of typical RF-PECVD chamber

At lower temperatures, more hydrogen is incorporated in the film and this will increase the bandgap of a-Si:H slightly. At higher substrate temperatures less H is incorporated and the bandgap is slightly reduced. The electrode spacing is usually set between 1 and 5 cm for a-Si:H deposition. A smaller spacing is useful for uniformity and a large spacing is set for the ease of maintaining a plasma. The flow rate is set between 0.002 to 0.02 sccm/cm^2. The flow rate required depends on the deposition rate and area of the reactor plates and this in turn depends on the reactor and chamber size. Thin film growth by PECVD can be monitored by different tools such as optical emission spectroscopy, optical absorption spectroscopy, *in situ* ellipsometry and residual gas analysis[60].

2.7.3 VHF plasma enhanced chemical vapor deposition

Curtins et al.[61] of University of Neuchatel examined the impact of increasing the plasma excitation frequency in PECVD from 13.56 MHz up to 150 MHz. It was found that by increasing the frequency from 13.56 MHz to 70 MHz at a constant plasma power, the deposition rate increased from 3 to 10 Å/s whilst maintaining a good quality of a-Si:H as shown in Figure 2.12. The reason for the high rate of powder free deposition is suggested to be related to the shift towards higher excitation frequencies which modifies

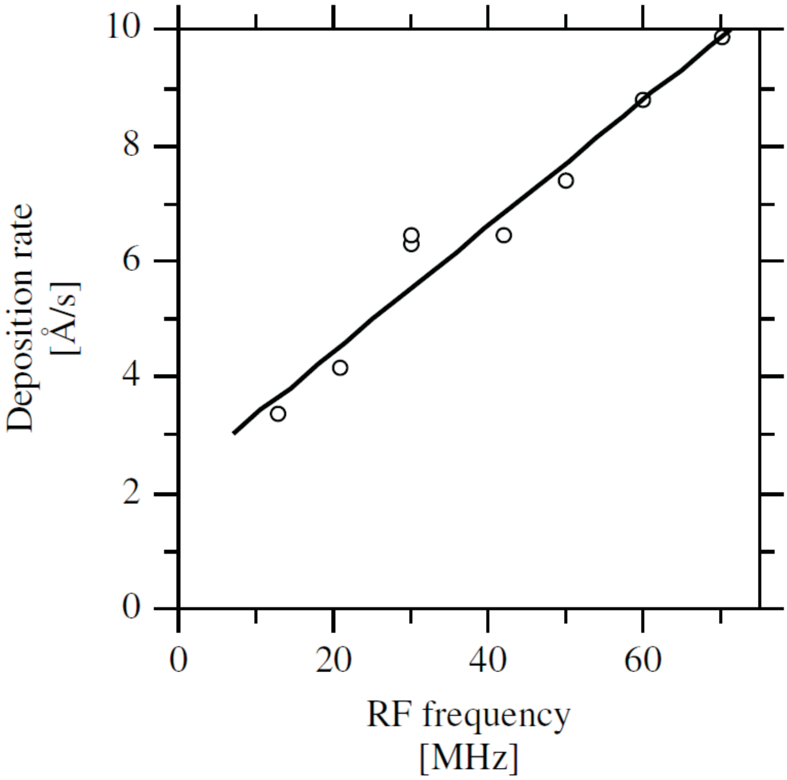

FIGURE 2.12: Deposition rate for a-Si:H films as a function of RF excitation frequency at constant power[8].

the electron energy distribution function in the plasma. This leads to a faster dissociation rate of source gases and thus higher deposition rates.

Using this technique it was possible to fabricate a *pin* a-Si:H cell with a stabilized efficiency of 9.5%. There are two principal challenges in applying VHF deposition at an industrial level. (i) the non-uniformity of the deposited layer on large substrates when the effect of standing electrical waves at high frequencies (> 60 MHz) limits its application. (ii) Effective VHF coupling of power to the plasma.

2.7.4 Hot-wire chemical vapor deposition

The schematic view of HW-CVD is very similar to RF-PECVD (Figure 2.11) except that the RF electrode is replaced by a heated filament. In the HW process, gases (SiH_4 or a mixture) are catalytically excited or decomposed into radicals or ions by a hot filament at a temperature of 1800 - 2000 ^{o}C[62]. The resulting silicon radicals diffuse inside the chamber and deposit onto a heated substrate placed several centimetres away. Low hydrogen content has been observed in deposited films which suggests that they should be stable against light induced degradation. HWCVD is considered promising because of the ability to deposit at very high rate (150 - 300^{o}A/s)[63]. Uniformity of HW films is poorer than RF-PECVD films and filaments need to be improved to reduce the maintenance time in production. HW-deposited solar cells have not yet achieved the same performance as cells prepared by RF-PECVD[64].

2.7.5 Microwave glow discharge deposition

Higher deposition rates are obtained when using a glow discharge deposition at a microwave frequency(MW) of 2.45 GHz[65]. When MW plasma is in direct contact with the substrate the deposited films show poor optoelectronic properties when compared with RF-deposited films, and are not suitable as an intrinsic layer for high efficiency solar cells. Generally, the structural properties of MW-deposited a-Si based films are also poorer than RF-deposited films. However, at a very high deposition rate ($\backsim$ 50 ^{o}A/s), the MW-deposited films will be superior to films made by RF and VHF deposition.

2.7.6 Remote plasma enhanced CVD

The remote plasma technique works on the basis of external thermal plasma chemical vapor deposition, and consists of three chamber system called CASCADE[66]. This system consist of three vacuum chambers: a load lock, an RF-PECVD chamber for the deposition of the doped layers, and an extending thermal plasma chemical vapor deposition (ETPCVD) chamber for the growth of intrinsic layers. The setup consists of a high pressure plasma source and a low pressure deposition chamber. In the cascade arc a power source in the range of 2-8 kW, the plasma is generated by DC discharge in a mixture of a non-depositing gases such as argon or hydrogen. The plasma expands quickly from a high pressure region (200 - 700 mbar) to a low pressure region (0.1 - 0.3 mbar). SiH_4 is injected at this point and dissociated by the reactive species coming from the plasma source[67]. Hydrogen flow plays an important role in high quality film deposition. The deposition rate depends on gas flows, current flow, and substrate temperature[68]. amorphous films and solar cell with remote PECVD method yielded poorer in quality and performance compared with RF PECVD deposited films and devices. They also could not be easily scaled up to provide large-area uniform films or for large-scale a-Si PV production.

2.8 Hydrogenated amorphous silicon solar cell configuration and structures

Amorphous silicon based solar cells can be deposited in different types of structures. These device structures are single junction cells, Schottky barrier cells and several types of multiple junction cells. A variety of different substrate materials including glass, metal foils and plastics can also be used depending on the application. Any substrate can be used for a-Si:H cells with conditions that it should not contaminate the amorphous silicon film and must be able to endure temperatures of 150 ^{o}C- 300 ^{o}C.

2.8.1 Single junction solar cells

Single junction a-Si:H solar cells are classified into two structures which are the *pin* configuration and the *nip* configuration. These structural configuration are actually based on the deposition sequence of a-Si:H on the substrate. In the *pin* configuration, *p*-type a-Si:H is deposited first followed by intrinsic a-Si:H and then *n*-type a-Si:H deposited last. The *nip* configuration is the reverse of *pin* configuration, where *n*-type a-Si:H is deposited first, intrinsic a-Si:H second and *p*-type a-Si:H last.

The *pin* configuration is also referred as superstrate configuration and this requires a transparent conductive substrate carrier. The thicknesses of the three thin layers are typically 10 nm for *p*-type, hundreds of nm typically for the un-doped intrinsic layers and 20- 40 nm typically for the *n*-type layers. These are deposited on a transparent substrate as shown in Figure 2.7. A transparent conducting oxide (TCO) film on glass is used as a substrate carrier which provides a platform where these layers are being deposited. During operation sunlight enters into the device through the glass and the TCO film which also serves as the front contact. There are some requirements for TCO film to work with solar cells, such as it should have high optical transmission in 350 nm to 950 nm wavelength range, low sheet resistance, temperature stability and chemical longevity. Further properties of TCO films are discussed later in this chapter. The back contact of this configuration is on the *n*-type layer and usually formed by evaporation or sputtering of around 500 nm of aluminium.

The *nip* configuration is known as the substrate configuration in which *nip* structure of a-Si:H is deposited on an opaque substrate. This opaque substrate works as back reflector which is again a two-layer structure with textured silver or aluminium and textured TCO[69 6]. The front contact in substrate configuration is a TCO film and is the first layer in the device to receive light. This opaque substrate material can be stainless steel or a temperature resistant flexible polymer, however, a textured surface is essential to scatter incoming and back-reflected light.

Generally glass plates are used for the superstate configuration while flexible metal or polymer foils are used in substrate configuration. In both configuration *nip* and *pin* structures become sandwiched between front and back contacts. Sunlight enters from the front contact and propagates to the thicker intrinsic layer where most of the light is absorbed. Each photon that is absorbed will generate one electron and one hole[6 70]. The photo-generated charge carriers are collected by the built-in electric field, which causes the drift of holes and electrons into the *p*-type and *n*-type layers, respectively.

Some charge accumulates in these regions and increase the potential dropped across the junction while many photogenerated carriers form a photocurrent and thus electricity is generated by the solar cell.

2.8.2 Multijunction solar cells

A solar cell with two or more junctions is called a multijunction solar cell. The first multijunction cells were used to enhance the output voltage of a-Si:H solar cell[71]. Soon it was realised that a-Si:H solar cells can be stacked to build multijunction cells for improved output voltage and stabilized performance[72]. The main benefit of amorphous silicon usage in multiple junction cells is that there is no need for lattice matching as would be required in a crystalline heterojunction. The fundamental concept behind multijunction solar cells is spectral splitting, but their design is more complex than a single junction cell. There are two requirements for a multiple junction cell to be successful.

- *Current matching*: The current generated at the maximum power point has to be equal for each component cell as the minimum current density cell will limit the total current flow of the device.
- *Tunnelling matching*: The internal series connection between the component cells has to feature low electrical losses.

Ideally, stacked based configuration approach has few advantage which are; (a) the optical absorption of sunlight can be enhanced by combining the materials having different bandgaps; (b) it is possible to obtain a higher open circuit voltage and, at the same time, work with lower current densities, so that the problems for electrical series resistance are relatively reduced, and (c) it is possible to reduce light induced degradation by the use of a thin amorphous top cell[6].

2.8.2.1 The Micromorph solar cell

The concept of micromorph first materialised by the Neuchatel group my making an a-Si:H *pin* junction as the top cell and a nc-Si *pin* as the bottom cell. A sketch of such device is shown if Figure 2.13. From computer modelling, it is determined that a bandgap of 1.7 eV for the top cell and 1.1 eV for the bottom cell would make near ideal combination for double junction configuration[50,73,74]. In order to obtained current matching requirement, both top and bottom cell have to generate same amount of current which enforces to make the absorber layer of the bottom cell more thicker than top cell as it has low bandgap. On the other-hand light induced degradation also forced to make top cell as thin as possible. Due to these constraints and to get higher currents, the

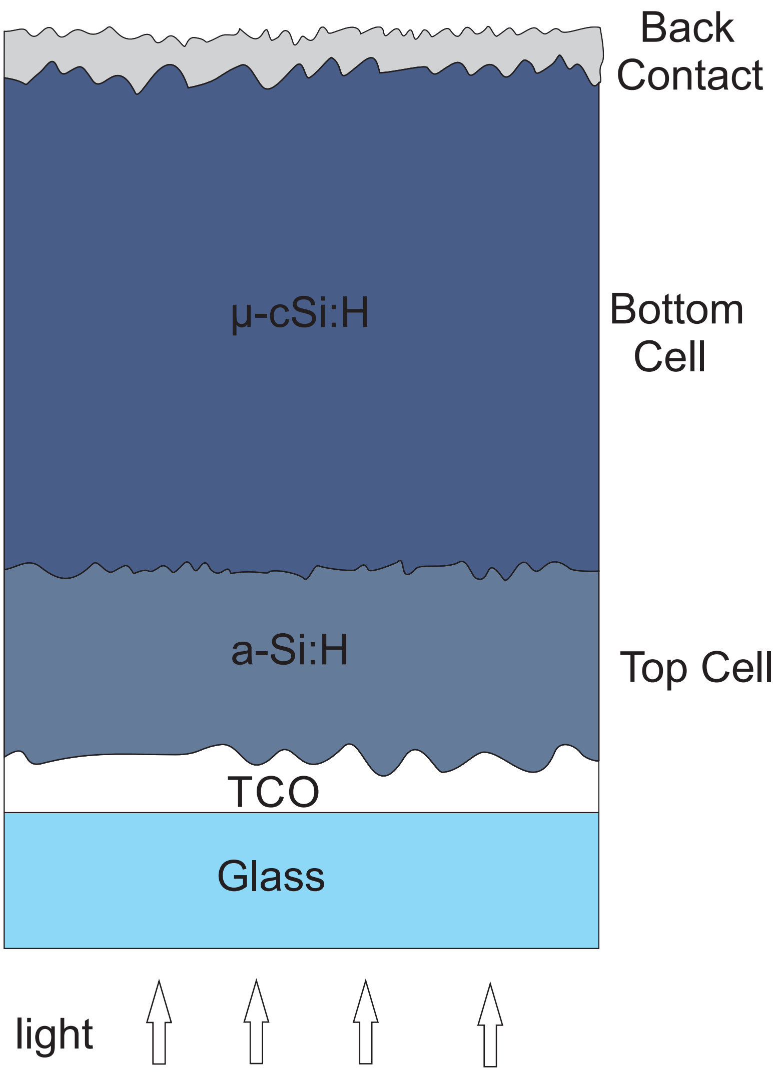

FIGURE 2.13: Schematic device structure of the micromorph tandem cell in the superstrate configuration (glass/TCO/p-i-n a-Si:H/p-i-n c-Si:H.

bottom cell is usually kept 1.5-2.5 μm thick where as top cell thickness kept at 250 to 300nm.

For the stabilized efficiencies in micromorph tandem cells, an approach of highly transparent but semi-reflective dielectric layer can be inserted at the tunnel junction between the top and the bottom cell[75] is used. The semi-reflective dielectric layer such as ZnO or SiO_2 enables current matching by increasing the current by interface reflection, without increasing the thickness of absorber layer of top cell. Current stabilized performance of micromorph cells have efficiency up-to 12%[76].

2.8.2.2 The triple-junction solar cell

The addition of third layer in tandem cell makes is triple junction solar cell. In this design approach, with 1.8 eV bandgap, a-Si:H based top cell with a 1.6 eV a-SiGe as

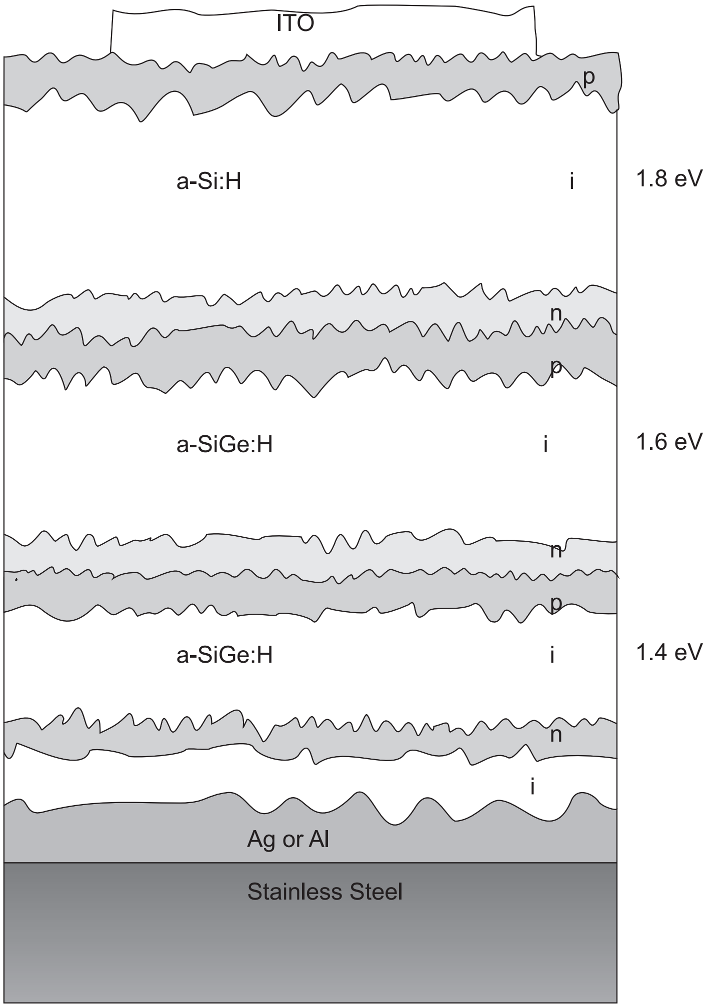

FIGURE 2.14: Structure of a a-Si:H/a:SiGe:H /a-SiGe:H triple junction with corresponding band gaps

middle cell and a μc-Si cell 1.1 eV bandgap as bottom cell are used[77]. For current matching, the short circuit current density can only be used as a rough guide. A triple junction cells, the top cell normally has a high FF, whilst the bottom cell has the lowest FF. As a result J_{SC} for the bottom cell needs to be be greater than J_{SC} for the middle cell, which in turn should be slightly greater than J_{SC} for the top cell. The intentionally mismatched value of J_{SC} normally lies in the range of 0.5 - 1 mA/cm^2. The presence of a back reflector in a multi-junction cell is most beneficial for the bottom cell.

2.9 Optimisation of solar cells

Since 1976, when the a-Si:H solar cell was first reported[53], every effort has been made to improve its performance. There are many research tracks where improvements have been sought, particularly light degradation, material optimisation, structure engineering and new amorphous alloys. In a-Si:H based solar cells either as single junction or multi-junction, absorption of incoming sunlight always takes place in the undoped intrinsic region regardless of the configuration. This absorption of incoming light carries provides current generation. Therefore a key requirement in a-Si:H device optimisation is to extend absorption in the intrinsic layer and at the same time minimize any photon or carrier loss. There are many other inter related parameters upon which solar cell performance depends and we will discuss one by one mainly focusing on single junction structures.

For an a-Si:H device to work properly and efficiently, its intrinsic layer must have sufficiently high optical absorption coefficient in the AM1.5 spectral range. The absorption coefficient of a-Si:H as a function of photon energy is shown in Figure 2.10. For photon energies above the bandgap, the absorption coefficient of intrinsic a-Si:H layer is significantly higher. For energies more than 2eV, a-Si:H is superior in absorption coefficient compared to c-Si and μc-Si as both materials are crystalline in nature and have indirect bandgap. Long range structural disorder of a-Si:H helps it to behave like a direct bandgap but still this is from being a real direct bandgap semiconductor in terms of absorption coefficient. Nevertheless the relatively high absorption occurs primarily by the transitions between valence band and conduction band extended states in a-Si:H. The penetration depth of a-Si:H is still very large at longer wavelengths specially in the red and infra-red regions of the spectrum, and to absorb this part of spectrum an intrinsic layer must be very thick. This will create serious carrier collection problems, so a compromise has to be found and light trapping techniques can provide real advantages.

The Conduction band tail distribution is narrower than the valence band tail distribution; and the slope of the absorption edge is evidence that there are band tails in the material. These in turn are the measure of structural disorder. The slope of exponential absorption edge determines the *Urbach energy*, and for a-Si:H, device grade material should have an *Urbach energy* less than 45meV[7].

In the low energy region, the absorption coefficient is relatively very small and is associated to transitions related defect to states such as dangling bonds and recombination centres. For device grade material, defect passivation is necessary for a-Si:H and it should have low defect absorption.

Device grade intrinsic a-Si:H layers must have sufficiently high carrier mobility and lifetime for photo-generated charge carriers. For intrinsic a-Si:H mobility-lifetime products have been calculated in the range 1×10^{-7} - 1×10^{-6} cm^2/V[78–81] which are relatively high, and according to these values an a-Si:H solar cell with 1000 nm thick intrinsic layer should collect significant photo-generated charge carriers without recombination loses[7]. However, in practice actual a-Si:H devices are unable to collect sufficient charge carriers, and device performance is seriously degraded. Actual mobility-lifetime product is found much lower than above mentioned values[82]], so is recommended that the intrinsic layer in a-Si:H solar cell should be kept under 400 nm to prevent severe recombination losses after light soaking stabilization. This poor charge collection is partly attributed to non-uniform electric field profile in the intrinsic region.

It is also essential that intrinsic layers must hold a high and uniform electric field profile created by doped layers. However charged dangling bonds, band tails states, and defect-rich interface regions are always present within the device which causes deformation of the internal electric field within the intrinsic a-Si:H layer. Direct measurements of the non-uniform electric field profile in the intrinsic regions are difficult to obtain, but an indication can be estimated using the time-of-flight technique[83,84]. The information about the spatial collection efficiency in a-Si:H solar cells is also be obtained from the Dynamic Inner Collection Efficiency (DICE) technique where influence of i-layer deposition parameters, such as the temperature and deposition time, on the spatial collection efficiency have been investigated[85]

The p-type layer in a a-Si:H based solar cell is called a *window* layer as sunlight enters through it into the intrinsic layer, preferably without being absorbed. High V_{OC} values can be partly obtained by optimizing p-type layer. The dopant incorporation into the intrinsic layer introduces extra defect states and additional dangling bonds which act as recombination centres[86]. As a result, doped layers cannot be used as an active absorber and any carriers that result from absorption in doped layers will be lost. Therefore window layers are always kept as thin as possible to reduce the levels of optical absorption. When illuminated, most of the photo-generated carriers are created near the surface of the solar cell and therefore holes have to travel less distance through the cell for collection. This is also beneficial due to the fact that holes have significantly lower mobility as compared to electrons, so hole collection efficiency can be increased by using this topology.

Even with smaller thickness, there is still considerable absorption in the p-type a-Si:H layer as boron doping introduces more defects. The alloying of carbon content into a-Si:H can tune its bandgap which can decrease the absorption in the p-type layer[40,87]. This carbon alloyed a-Si:H layer is denoted by a-SiC:H and its bandgap can be tuned up to 2.3eV. This boron doped μc-Si:H layers have also been used as window layers and it is argued that V_{OC}, FF and I_{SC} can be improved[88,89]. Use of a double p-type window layer composed of μc-Si:H and a-SiC:H has been reported in order to improve the p/i interface[90].

The a-Si:H based solar cell in any configuration always uses a wide band-gap window layer and narrow band-gap layer(s) in the absorber regions. This band offset at the P/I interface plays a crucial role in device performance as it creates a barrier in valence band for photo-generated holes to the doped layer. To hold back diffusion of electrons into the p-type layer and to optimise the electric field profile, generally a thin, wide band-gap, high quality intrinsic film or lightly doped a-Si:H or a-SiC:H buffer layer is deposited at the p/i interface[91]. These buffer layers also prevent boron diffusion from p-type into the intrinsic layer[92].

The a-Si:H based solar cell optimization proceeds to the use of double and triple junction technologies but we will focus on textured TCO usage which is discussed in next section as well as in Chapter 5.

2.10 Transparent conducting oxides and light trapping

Thanks to great technological interests in both, a wide variety of materials available for photovoltaic and related technologies have been created. In case of a-Si:H based devices, efficient light trapping is an active research area. Efficient light trapping enables us to enhance optical path-lengths for the light within the absorber layer of the device.

The main aim of light trapping is to absorb as much as light as possible and prevent it from escaping from the device. In a-Si:H based solar cells, light trapping is based on the principals of light scattering at rough surfaces, usage of highly reflective back contacts, and refractive index matching layers within the device. Light scattering at rough surfaces enables longer average optical paths in the absorber layers. Repeated reflection of scattered light between the back reflector contacts and front contact creates multiple passes of light through the absorber layer and thus prevents the light from escaping. The process of light trapping considerably enhances the optical absorption in absorber layers, and increases the photo-current of the device. Textured transparent conducting oxide layers (TTCOs) play a vital role in the light trapping in both superstate and substrate configuration of a-Si:H based devices.

In the superstrate configuration, it is the TTCO film which introduces a rough surface interface to the absorber layer of the device. This TTCO film also serves as the top contact of the device. In case of substrate configuration, a textured back reflector introduces the rough surface. However in some circumstances current enhancement can be limited by surface plasmon absorption in the back reflector metal[93].

For TCO materials to be considered as devices grade, they should qualify following fundamental requirements[94].

- Exhibit a large enough bandgap so that absorption due to band-to band transitions is limited to the ultraviolet regions and will not diminish cell current.
- Have suitable extrinsic or intrinsic dopant that form shallow states and can be introduced in a sufficient quantity.

- The material should not be liable to formation of compensating defects upon shifts of the Fermi level

The band-gap requirement of TCO is based on the minimum of luminosity function of the human eye, which is 380 nm. The corresponding band-gap is about 3.3eV which is a suitable minimum band-gap for photovoltaic applications.

The optical transmission in TCO devices as function of wavelength can be distributed into three regions. In first region, photons with energy larger than the band-gap (short wavelength) of TCO film are absorbed. In the second region, photons with visible wavelength are transmitted through the TCO. In this high transmitted region, optical absorption is low but not negligible. In the third region infra-red photons are reflected by the TCO.

The electrical properties of TCO layer are defined by its conductivity (σ) which is determined by the free carrier concentration and the carrier mobility. The reciprocal of the conductivity is called resistivity (ρ). The sheet resistance (R_{sh}) TCO film is given by

$$R_sh = \frac{\rho}{t} \tag{2.5}$$

Where t is the TCO film thickness.

A high doping level is essential for TCO films, as at high doping levels films are metal-like in behaviour. This can be done by achieving doping levels above 10^{20} cm^{-3}. In addition to these electrical and optical properties, TCO films require other considerations such as surface morphology, in-process physical and chemical stability, and toxicity. The formation of compensating intrinsic defects can severely limit oxides applicability as transparent semiconductors.

In TCO material selection, there is delicate trade-off between film optical absorption and sheet resistance. The sheet resistance of a film at given resistivity can be decreased by increasing the film thickness but it will decrease the optical absorption. Therefore optimal film thickness is essential in TCO films in order to minimise the total power loss.

In photovoltaic application most commonly used TCO materials are described below.

ZnO: The transparent conductive zinc oxide is usually prepared by sputtering or by LPCVD with Al or Ga doping. The ZnO TCO has optical transmittance over 85% with resistivity 3×10^{-4} Ω-cm, and higher mobility of 44 cm^2/V-s[95].

SnO_2: Tin oxide TCOs are usually deposited by APCVD in which doping element Fluorine (F) is used. The SnO_2:F films have sensitivities in 5-8 $\times 10^{-4}$ Ω-cm range, with carrier mobility of 70 cm^2/V-s[96].

In_2O_3: The popular method for Indium(III) oxide as a TCO material is with Tin dopant in e-beam evaporation. This TCO material has very lowest resistivity 0.44 $\times 10^{-4}$ Ω-cm and higher mobility value 103 cm^2/V-s[97].

Generally for a-:Si:H based solar cells, TCO films made with fluorine-doped tin oxide are used with thickness 550-900 nm range whereas the sheet resistance 8-16 $\Omega/\Box$ range. As the absorption coefficient in a-Si:H based thin film solar cells is low in the near infrared region, light trapping by textured TCO is essential. A textured TCO film has ability to scatter light and enhance the optical path-length, therefore TCO morphology has considerable effects on the performance of thin film solar cells.[98]. The light scattering capability of a TCO material is determined by the a parameter called *Haze* which is the ration of the diffuse transmittance to the total transmittance of the the film. Additionally surface features play very important role in the determining the capability TCO film generating light trapping[99].

To summarise, the detailed information to understand a-Si:H material, its atomic and band structure with density of states are discussed. The absorption capability in a-Si:H is much stronger that c-Si and a thin layer of a-Si:H can absorb more than 90% of available incident light. The deposition parameters can be used to control certain properties of a-Si:H such that material's bandgap can be tuned to particular application requirement such as single junction or multijunction device. The a-Si:H can easily be doped n-type or p type and its allows can be grown accordingly. Low temperature growth capability enables a-Si:H to be deposited virtually on any substrate such as from expensive glass to low cost opaque or flexible materials. We have also discussed solar cell configuration as a single junction, double junction and triple junction devices, and device requirements. At the end textured TCO films are briefly discussed which are integral part of a-Si:H based devices. In the next chapter this information has been used to fabricate device grade a-Si:H layers, their optical and electrical properties are extensively discussed.

Chapter 3

Experimental details

In this chapter, the fabrication methods and characterisation techniques used in this work are presented. The techniques have been broadly split into two sections, optical and electrical characterisation.

3.1 Film Deposition and Device fabrication

3.1.1 Sample preparation

In this report, plain soda lime glass and various types of TCO coated glass are used as substrate materials for films and devices. To remove dust and organic contaminations, substrates were cleaned using the following steps.

1. Each substrate was washed in de-ionized water with 4% of Decon-90 detergent for removal of any finger grease and other organic contaminations.
2. Drying with nitrogen and cleanroom soft tissue paper.
3. Pressurized wash with de-ionized water and dried with nitrogen.
4. 15 minutes ultrasonic bath in acetone and dried with nitrogen.
5. 15 minute ultrasonic bath in isopropanol and dried with nitrogen

Gloves are used in all processes and finally all sample substrates kept in clean boxes for a-Si:H growth steps. All substrate dimensions are 50 × 50 mm.

3.1.2 PECVD procedures for deposition of films and devices

The detailed growth mechanism of a-Si:H by a typical PECVD system is discussed in section 2.7. This section provides additional operational information about the plasma deposition tool. All intrinsic, doped a-Si:H films and solar cells produced in this work were deposited by an Oxford Instruments PLasmaLab System 100 capacitive PECVD system. This system is also able to deposit micro, and poly-crystalline silicon/germanium. It has a heated stage which allows growth of semiconductors from the amorphous to the poly-crystalline phase up to a maximum temperature of 650^{o}C. A dual frequency mix of low frequency (LF) and radio frequency (RF) for plasma excitation is available.

This system features 7 input gases including silane, phosphine, diborane, germane, argon, hydrogen, and nitrogen for use during film deposition and 2 additional gases tetrafluoromethane and oxygen for chamber cleaning. This system uses 100% silane as the silicon source for the growth of basic intrinsic amorphous deposition while the *p* and *n*-type doping of deposited layers is achieved using diborane and phosphine supplied as process gases diluted in argon. Pure hydrogen was connected to the system to enable dilution of silane.

TABLE 3.1: The list of the gases available to the PECVD system with dilution and MFC maximum flow

Gas -	Dilution (%)	MFC Max (%) (sccm)
SiH_4	0	100
PH_3	10	50
B_2H_6	10	50
GeH_4	10	50
H_2	0	100
Ar	0	500
N_2O	0	500
CF_4	0	500
O_2	0	100

The PECVD system is fully automated and operated via a PC2000 user interface running on a desktop PC. A typical process control screen window is shown in Figure 3.1. The PECVD system configuration incorporates:

- Full-diameter gas inlet shower-head
- Edwards EH250/E2M40 pumping system
- Heating table with ”PID” controller
- 10-300 W, 13.56 MHz solid state RF generator
- Digital close-coupled automatic impedance matching unit

- Automatic process pressure control unit.

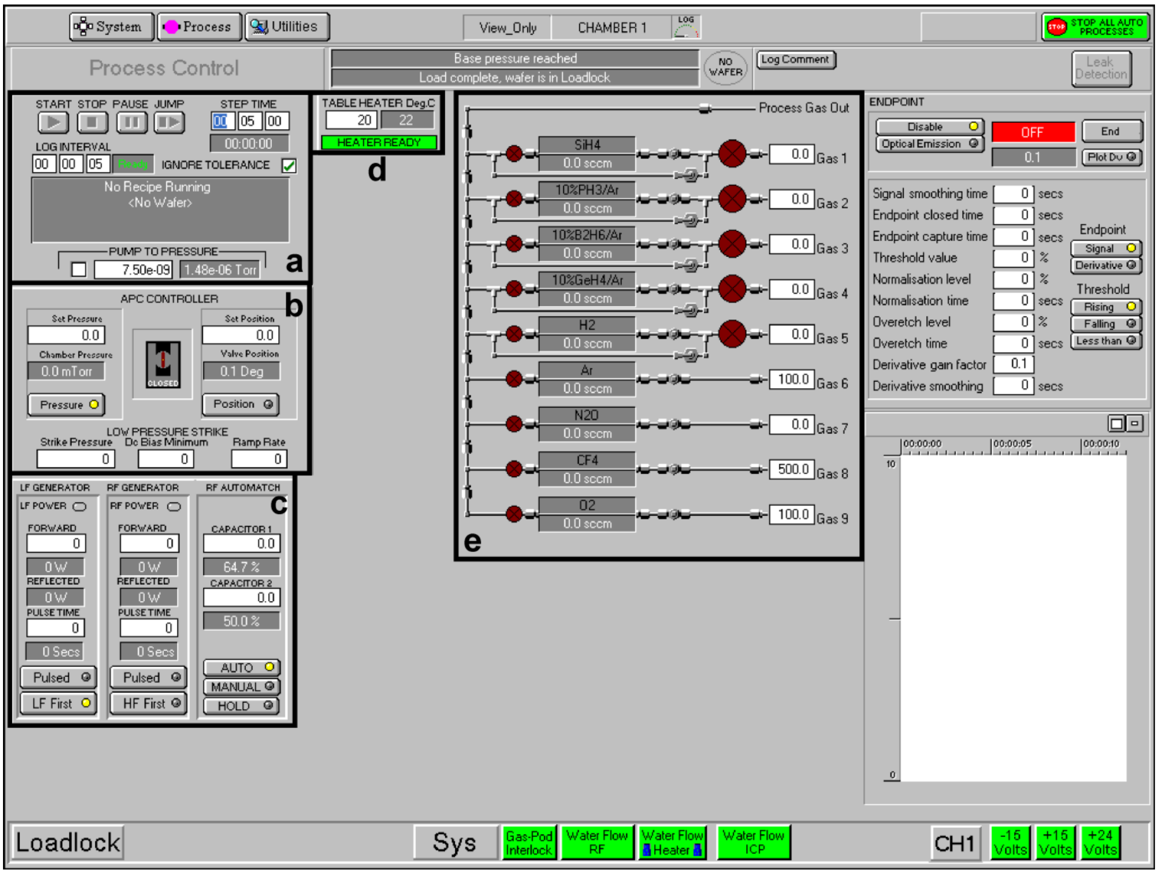

Base pressure reached
Load complete, wafer is in Loadlock

STEP TIME 00 05 00
00:00:00
LOG INTERVAL 00 00 05
IGNORE TOLERANCE ☑

No Recipe Running
<No Wafer>

PUMP TO PRESSURE ☐ 7.50e-09 1.48e-06 Torr

TABLE HEATER Deg.C 20 22

Set Pressure 0.0
Chamber Pressure 0.0 mTorr
Set Position 0.0
Valve Position 0.1 Deg

Strike Pressure 0
Dc Bias Minimum 0
Ramp Rate 0

LF GENERATOR: FORWARD 0, 0 W; REFLECTED 0 W; PULSE TIME 0, 0 Secs
RF GENERATOR: FORWARD 0, 0 W; REFLECTED 0 W; PULSE TIME 0, 0 Secs
RF AUTOMATCH: CAPACITOR 1 0.0, 64.7 %; CAPACITOR 2 0.0, 50.0 %

Gas	Flow	Set	
SiH4	0.0 sccm	0.0	Gas 1
10%PH3/Ar	0.0 sccm	0.0	Gas 2
10%B2H6/Ar	0.0 sccm	0.0	Gas 3
10%GeH4/Ar	0.0 sccm	0.0	Gas 4
H2	0.0 sccm	0.0	Gas 5
Ar	0.0 sccm	100.0	Gas 6
N2O	0.0 sccm	0.0	Gas 7
CF4	0.0 sccm	500.0	Gas 8
O2	0.0 sccm	100.0	Gas 9

Signal smoothing time	0	secs
Endpoint closed time	0	secs
Endpoint capture time	0	secs
Threshold value	0	%
Normalisation level	0	%
Normalisation time	0	secs
Overetch level	0	%
Overetch time	0	secs
Derivative gain factor	0.1	
Derivative smoothing	0	secs

FIGURE 3.1: The process chamber control screen of PC2000 for PECVD growth deposition.

To deposit a typical amorphous film, a combination of various gases, and selection of appropriate control parameters were required. A typical base process recipe for amorphous film is:

- 100% SiH_4 25sccm
- Ar flow 475 sccm
- B_2H_6 flow 5-15sccm (p-doping option)
- PH_3 flow 5-15sccm (n-doping option)
- Pressure 1000 mTorr
- R.F. power 10 Watts @ 13.56MHz
- Temperature 250^{o}C

Process optimisations for amorphous films with specific properties to suit photovoltaic applications is discussed in chapter 4. A Leybold Optics BAK600 e-beam evaporator was used to deposit the aluminium contact grid for electrical characterisation of a-Si:H devices and films. A chamber at a pressure level between 10^{-5} and 10^{-6} mbar was required for evaporation, evacuated using a rotary pump and pumped further using a diffusion pump prior to deposition. During its operation, the generated electron beam is directed at the aluminium source material where its energy in converted into heat. The beam power can be controlled by an Inficon IC-5 Deposition Controller to provide variable heating energy. The aluminium is vaporized to produce an evaporation cloud which rises and then condenses on the substrate, forming thin layers of the material. Layer thickness is built up over a period of time and measured by a quartz crystal thickness monitor, located at the substrate level. The deposition rate is directly related to the evaporation rate which is controlled by adjustment of the cathode filament supply. Most of the time, 500nm of layer was deposited on substrate as back contact.

3.2 Optical characterisation

Ellipsometry was chosen as the primary method to determine the optical properties of a-Si:H based thin films. A J.A. Woollam variable angle M-2000D Ellipsometer system was used fitted with deuterium and tungsten halide light sources. This dual beam configuration allowed fast spectroscopic measurements across the 200-1800nm wavelength range. The ellipsometric optical analysis technique is a non-contact and non-destructive method for the characterization of thin films and multi-layer semiconductor structures. Ellipsometry determines the change in polarization state of light reflected from a sample, and uses a model based technique to characterize film thickness and complex refractive index. The film can be transparent or absorbing on a transparent or opaque substrate.

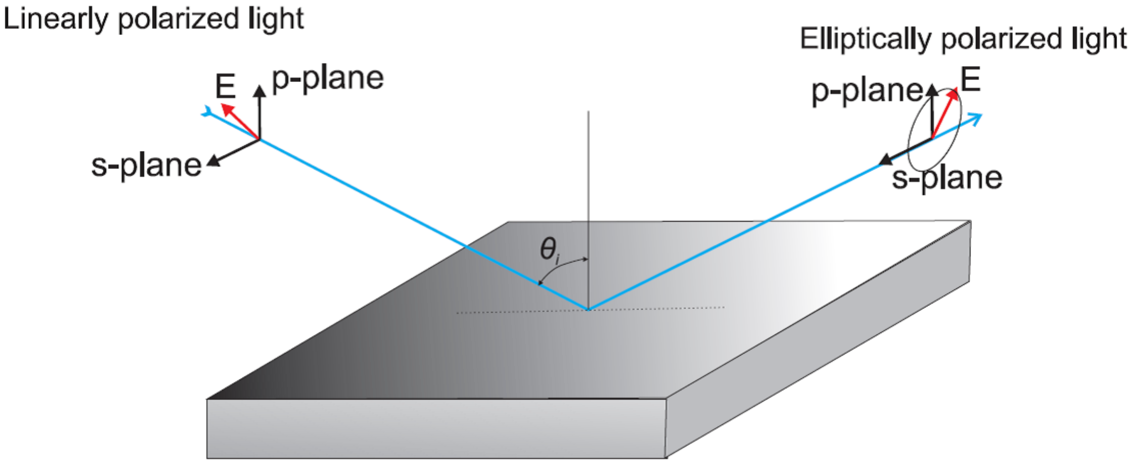

Figure 3.2: In Ellipsometry characterisation, interaction of polarized light with a sample to determine optical parameters.

There are two polarization directions for reflected light as shown in Figure 3.2. The plane of incidence of light is the plane containing the incident beam and the normal to the surface of the sample. Light polarized parallel (p-plane), and perpendicular (s-plane) to this plane will remain plane polarized upon reflection. The ellipsometer measures the polarization change of reflected light in terms of the ratio of the reflected p- and s- components (ψ) and the phase difference (Δ) between these two components. These two parameters are related by:

$$tan(\psi).e^{(i\Delta)} = \frac{r_p}{r_s} \tag{3.1}$$

Where r$_p$ is the reflectivity of the p-polarized light and r$_s$ is reflectivity of the s-polarized light. Both parameters are used to build an optical model that represents the nominal structure of the sample. This model is used to generate the material data. Model fit parameters are defined and then automatically adjusted by the software to improve the agreement between the measured and model-generated ellipsometric data. This is known as fitting. Various optical functions or oscillators are available for data extraction such as the Cody-Lorentz oscillator to model absorption in an a-Si:H film. The quality of the fitted data is quantified by the mean squared error (MSE) which summed over all the measurement wavelengths and represents the differences between the measured data and the model-generated data. The lower the MSE value the better the fit or agreement between the measured and model generated data. The data obtained from ellipsometry consists of film thickness, roughness, bandgap energy, refractive index and extinction coefficient. This data is then used to calculate the absorption coefficient $\alpha(\lambda)$ of the deposited layer. The absorption coefficients of the intrinsic a-Si:H films as a function of photon wavelength which determined by the equation:

$$\alpha(\lambda) = \frac{4\pi k(\lambda)}{\lambda} \tag{3.2}$$

Where $k$is the extinction coefficient that describes the attenuation of light in a medium (thin film). The absorption in the intrinsic layer is calculated by a Matlab program using data obtained from ellipsometry with equation 3.3 in which d_p, d_i, α_p and α_i are the thickness and absorption coefficient of p and intrinsic layer respectively:

$$\alpha(\%) = e^{-d_p\alpha_p(\lambda)}\left(1 - e^{-d_i\alpha_i(\lambda)}\right) \tag{3.3}$$

3.3 Transmittance and Reflectance

The direct measurement of transmittance and reflectance spectra were carried out using Bentham PVE 300 system as shown inFigure 3.3. This system uses an integrating sphere which is coated with Barium Sulphate which provides highly diffuse reflection. A monochromatic probe based on a Bentham TMc300 single monochromator and typically a Xenon/Quartz halogen light source, was directed onto the sample under test, giving coverage over the spectral range 350-1800nm.

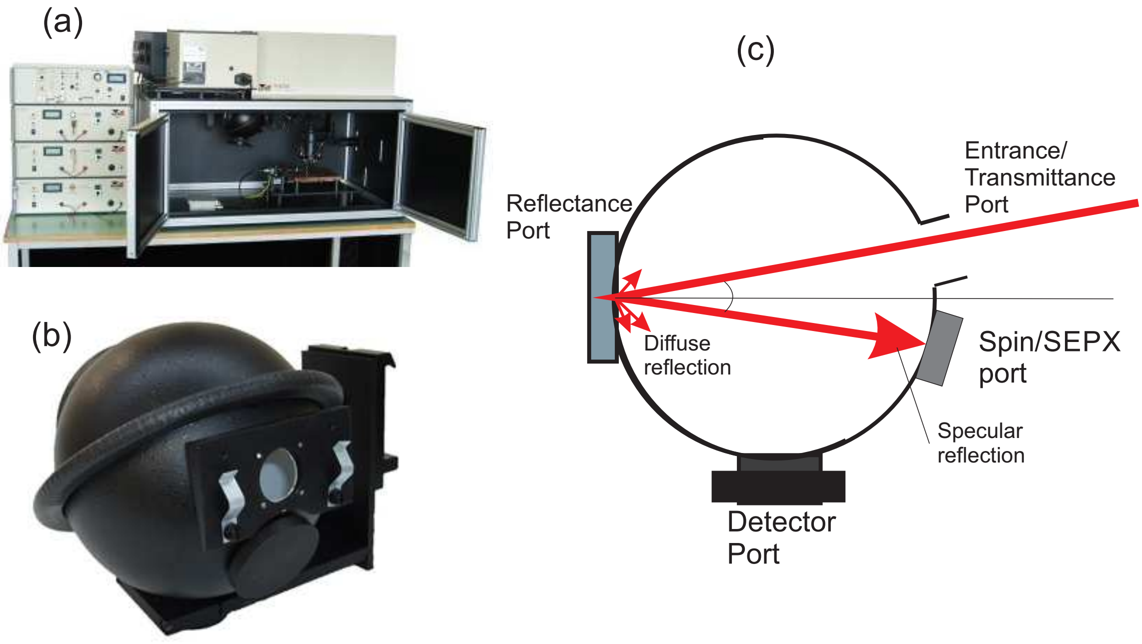

Figure 3.3: Bentham system for optical measurements. (b) The integrating sphere with sample and detector mount port for measurements. (c) typical sketch of reflectance measurement inside integrating sphere.

The reflectance of film is made with respect to a reference standard of reflectance. The sphere is positioned so that the probe beam is focussed onto the plane of the reflectance sample port as shown in Figure 3.3-(c). There are two selections available for the measurements, specular and diffuse reflection. The specular reflectance can be measured by placing a reflective plug at the SPIN/SPEX port, while the diffuse reflectance can be measured by mounting light trapping port at respective positions in the integrating sphere.

The transmittance measurement is done with respect to system default measurement with no reference sample in place. During this measurement, transmitted light is collected through 2π steradians behind the device in integrating sphere.

3.4 Raman spectroscopy

Raman spectroscopy was used to determine he structural information of intrinsic microcrystalline silicon and germanium films. Raman spectroscopy is the shift in wavelength of the inelastically scattered radiation when sample is illuminated by laser beam. This scattered light is shifted in energy from the laser frequency due to interactions between the incident light and the vibrational energy levels of the molecules in the sample. Plotting the intensity of this *shifted* light with respect to frequency results in a Raman spectrum of the sample. The Raman data was then processed and fitted to extract film information which is explained later in chapters 5 and 7. In this work Renishaw inVia microscope Raman system was used.

3.5 Atomic force microscopy

The surface morphology of TCO materials were determined by atomic force microscopy (AFM). A three dimensional profile of film surface can be generated measuring force between a probe (scanning tip) and the sample. A general working principle of AFM is shown Figure 3.4. The image is obtained by measuring the vertical and lateral deflections of the tip. A laser beam reflected off the cantilever and operate the optical lever. The reflected laser beam strikes a position and photo sensitive detector. In this work, Veeco Calibre SPM system was used for AFM characterisation of TCO materials.

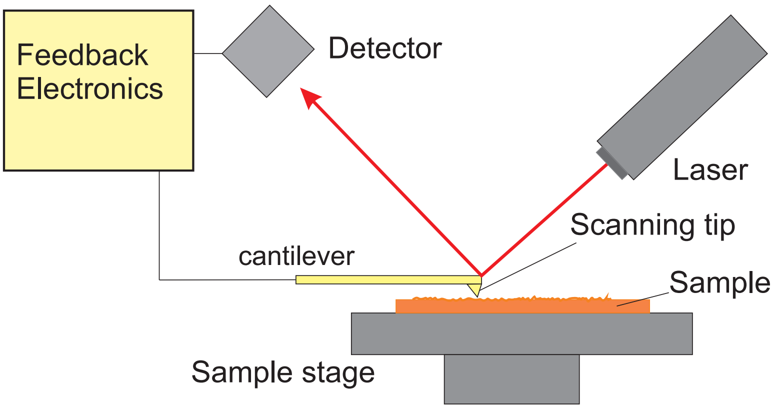

FIGURE 3.4: The block diagram of AFM principle of operation.

3.6 Electrical characterisation

In this work, two types of electrical measurement were performed. For a-Si:H solar cell performance, IV-characteristic measurements were used and for single layer, room temperature electrical conductivity was used to determine the film quality and doping levels.

Under dark conditions, the current and voltage of a p-$n$junction are related to each other by an exponential expression which can be used to determine the performance of a solar cell. When the solar cell is illuminated, light creates electron-hole pairs. The electric field at the junction separates these charges and drives them in opposite directions. The IV-characteristic of solar cell is given by

$$I = I_{pl} - I_s(e^{qV/nkT} - 1) \tag{3.4}$$

Where $\mathbf{I}_{pl}$ is the photo-generated current, I_s is the diode saturation current in the dark, T is absolute temperature, k is Boltzmann constant and n is diode ideality factor.

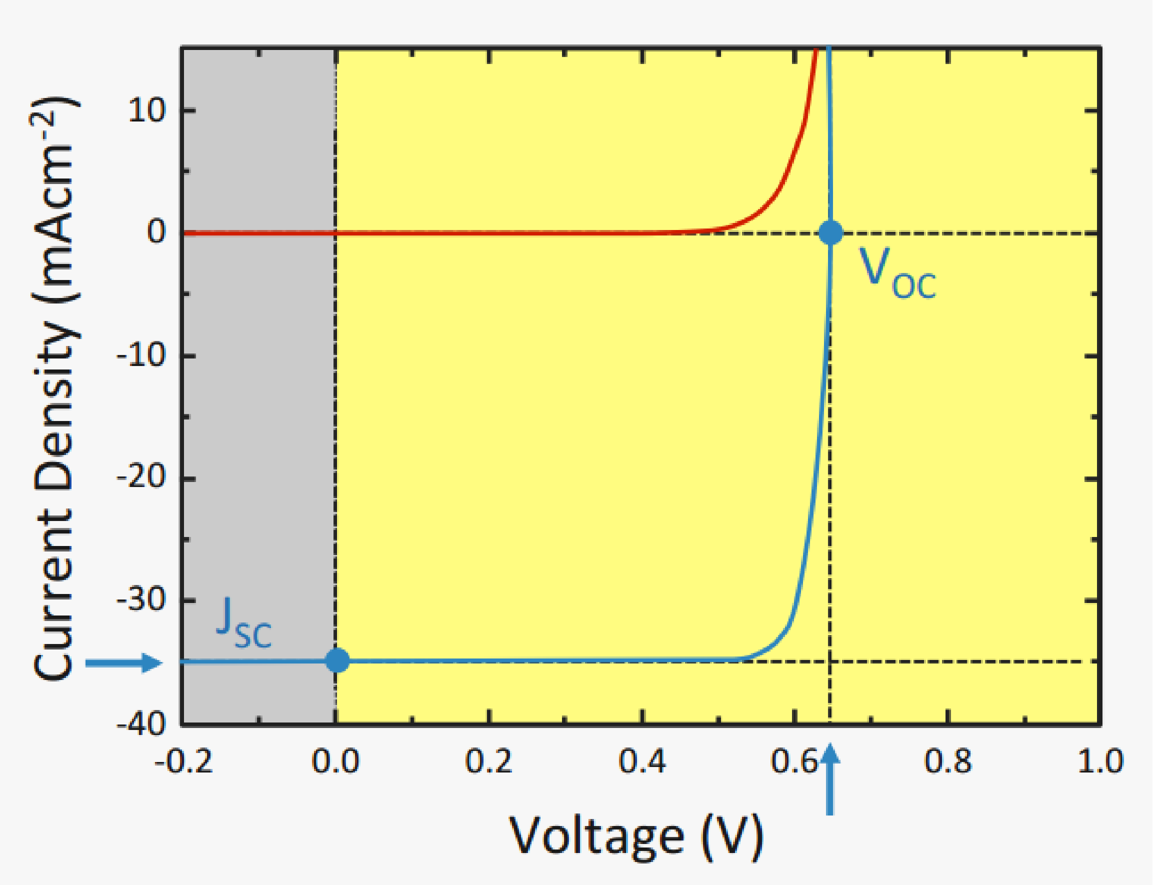

FIGURE 3.5: Typical current-voltage-characteristic curve of an ideal diode (red line) and ideal solar cell (blue line).

The current voltage curve of a solar cell (Figure 3.5), provides important parameter information. When there is no resistance in the external circuit (short circuit), there would be maximum current and this current is called the short circuit current (I_{SC}) or short current density (J_{SC}) . At this point, the voltage is zero in the circuit. If circuit is open there would be no current, and the voltage would be maximum. This voltage is called the open circuit voltage (V_{OC}) and at this point the load resistance is maximum. These two extreme conditions are shown in Figure 3.5. At any point along the curve, the product of current and voltage will gives the power output. At both short circuit and open circuit conditions, the power output is zero. There is a point where there is a maximum power. The current and voltage densities at this point are called J_M and V_M respectively. The parameter *Fill Factor FF* is given by:

$$FF = \frac{J_M V_m}{J_{SC} V_{OC}} \tag{3.5}$$

The fill factor describes the squareness of JV-curve. The efficiency of the solar cell is defined as the ratio of the power delivered at the maximum power point to the incident optical power density P_{IN},

$$\eta = \frac{J_M V_M}{P_{IN}} \tag{3.6}$$

As the efficiency is related to J_{SC} and VI_{OC}, we can write,

$$\eta = \frac{J_{SC} V_{OC} FF}{P_{IN}} \tag{3.7}$$

The standard test conditions describe the conditions for P_{IN} and the temperature of the solar cell during the JV measurements. The temperature of solar cells under standard test conditions is determined to be 25^{o}C. The solar spectrum has the spectral shape of AM1.5 and a total irradiance rounded to 1000 Watts per square meter.

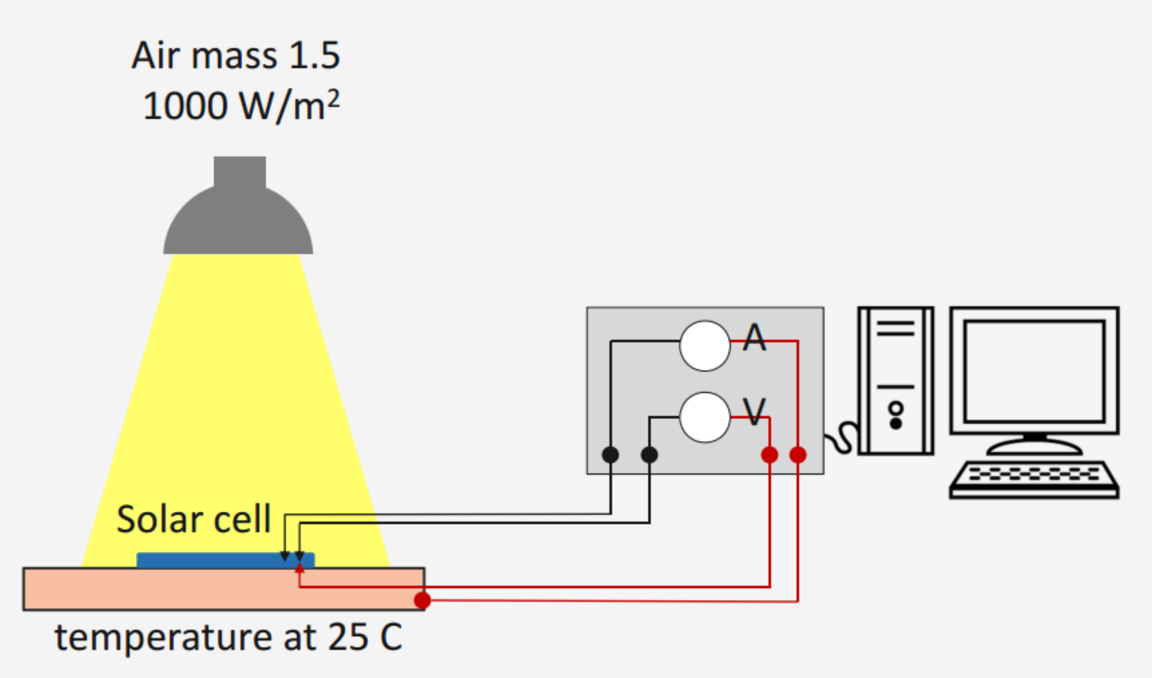

FIGURE 3.6: Block diagram of solar cell simulator system to measure current-voltage characteristics of a solar cell.

In practice, the efficiency of a solar cell is measured by solar cell simulator system as shown in Figure 3.6. A typical solar cell simulator consists of a light source which simulate both the AM1.5 solar spectrum and the irradiance of 1000 W/m^2.

The system has a source-meter which can apply voltage and measure the photo-generated current. Additionally system is also temperature controlled which maintains the standard room temperature during measurement. In this work, all solar cells were characterised with an Abet Technologies SUN-3000 Class AAA solar simulator. IV-characteristics were recorded by biasing devices with a Keithley 2400 source meter. The sub-module size of solar devices were kept 50×50 mm and each device had 9 cells in 3×3 array as shown in Figure 3.7

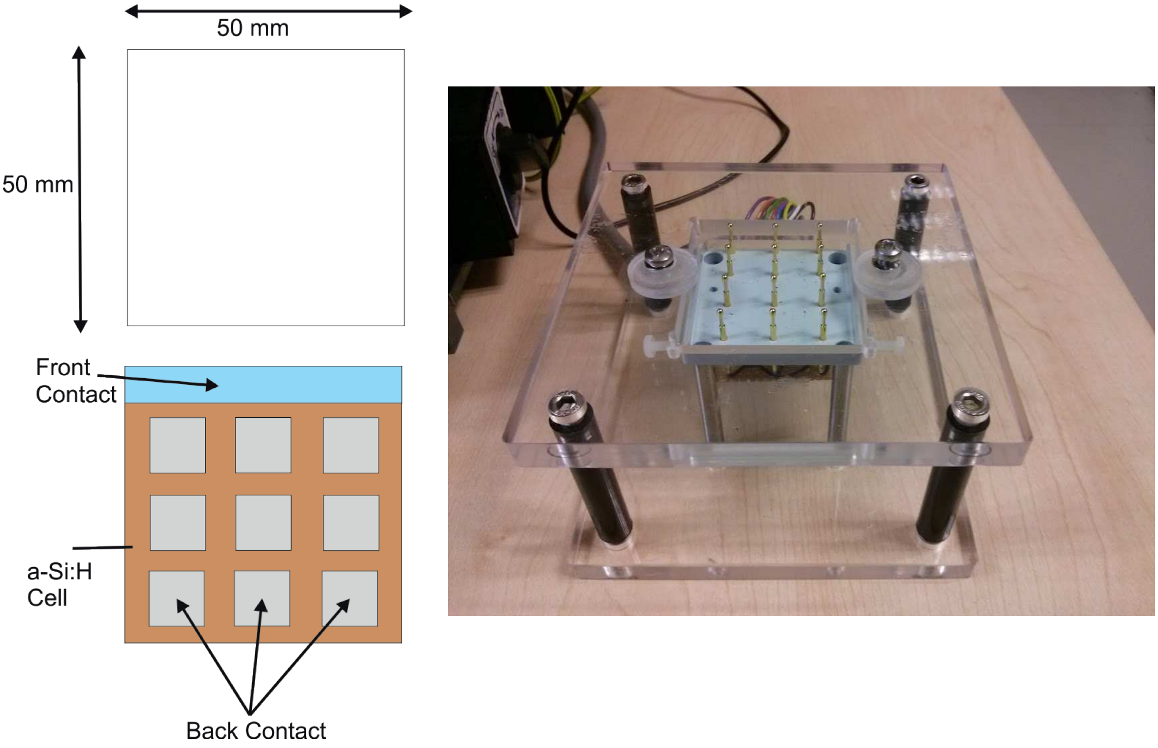

FIGURE 3.7: (left) Sketch of solar cell sub-module which consists of 9 cell of size 1×1 cm. (right) a custom build solar cell stage mount of IV measurement. It has 9 gold pallet spring mount connector for front and back contact.

Each cell has a standard area of 1cm^2. A customized stage mount was built for the measurement which consists of 12 gold plated spring mount connectors for current collection as shown in Figure 3.7. Every data set measured for specific cell is automatically recorded by the LabVIEW software written by the author.

3.7 Quantum Efficiency

The performance of a solar cell can also be understood by its ability to convert light into current at various wavelengths. This kind of measurement is called *Quantum Efficiency* (QE) which is defined as the ratio of the number of charge carriers collected by a solar cell to the number of photons incident on the solar cell at each wavelength. If the optical losses such as transmission of light through the device or reflection of light from the device are included in the QE measurements, then it is called *external quantum efficiency*

(EQE) which are present in this work. By adjusting transmittance and reflectance of solar cell, the QE can also be corrected to obtain *internal quantum efficiency* (IQE). The QE measurements require a calibrated reference device. Results presented here use a general purpose UV-enhanced silicon photodiode over the wavelength range of 300-1100nm whose QE is referred here as $QE_{cell}(\lambda)$ and the current response is $I_{ref}(\lambda)$. The QE of the solar cell is obtained from equation:

$$QE_{cell}(\lambda) = QE_{ref}(\lambda)\frac{I_{cell}(\lambda)}{I_{ref}(\lambda)} \tag{3.8}$$

Where $I_{cell}(\lambda)$ is the current response of solar cell under test.

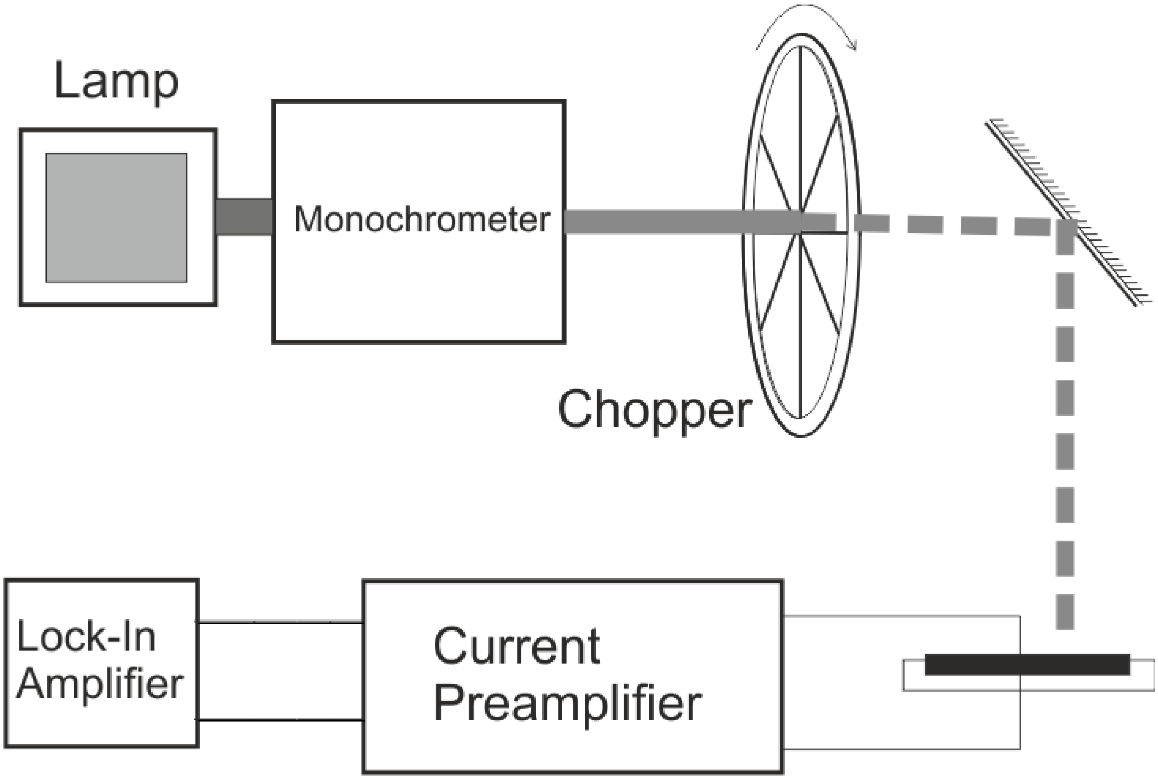

FIGURE 3.8: Schematic diagram of QE measurement apparatus

In this work, QE measurements are obtained using the Bentham PVE300 system (Figure 3.8). A monochromatic probe source capable of providing a wavelength range of 300-1800nm, is assembled from a dual Xenon/ quartz halogen light source at the input slit of the monochromator. This is a device which permits the determination of the spectral output of a source by separation and measurement of the component wavelengths. The component wavelengths have been achieved by reflection diffraction gratings using single Bentham TMc300, 300mm focal length monochromator. The beam passes a motor driven chopper with a fifteen slot chopping blade, the beam is then collimated and focussed into a 2×2 mm spot on the solar cell under test. The solar cell is connected a Bentham 477 current pre-amplier which converts the photocurrent into 0-10 V output voltage. The output of the current amplifier is connected to input of the lock-in amplifier (Bentham 485 module) which measures the output voltage. The lock-in reference input frequency comes directly from the chopper control module (Bentham 218 Chopper controller), and a time-constant of 100 ms is generally used for data acquisition. The quantum efficiency measurement is computed by the LabVIEW Benwin+ software. The data of the QE measurement is measured over the range of 350-11000 nm with 5 nm intervals.

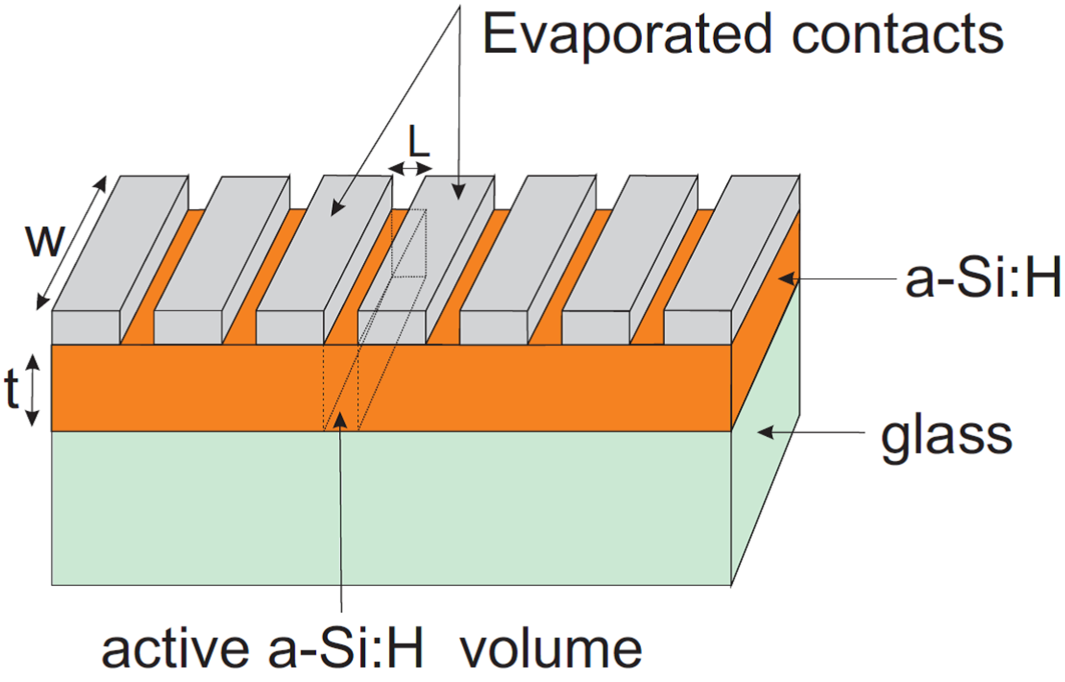

FIGURE 3.9: Sample set-up of conductivity measurement of intrinsic/ doped amorphous layer deposited on glass.

3.8 Electrical Conductivity

In this report, the electrical properties of intrinsic and doped a-Si:H were characterised in terms of dark conductivity and photoconductivity which is a general way to acquire information about the quality of thin film obtained via PECVD. The dark conductivity of a-Si:H films is measured in room temperature under dark condition. A Keithley 2400 SourceMeter is used to apply voltage and measures the output current. This process carried out immediately after PECVD film deposition in order to avoid any moisture in the films.

A voltage of 10V is applied to $L = 1$ mm wide and $W = 5$ cm long intrinsic a-Si:H film deposited on soda lime glass as shown in Figure 3.9. The contacts are deposited via thermal or electron beam evaporation. Generally the dark conductivity of device quality intrinsic a-Si:H is less than $1{\times}10^{10}$ Ω^{-1} cm^{-1} is needed for efficient solar cell applications. The photo-conductivity of intrinsic a-Si:H film is determined by illuminating the AM1.5 light to same samples which are used for dark conductivity measurement. The Photoconductivity is measured again at room temperature with 100 mW/cm^2 of power from the Abet Sun 3000 Solar Simulator. The conductivities of the measured devices is given by:

$$\sigma = \left(\frac{I}{V}\right)\left(\frac{L}{Wt}\right) \tag{3.9}$$

Where L is the length, W is width and t is film thickness.

Chapter 4

Amorphous and Microcrystalline layers

In this chapter, PECVD deposition of single layers of a-Si:H and microcrystalline (μc-Si:H) is described, with details of growth procedures the optimisation of device-grade optimization intrinsic, and doped a-Si:H layers. Each layer is characterised using optical and electrical techniques. The principal aim is to find optimum deposition parameters for layers that would eventually form the component layers of high efficiency thin film solar cell. At the start of this study, Southampton University had recently re-opened its Nanofabrication Facility after the significant fire of late 2007, the new facility was built with investment in a suite of multi-purpose PECVD deposition tools including one Oxford Instruments Plasma-Lab System 100 tools intended for Si and Ge deposition for a variety of purposes. In the initial commissioning phase it was felt that the development of a *pin* and *nip* a-Si:H solar cell fabrication capability would provide a valuable resource for various ongoing photonics and plasmonic light-trapping projects. It was also a project of device grade single layers, measured before any light induced degradation and every effort was made to ensure all fabrication, characterisation and fitting procedures were performed consistently.

4.1 Optical properties of intrinsic a-Si:H

The refractive index, absorption coefficient, and the bandgap are key optical parameters used for characterisation of thin films. The JA Woollam spectroscopic ellipsometer with multiple angle capability was used to determine the bandgap energy (E_g) and Urbach energy (E_U) with refractive index n and extinction coefficient k for absorption. The extracted data is used in a MATLAB simulation to investigate the layer absorption and transmission which are discussed below.

4.1.1 The thickness and uniformity

The intrinsic a-Si:H thin films were fabricated usingusing the Oxford Instruments PlasmaLab System 100, under constant RF power of 10 W and constant source gas flow of 500 sccm. The source gas was a mixture of silane 25 sccm and argon 475 sccm as recommended by the system suppliers In the first experiments the other growth parameters were varied in the first phase of experiments to determine the optimum deposition process and proceedures. Film uniformity, was also verified by ellipsometry. The thickness profile of an intrinsic layer is shown in Figure 4.1 which is determined by ellipsometry using the graded layer technique. This intrinsic a-Si:H film is 360 nm thick and apart from few small segments in the edges, almost all of the film shows good uniformity which certainly helps in maintaining device performance. The average roughness in the film is 3.14 ± 0.132 nm.

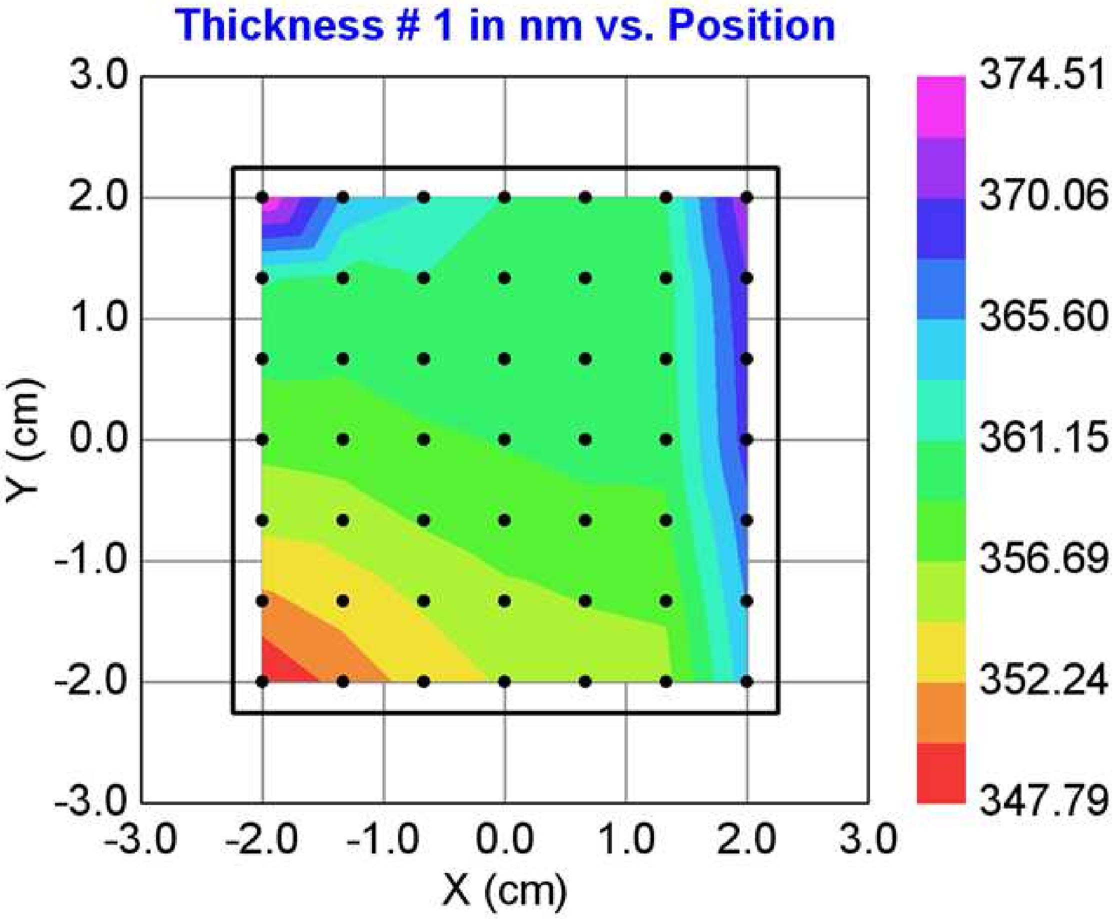

FIGURE 4.1: Thickness profile of an intrinsic a-Si:H film deposited on 5×5 cm glass substrate. The deposited film scanned at 4 cm×4 cm by ellipsometry. The deposited film is relatively uniform in thickness for most of the substrate. There is some non-uniformity at the corners or edges due to sample hight.

4.1.2 Film deposition rate

The intrinsic a-Si:H deposition rate was studied under constant RF power and constant gas flow, with increasing chamber pressure. The RF power used is 10W and of 500 sccm of source gas (silane and argon) at constant temperature of 200^{o}C. It is found that at lower pressures (40-100 mTorr) film quality is poor and non-uniform, and in some cases the low pressure is not enough to maintain the RF plasma. Deposition rate as a function of pressure in the range 250 to 1500 mTorr, is shown in Figure 4.2.

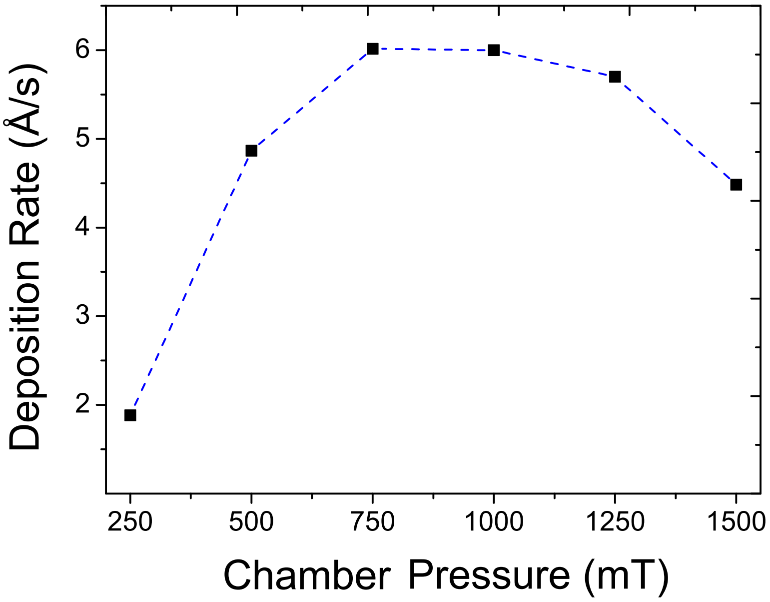

FIGURE 4.2: The Deposition rate of intrinsic a-Si:H as a function of pressure.

The deposition rate is found to be at its highest and relatively constant at around 6Å/s in the 750 -1000 mTorr pressure range and decreases at higher pressure ranges. Thus the optimum pressure for film growth at 1000 mTorr, this was initially fixed for future work.

At every point the deposition rate is measured by average thickness of the film and time of deposition. The average thickness is provided by ellipsometry. The error in thickness and deposition rate were estimated from standard deviation of data points in each film but found to be small.

4.1.3 Absorption coefficient

The absorption coefficient of intrinsic a-Si:H deposited at various chamber pressures and temperatures are shown in Figure 4.3 and Figure 4.4, respectively. The absorption coefficient over various wavelengths can be divided into three segments for better understanding.

In the region below 688 nm, the absorption coefficient relates to a band transition such as transition between the extended states of the valence band and conduction band. In this region the absorption coefficient is marginally higher at lower chamber pressures and higher temperatures.

The absorption coefficient of deposited intrinsic a-Si:H at various chamber pressures and deposition temperatures are shown in Figure 4.3 and Figure 4.4 respectively. At lower pressure the absorption coefficients in the visible range is are better than that at higher pressure Figure 4.4 shows absorption coefficient obtained over different substrate temperatures during film deposition The absorption coefficient of intrinsic a-Si:H is found to increase with higher substrate or stage temperature. The absorption coefficient over various wavelengths can be divided into three segments for better understanding.

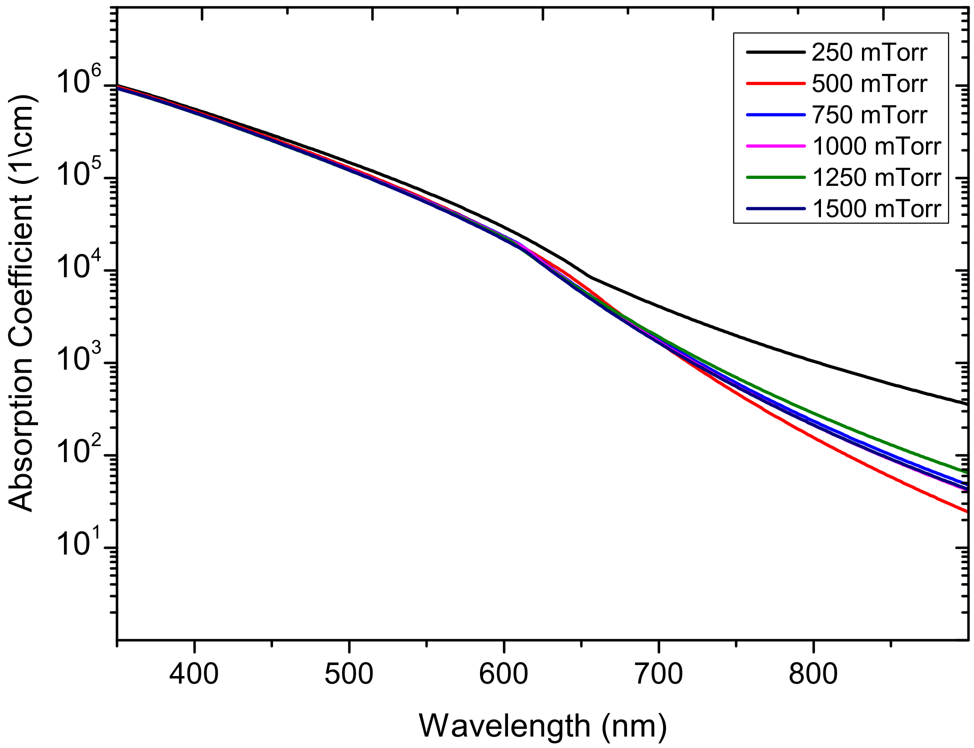

FIGURE 4.3: Absorption coefficient of intrinsic a-Si:H layers deposited as a function of deposition pressure. The absorption coefficient is calculated from the optical data of films analysed by ellipsometry.

In the region below 688 nm, the absorption coefficient relates to a band transition such as transition between the extended states of the valence band and conduction band. In this region absorption coefficient is marginally higher at lower chamber pressures and higher temperatures.

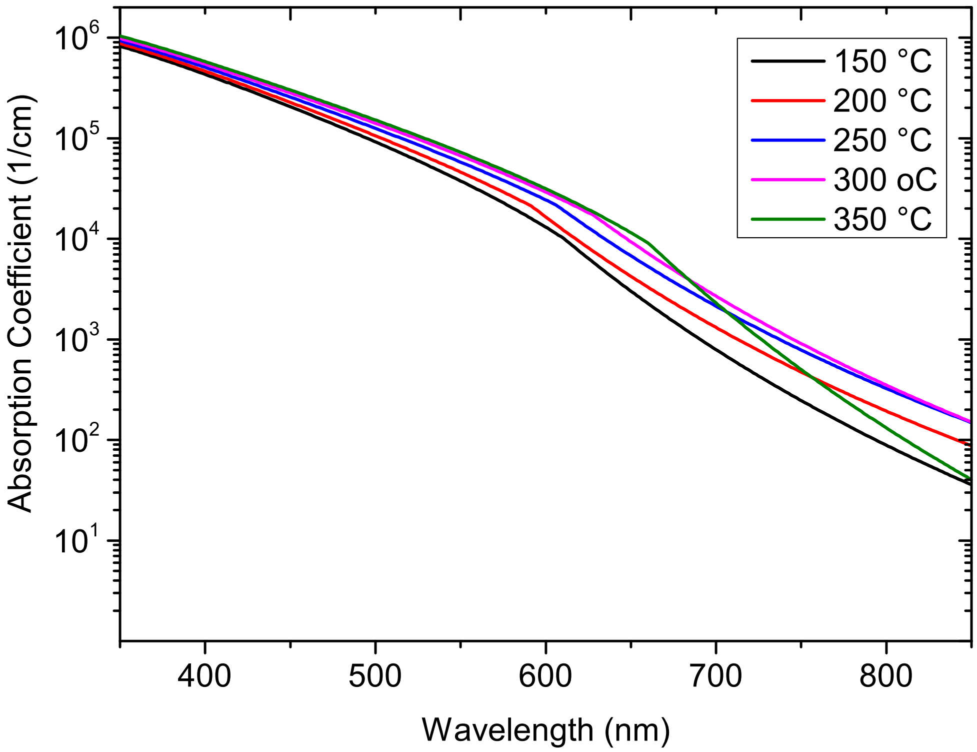

Figure 4.4: Absorption coefficient of intrinsic a-Si:H layers deposited as a function of deposition temperature. The absorption coefficients are calculated from the optical data of film analysed by ellipsometry.

In the region 688-826 nm, transitions involve the valence and conduction band tails and this region is known as the Urbach edge. In this region, the absorption coefficient at lower temperatures is decreasing. Similarly the absorption coefficient of films fabricated at higher pressure have significantly lower absorption coefficients at the Urbach edge. At higher wavelengths (above 826 nm) transitions involve the defect states (dangling bonds), and at this region the absorption coefficient of film fabricated at 250 ^{o}C show the highest absorption.

The substrate temperature is an important parameter in determining the quality of silicon thin films because temperature controls the rate of surface reactions and the growth rate, as well as the mobility of adatoms and thereby the crystallinity of the silicon. Hydrogen incorporation can also be controlled by substrate temperature, and this is also critical factor for surface mobility of the precursor. Substrate temperature is often a trade-off between any increase in surface diffusion and the desorption of hydrogen that leaves behind the un-passivated dangling bonds[42]. We have carried out thin film fabrication over a wide range of temperatures and found that 250 ^{o}C is the optimum balance of deposition rate and hydrogen incorporation.

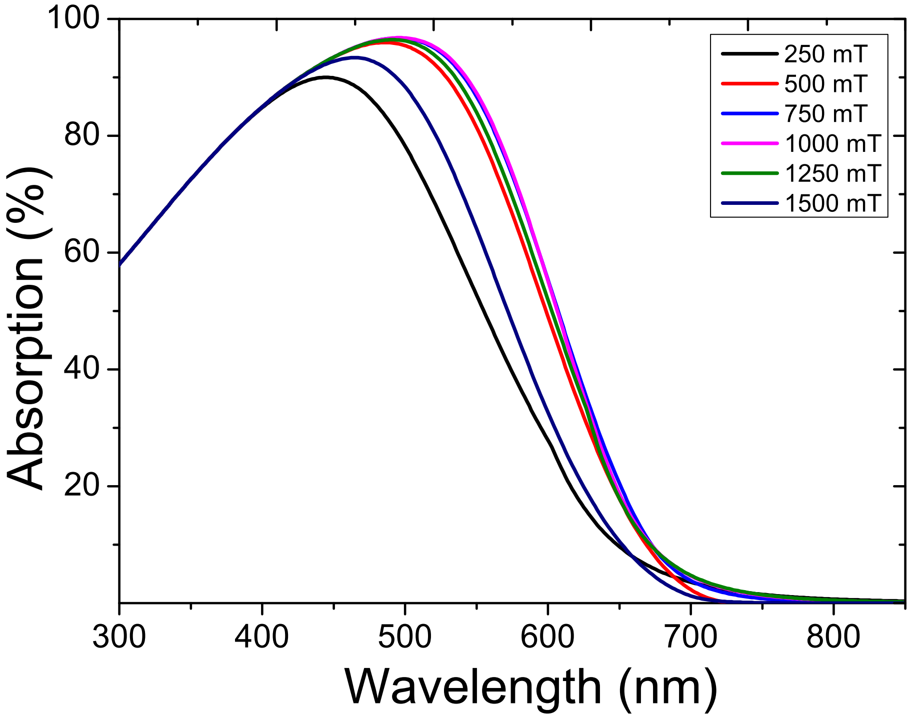

FIGURE 4.5: Calculated optical absorption in individual intrinsic a-Si:H thin film deposited at different chamber pressures. A 10 nm p layer effect on absorption is included in this data as in real *pin* device is always present.

Optimisation of the deposition conditions, to a first approximation, should focus on maximising absorption in the intrinsic layer of a pin device. Figure 4.5 shows the calculated absorption in individual intrinsic layers deposited at different chamber pressures whereas Figure 4.6 shows the calculated absorption as a function of the temperature at which each layer is deposited. The absorption of p layer (window layer) was taken into account as in real pin device and devices used in this report, always had p-layer. Figure 4.5 shows that absorption at 1000 mTorr is higher, so this was determined as the optimum value for future growth. With increasing substrate temperature absorption in the resulting intrinsic film increases, (Figure 4.6).

Using optimum growth parameters, a thin intrinsic layer (for example 360 nm) shows more than 90% absorption in the blue - green region (400 nm to 475 nm), while at higher wavelengths in the visible range, there is noticeable decrease. In the yellow to red region (570 nm to 650 nm) absorption reduces from 75% to 20% and lower. We could use a 100 nm thick layer in a multijunction device to collect the blue region effectively, but 100 nm cannot be used in a *pin* or *nip* device. A thick intrinsic a-Si:H layer (300 nm to 500 nm) can achieve more than 90% absorption in the green region. In the 650 nm to 800 nm range, intrinsic a-Si:H only absorbs 25% or less of light regardless of thickness, this is the most challenging region for a-Si:H solar cells.

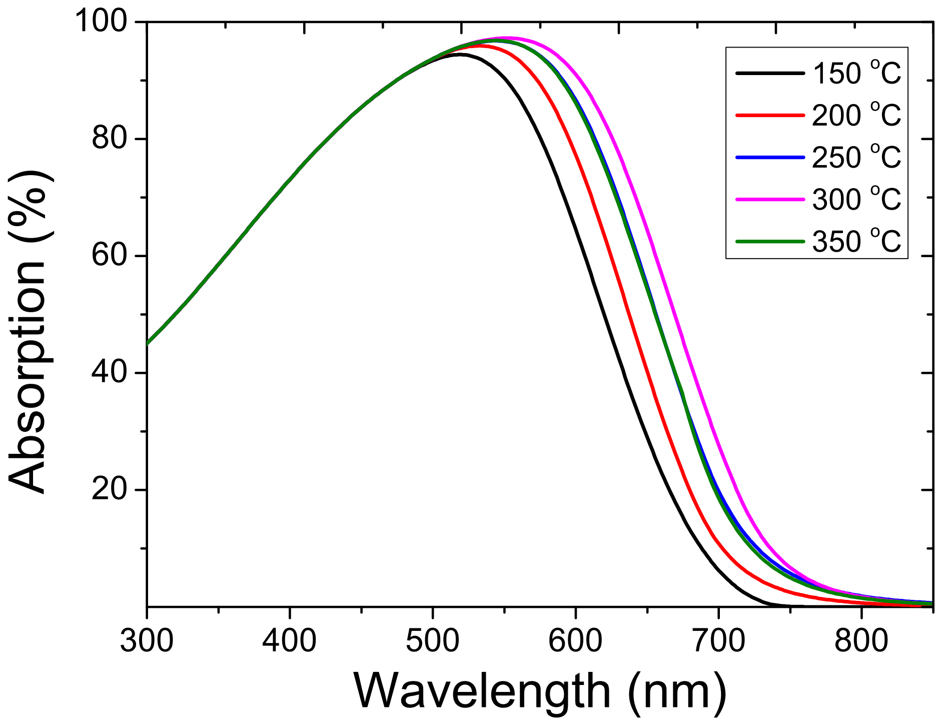

FIGURE 4.6: Calculated optical absorption in individual intrinsic a-Si:H thin film deposited at different substrate temperatures. Absorption of a 10 nm p layer on absorption is included in this data.

4.1.4 Bandgap and Urbach energy

The optical band-gap in intrinsic a-Si:H varies substantially with deposition conditions and alloying. Deposition at low substrate temperatures can increase the bandgap in a-Si:H, as a result of increased hydrogen incorporation in the film[100 101]. This effect is shown in Figure 4.7. However, lower substrate temperature (<150^{o}C) can form silicon polyhydride powder due to the thermal enhancement of the surface diffusivity of adatoms during growth, especially at higher temperature, where the silicon network is more ideal and binds less hydrogen[98]. However higher temperatures (>350^{o}C) can damage the underlying layers of the solar cells[102] and damage the quality of material. This is due to loss of hydrogen passivation of dangling bonds.

Figure 4.8 shows the optical band-gap of intrinsic a-Si:H as a function of chamber pressure during PECVD growth. The band-gap increases slightly with increasing pressure. The exponential slope of the The Urbach energy for device quality a-Si:H is 50 meV or less. In this work, the Urbach energy is calculated from ellipsometric fitting model with bandgap of the film.

Figure 4.9 shows the Urbach energy calculated from ellipsometry data. The Cody-Lorentz oscillator is chosen to model absorption to determine Urbach energy. In this

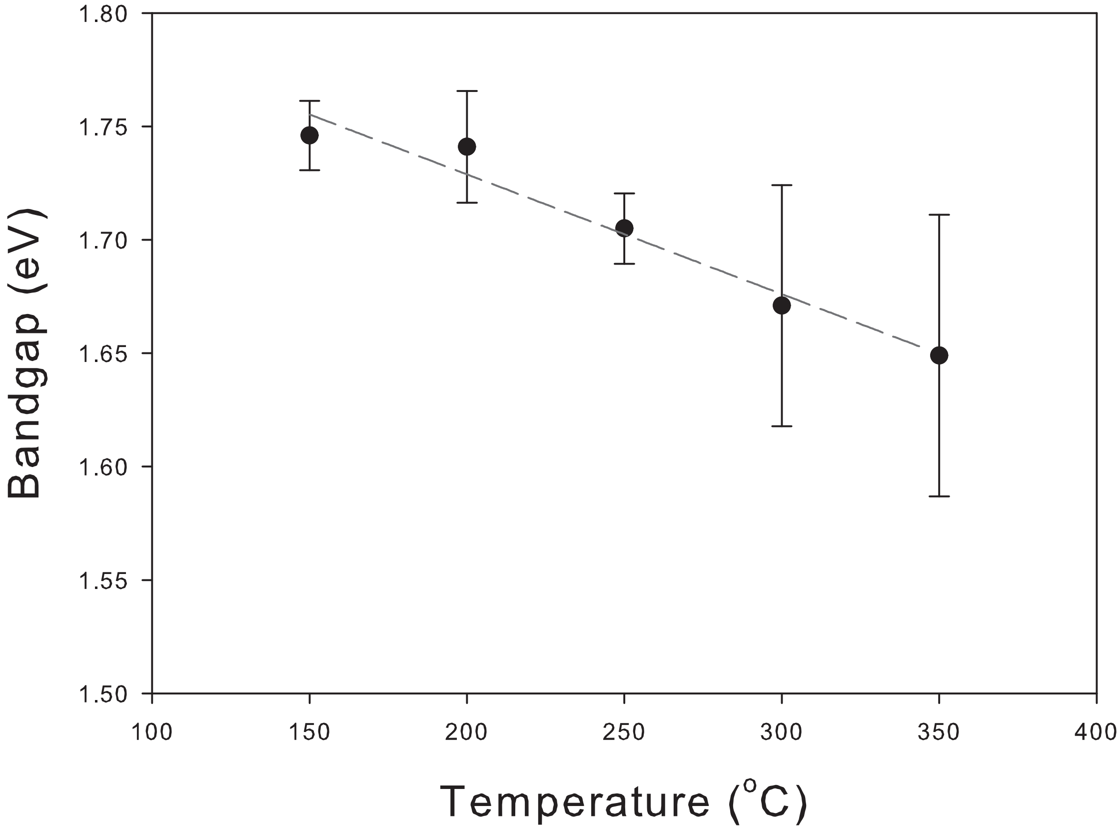

FIGURE 4.7: The optical bandgap of single intrinsic a-Si:H layers deposited as a function of deposition temperature. Error bars are calculated from the fitting parameters of the ellipsometric Cody Lorentz oscillator.

report Urbach energy for the sample is higher than the optimum value.

4.2 Electrical properties of intrinsic a-Si:H

In this report, the electrical properties of intrinsic a-SiH thin films were characterised in terms of dark conductivity and photoconductivity, which is a general method to understand information about the quality of thin films obtained by PECVD. The dark conductivity of a-Si:H films is measured at room temperature under dark conditions.

A Keithley 2400 SourceMeter is used to apply voltage and measures the output current. This process is carried out immediately after PECVD film deposition so represent initial values. A voltage of 10V is applied to 1 mm wide and 50 mm long intrinsic a-Si:H film. Generally the dark conductivity of device quality intrinsic a-Si:H should be less than$1\times 10^{-10}\ \Omega^{-1}\text{cm}^{-1}$ for efficient solar cell application.

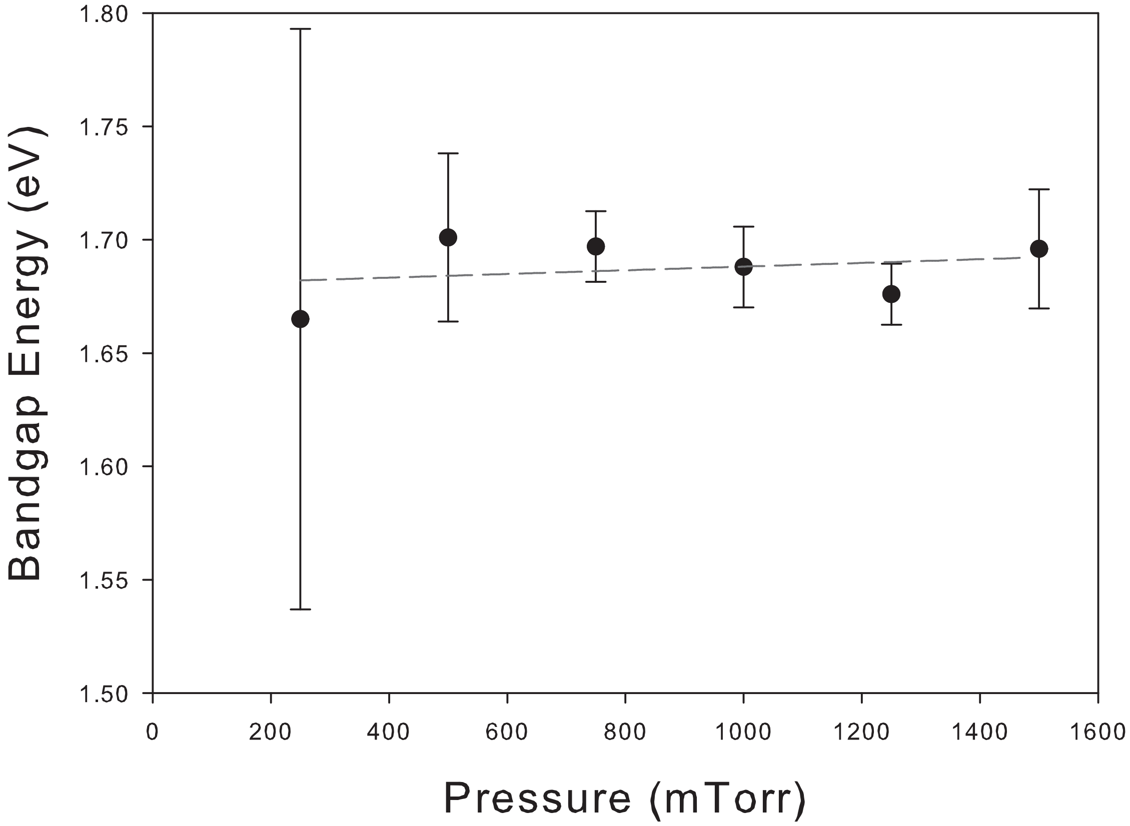

FIGURE 4.8: The optical bandgap of intrinsic a-Si:H layers deposited as a function of chamber pressure. Error bars are calculated from fitting parameters ellipsometric Cody Lorentz oscillator.

The photo-conductivity of intrinsic a-Si:H thin films is determined by illuminating the sample under AM1.5 illumination. The Photoconductivity is measured at room temperature with 100 mW cm2 of power from an Abet Sun 3000 Class AAA solar simulator. For the solar cell device quality, the photo-conductivity of intrinsic a-Si:H film should be greater than 1× 10^{-5} Ω^{-1}cm^{-1}.

Figure 4.10 shows the dark photoconductivity and photoconductivity of a-Si:H as a function of pressure. It is seen that the photo conductivity and dark conductivity of the thin film show a linear decreasing with increasing pressure, although this slight change is very small in both curves. However the dierence between dark and photoconductivity is almost constant at every pressure, which suggests that the chamber pressure does not significantly affect the photo-response (the ratio of the photoconductivity and dark conductivity) of the film. The maximum photo-response is shown when 1000 mTorr pressure is used during film growth. .

Figure 4.11 shows the dark and photo-conductivity as a function of temperature. It is found that both dark and photoconductivity significantly increase with higher temperature. This increase is not linear but a clear trend can be observed. At low temperature,

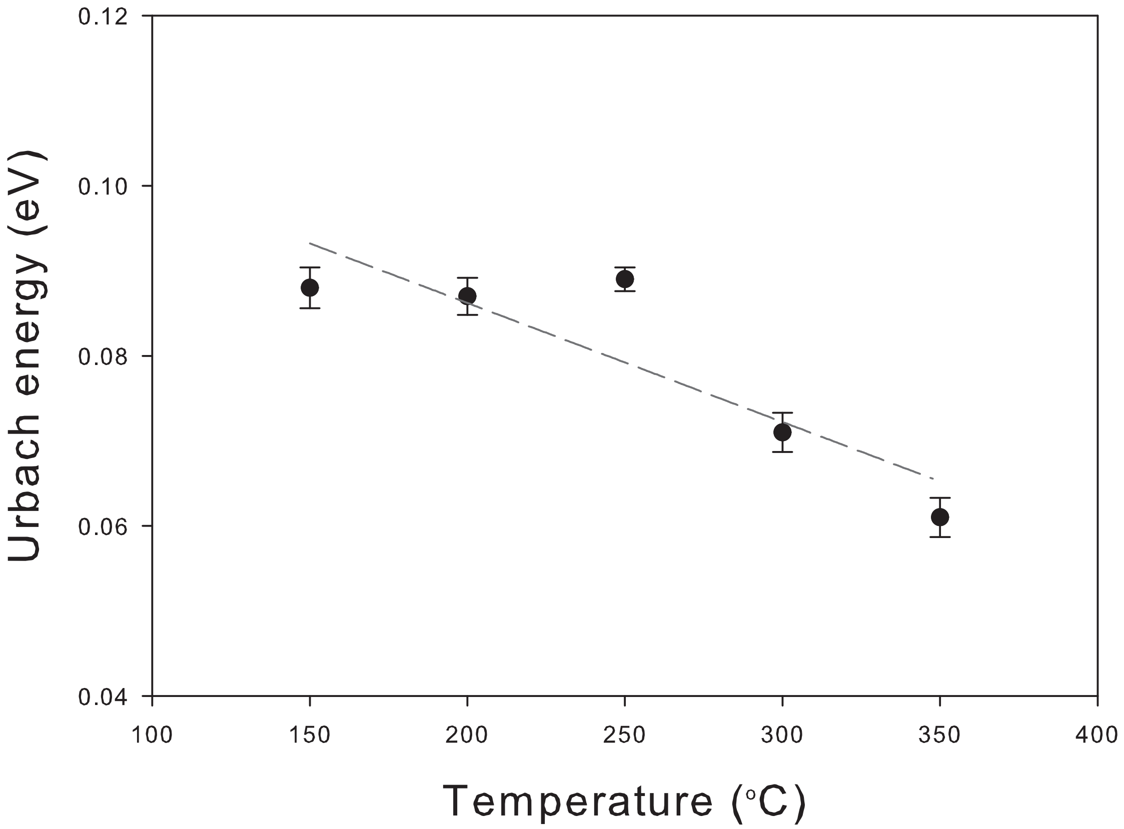

FIGURE 4.9: Urbach energy of intrinsic a-Si:H layers as a function of substrate temperature. Single point are linearly fitted.

the dark conductivity and photo-conductivity are very close to each other and hence photo- response of the film is very small. It is likely that at low temperatures the film quality starts to deteriorate due to void fraction and defect density. The photo-response is constant in the temperature range of 200-300^{o}C but higher temperatures degrade the material quality as a result of the loss of hydrogen passivation of the dangling bonds[100].

4.3 Optimisation of doped a-Si:H layers

Doping of a-Si:H layers has been optimised in two stages. In the first stage, initial depositions are made to check the doping efficiency of dopant gas. Both *p*-type and *n*-type films were deposited using the conditions established for intrinsic a-Si:H but with the addition of dopant gases. So, each doped film was deposited under 1000 mTorr pressure at 250 ^{0}C and with 10 watt of RF power. The first experiments were carried out before argon was found to be detrimental to film deposition. So, in this case although a flow of 25 sccm silane and 475 sccm of Argon was used. A number of n-type doped films are deposited with different phosphine ratios from 0.4% to 12% to determine the

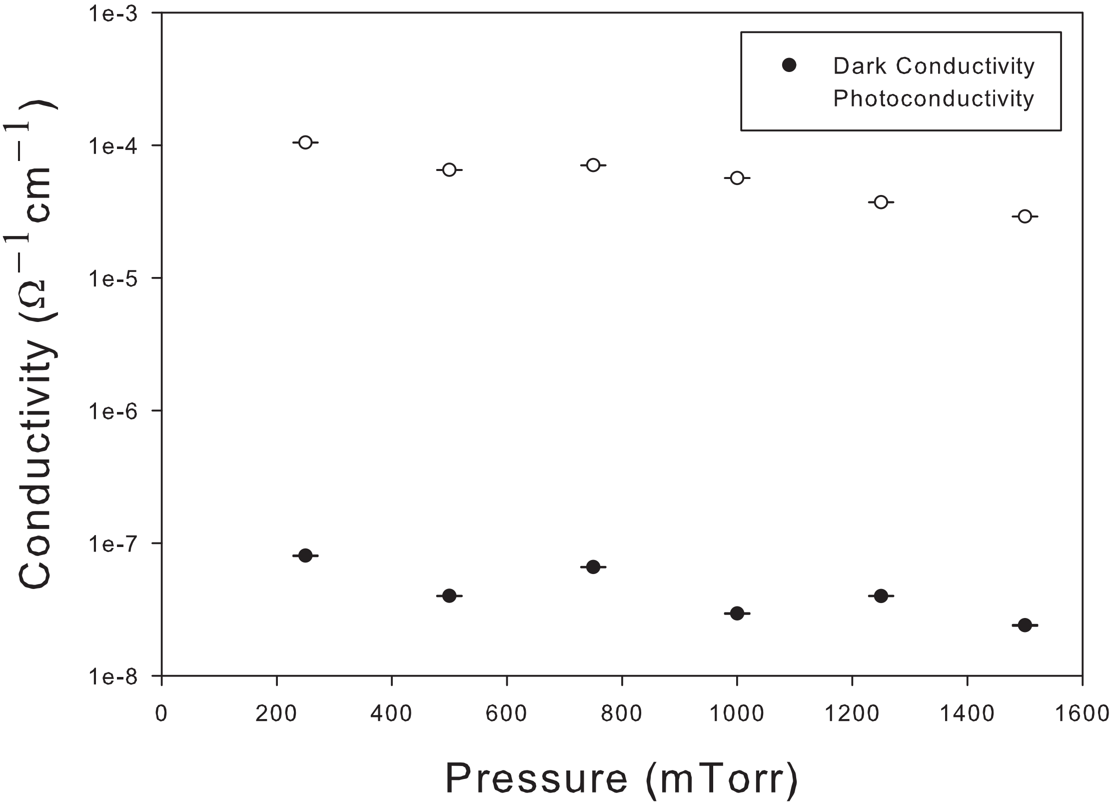

FIGURE 4.10: Dark conductivity and photoconductivity of intrinsic a-Si:H films deposited as a function of pressure.

quality doping. The room temperature electrical conductivity measurements of n doped films are shown in Figure Figure 4.12.

We have observed that conductivity of n doped films increases when there is a decrease in phosphine ratio in phosphine ratio in the source gas. The high value of 4.8×10^{-3} photoconductivity is found at 0.4% phosphine to silane ratio. At one position on a 50 by 50 mm film was found to be as high as 1.6×10^{-1} which is in close agreement with published work[103]. The value of dark conductivity at 0.4% phosphine ratio is measured at 2.41×10^{-3}.

The room temperature conductivity of p-type doped films is shown in Figure 4.13. Unlike n-type doped film, p doped films shows higher conductivity at high doping concentration which is found at 2% diborane ratio. The highest photoconductivity found was 1.5×10^{-3}. At this point, the dark conductivity is almost same at 1.4×10^{-3}.

In the second stage, more detailed study of the doped layer have been performed. The amount of silane gas is increased from 25 sccm to 50 sccm and Instead of Ar, H_2 is used. The 5 minutes of deposition time for n-type layers is kept constant. The dopant gas is varied from 1 sccm to 10 sccm at different deposition pressures while keeping RF

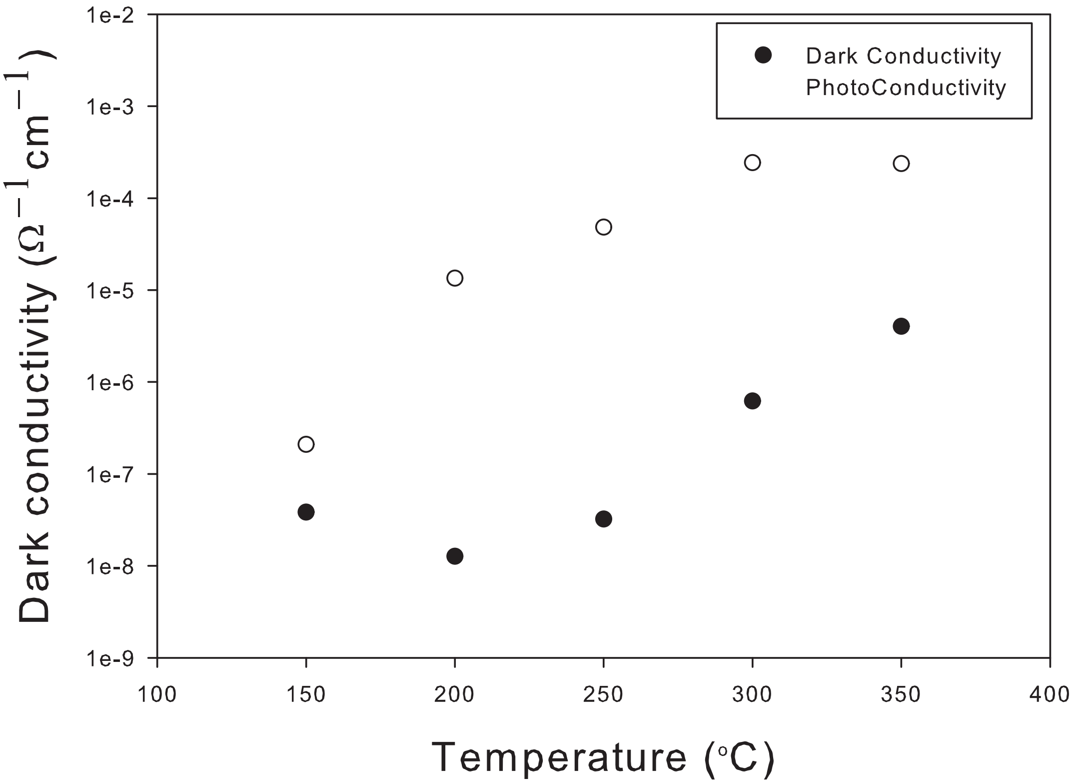

FIGURE 4.11: Dark and photoconductivity of intrinsic a-Si:H films deposited as a function of temperature.

power and temperature constant. The dopant gas percentage in comparison with silane is explained in following table(4.1).

Silane Used (sccm)	Doped Gas Used (sccm)	Doping Percentage (%)
50	1	0.2
50	2	0.4
50	3	0.6
50	4	0.8
50	5	1.0
50	6	1.2
50	7	1.4
50	8	1.6
50	9	1.8
50	10	2.0
50	11	2.2
50	13	2.4

TABLE 4.1: Doping gas percentage during PECVD deposition of *p*-type and *n*-type a-Si:H layers

The dark conductivity measurement of for all n type layers is shown in Figure 4.15. At lower PH_3 dopant percentage, the dark conductivity of the *n*-type layers is almost the

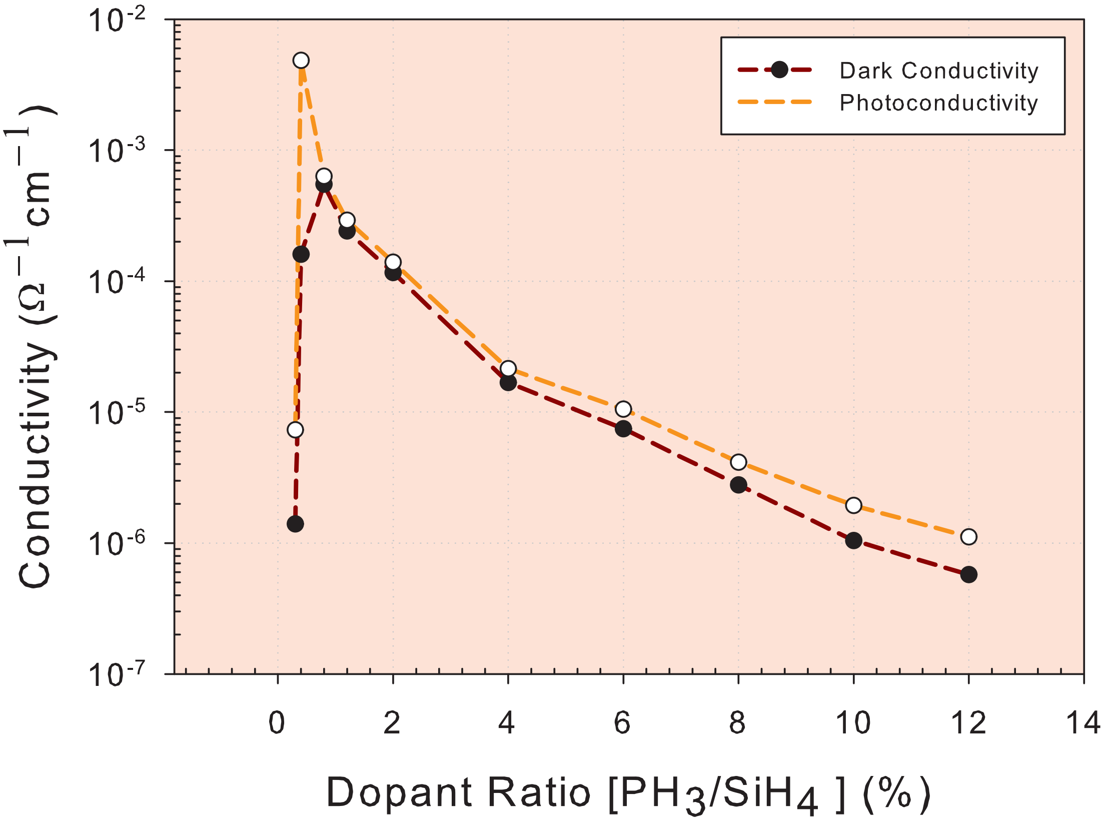

FIGURE 4.12: Room temperature conductivity of n-type a-Si:H layers as a function of doping ratio.

same as for the intrinsic regions. At higher PH_3 percentage, , the dark conductivity is dependent on chamber pressure. At lower pressures, dark conductivity is higher and at higher pressures, it is low. At lower pressures, dark conductivity is roughly uniform for increasing dopant ratio, at higher pressures it is uniformly decreasing. It is observed that chamber pressure during deposition is an important factor controlling the conductivity of n-type layers.

The photoconductivity of n-type layers is shown in Figure 4.15. The photoconductivity also seems to be dependent on chamber pressure. Overall photo-conductivity is lower for higher pressures and found higher at lower pressures. Lower dopant percentages and higher dopant percentages both produce low photo conductive layers. At 0.4% of PH_3, the photoconductivity is the same for all layers at every pressure value.

It can also be observed in Figure 3.14 and Figure 3.15 that dark and photoconductivity of n-type layers overlap each other and their photoresponse is very low. Therefore these doped layers cannot participate in photo generation when used in a solar cell device. The conductivity of n-type layers is very high as compared to intrinsic layers; therefore

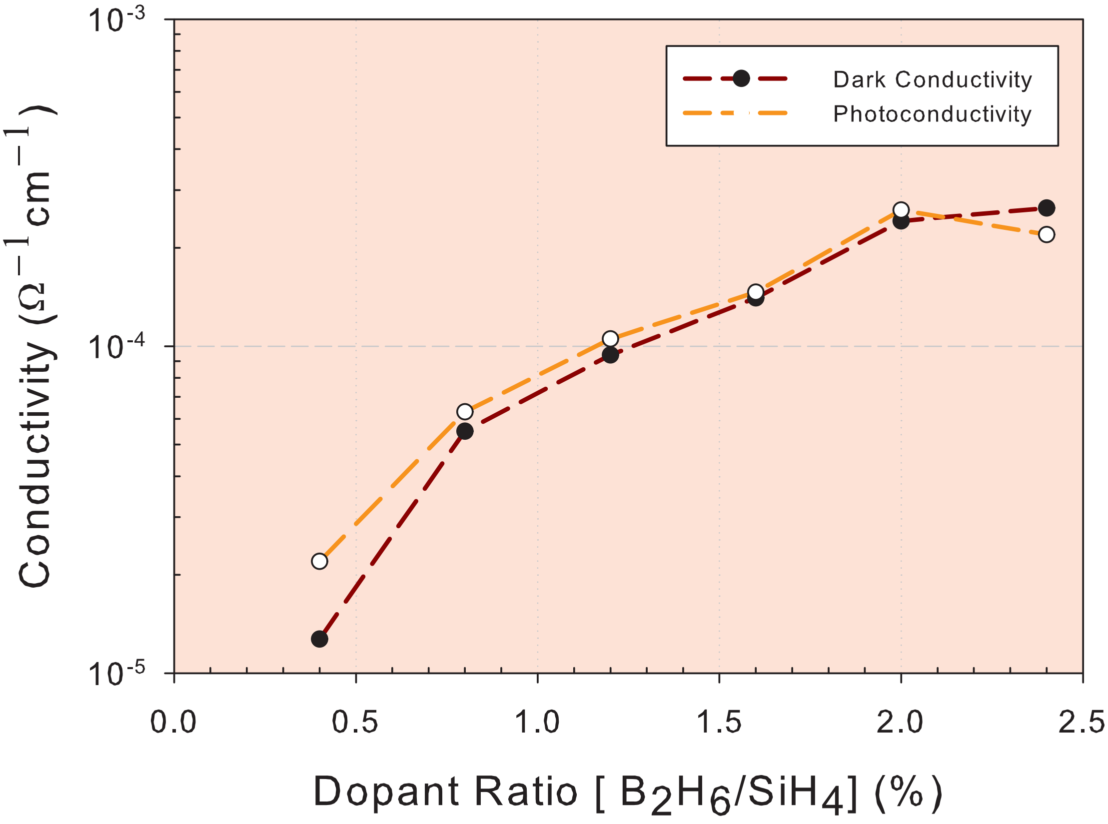

Figure 4.13: Room temperature conductivity of p-type a-Si:H layers as a function of doping ratio.

they are suitable for use on the back contact and will contribute to forming the built-in electric field for carrier collection.

It can also be observed in Figure 4.14 and Figure 4.15 that dark and photoconductivity of n-type layers overlap each other and their photo response is very low, in the order of 1000 or less. Therefore these doped layers cannot participate in photo generation when used in solar cell device. The conductivity of n-type layers is very high as compared to intrinsic layers; therefore they are suitable for use on the back contact and will also contribute in *built-in electric field* for carrier collection.

As n-type layers will always be the cause of parasitic absorption, the thickness is very important in device formation, the optimum process should provide maximum control of thickness parasitic absorption while ensuring that the electrical properties are maintained. The deposition rate of n-type layers for different PH_3 dopant ratio is shown in Figure 4.16.

At low chamber pressures, the effect of increasing the dopant content is relatively small. However this effect is large at high pressure. At low pressure, the dark conductivity is roughly proportional to the boron concentration which is shown in Figure 4.17. At

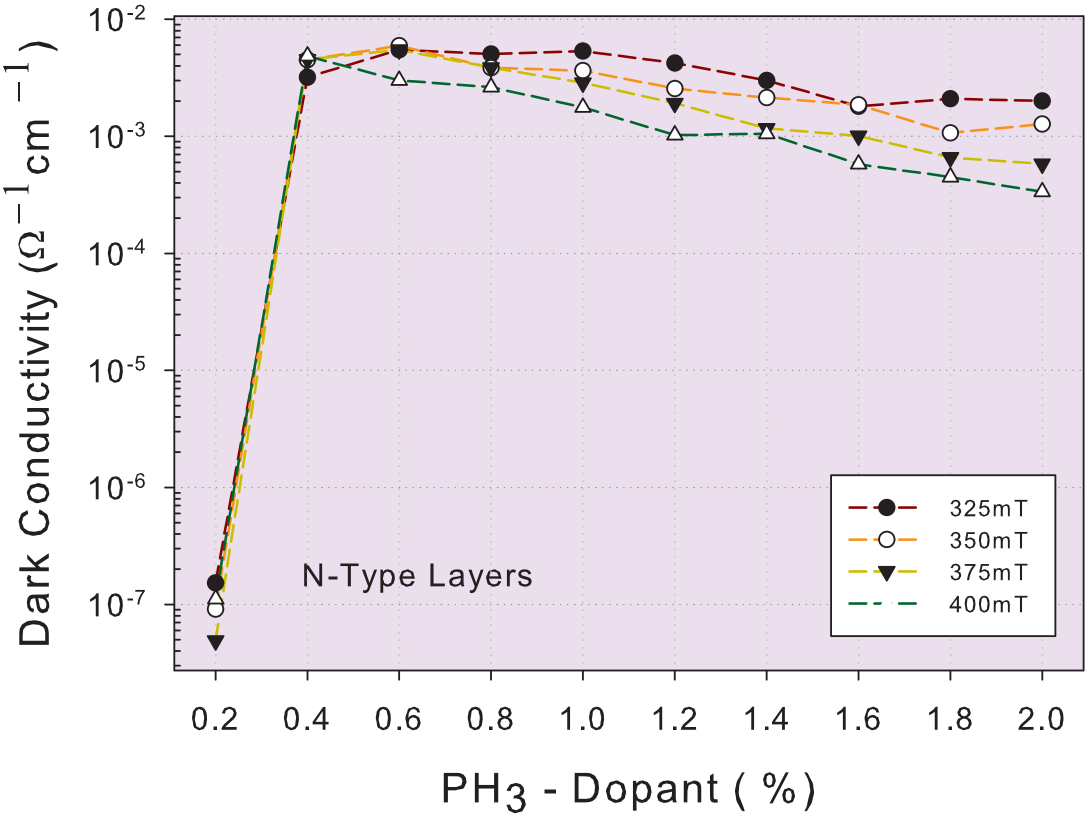

FIGURE 4.14: Room temperature dark conductivity of n type layers deposited with increasing dopant percentage at four different pressure points.

higher values of chamber pressures, dark conductivities only gradually increase, The value of dark conductivity levels at higher boron dopant levels this suggests the doping limit of boron.

The photoconductivity of *p*-type layers does not vary significantly with boron dopant concentrations. The photoconductivity of p-type layers lies between 10 $^{-5}$ and 10^{-4} Ω $^{-1}$cm $^{-1}$. Chamber pressure is the parameter upon which the photoconductivity of the p-type mostly depends, however at very low pressure some slight variations with dopant content can be observed. We can also see that boron doping is efficient, resulting in *p*-type layers which are very active so that normal room temperature photoconductivity measurements are unable to determine any noticeable change or variations in the layers As the thickness of p-type film is one of the most decisive factors, therefore it is the optimisation of thickness control that is most important.

We know that in an operational device, light enters through the *p*-type layer. Thicker layers can absorb a large proportion of the incoming spectrum, it is therefore an essential requirement that thickness of *p*-type layer should be kept as low as possible without compromising its conductivity. We have already found that at every doping concentration, photo-conductivity is similar. The actual test of *p*-type layer in device is only

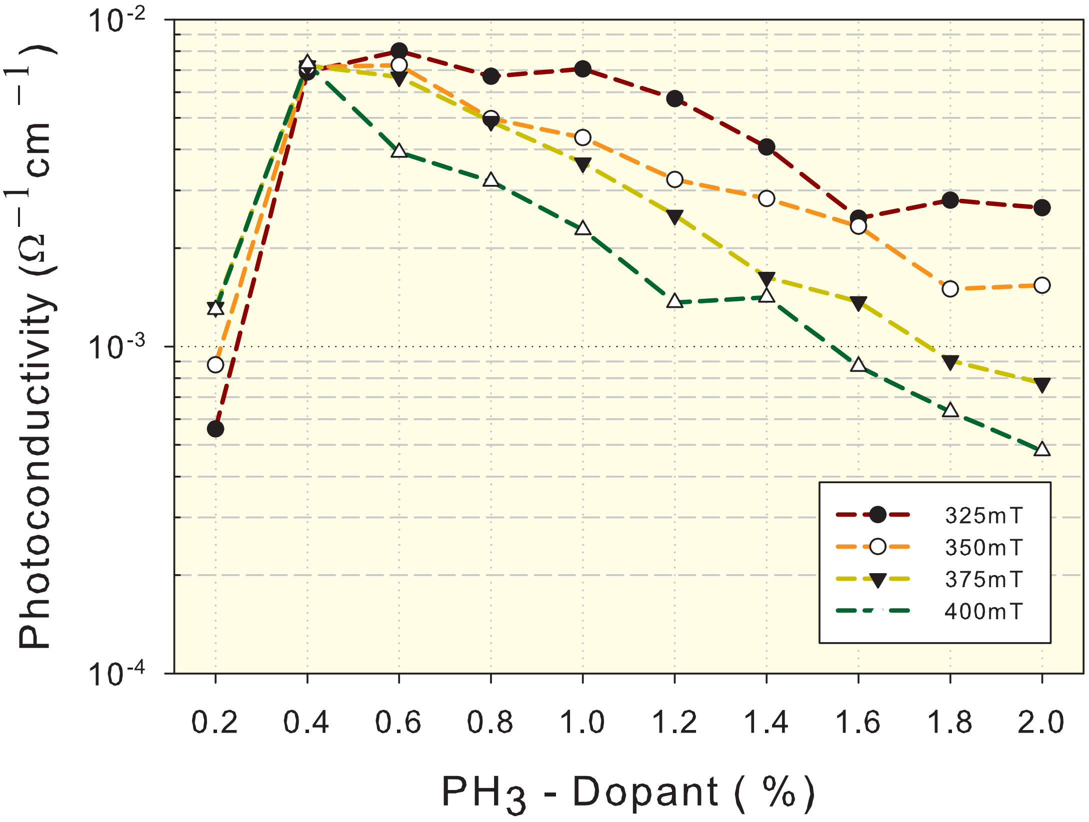

Figure 4.15: Room temperature photoconductivity of n type layers deposited with increasing dopant percentage at four different four pressures.

possible when checked in an actual device.

The quality of doped a-Si:H layers has also been tested through Secondary Ion Mass Spectrometry (SIMS) measurements, which provide accurate depth profiles. Substrate and surface roughness play a large role in aecting the depth resolution of SIMS depth profiles[104]. Therefore doped layers with different film thicknesses were deposited on plain glass substrates which have negligible roughness. The SIMS Measurement was carried out by Loughborough Surface Analysis Ltd and the SIMS data of n-type film is shown in Figure 4.20. The SIMS data shows identical initial noise at zero depth. The phosphine concentration through the entire film thickness is found to be constant. At 0.8% of phosphine flow, the atomic concentration is found in the range of 110^{21} atoms/cm^3 is slightly improved when the phosphine flow is increased to 1.2%. As expected, high concentrations of phosphine are found when dopant flow is high which in our case is 2%. The n-type film thickness for each substrate independently measured using ellipsometry also is now verified by SIMS profile depth.

The SIMS depth profile of boron in p-doped a-Si:H films deposited on glass substrates with three different film thickness is shown in Figure 4.20. The distinct concentration

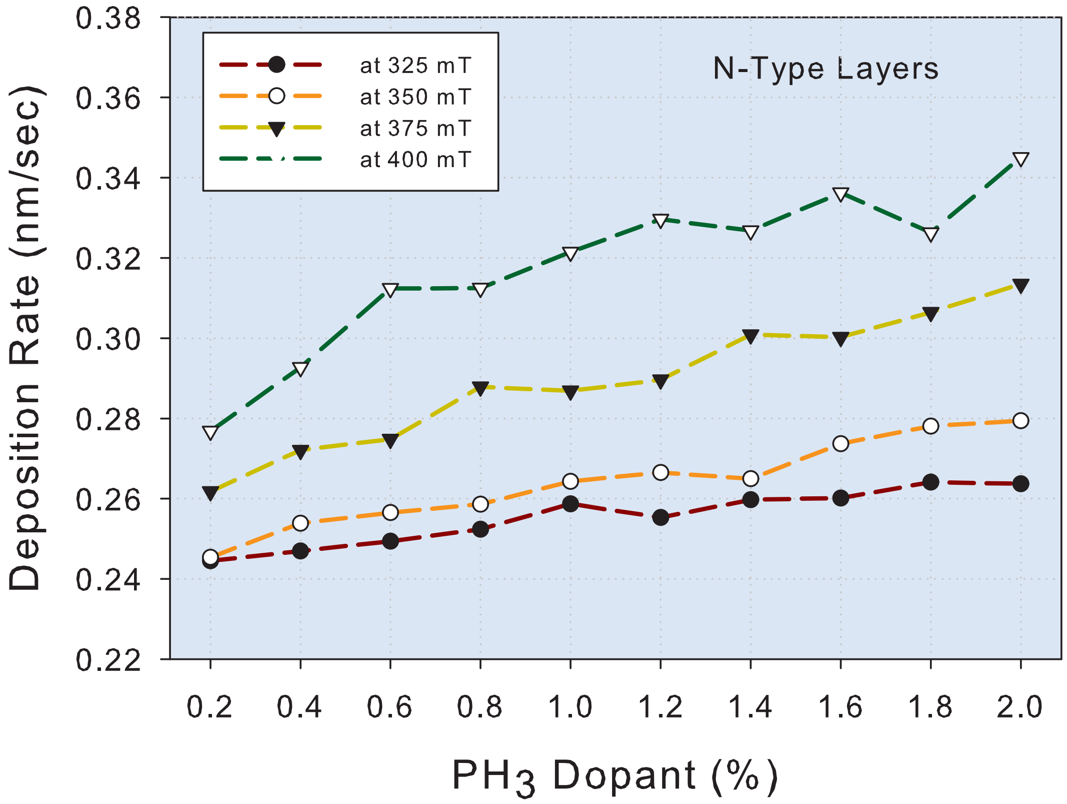

Figure 4.16: Deposition rate of n-type layers at various pressures mapped with respect to increasing dopant percentage.

profiles of the p-type layers with different boron dopant flow is clear. With higher dopant flow, the atomic concentration is increasing to higher level. All three p doped layers show atomic concentration in the range of 10^{20} and 10^{21} atoms/cm^3. Independently measured film thickness is also verified by the SIMS depth profile. The noise at the higher depth simply verifies that doped film thickness has been crossed.

4.4 Intrinsic Microcrystalline Silicon layers

Microcrystalline silicon (μc-Si:H) entered in photovoltaics due to drawbacks in standard silicon photovoltaic technology. Those drawbacks are high energy manufacturing processes, material wastage during processing, much thicker absorber materials than are needed optically, and the difficulties in large area module fabrication. However, for standard crystalline silicon photovoltaics, the conversion efficiencies are high and based on a well advanced technology that is already commercially established. A series of difficult challenges must be met in order to significantly reduce the cost or increase the efficiency of crystalline silicon modules. The thin film silicon solar cell on glass is a strategy to address many of the issues effectively. By using thin film technology, the material

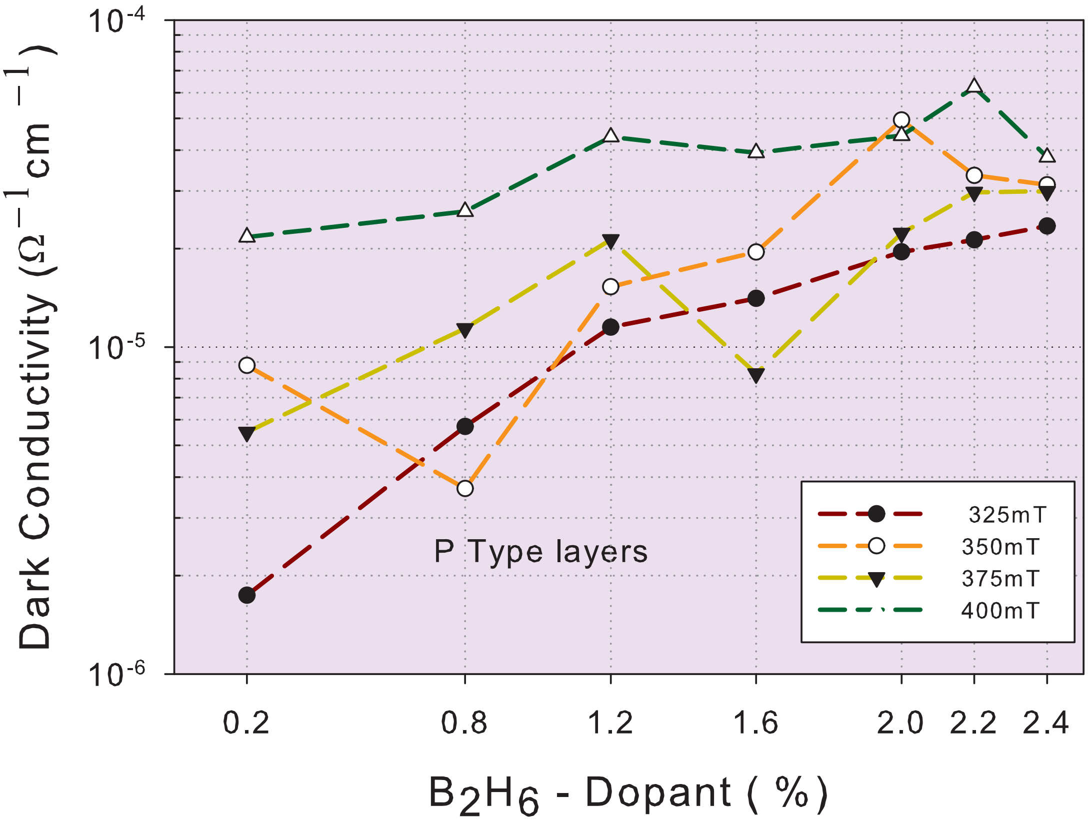

FIGURE 4.17: Room temperature Dark conductivity of *p*-type layers deposited with increasing dopant percentage at different four pressure points.

quantity can be reduced significantly. The thin film technology could be sufficient to complete with standard crystalline silicon in respect to solar light absorption. The material consumption can reduced along with the process temperatures and can therefore allow low-cost substrates which in turn allow easy large area fabrication and integration into different modules. A-Si:H and its alloys with germanium and carbon are already commercial materials in microelectronics, and thin film technologies associated with this materials is mature but also has far to go to capture a significant share of PV market. Currently the best way of using μc-Si:H in photovoltaics is in a tandem or multijunction solar cell with amorphous silicon. The current approach is to use μc-Si:H as a low band gap red absorber together with an amorphous silicon in a tandem (or triple) cell design. To be able to reduce the layer thickness further, light scattering and light trapping techniques gained much importance in μc-Si:H based solar cells and an active subject of current research[105]. Advanced light-trapping in combination with novel recrystallization schemes could provide thin deposited silicon layers with optoelectronic properties similar to those of C-Si. This convergence of C-Si and thin film silicon technologies is perhaps one of the most likely disruptive PV technologies that could ultimately replace C-Si as the commercially dominant technology.

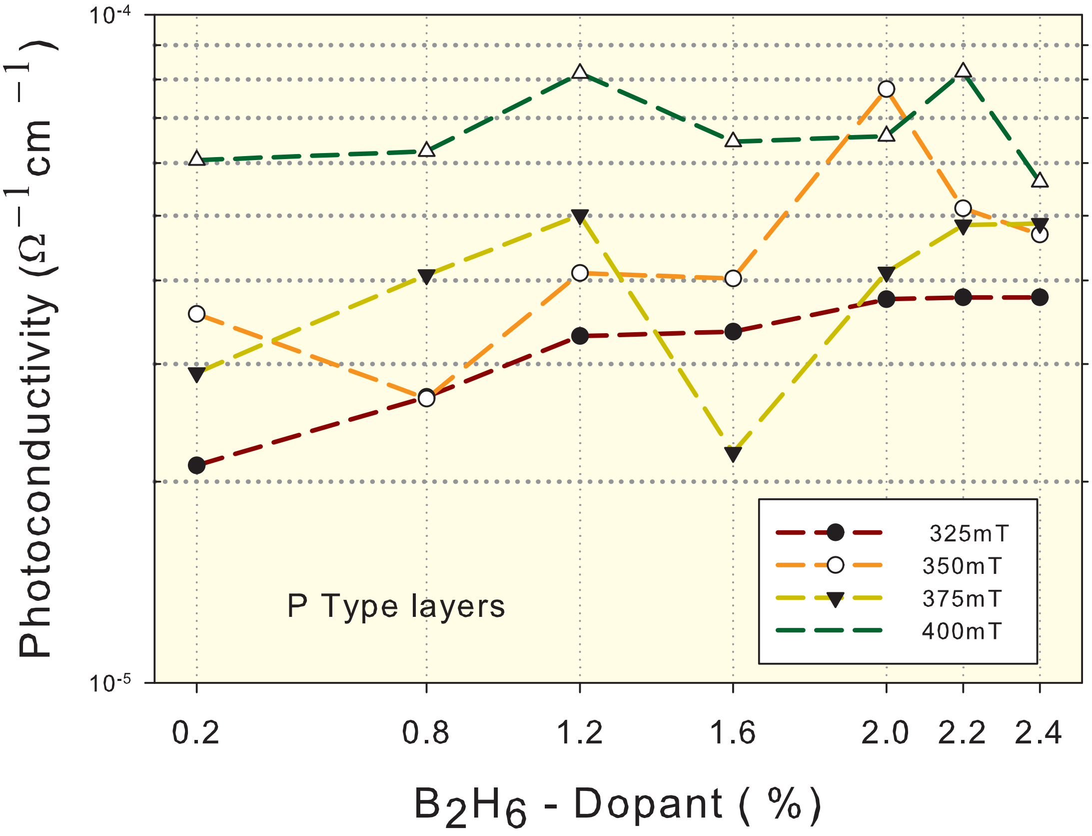

Figure 4.18: Room temperature photoconductivity of p type layers deposited with increasing dopant percentage at four different pressures.

4.4.1 Deposition techniques

The technology for manufacturing microcrystalline silicon layer and solar cells is virtually the same as for amorphous silicon which is discussed in (section 2.7). Using this same technology a different quality material can be obtained. The μc-Si:H deposition technologies are PECVD, VHF-glow discharge, microwave plasma deposition and hot-wire deposition. As μc-Si:H solar cells need a thicker layer of several micron as compared to a-Si:H, the high deposition rate is a crucial industrial demand which should be fulfilled in order to be successful in photovoltaic market.

The technology for manufacturing microcrystalline silicon layer and solar cells is virtually the same as for amorphous silicon which is discussed in (section 2.7). Using this same technology a different quality material can be obtained. The μc-Si:H deposition technologies are PECVD, VHF-glow discharge, microwave plasma deposition and hot-wire deposition. As μc-Si:H solar cells need a thicker layer of several micron as compared to a-Si:H, the high deposition rate is a crucial industrial demand which should be fulfilled in order to be successful in photovoltaic market.

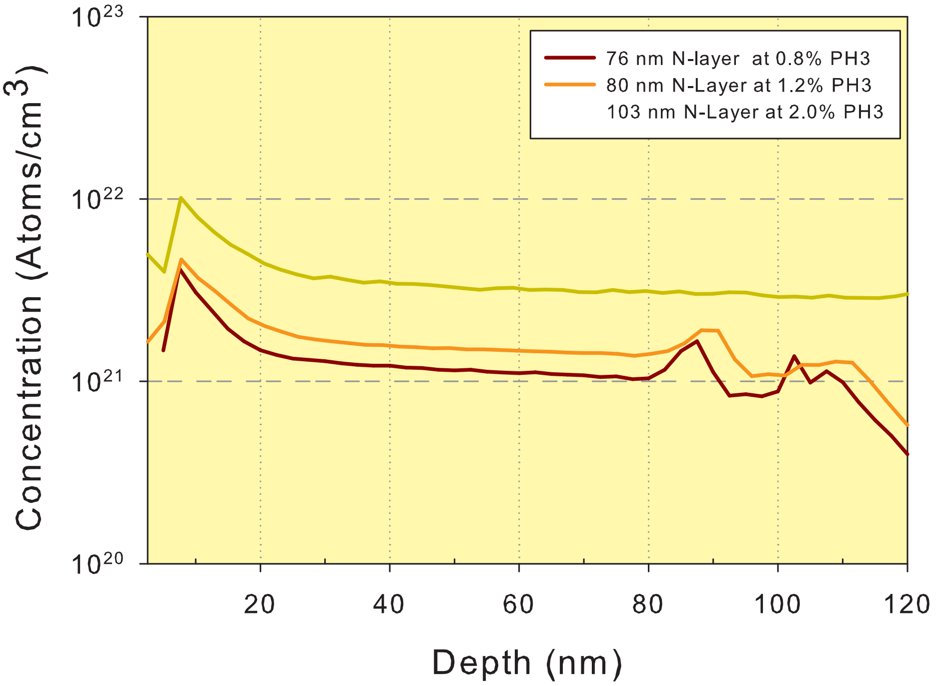

FIGURE 4.19: SIMS depth profile of phosphine in n-doped a-Si:H films deposited on glass substrates.

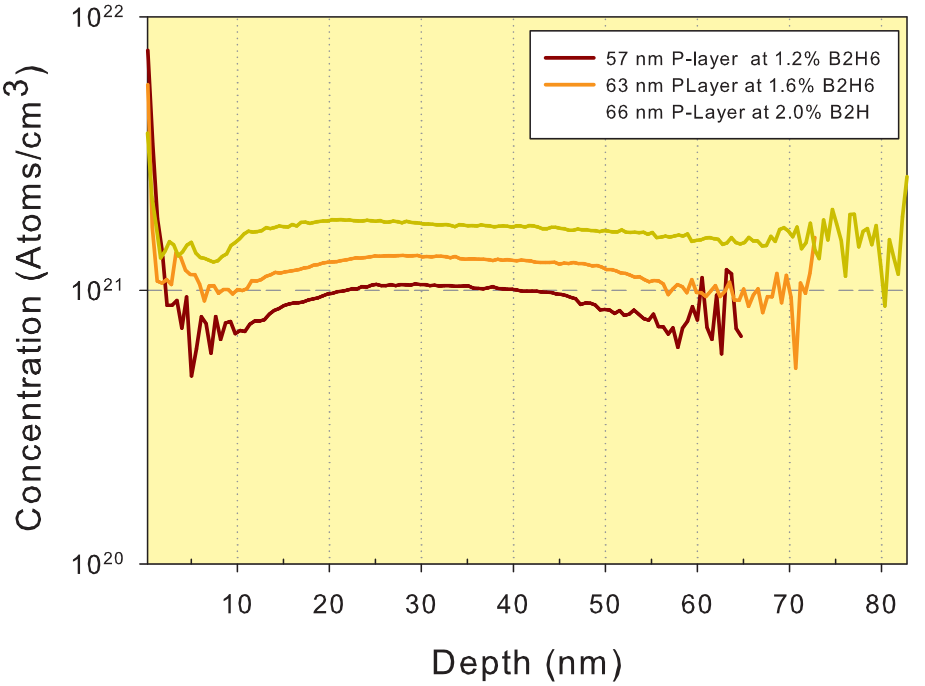

FIGURE 4.20: SIMS depth profile of boron in p-doped a-Si:H films deposited on glass substrates.

4.4.2 Growth and micro structure of μc-Si:H

The atomic hydrogen plays an important role in the growth of μc-Si:H as high hydrogen dilution increases the crystallinity of the film[56]. Since high hydrogen dilution induces a slow deposition, a different interpretation of μc-Si:H formation mechanism is very essential. The microstructure of μc-Si:H is composed of nanocrystals of diameter ranging 10 to 20 nm embedded in amorphous silicon. This combination of μc-Si:H with amorphous silicon is separated by grain boundaries and/or cracks as shown in Figure 4.21. Optical emission spectroscopy measurements confirm that there exists a threshold for atomic hydrogen flux density to the growing surface but its amount depends on other deposition conditions[106] therefore the microstructure of μc-Si:H depends on the fabrication conditions and ultimately on the underlying substrate on which nucleation and then growth take[9] [107].

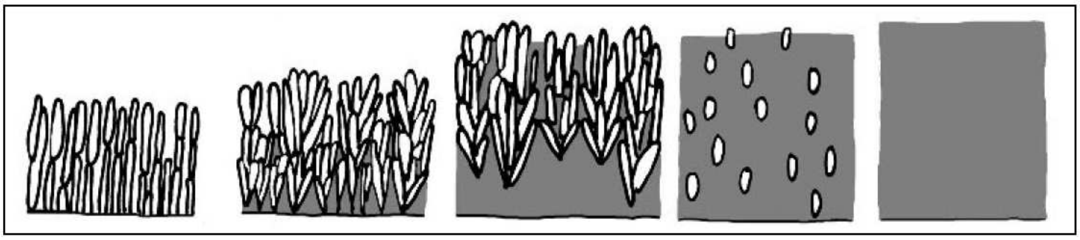

FIGURE 4.21: Schematic evolution of the microstructure of microcrystalline silicon layers as a function of crystallinity. Nanocrystallites of silicon are white in this sketch, whereas amorphous silicon is grey. The increasing thickness is a schematic representation of the increasing growth rate of microcrystalline silicon with decreasing crystallinity[9].

The growth of μc-Si:H can be controlled by an important parameter called the nucleation density which mainly depends on the chemical nature of the substrate and local epitaxy[9]. Like a-Si:H, the radical SiH_3 is the mail film precursor in the formation of μc-Si:H. Atomic hydrogen plays a vital role in the crystal formation of μc-Si:H and at higher temperature films become amorphous[56]. The sticking probability of SiH_3 does not depend on temperature but reflection probability does depend on temperature[56].

Three models have been proposed to explain the specific phenomenon in the formation of μc-Si:H, as no single model sufficiently explains all formation mechanisms[108]. The first model is the surface diffusion model[109] and according to this, a high atomic hydrogen flux from the plasma results in full surface coverage by bonded hydrogen and this creates local heating through hydrogen-exchange reactions on the film-growing surface. This develops the surface diusion of film precursors SiH_3 and as a result, SiH_3 adsorbed on the growing surface always find energetically favourable sites, leading to the formation of atomically ordered structure (nucleus formation). After the formation of nuclei, epitaxial-like crystal growth takes place with enhanced surface diffusion of SiH_3[56,110].

The second is the etching model[111] which explain that μc-Si:H film-growth rate is reduced with an increase of the hydrogen dilution. Atomic H reaching the film-growing surface breaks Si-Si bonds, the preferentially weak bonds involved in the amorphous net- work structure, leading to a removal of Si atoms that are weakly bonded to other Si atoms and this site is replaced with a new film precursor, SiH_3, which forms a rigid and strong Si-Si bond, giving rise to an ordered structure[56].

The third model is the chemical annealing model[112] which suggests that crystal formation during hydrogen plasma treatment as due to many hydrogen atoms permeating into the subsurface (growth zone) and causing the crystallization of the amorphous network through the formation of a flexible network, when there is a sufficient amount of atomic hydrogen in the subsurface region, and without significant removal of Si atoms[56].

In this report, all intrinsic c-Si:H film were fabricated on PECVD system and now we will discuss some data and results. These depositions were the first carried out at Southampton using the OPT PECVD tool.

4.4.3 Deposition rate

The deposition rate is one of the crucial factors which limits the wide industrialization of μc-Si:H based solar cells. In in very advanced research facilities current deposition rate falls in 5-10 Å/sec category and normal PECVD growth rate is 1-5 Å/sec range. Figure 6.2 and Figure 4.22 show the deposition rates for intrinsic μc-Si:H grown for this report as an initial study. The deposition rate during constant temperature of 250 ^{o}C and pressure of 1000 mTorr with increasing power does not vary significantly and remains in 1.40-1.41 Å/sec range. When plasma power of 30 W, substrate temperature of 250 ^{o}C, and chamber pressure of 1000 mTorr and 7% silane concentration are set, the deposition rate goes to the higher value of 3.63 Å/sec. The second highest deposition rate of 2.66 Å/sec is achieved at 5% silane concentration as shown in Figure 4.23.

The deposition rate is one of the crucial factors which limits the wide industrialization of μc-Si:H based solar cells. In in very advanced research facilities current deposition rate falls in 5 - 10 Å/sec category and normal PECVD growth rate is 1-5 ^{o}A/sec range. Figure 4.22 and Figure 4.23 show the deposition rates for intrinsic μc-Si:H grown for this report as an initial study.

This variation in deposition rate might be influenced by the ion bombardment by the plasma in certain situations. It is found that for some time ions play a beneficial role and sometime its plays as disruptive role during the growth of μc-Si:H[106] The deposition of μc-Si:H deposition by PECVD is slow as compared with the VHF growth technique , because the excitation frequency for growth is increased from 13.56 MHz to a range of 30-300 MHz. Its seems that due to softer but more intense ion bombardment on growing

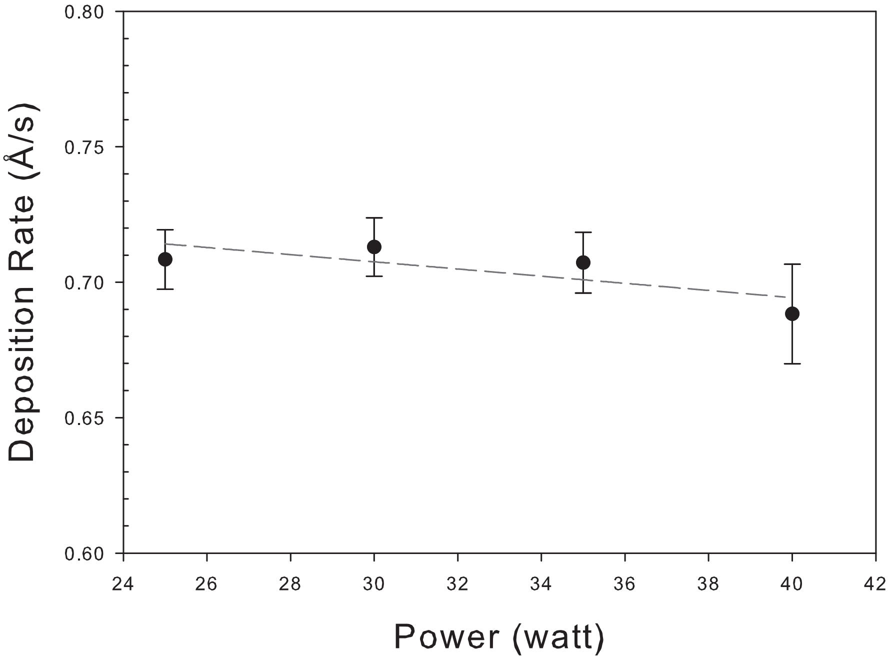

Figure 4.22: The deposition rate of intrinsic μc-Si:H as a function of increasing RF power during deposition in PECVD. The dashed line is a linear fitting to scattered data points to view the general trend of deposition rate.

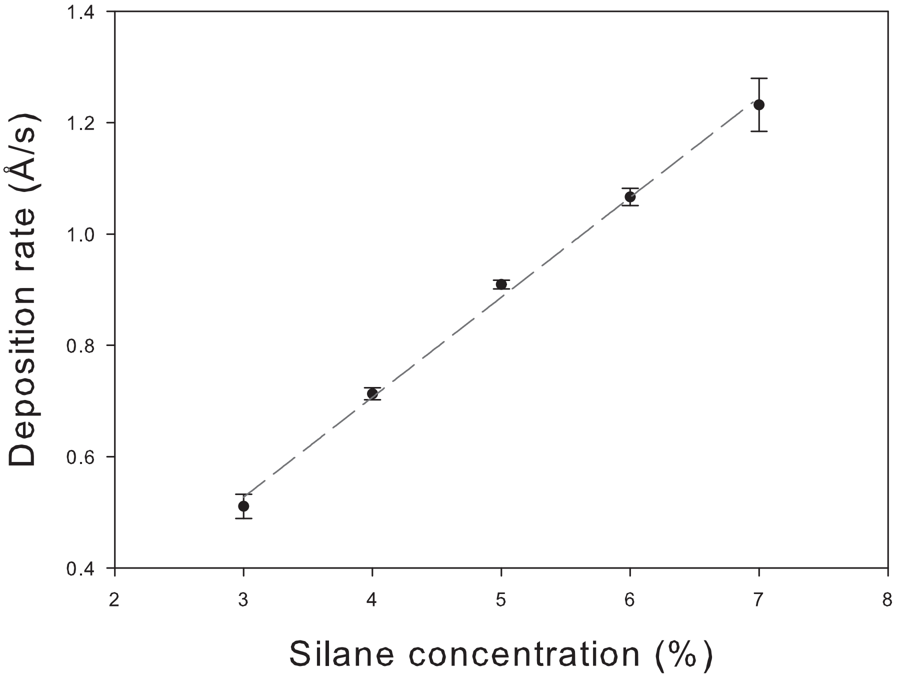

Figure 4.23: The deposition rate for intrinsic μc-Si:H as a function of silane concentration during deposition in PECVD. The dashed line is a linear fitting to scattered data points to view the general trend of deposition rate.

surface , the VHF process favours the c-Si:H as compared to conventional PECVD deposition[9].

4.4.4 Bandgap Energy

The bandgap energy of intrinsic μc-Si:H is shown in Figure Figure 4.24 and Figure 4.25. In the first films deposited films it is found that there is constant change in bandgap energy when the RF power is increasing from 30 to 40W as the material is varying mixture of amorphous and microcrystalline silicon. Initial growth at low power is also showing a high band gap. The possible reason for this behaviour is the improper ellipsometry model from which optical data has been calculated as at the start it was very difficult to find the correct model for μc-Si:H because of the complex mixed nature of the material

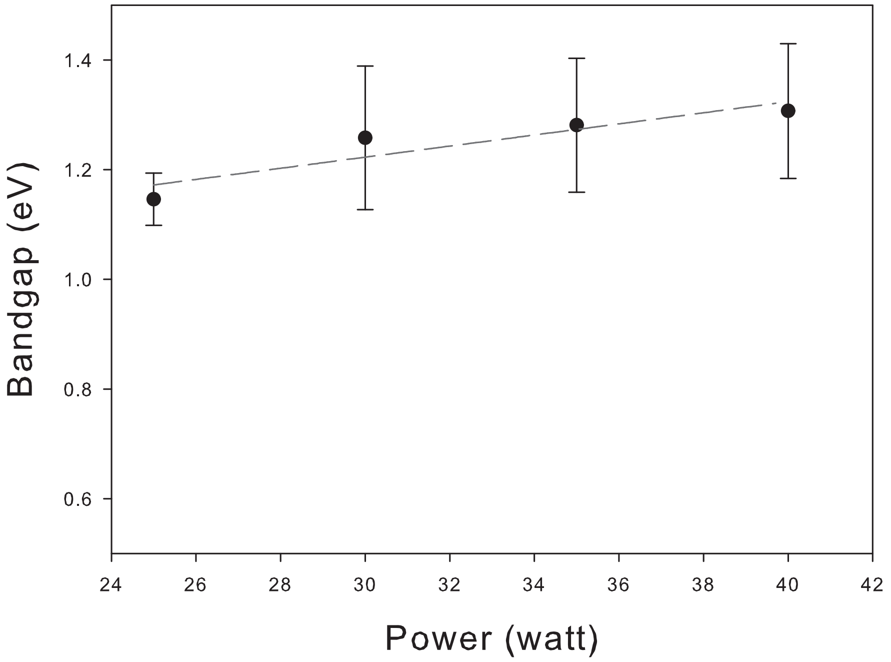

FIGURE 4.24: Bandgap energy of intrinsic μc-Si:H as a function of increasing plasma power.

The bandgap energy is found to increase with silane concentration though this change is not linear. At 4% silane concentration, the material is found to be more crystalline in nature.

4.4.5 Electronic properties

The dark conductivity and photoconductivity are measured at room temperature shortly after the deposition and results are shown in Figure 4.26 and Figure 4.27 as a function

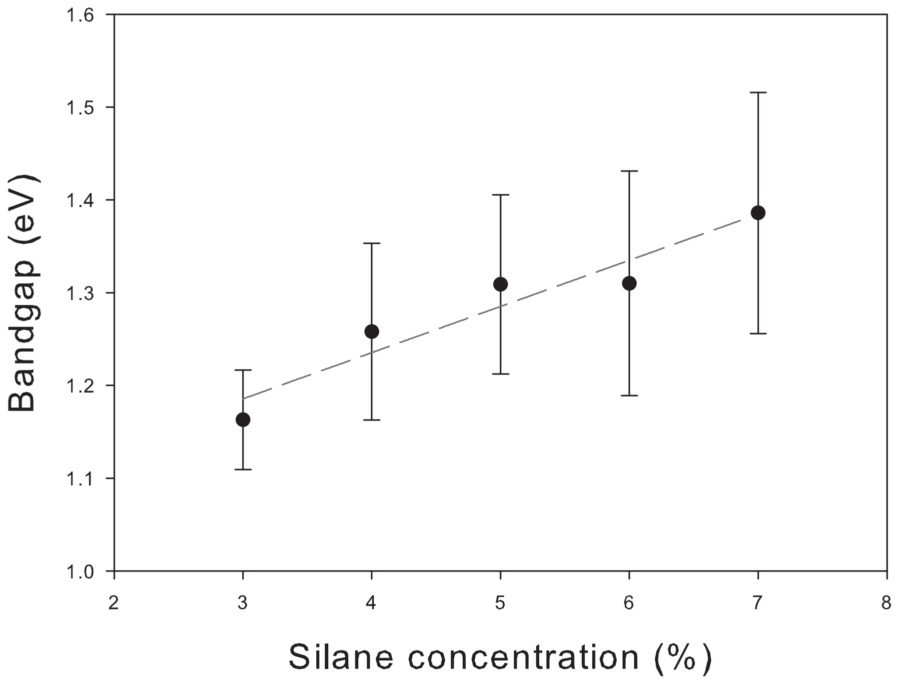

FIGURE 4.25: Bandgap energy of intrinsic μc-Si:H as a function of increasing silane concentration. The bandgap data points are linearly fitted to indicate trend-line to generalized bandgap dependency on silane gas during deposition.

of plasma power and silane concentration, respectively.

It is found that the photoresponse of μc-Si:H is constant for plasma powers from 25 W to 40 W, while the magnitude of the photoresponse found to be smaller. The dark and photoconductivity both are decreasing with increasing power. This decrease could be due to local temperature increase because of increasing plasma power. Similarly the photocurrent was found to be similar for different silane concentrations, while photoconductivity and dark conductivity show a slight increase in magnitude.

4.4.6 Raman Spectroscopy

The Raman spectra of the grown intrinsic μc-Si:H films at wavelength of 532 nm are obtained using Renishaw inVia Raman Microscope system and are shown in Figure 4.28 and Figure 4.29. All spectra show a sharp peak at 520 cm^{-1} suggesting that all grown layers are strongly crystalline in nature. It is found that increasing power, produces longer and sharper peaks in spectra as shown in Figure 4.28. With every sharp peak, there is one additional broad peak associated at 480 cm^{-1}, this suggests the presence of a-Si:H in the thin crystalline film. One spectra from the intrinsic a-Si:H film is showing a broad peak near 480 cm^{-1} which is also included for reference. We can observe the

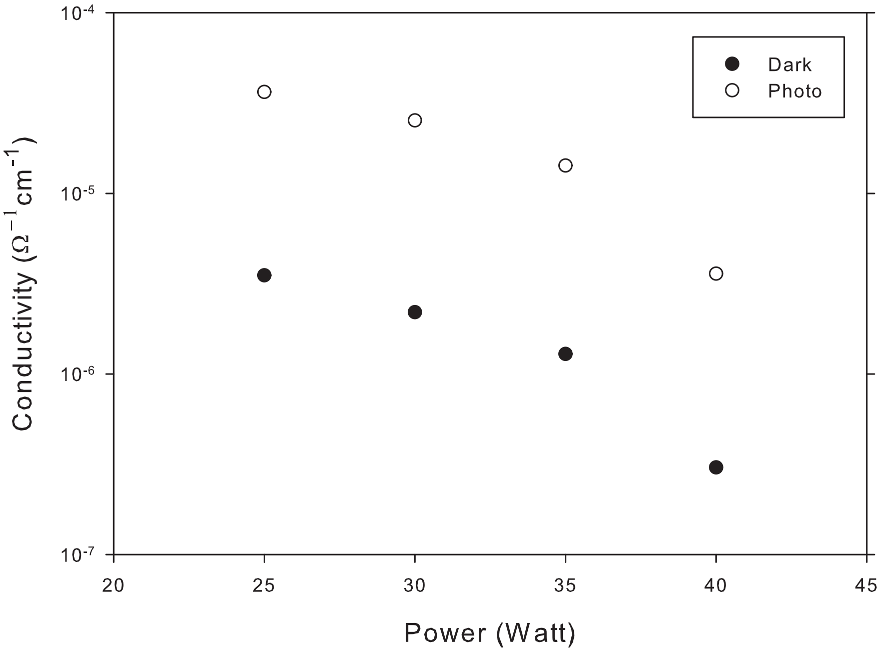

FIGURE 4.26: The room temperature dark and photoconductivity of intrinsic μc-Si:H as a function of plasma deposition power in PECVD.

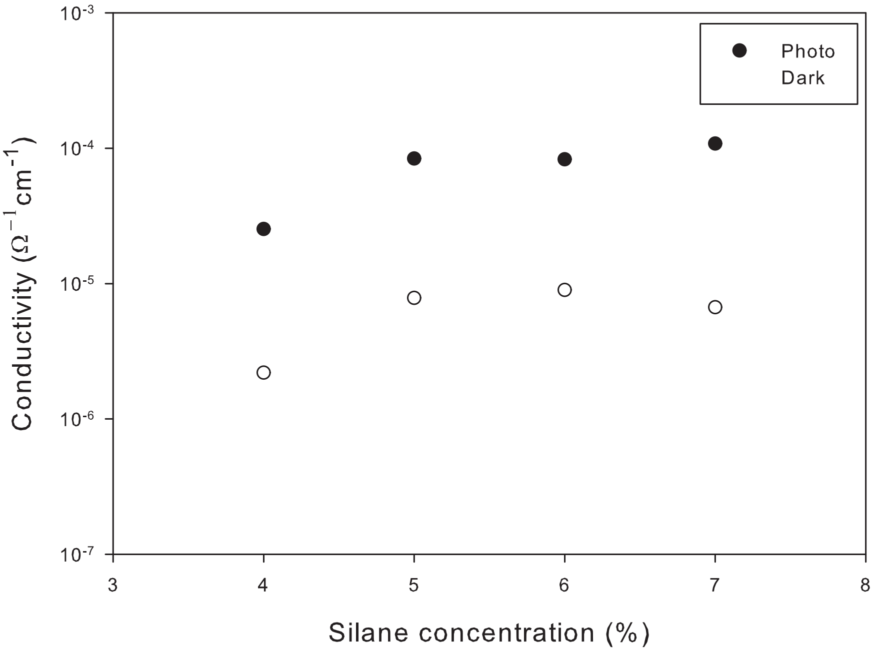

FIGURE 4.27: The room temperature dark and photoconductivity of intrinsic μc-Si:H as a function of silane concentration.

same kind of behaviour in films fabricated with different silane concentrations as shown in Figure 4.29.

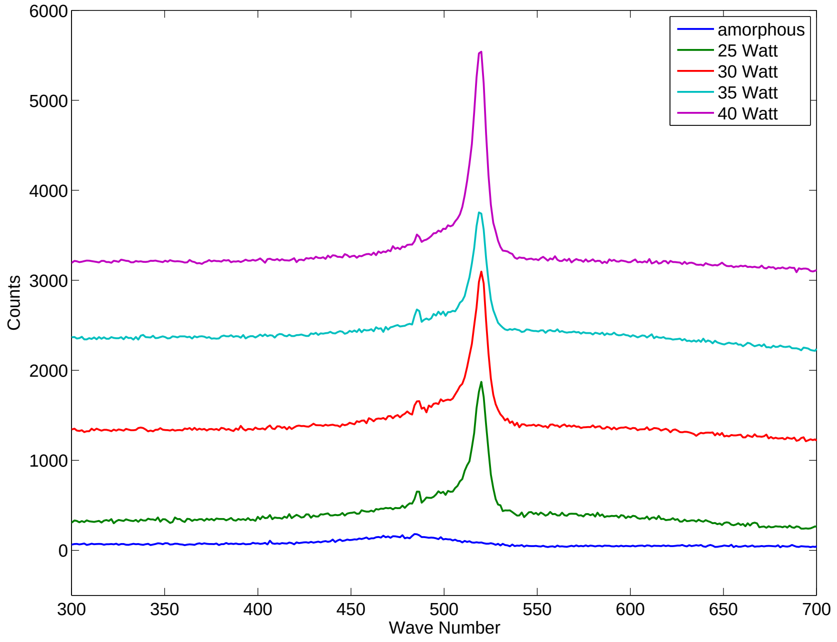

Figure 4.28: The Raman spectra of intrinsic μc-Si:H thin film deposited as a function of power in a PECVD system identify the crystal nature of the film. These spectra are generated at laser excitation wavelength of 532 nm.

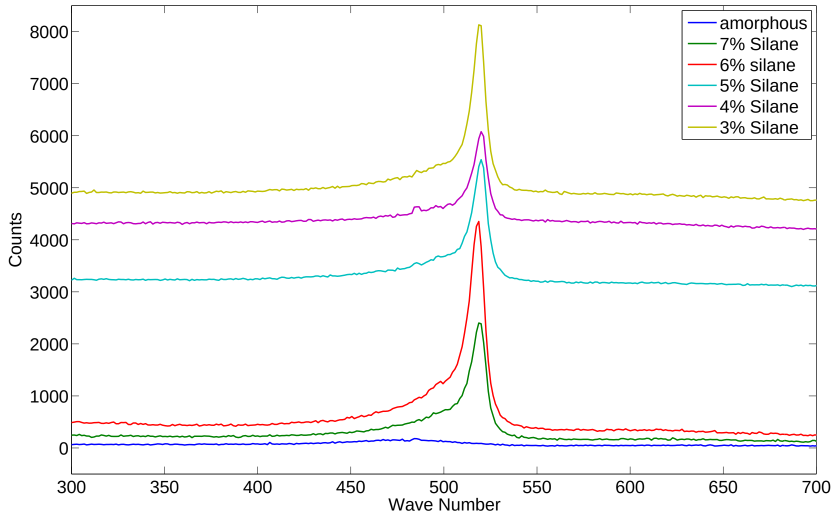

Figure 4.29: The Raman spectra of intrinsic μc-Si:H thin film deposited as a function of silane concentration in a PECVD system to identify the crystal nature of the film. These spectra are generated at laser excitation wavelength of 532 nm.

The measured Raman data is used to calculate the crystal volume present in film and this is done by fitting spectra using a Gaussian fitting method[113 114], as shown in Figure 4.30.

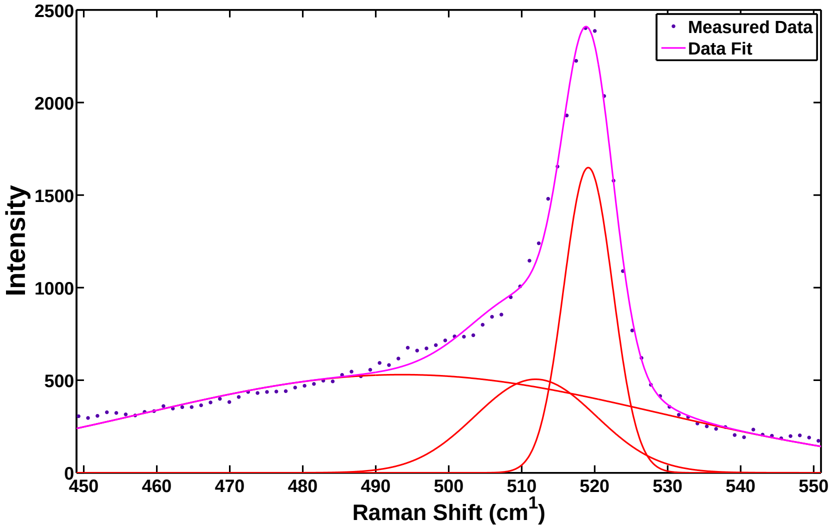

FIGURE 4.30: Gaussian fit to the Raman spectra of intrinsic μc-Si:H thin film. The doted line shows the original Raman data, pink line shows the overall fitting and red lines show individual Gaussian

The fitted data has been divided into three park peaks as shown. The first peak near 521 cm^{-1} indicates crystalline features. The second peak at 510 cm^{-1} represents a mixture of amorphous-crystalline features in film. The third broad peak near 480 cm^{-1} represents the pure amorphous in the film, where the breadth of the feature is indicative of a diversity of Si-Si bond lengths and bond angles. It is noted that the presence of a broad amorphous peak is a dominating feature in the film. The degree of crystallinity in μc-Si:H film is estimated by the crystal volume fraction (X_c) from the Raman spectra using the equation 4.1[115]:

$$X_c = \frac{I_c}{(I_c + I_a)} \tag{4.1}$$

Where I_c is the combined area of sharp peaks at 520 cm^{-1} and 510 cm^{-1} and I_c is the area of broad peak at 480 cm^{-1}. The table (4.2)shows crystal volume of of μc-Si:H thin films at various silane ratio during PECVD deposition.

Silane Ratio (%)	Crystal Volume (%)
7	34.18 ± 1.99
6	33.60 ± 0.93
5	32.20 ± 1.90
4	18.36 ± 2.50
3	25.33 ± 2.10

TABLE 4.2: Estimated crystal volumes of μc-Si:H thin films at various silane ratio during PECVD deposition

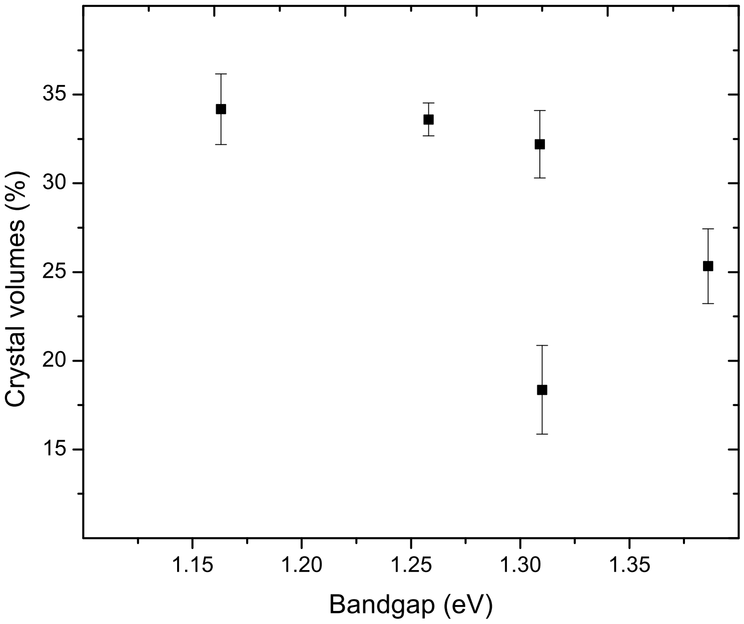

(a)

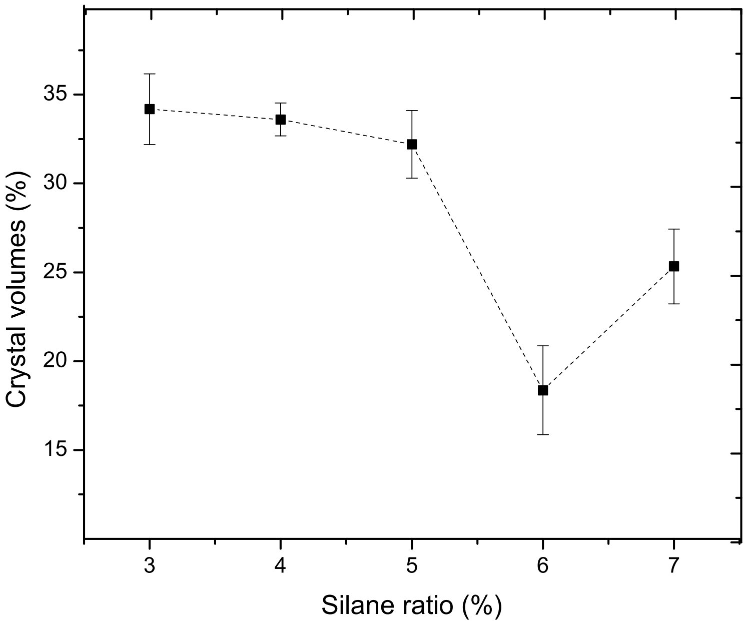

(b)

Figure 4.31: Crystal volume in μc-Si:H is plotted against, (a) bandgap of the film and (b) the silane ratio during film deposition.

The results in table (4.2) are in close agreement with the result published elsewhere[114,116]. It is noted that bandgap of μc-Si:H has correlation with crystal volume as shown in Figure 4.31. It is may have indicated that crystallinity of μc-Si:H may increase with decrease in the bandgap.

4.5 Summary

The device-grade single a-Si:H layers have been characterised optically and electrically, using different characterisation methods. It is found that thickness profile of PECVD deposited single layers is uniform and deposited layers have good uniformity. Deposition rates can be effectively controlled by chamber pressure, RF power and gas flow. It is also observed that intrinsic a-Si:H layers showed excellent optical absorption in the visible range. The optical absorption is also tested for chamber pressure and table temperature variations in order to get optimised control parameters. The simple simulated absorption spectra confirmed that intrinsic layers can absorb 90% of incoming visible spectrum. The band-gap and Urbach energy of intrinsic layers can be tuned accordingly. It is also verified that chamber pressure has little effect on band-gap to intrinsic layers.

The room temperature conductivity measurement verified that deposited intrinsic layers are device grade as photoresponse (ratio of the photoconductivity and dark conductivity) is found in the order 10^3 - 10^4 at different deposition conditions. The dark conductivity of deposited intrinsic layers measured in ranges which are less than 1   1010   1cm 1 requirement. Similarly photoconductivity of deposited intrinsic layer found the range 1 $\times 10^{-4}\ \Omega^{-1}\text{cm}^{-1}$ which is higher than the required $\times 10^{-5}\ \Omega^{-1}\text{cm}^{-1}$.

The *p*-type and **n**-type a-Si:H films are found highly doped such as 10^{21} atoms/cm^3 and 10^{22} atoms/cm3 respectively which are in excellent agreement required for device grade doped layer. The thickness of thin doped films are independently verified by ellipsometry and SIMS and demonstrated effective control which is essential for device fabrication.

It is observed that μc-Si:H deposition can be achieved using the deposition parameter baseline of a-Si:H. It is found that bandgap of intrinsic μc-Si:H can be tuned heavily by using appropriate silane concentration with low dependency to RF power. It is found that electrical conductivity of μc-Si:H films loosely depend on silane concentration but heavily depend on RF power. The photoconductivity to dark conductivity ratio always remains in the same range, which suggests that those layers are device grade. The Raman spectroscopy data and their Gaussian fitting demonstrate that 18 to 34% crystal volume is present in each film and this crystal nature depends on silane ratio. This crystallinity percentage of μc-Si:H suggest that, there is still room for improvement in this regards. Nevertheless the capability has been of value to the Southampton Nanofabrciation Centre, particularly in the study of light-trapping effects for C-Si like thin films.

Chapter 5

Single Junction Devices

In this chapter, the effects of varying the deposition conditions on the energy conversion efficiencies of single junction thin film silicon solar cells are discussed. The single layer deposition parameters from previous chapters are applied in complete devices as a starting point to device optimisation. Solar cells devices are deposited using the Oxford Instruments PlasmaLab System 100 on to Pilkington TEC-8 TCO glass, and thoroughly investigated by electrical characterisation. For device performance, the deposition conditions, including substrate temperature, gas flow rates, RF power, chamber pressure and film thickness are all interrelated and here all are explored to determine the optimum cell performance.

In this chapter all measurements for single junction devices are *initial* properties of cells, measured before any light induced degradation and every effort was made to ensure all fabrication, characterisation and fitting procedures were performed consistently.

5.1 Chamber pressure effects

The deposition parameters for initial single junction *pin* a-S:H devices based on single layer optimisation processes described in chapter 3. It was decided to use following parameters (table 5.1) while varying the chamber pressure.

TABLE 5.1: Initial deposition parameters for single junction *pin* a-Si:H devices

Layer type	RF Power	Temp.	Thickness	Silane Flow	Argon Flow
-	(W)	(°C)	(nm)	(sccm)	(sccm)
P	10	250	10	25	475
I	10	250	370	25	475
N	10	250	45	25	475

The chamber pressure was varied between 300 mT and 1000 mT and the result of these experiments are shown in Figure 5.1. It observed that the variations in chamber pressure affect every characterisation parameter specifically short circuit *current density* (J_{SC}), *fill factor* (FF), *open circuit voltage* (V_{OC}) and *efficiency*. Improvements to all device characterisation parameters are observed when the deposition chamber pressure is at lower values. At higher pressure such 1000 mT, 370 nm of an intrinsic layer takes 11 minutes which is relatively fast when compared with same thickness deposited under low chamber pressure such as 300 mT which takes 16 minutes. In industry, lower deposition rate may not be beneficial in terms of time but in this case it has positive effects on device performance. As shown in Figure 5.1, the short current density photo current has been enhanced by 7 times. There are also considerable improvements in FF, V_{OC} and the final efficiency of the device.

During the deposition of a-Si:H , the initial growth process that takes place, is the electron-impact dissociation of source gas material into monosilane (SiH_4) and monosilane-hydrogen glow discharge plasma in excited state which spontaneously dissociate to radicals such as SiH_3, SiH_2, SiH, Si and others[56]. The higher order silane radical SiH_3 is the dominant chemical species for a-S:H growth[56]. At higher chamber pressure, the deposition rate of the film also tends to increase. When silane pressure is increased, the amount of those higher order radicals in the plasma is known to increase, while short life-radicals SiH_2, SiH, Si contribute to the film growth under silane depletion conditions in such a way that it cause changes in film growth precursor and on the growth surface resulting in inferior film properties[117]. There are other related deposition parameters aecting device quality in addition to the higher deposition rate.

5.2 The effect of hydrogen and argon

In the previous section, during device deposition only argon was used with silane source gas to assist plasma generation. In this section, devices with and without argon and hydrogen dilution are discussed. The H_2 dilution is defined as $R = [H_2]/[SiH_4]$, where brackets indicate flow rate of the gas. The gas flow rate arrangements for the deposition of the intrinsic layer of the single junction *pin* a-Si:H devices are shown in the table 5.2, whereas the rest of the deposition parameters are provided in table 5.3.

TABLE 5.2: Dilution ratio of silane and hydrogen with argon flow for the deposition of the intrinsic layer in the single junction *pin* a-Si:H devices

Silane Flow (sccm)	H_2 Flow (sccm)	Argon Flow (sccm)	Dilution Ratio R
50	50	0	1
25	25	100	1
25	0	475	0

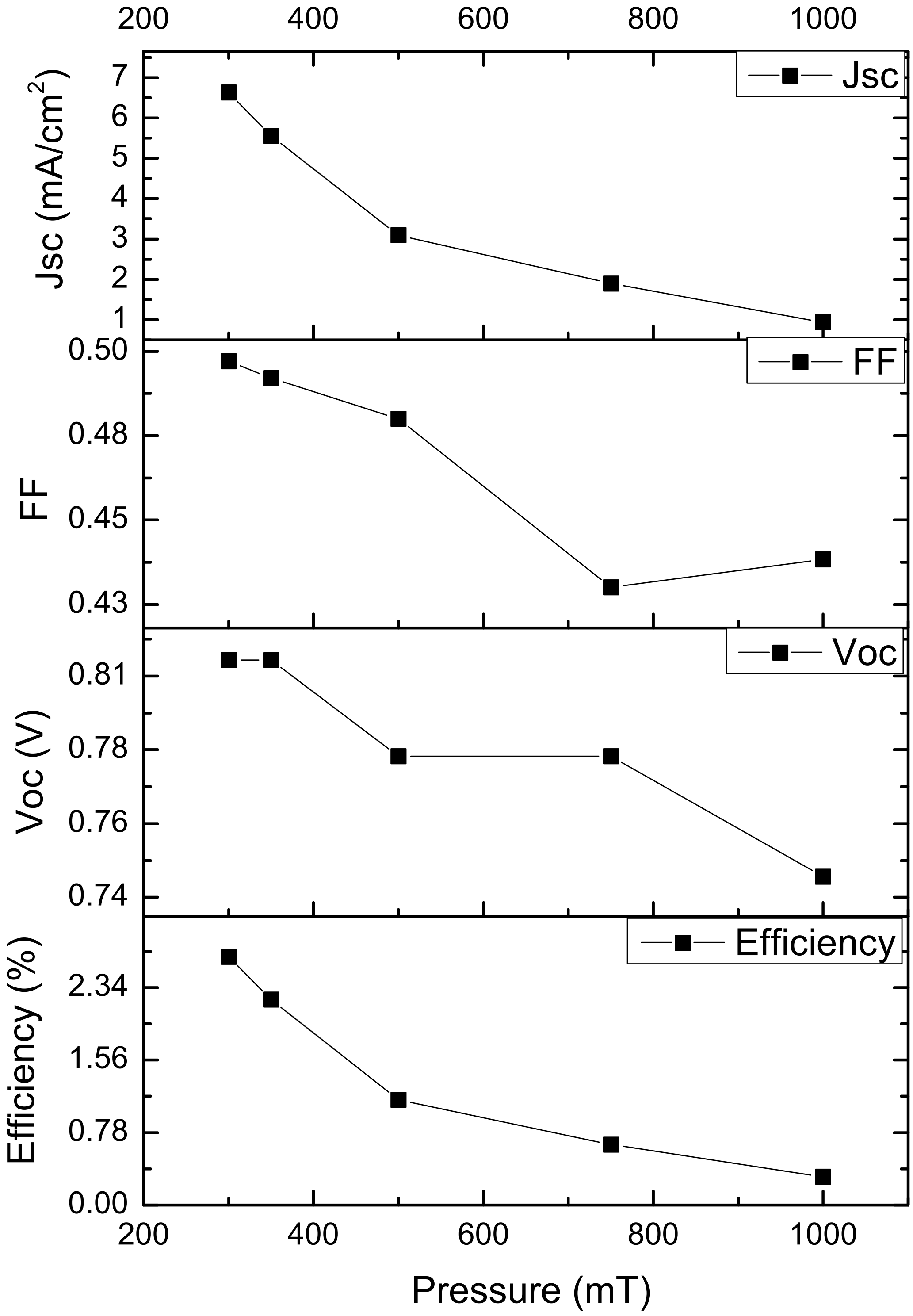

FIGURE 5.1: The characterisation parameters of single junction *pin* a-Si:H device with deposited with varied chamber pressure.

Table 5.3: Deposition parameters for single junction *pin* a-Si:H devices deposited with varied H_2 dilution and argon

Layer type	RF Power	Temp.	Thickness	Silane Flow	H_2 Flow
-	(W)	(°C)	(nm)	(sccm)	(sccm)
P	10	250	10	25	25
I	10	250	400	-	-
N	10	250	45	25	25

The resultant solar cell characterisation parameters are shown in Figure 5.2. H_2 dilution and argon dilution both have altered the short-circuit current density of the device. In the presence of both H_2 and argon short-circuit current density is enhanced while if argon is completely removed from the chamber and the H_2 is not changed, the short-circuit current density is further increased. This is an indication that argon plasma is detrimental to the film growth process.

Argon plasma has a strong effect on the *FF* of the device however, the level of dilution with H_2 does not alter the *FF* of the device significantly. H_2 dilution does not change the *FF*. While the absence of argon during the deposition process, increases the *FF* from 0.53. On the other hand V_{OC} remains unchanged for both levels of argon dilution but decreases from 0.81 V to 0.75V when argon is removed. The reduction in V_{OC} may be attributed to the properties of the doped layers which are discussed later in this chapter. Device deposited with argon have maximum efficiencies of 2.5%. In the presence of both H_2 and argon diluted silane the devices efficiency goes to 3.5%. The devices deposited in the absence of argon in the source gas increases the efficiency to 4%. This indicates that just by removing argon, device efficiency increased almost double of its original value.

It is a well-known fact that during a-S:H deposition, H_2 diluted silane source gas mixture has been found to reduce the density of defect state and also improve the stability of material against light degradation effects[6,118,119]. These effects of H_2 dilution during growth are due to some interactions which are[6]:

1. Atomic hydrogen tending to remove weaker bonds which are not bonded in energetically strong locations;
2. The surface diffusivity of adatoms is promoted by high stream of atomic H2 so that they can occupy electronically stable positions;
3. Reconstruction of the atomic network due to the diusion of atomic H2, with a strong and more stable structure.

The devices discussed in this section may not be showing that strong effect of H_2 dilution as here only one kind of dilution is mentioned which is 1R (where R=$[H_2]/[SiH_4]$). The strong effect of H_2 dilution is more visible when dilution value goes to more then

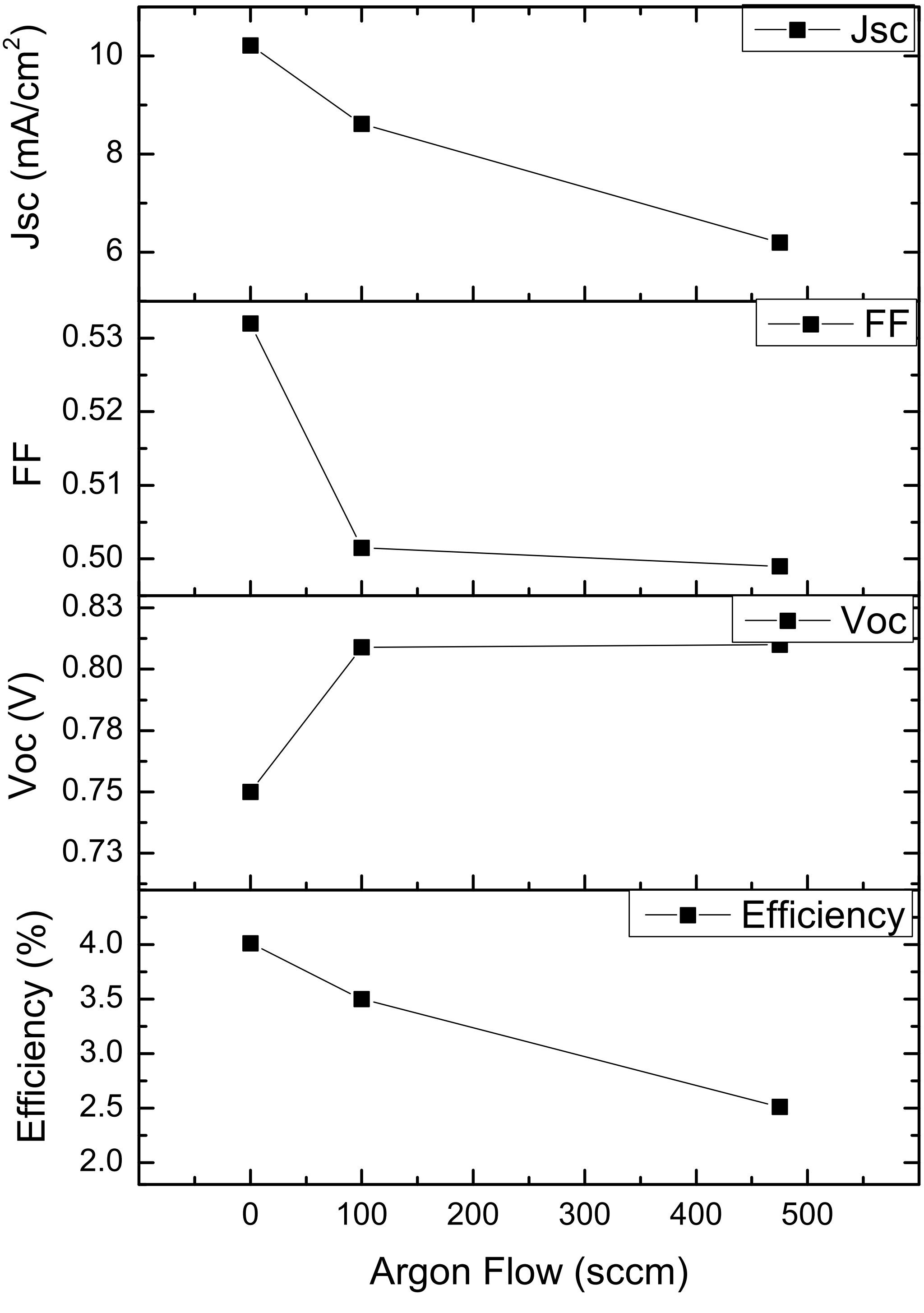

Figure 5.2: The characterisation parameters of single junction *pin* a-Si:H device deposited with three different amounts of argon used as dilute gas.

10R[120,121]. On the other hand, in this work, it was found that argon dilution actually deteriorates the *FF* and J_{SC} of single junction *pin* a-S:H solar cell. Some experimental work by others clearly show that the introduction of argon deteriorates the crystallinity of nanocrystalline silicon (nc-Si:H) and increased flow rate adversely affects the crystallisation of films[119]. The basic principle of the deposition of nc-Si:H film and a-Si:H is the same, therefore a similar kind of mechanism may also be applied to a-S:H films.

5.3 RF power effects

In PECVD, a higher RF power increases the plasma excitation which in turn increases the deposition rate, but this also results in higher defect densities in the film. By staying within the ideal range, and obtaining higher deposition rate, it is essential to find the safe range of RF power levels where the lowest defect densities are produced in the film occur. In this work, during a-Si:H solar cell growth, RF power was varied from 10W to 25W, while other deposition parameters remained unchanged as described in table 5.4.

TABLE 5.4: Deposition parameters for single junction *pin* a-Si:H devices deposited with varied RF Power

Layer type -	Pressure (mT)	Temp. (°C)	Thickness (nm)	Silane Flow (sccm)	H_2 Flow (sccm)
P	350	250	10	25	25
I	350	250	400	50	50
N	350	250	45	25	25

The resultant performance of a-Si:H devices, fabricated with RF power variations are shown in Figure 5.3. One thing which is clearly shown in these results is that higher RF powera degrades the device performance in accordance with the likely degeneration of high defect densities in the intrinsic layer. It is concluded that at the deposition temperate of 250 °C, the maximum RF power must be less than 25W if using other similar deposition conditions.

As mentioned earlier, during plasma deposition, silane molecules decompose into radicals SiH_3, SiH_2, SiH, Si and H, and SiH_4 is the most predominant film precursor in PECVD process[122]. The contribution of other radicals to the main deposition process may be small but they do influence electronic properties remarkably[106]. The relationship between deposition rate of the intrinsic a-Si:H film on the *FF* of the device is shown in Figure 5.4, It is observed that as deposition rate is increased, the *FF* of the device decreases.

On the basis of results shown in Figure 5.3 and Figure 5.4, and experimental work by others[106,117,122,123], one can argue that SiH_2 radical density increases with higher deposition rate under conventional PECVD method resulting in a decrease in the solar cell efficiency. The V_{OC} seems to be unaffected during RF power variations. It suggested

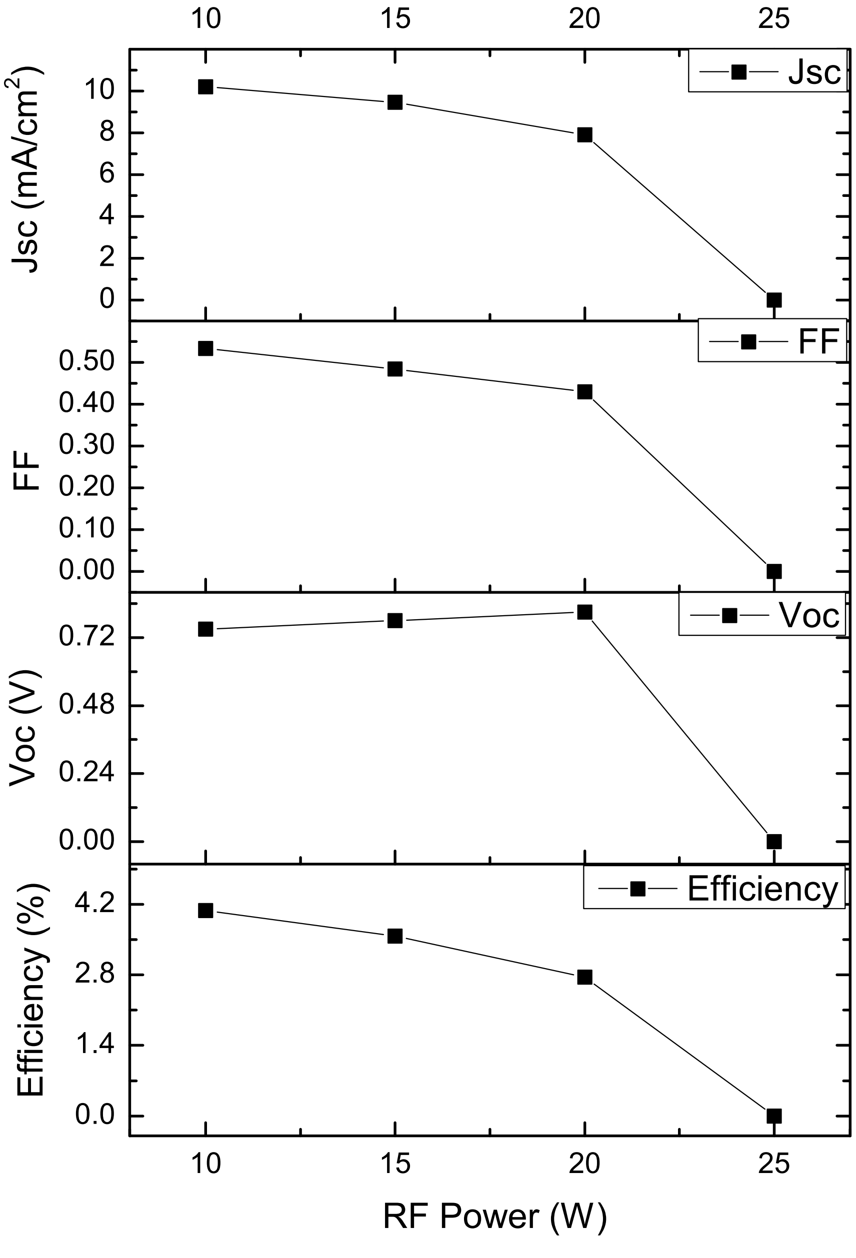

FIGURE 5.3: The characterisation parameters of single junction *pin* a-Si:H device with deposited with different RF powers.

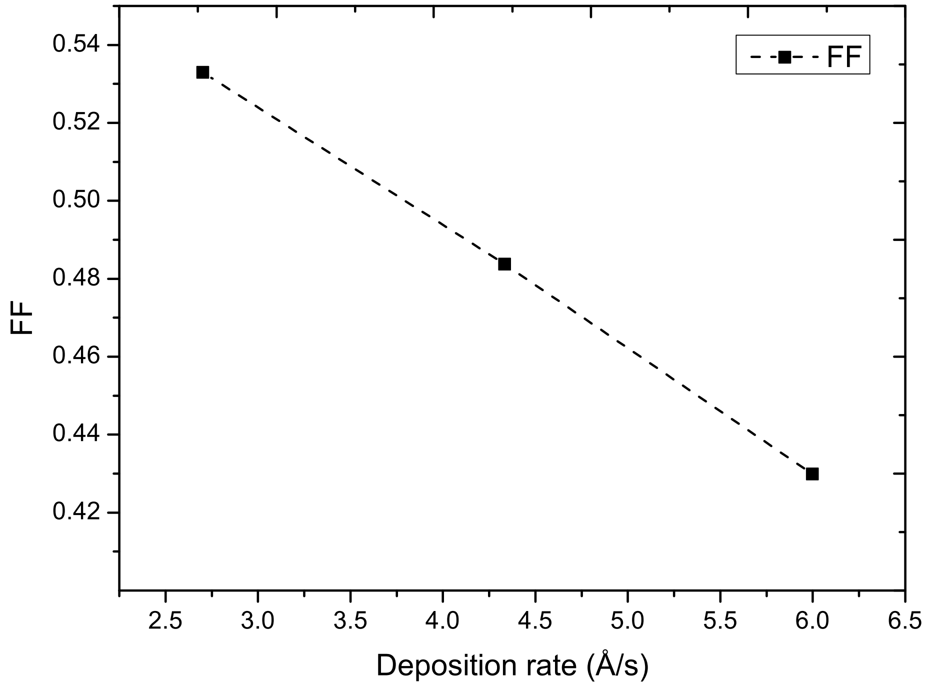

Figure 5.4: The effect of RF powered deposition rate of intrinsic a-Si:H film on the *FF* of the device.

that high RF power has no effect on doped layers. If SiH_2 radicals could be suppressed by proper deposition conditions, the PECVD tool could grow high quality a-Si:H devices at higher deposition rates without upgrading the system.

5.4 Intrinsic layer thickness

The intrinsic layer thickness is fundamental in determining the performance of the photovoltaic device. It is this layer in which, the absorption of photons occurs and so the layer must exhibit exceptional intrinsic properties such as a small dark/photo conductivity ratio. A peak in performance with layer thickness will exist for this layer; if it is too thin then absorption will be reduced and I_{SC} will suffer, whilst if it is too wide then the electric field will be reduced causing impaired V_{OC} and reduced carrier collection and I_{SC}.

Contamination of amorphous silicon with impurities can also detrimentally affect the performance of this layer, resulting in significantly impaired photocurrents, regardless of other conditions. It is therefore essential that the deposition chamber is clean of all metal and other contamination, and dopant gases sufficiently cleared from the chamber using flows of inert gas after the doped layers.

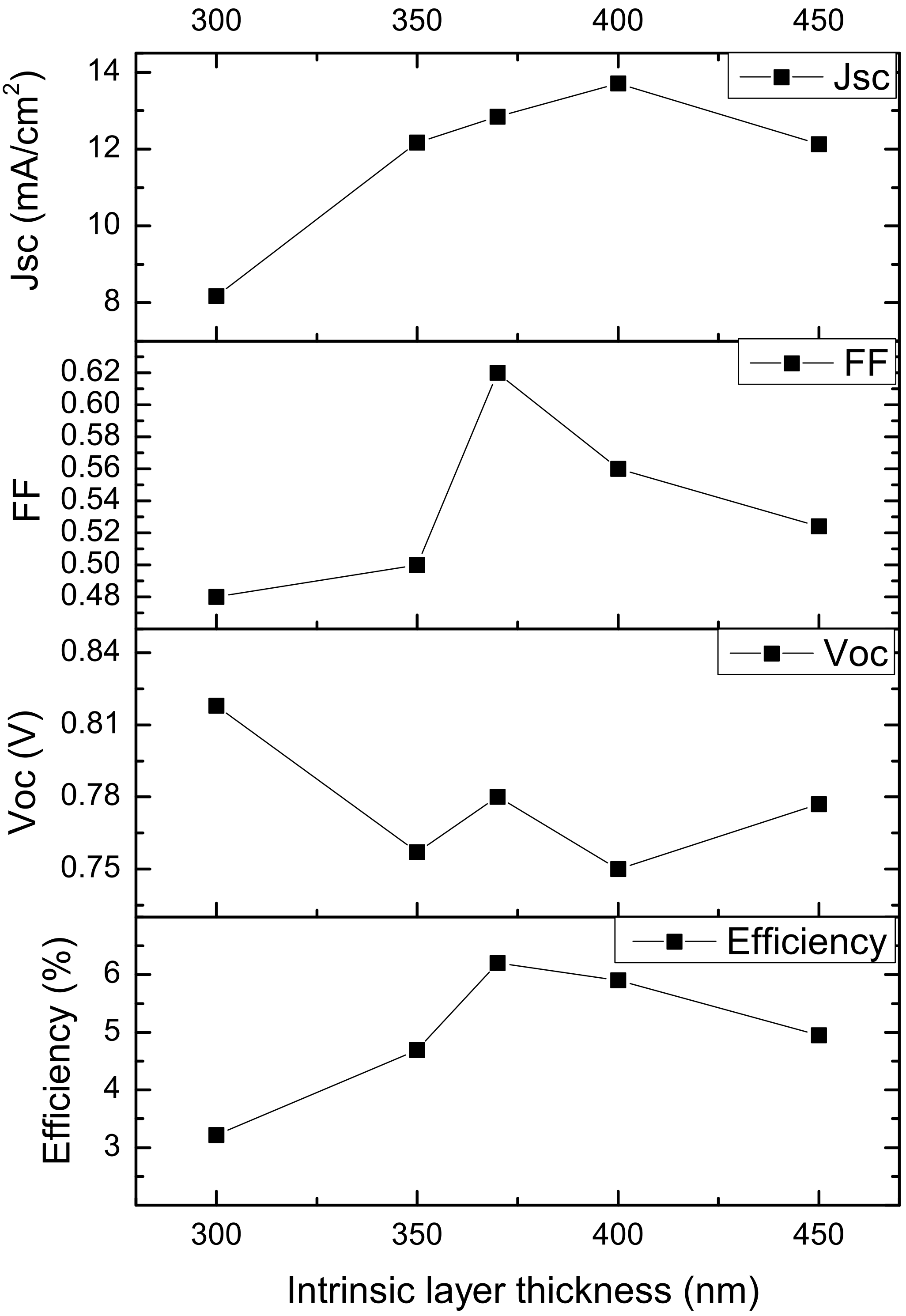

FIGURE 5.5: The characterisation parameters of single junction *pin* a-Si:H device deposited with different intrinsic layers in search of optimum absorber layer thickness.

Table 5.5: Deposition parameters for single junction *pin* a-Si:H devices deposited with varied intrinsic thickness

Layer type -	Pressure (mT)	Temp. (°C)	RF (W)	Silane Flow (sccm)	H_2 Flow (sccm)
P, I and N	350	250	10	50	50

To see the effect of intrinsic layer quality on overall device performance and individual characterisation parameter, devices were made according to deposition parameters described in table 5.5. One can immediately find from results shown in Figure 5.5 that for single junction *pin* a-Si:H cell, the maximum intrinsic layer should not be more than 400 nm where short-circuit current density is at maximum value. Under normal conditions, without employing light capturing techniques, or a buffer layer, for these particular set of devices it was found that intrinsic thickness from 350 nm 400 nm works best.

The *FF* of a-Si:H solar cell in intrinsic thickness variation drops just below 0.5 for thinner layers, for all other thickness it remained more than 0.5 and rose to a maximum of 0.622 which is the second highest achieved during this work. The V_{OC} of devices mostly depends on the doped layers which were kept constant during all experiments on the intrinsic layers, however V_{OC} is weakly dependant on absorber layer thickness as mentioned in chapter 2.

In this section, we have found that the V_{OC} of devices varied between 0.75 V and 0.81 V for different thicknesses. These variations could be attributed to deposition conditions, deposition chamber contamination or thickness uncertainties with the doped layer which are deposited for very short time due to higher deposition rate. The uncertainties in thickness of doped layers are further discussed later in this chapter.

As expected the efficiencies of the single junction a-Si:H devices vary significantly with thickness. We have found that at intrinsic layer thicknesses of 300 nm, the device efficiency is a little over 3%, the efficeny increase to 6.23% at 370 nm of intrinsic layer thickness, and from there efficiency decreases with 5% at 450nm of intrinsic layer.

5.5 Doped layers optimisation

The a-Si:H solar cell is a sandwich of an intrinsic layer between two doped layers of are *p*-type and the *n*-type a-Si:H. These highly conductive layers produce the electric field required to collect the photo-generated carriers and also provide a suitable interface for the formation of external contacts to transport current out of the cell. We will discuss the optimisation of both layers in turn.

5.5.1 The *p*-type layer of the device

The *p*-type layer thickness is fundamental in determining the performance of the a-Si:H based photovoltaic device. As light enters via this layer, the device performance is very sensitive to any thickness variations. It is always recommended that *p*-type layer must be kept as thin as possible whilst retaining an adequate ability to provide charge carrier separation together with the *n*-type layer at the rear of the device. During a- Si:H device fabrication, *p*-layer optimisation has been performed by varying dopant flow rates, using different combinations of gases, and using different film thickness. During these optimisations other parts of the device structure, namely the intrinsic layer, the *n*-type layer and the front and back contacts were kept unchanged for all sets of experiments. In this first set of experiments argon was still used in the gas mixture during the deposition. The deposition parameters for single junction pin a-Si:H devices deposited with different *p*-type layer thickness with argon presence during deposition are shown in table 5.6. The characterisation parameters of the device is shown in Figure 5.6

TABLE 5.6: Deposition parameters for single junction *pin* a-Si:H devices deposited with different *p*-type layer thickness with argon presence during deposition.

Layer type -	layer thickness (nm)	Pressure (mT)	Temp. (°C)	RF (W)	Silane Flow (sccm)	H_2 Flow (sccm)	Ar flow (sccm)
P	-	350	250	10	25	0	475
I	400	350	250	10	25	0	475
N	50	350	250	10	25	0	475

As discussed in the section (5.2), we have found argon to have a profound detrimental eect on the properties of intrinsic layers and the performance of a-Si:H devices In the results presented in Figure 5.6. we can see that the presence of argon continues to adversely effect device properties, nevertheless useful data was obtained during this exercise. The most valuable parameter in this case is V_{OC} is low but also demonstrates trends that strongly suggest the appropriate thickness range for the *p*-type layer. It is observed that a reasonable device thickness of the *p*-type layer lies between 7 nm and 20 nm. We see that a higher V_{OC} is obtained at 16 nm of thickness where the *FF* is reasonably good along with efficiency, but the short-circuit current is not at its maximum at that thickness. This means that not enough light is reaching the absorber layer of the device. The highest short-circuit current density is generated at around 10 nm. From single layer optimization which is mentioned in 4, we already know that boron dopant flow between 6 to 16 sccm is sufficient, to get highly doped *p*-type layer. It is now matter of selecting the optimum flow within the given thickness range. For this purpose, initially, two different boron dopant flows were chosen at different film thickness. The devices characteristics are shown in Figure 5.7. The deposition parameters for this set of devices are described in table 5.7.

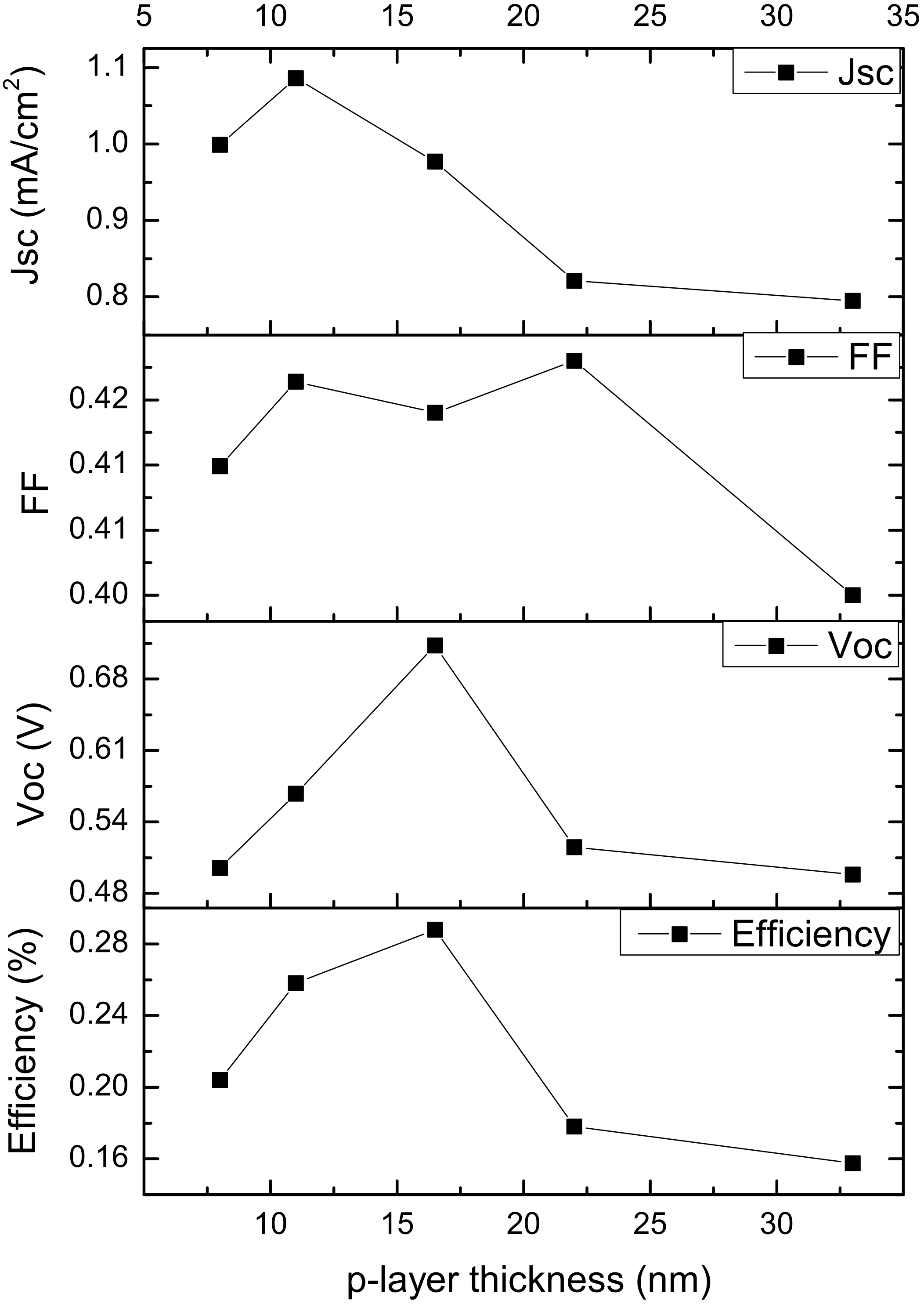

FIGURE 5.6: The characterisation parameters of single junction a-S-:H solar cells with *p*-type thickness variations deposited in the presence of Argon with fixed flow rate of 5 sccm of boron dopant.

TABLE 5.7: Deposition parameters for single junction *pin* a-Si:H devices deposited with different *p*-type layer thickness.No argon is used during these depositions.

Layer type	layer thickness	Pressure	Temp.	RF	Silane Flow	H_2 Flow	Ar flow
-	(nm)	(mT)	(°C)	(W)	(sccm)	(sccm)	(sccm)
P	-	350	250	10	50	50	0
I	400	350	250	10	50	50	0
N	50	350	250	10	50	50	0

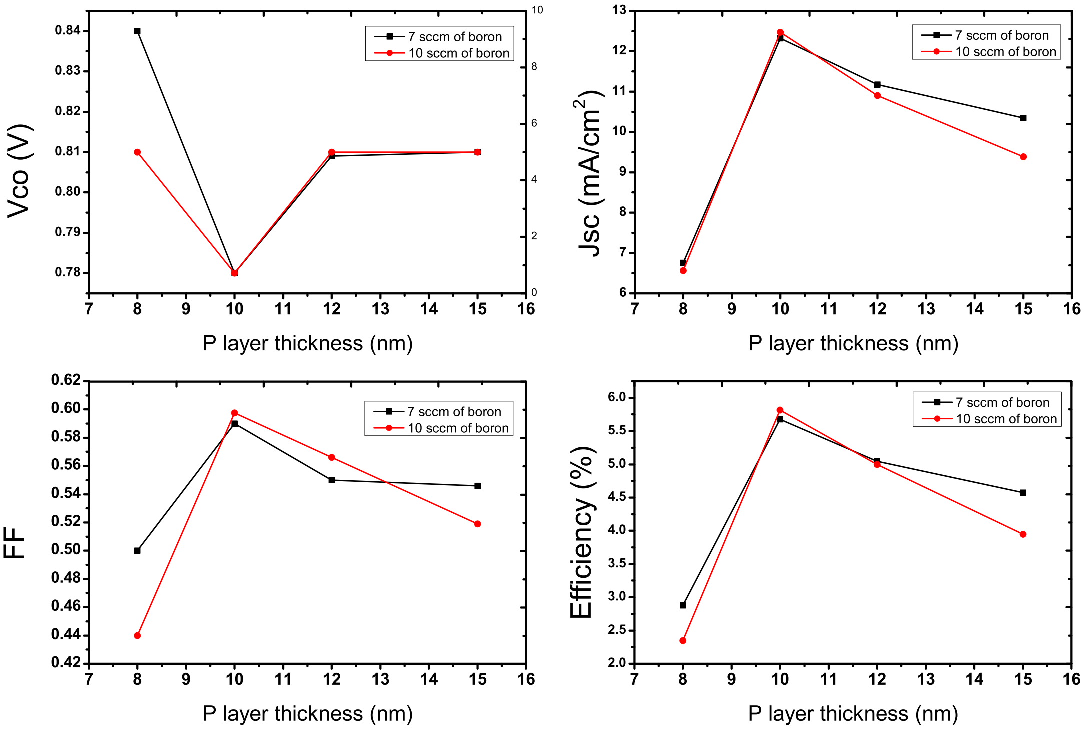

FIGURE 5.7: Born flow rate with P thickness.

The V_{OC} at lower dopant flow rates for thin *p*-type is high 0.84 V is in face the highest achieved during this work. At 10 nm of *p*-type, both 7 sccm and 10 sccm of boron dopant flow gave the same V_{OC}. For the other *p*-type thickness, both dopant flow rate gave the same value of V_{OC} 0.81V. This behaviour of V_{OC} suggests that the layer is either non uniform or not as thick as predicted by our thickness tooling . The short-circuit current for each dopant flow is identical which suggests that the intrinsic layer is uniform and current collection is effective. The J_{SC} plot in Figure 5.7 suggests that highest current collection has taken place at the thickness of 10 nm while the highest V_{OC} is generated at 8 nm. This suggests that the optimum thickness of *p*-type layer is somewhere between 8 nm and 10 nm. At this stage, only two dopant flows are checked. To confirm the dopant flow, an other set of devices deposited with fixed 10 nm *p*-type

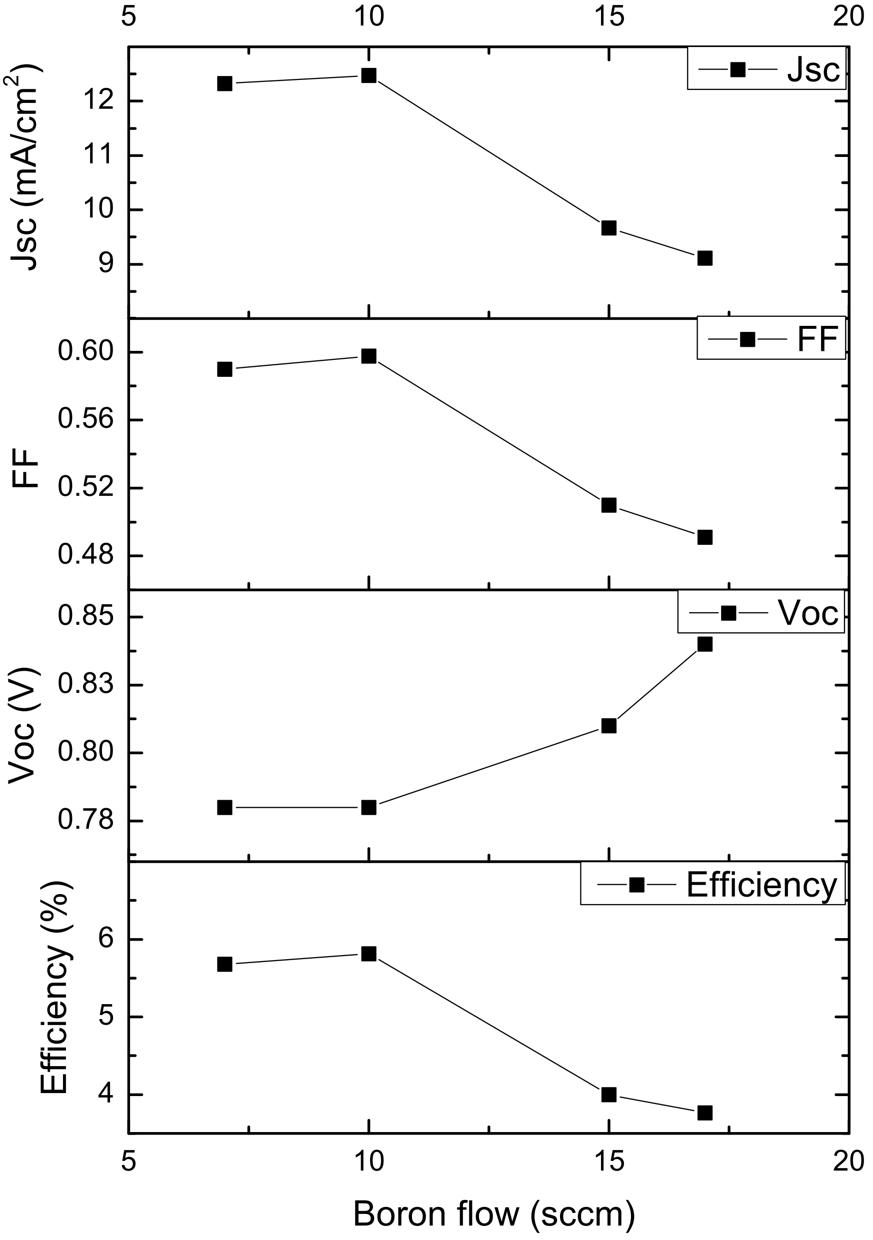

FIGURE 5.8: Boron flow rate.

with different dopant gas flows were produced while the other deposition parameters are kept constant as described in table 5.7.

The result of boron dopant variation at fixed *p*-layer thickness confirmed that both 7 sccm and 10 sccm dopant flows are roughly equal. The FF and V_{OC} values of the device are also similar, but V_{OC} values at higher dopant flows are also higher but at this flow the photocurrents collected are low. These low photocarrier collections were expected as it is in the over-doped regions where device performance is low. These results also confirm that for the specified thickness of the *p*-type layer, low boron dopant (between 7 sccm and 10 sccm), the device performance is unchanged.

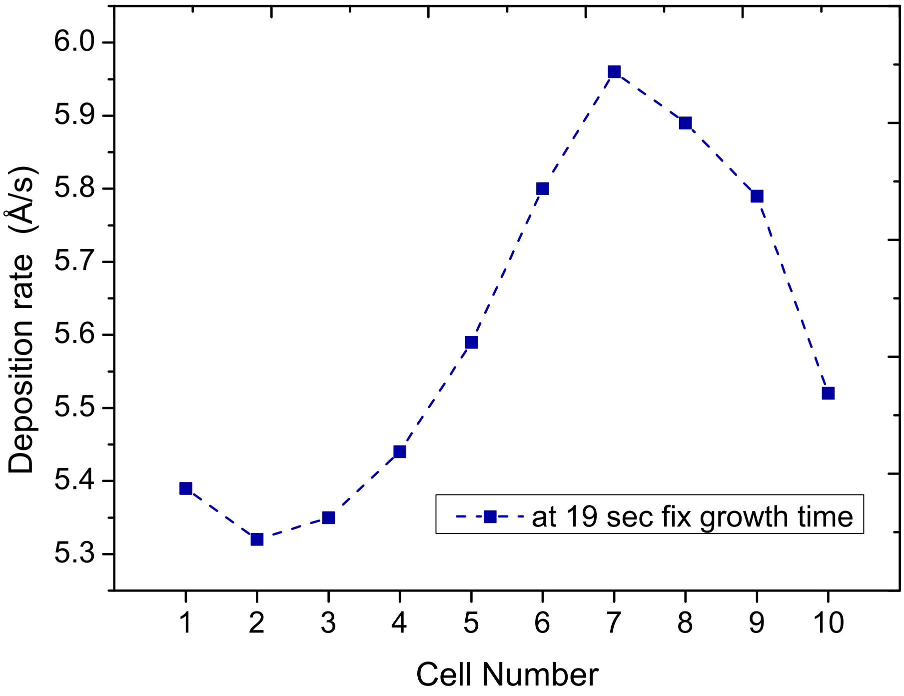

FIGURE 5.9: The *p*-layers deposition rate at constant growth time and other deposition parameters.

During *p*type layer optimisation, some observations are made which highlighted some ambiguity in the film thickness. It was found that for similar deposition parameters, deposited devices gave different results. The thickness of device grade individual layers deposited in the same conditions used for making a single junction a-Si:H device and monitored closely. The deposition rate of the*p*-type layers are shown in Figure 5.9. In total 10 devices (based on 3 layers) were deposited under exactly same deposition parameters. One simulated device contains three layers which are *p*-type, *i*-type and *n*-type. After completion of each layer, the substrate was immediately replaced for the next layer deposition. The deposition rates for *i*-type and *n*-type were found similar all the time but *p*-type rate was found to vary each time, which as described in Figure 5.9. The

10 nm of thin *p*-type layer can be deposited in 10 to 18 second depending on the growth parameters. During this time, first few seconds are devoted for plasma generation. After 4 to 6 seconds, the plasma is generated in the chamber, and growth process starts. In such a short time, a thin film of 10 nm or less is really a challenge to deposit. The deposition time could be prolonged by diluting the silane source plasma with argon, but results in section (5.2) and argon based intrinsic layer suggest that argon usage in dilution is not beneficial. The *p*-type layers are already being deposited at low pressure 350mT and the layers deposited at lower pressure gives non-uniform layer thickness. The only choice left is to increase the hydrogen dilution to 2R to 3R.

5.5.2 The *n*-type layer of the device

The thickness of the *n*-type layer has less influence on the performance of the device as compared to the other two layers since it is the final layer of the device. In a similar way to the *p*-region, this layer only serves to create the electric field and external contacts, and does not contribute to carrier generation but will be responsible for the parasitic absorption of photons that would ideally be reflected from the rear contact reflector to be absorbed within the intrinsic layer during subsequent passes through the device. In order to reduce recombination losses, the doping levels in this region are lower than in the *p*-type. Additionally, lower doping levels increase the silicon layer quality around the interface between the intrinsic and amorphous material. The layer may be wider in order to create an adequate electric field with very thin *p*-type layer.

The deposition parameters set for the *n*-type layer for device optimisation as a function of layer thickness at 10 sccm of phosphine flow, are described in table 5.8. The device characterisation parameters plotted as the n-type layer thickness was varied from 30 to 60 nm, in Figure 5.11.

TABLE 5.8: Deposition parameters for single junction *pin* a-Si:H devices deposited with different phosphine flows for *n*-type layer thickness. No argon was used during this deposition.

Layer type -	layer thickness (nm)	Pressure (mT)	Temp. (°C)	RF (W)	Silane Flow (sccm)	H_2 Flow (sccm)	Ar flow (sccm)
P	10	350	250	10	50	50	0
I	400	350	250	10	50	50	0
N	-	350	250	10	50	50	0

It is observed that the *n*-type layer does not have a strong effect on current collection in the 40 nm to 60 nm range. The device *FF* is decreased for the thickest layer though only shows a small change in the 40nm to 50nm range. The V_{OC} varies inconsistently, between 0.78V and 0.81V, which may suggest non-uniformity in the *p*-layer. With 20 nm variation in the intervals of 5 nm in the *n*-layer thickness, all devices were found

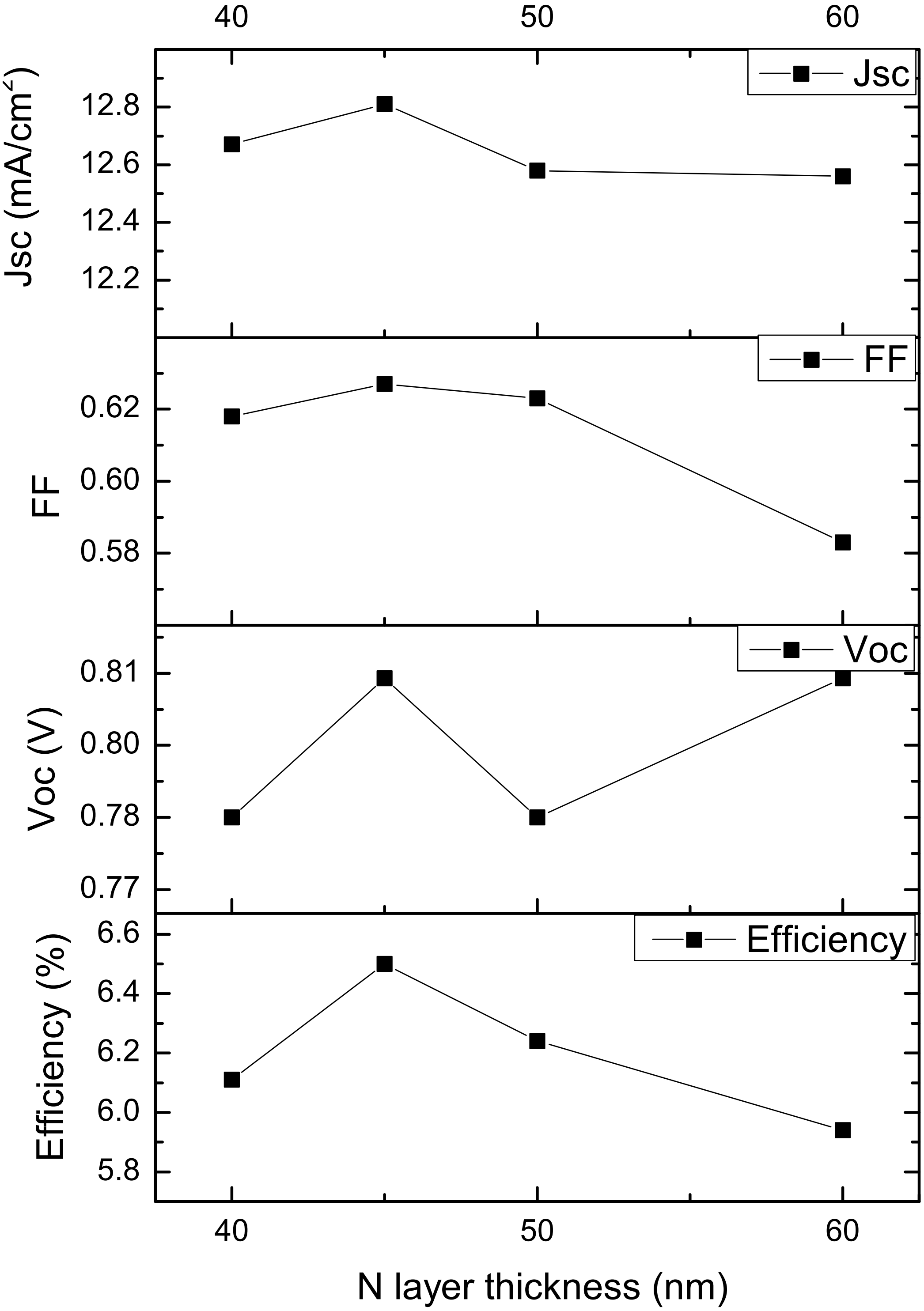

FIGURE 5.10: N layer thckness.

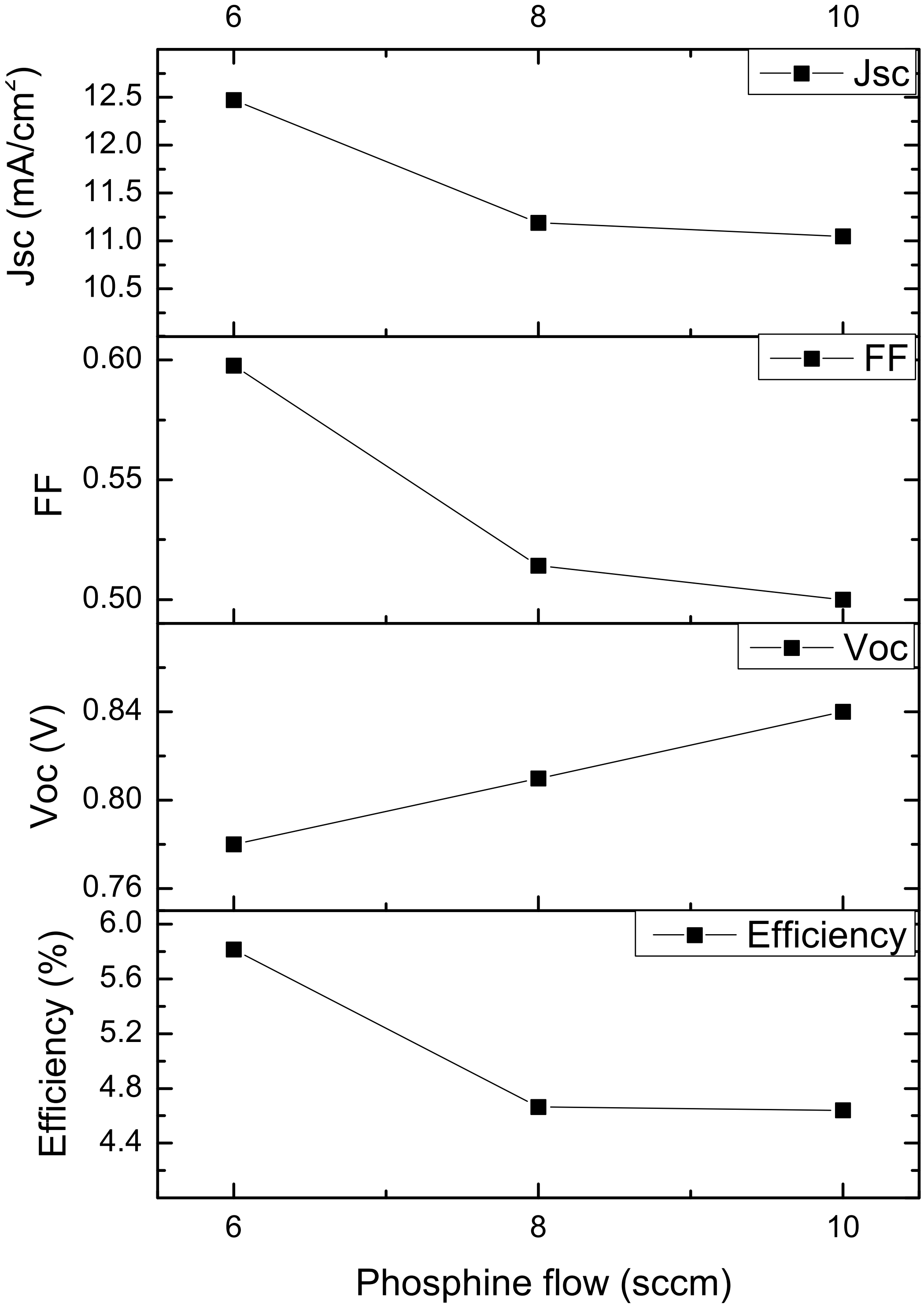

FIGURE 5.11: Phosphine flow rate

to have efficiencies over 6%. The highest efficiency devices are found at the n-layer thickness of 45 nm. This layer was therefore chosen as the optimum layer for these growth conditions.

The thickness optimisation of n-type layer was processed at phosphine flow rate of 10 sccm. To understand the effect of dopant flow rate, three devices with otherwise identical growth parameters were deposited with 3 different phosphine flow rates. The characterization parameters of these devices are shown in n Figure 5.11. Within this particular set, the device deposited with 6sccm phosphine flow were produced the best devices in this experimental set.

Following the individual layer optimisation within the single junction a-Si:H based *pin* device, optimised growth parameters were picked for best device deposition. It was decided to deposit a *pin* device with p-type window layer 10 nm thick at a temperature of 250 °C, by applying RF power of 10 W with gases flow rate of silane 50 sccm, H_2 50 sccm, and boron dopant 10 sccm. The optimised 370 nm intrinsic layer was deposited under similar parameters with no dopant flow. The 45 nm optimised n-layer was deposited in the same way just like window layer, with phosphine dopant flow rate of 6 sccm.

5.6 Towards optimized amorphous based single junction *pin* device

This device work at Southampton University was based on a newly commissioned PECVD system and inevitably started with many unavoidable problems. From the first cell structures produced were of zero efficiency and without any verifiable initial parameters. Reaching a respectable efficiency was never going to be an easy task. It took a great deal of experimental and practical effort and resources to get the first device with 0.1% efficiency after many non- functional devices. Some of early device progress in terms of efficiency is plotted with respect to number of devices is shown in Figure Figure 5.12, though even this plot does not contain many initial devices that were either non-functional or of very low efficiency. The work of single layer optimisation is different from functional device fabrication. As mentioned in Figure 5.12, cell progress had to be carried out in three distinct phases. The first phase is where efficiency of the devices are very low, with most devices less than 0.5% efficiency. In this region the gas deposition parameters, gas flow rates and pressure play the most important role. After getting the first optimisation in growth parameters, significant development was carried out so that devices could reach 2% efficiency. In the second phase of activity, most work was carried out on gas selection and doping optimisation. In the final optimisation stage, devices were obtained with more than 4% efficiency and work on doped layer optimisation, deposition chamber environment, and system stability was carried out therefor these devices can be made with reproducibility provided identical chamber conditions.

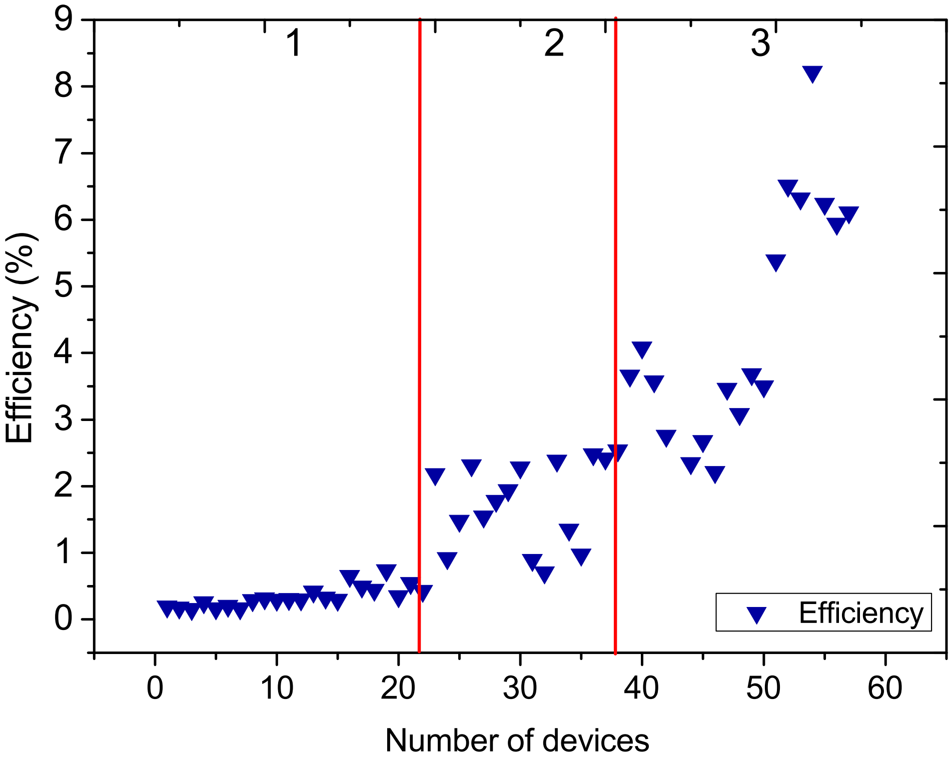

FIGURE 5.12: Device progress starting from very low efficiency of 0.1% and reaching at some higher values. This plot consist of 60 devices.

The physical layout of a typical single junction a-Si:H solar cell is shown in Figure 5.13. Most devices deposited in this work are deposited on commercially available Pilkington TEC8 substrate. The thickness of glass is 3.3 mm and roughly 700nm to 900 nm of textured TCO is deposited on the glass which also serves as the front contact. The substrate dimensions are 50x50 mm, on which an array of 3x3 devices each with area of 1.05 cm^2 are formed. The back contact are deposited by the e-beam evaporation of 500 nm of Aluminium at vacuum of 1×10^{-5} Torr.

The initial JV curve of the optimized device is shown in Figure 5.14. The characterization parameters of this device are shown in table

TABLE 5.9: IV characterisation parameters of an optimized single junction a-Si:H solar cell.The deposition parameters are: temperature 250^{o}C, chamber pressure 350 mTorr, 50 sccm of silane and hydrogen

V_{OC}=	0.8139 V	Imax	12.199 mA
I_{SC}=	13.813 mA	Vmax	0.645 C
J_{SC}=	13.813 mA/cm^2	Pmax	7.869 mW
FF =	70.08 %	Efficiency	8.22 %

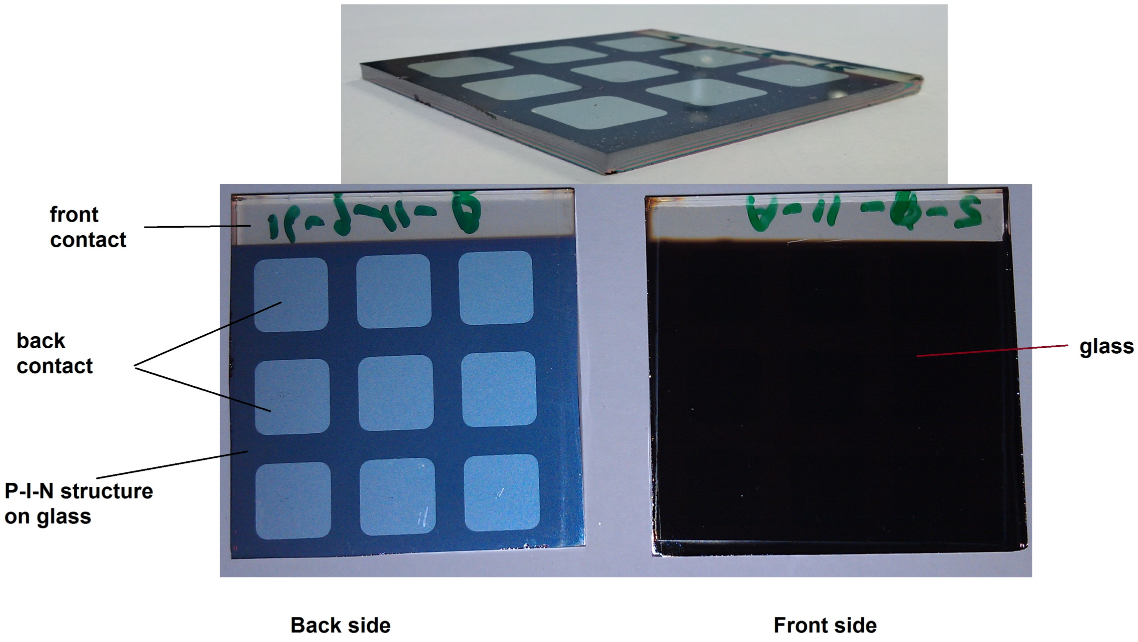

FIGURE 5.13: The external physical layout the a typical single junction a-Si:H solar cell deposited for this work.

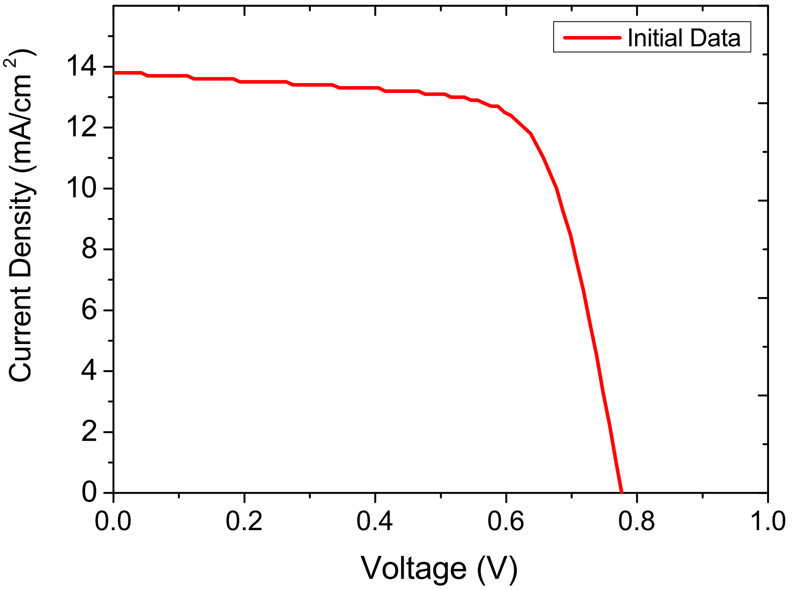

FIGURE 5.14: The *IV* characteristics curve of an optimized single junction a-Si:H solar cell in *pin* measured under AM1.5 spectrum.

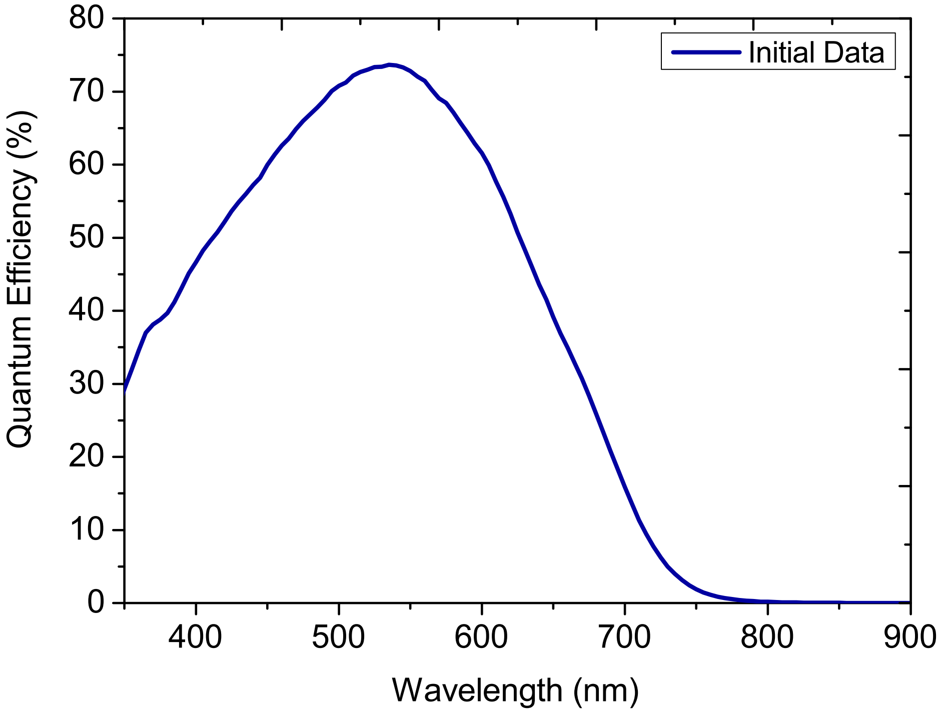

FIGURE 5.15: The initial external quantum efficiency of this optimized single junction a-Si:H solar cell.

The initial external quantum efficiency of this optimized single junction a-Si:H solar cell in *pin* configuration is shown in Figure 5.15. Quantum efficiency of this device reaches a level of reasonable 74 % in the important part of the cell absorption with out any light capturing techniques. In the ultraviolet and the initial part of visible spectrum, the device absorbs good 30% which is remarkable. In the green to yellow region (550 nm to 630 nm) it has absorption from 50 % to 70 %. The red part of spectrum shown poor absorption as no back-side texturing modification has been done. This is a simple device which has shown a good respectable performance in very important part of the visible spectrum.

5.7 Light soaking effects

It is well known fact that the efficiency of a-Si:H based devices decreases during initial stage of performance under illumination and this degradation has been link to light induced effect[43]. In many cases, this reduction in efficiency takes 15 to 30% of the initial as-deposited efficiency. So far every efficiency mentioned in this work is initial as-deposited efficiency. Every a-Si:H based solar cell requires a degradation test to get a stabilised efficiency. In many cases, a degradation test requires a 300 to 600 hours of light soaking under constant 50 °C under open circuit conditions.

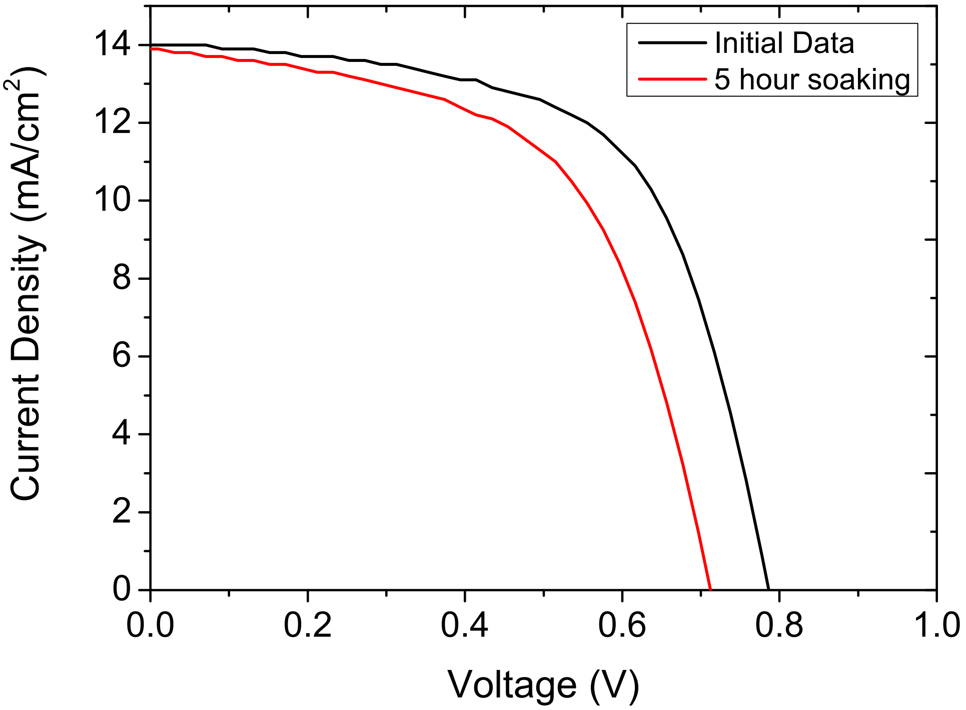

FIGURE 5.16: The IV characteristic curve of single junction a-Si:H cell measured initially as-deposited and after 5 hour light soaking.

Due to unavailability of proper experimental set-up, it is difficult to run a degradation test on every optimized device deposited for this report. However, one device has been tested for 5 hours (300 minutes). The *IV* characteristics of the cell tested at 20 minute intervals to record degradation effect. The initial as-deposited and stabilized efficiency of one single junction a-Si:H solar cell is show in Figure 5.16.

The initial as-deposited efficiency of this device measured immediately after the growth process and found 6.75%. After 5 hours of light soaking, its initial efficiency reduced to 5.64% with a change of 16%. The initial maximum power of the device was 6.759 mW, which went down to 4.56 mW after 5 hours of light soaking. The 20 minute track record of device efficiency and maximum power is shown in Figure 5.17. The major reduction in the efficiency and power occur during first hour when a 15% change recorded in the efficiency and over 29% change recorded in maximum power. After one hour of light soaking, the degradation rate remarkably slows down.

The light degradation track record of V_{OC}, *FF* and J_{SC} is shown in Figure 5.18. The degradation of V_{OC} is unusual as compared to other characterization parameters. After 20 minutes, its value goes down from 0.8 V to 0.7 and then jumps to a higher value of 0.96 V. After further light soaking, the V_{OC} stabilized to 0.71 V. This bump may have been related to temperature as the device kept under illumination of AM1.5 without any cooling system. Total 10% of reduction has been recorded for V_{OC}. The *FF* of the

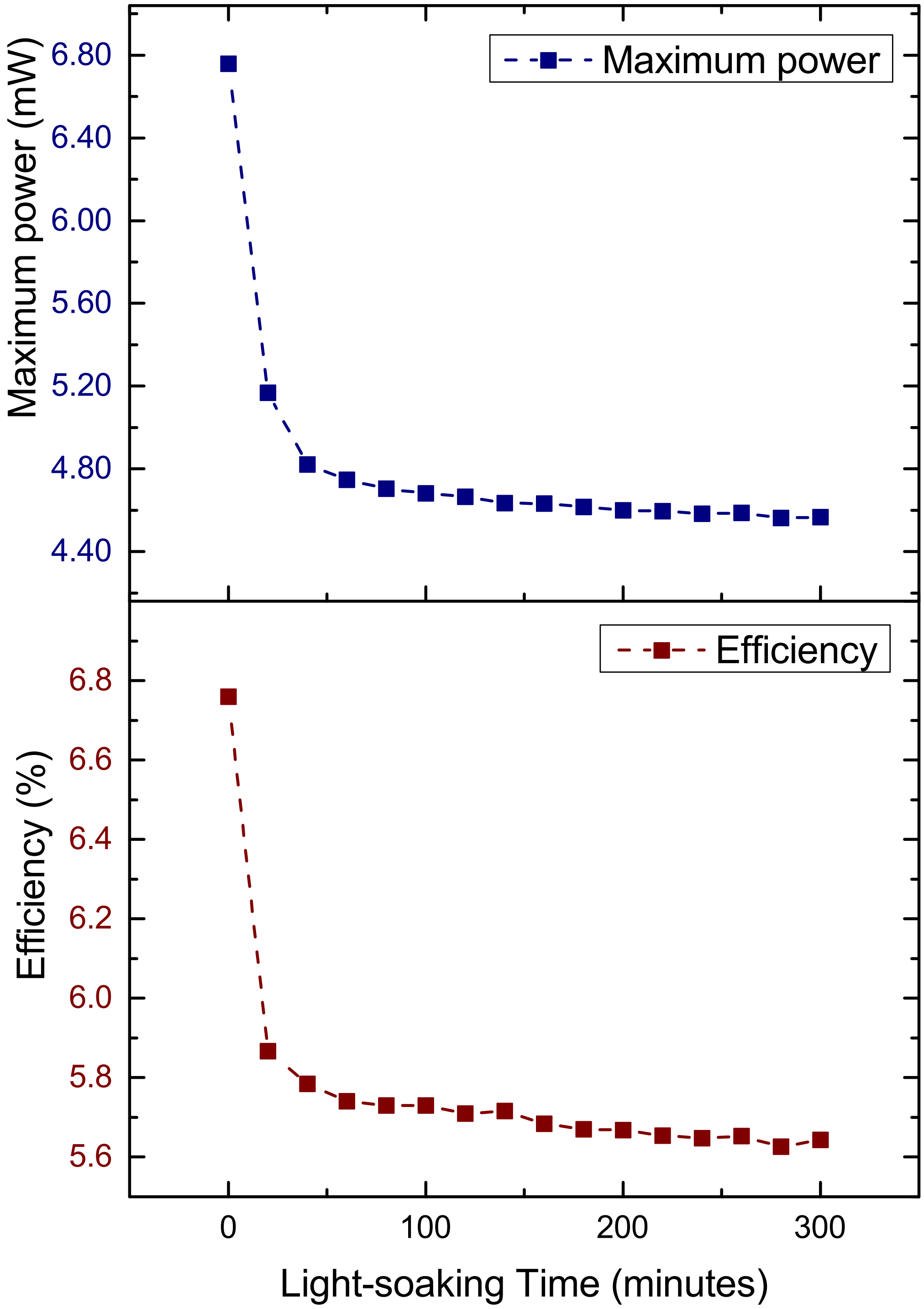

FIGURE 5.17: The maximum power of the and efficiency of single junction a-Si:H device measured every 20 min during light soaking test. A big reduction in both values are seen during first 20 minute of light soak.

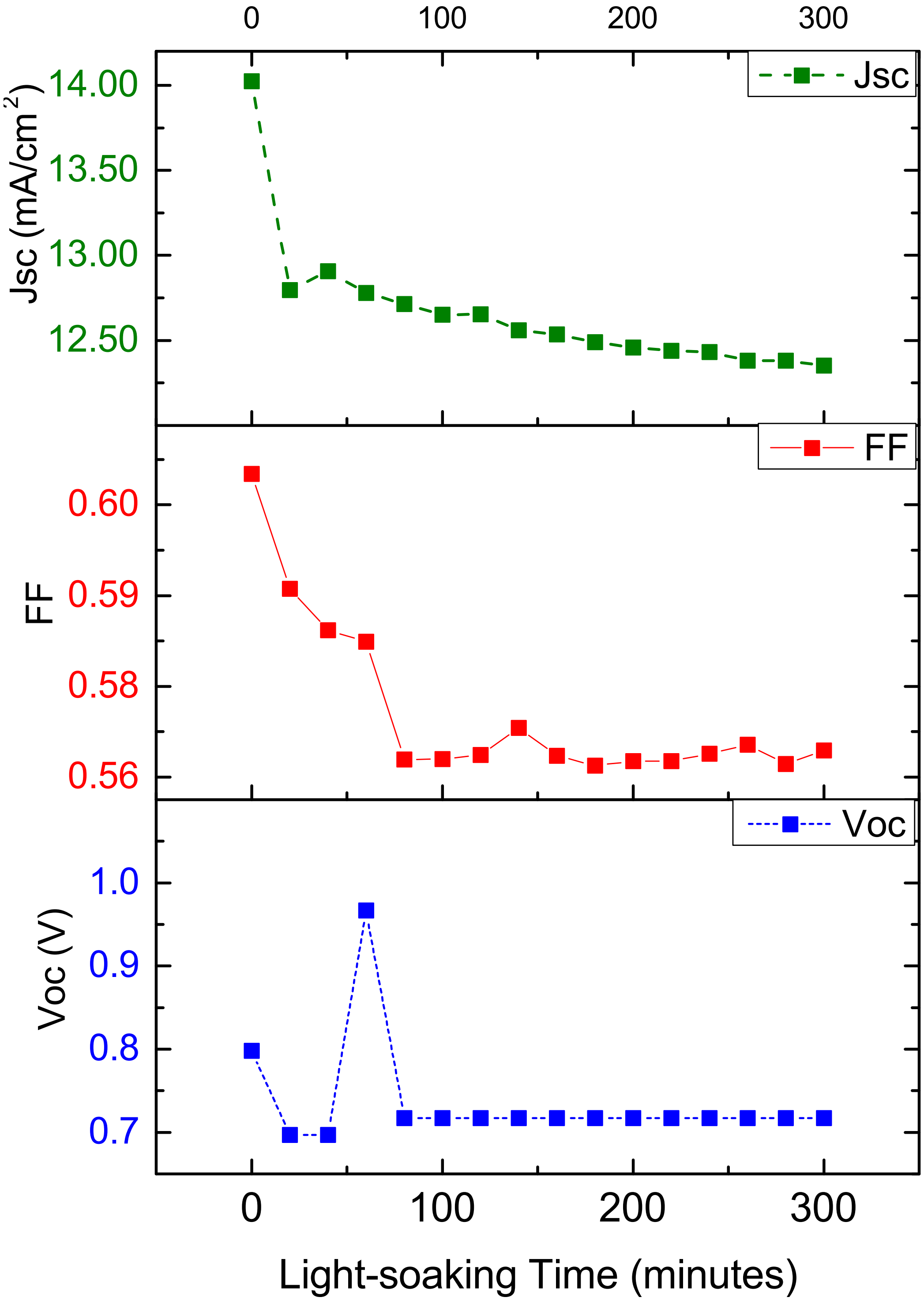

FIGURE 5.18: The V_{OC}, FF and J_{SC} values of single junction a-Si:H device measured every 20 min during light soaking test.

device decreases from 0.6 to 0.56 with just 6% degradation. Total 11.9% degradation recorded in photocurrent of the device.

In the chapter each deposition parameter is tried to get an optimised single junction a-Si:H solar cell. To summarise all; the chamber pressure variation for the PECVD system shows that higher efficient device can only me fabricated under lower pressure which means that deposition rate for a-Si:H would be lower. It is found the presence of argon gas is not as beneficial. The devices grown in the absence of argon have higher efficiencies. The absence of argon mean, hydrogen gas must be present in the chamber, otherwise plasma can be generated with silane only. The present of hydrogen is also beneficial. The RF power create dust in the chamber and chances are that device would be shunted. The optimum RF power is found 10 W but slightly lower efficient devices were reported at 15 W of RF power.

It is noted that optimum intrinsic layer thickness in a-Si:H lie in range 350-380 nm. The optimum p-type layer thickness is range of 7-10 nm and n-type layer thickness is in 35-45 nm range. The thickness of p-type layer been found very crucial in determination of the final device efficiency. As p-type layer is kept very thin, small process or system non-uniformity could result in more thin ot slighter thicker layer which drastically affect the device efficiency. By using optimum deposition parameters, 8.22 % efficient device has been reported in single junction *pin* configuration before light soaking. This using a base-line single junction a-Si:H has been achieved. In the next chapter, this optimised single junction device is used to determine the effect of textured TCO film.

Chapter 6

Single junction devices on different Commercial TCO Layers

Unlike conventional c-Si devices, a-Si:H based thin film solar cells require totally different contact design. The most common approach is to use transparent conducting oxide (TCO) layers at the front or sometimes at the back and/or middle of the device. In this chapter, a variety of different commercially available TCOs and devices are analysed in detail using a range of techniques including a new technique developed at Southampton that allows measurement of the *wavelength and angle resolved scattering* (WARS) of layers and devices.

WARS along with the total and diffuse transmittance and reflection measurements taken using an integrating sphere in the double-beam mode are used to fully analyse the optical behaviour of TCOs and cells and evaluate the different TCOs light-trapping performance. The surface topology of the commercially-available TCO materials are first determined using Atomic Force Microscopy (AFM) measurements, which provide vital information on the roughness of the material. The four different types of commercially available TCO materials which are used in this investigation are summarised in the table (6.1) below. The glass thickness of Asahi-U is 1.1 mm whilst TEC-8, TEC-15 and NSG have similar glass thickness of 3.3 mm.

Table 6.1: The four different types of commercially available TCO materials which are measured in this investigation are summarised in the table

TCO type	Sheet resistance ($\Omega/\Box$)	TCO thickness (nm)
TEC8	8	600
TEC15	15	300
NSG	7	600
Asahi-U	9	900

The TCO materials which are measured in this investigation are TEC8, TEC15, NSG, and Asahi-U. Out of four, only one TCO TEC15 is flat and while all other TCOs are textured. Now we will discuss optical characterisation of all TCO materials used in this report.

6.1 AFM Analysis of TCO Materials

The surface structure and topology of each of the textured TCOs determined using Atomic Force Microscopy (AFM) measurements, which provide vital information on the roughness of the material. These measurements are carried out using a Veeco Caliber AFM with specialised high aspect ratio tapping probes to ensure accurate characterisation of sharp features. The statistical roughness parameters of all TCOs used for this investigation are summarised in the table (6.2).

Table 6.2: The statistical roughness parameters for four different types of commercially available TCO materials obtained by AFM measurements.

TCO type	Ra (nm)	RMS (nm)	Max peak (nm)
TEC-8	32.8	40.9	299.7
TEC-15	8.68	10.94	90.54
NSG	31.7	39.7	344.3
Asahi-U	30.2	38.1	291.6

The topographical images of surface structure of the commercially available textured TEC-8 material determined by AFM with three dimensional and top views is shown in Figure 6.1.

The average roughness of textured TEC-8 material was determined as 32 nm and the RMS value of roughness was determined as 40 nm. The vertical height of the surface in terms of peak-to-valley roughness for TEC-8 was found to be 300 nm. This roughness data describes TEC-8 as a good textured material that can provide effective light diffusion and scattering. The four point probe measurements show that TEC-8 has very low sheet resistance of 7 to 8 Ω/□.

The average roughness of TEC-15 substrates was determined as 8 nm and the RMS value of roughness was determined as 11 nm. The vertical height of the surface in terms of peak-to-valley roughness for TEC-15 was found to be 90 nm. This low roughness of TEC-15 will have a profound effect on the ability of the material to effectively scatter light. The same trends are repeated for RMS values and peak data. The four point probe measurements show that TEC-15 material has very slightly higher sheet resistance of 15 Ω/□. The topographical images of surface structure of the commercially available non-textured TEC-15 material determined by AFM with three dimensional and top views are shown in Figure 6.2.

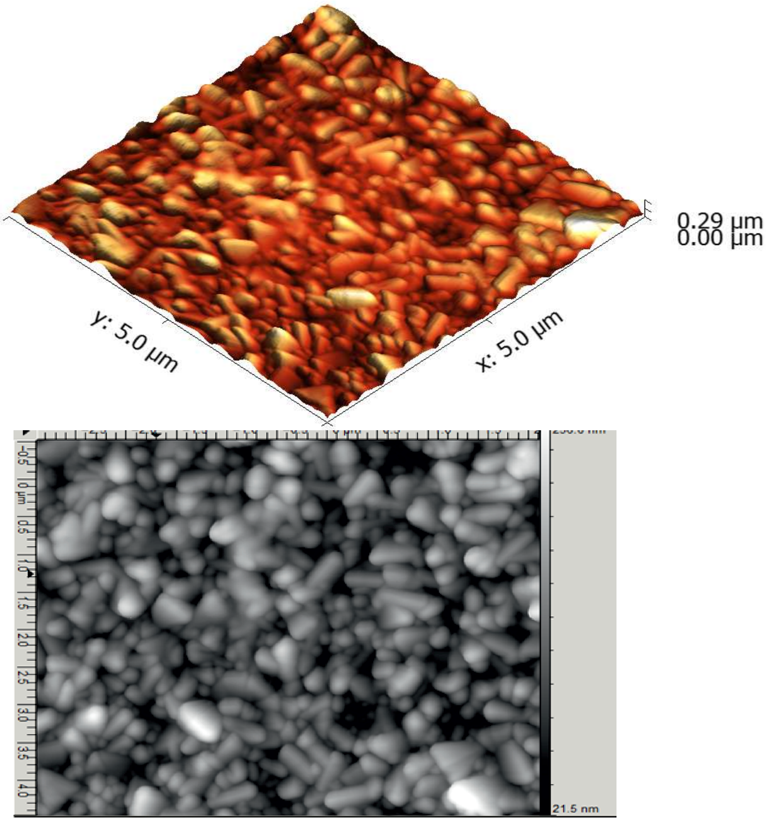

Figure 6.1: The topographical images of surface structure of the commercially available textured TEC-8 material determined by AFM with three dimensional and top views.

The NSG TCO material is very similar to the TEC-8 in almost every way when characterized by AFM. The average roughness of textured NSG was determined as 31 nm and the RMS value of roughness was determined as 40 nm. The vertical height of the surface in terms of peak-to-valley roughness for NSG was found at 344 nm which is 45 nm higher than that of found for TEC-8, therefore we may expect a better performance in terms of effective light scattering. Just like TEC-8, the four point probe measurements show that the NSG substrate has a very low sheet resistance of 7Ω/□. In terms of surface topology and textured structure shown in Figure 6.1 and Figure 6.3, it was confirmed that the NSG TCO substrate is simply a alternate version of TEC-8 TCO with only minor improvements.

Out of these four commercially available TCOs, Asahi-U has more textured profile as compared to others. Asahi-U has low sheet resistance of 9 Ω/□ determined by four-point probe measurement. The average roughness of highly textured Asahi-U material was determined as 30 nm and the RMS value of roughness was determined as 38 nm. The peak-to-valley roughness for Asahi-U was found at 291 nm which is slightly less than the equivalent value found for TEC-8. The topographical image of surface structure of the commercially available textured Asahi-U determined by AFM with three dimensional and grey scale image is shown in Figure 6.4.

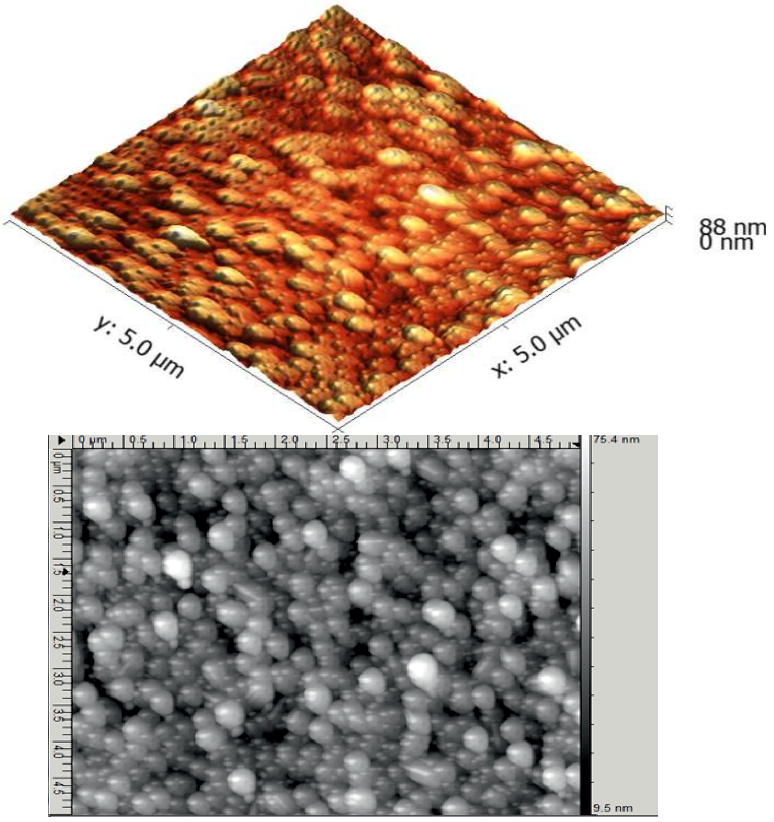

FIGURE 6.2: The topographical images of surface structure of the commercially available non-textured TEC-15 material determined by AFM with three dimensional and top views.

The average roughness of TEC-8, NSG, and Asahi-U as measured using the AFM have very similar values while TEC-15 has material has very low RMS. It is therefore expected that three identical TCOs to have similar light scattering performance as compared with flat TEC-15 material.

6.2 Transmittance and reflectance analysis of TCO materials

The TCO materials used in photovoltaic application possess a much larger bandgap than the absorber material, which is an essential requirement for optical transparency. The transmittance curves of the four commercial TCO material used in this investigation are shown in Figure 6.5. As mentioned previously, the average roughness of Asahi-U, NSG, and TEC-8 as measured using the AFM have very similar values and are therefore have similar light transparency. In fact at low wavelengths, all TCO films behave similarly and their transmittance values range from 60% to 85%. Between 550 nm and 650 nm, all three TCOs have identical transparency of 85% or more but for long wavelengths,

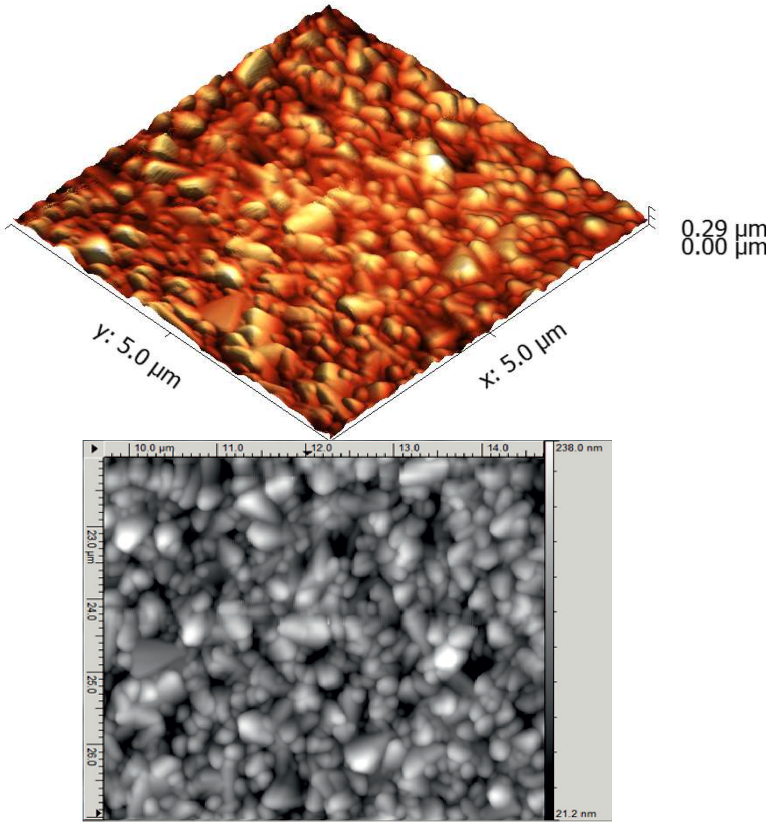

FIGURE 6.3: The topographical images of surface structure of the commercially available textured NSG material determined by AFM with three dimensional and top views.

NSG and Asahi-U show similar behaviour over 85%, while TEC-8 lies between TEC-15 and the other two films at 80% to 75%.

The diffuse transmittance of the TCO films is shown in Figure 6.6. At lower wavelengths TEC-15 exhibits a slightly higher transmission in comparison the other three TCOs, however, as expected, TEC 15 exhibits very poor overall light scattering as shown in the diffuse transmittance characteristics which is found less than 2% over all wavelength range from 450 nm to 900 nm. Asahi-U exhibits the highest diffuse transmittance, whilst the diffuse transmittance of TEC-8 and NSG appears to be almost identical as might be expected from the AFM analysis.

The reflectance curve of all commercial TCO materials deposited on glass are shown in Figure 6.7. It appears that throughout whole wavelength range, TEC-8, TEC-15 and NSG reflect similar levels of incoming light which is 8% to 10%. One the other hand Asahi-U reflects more light in the 400 nm to 700 nm wavelength range as compared to other three TCO materials. Despite more loss in terms of reflection, there is higher light scattering and transmittance in Asahi-U as compared the other three TCO material which suggests that among all TCO films, Asahi-U appears to better optical layer in terms of surface textures and optical transparency.

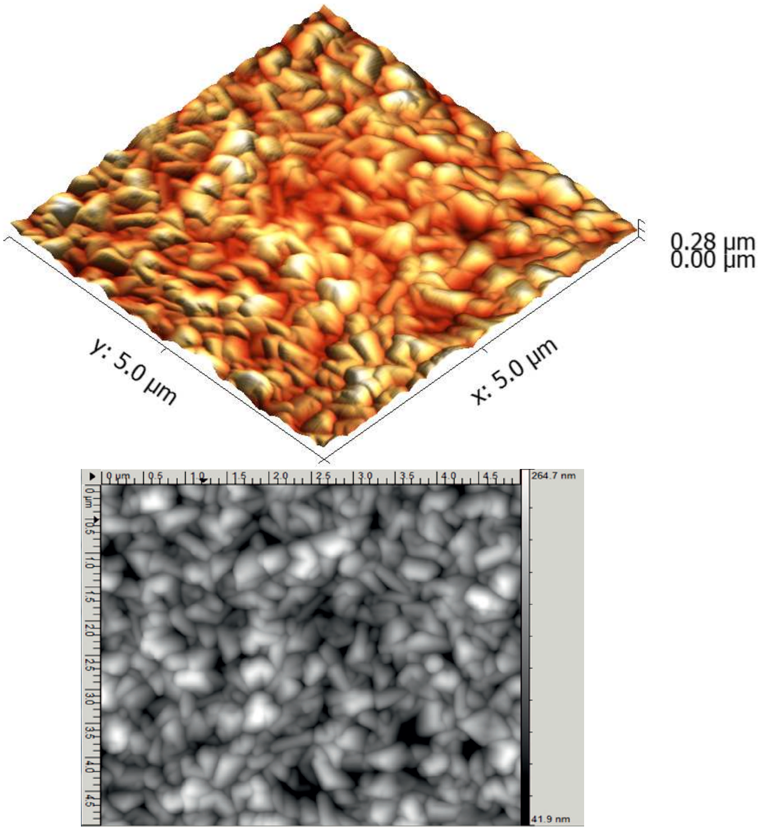

FIGURE 6.4: The topographical images of surface structure of the commercially available textured Asahi-U material determined by AFM with three dimensional and top views.

6.3 Wavelength and angle resolved scattering analysis of TCO materials

The effects of haze on the light entering the amorphous silicon solar cell are well understood[124]. As the light enters the front surface of the solar cell, it does so at a particular angle of incidence. A certain amount of this light is lost to reflection from the front surface, and the remainder transmits through the glass surface, into the TCO material. Texture in the TCO can then cause the light to scatter as it propagates into the absorbing a-Si:H layer, effectively enhancing the path length of light within the amorphous silicon absorber. This has the advantage of increasing the probability that a charge carrier pair will be created near to the doped collection regions, and therefore increasing the overall efficiency of the device.

The standard haze measurements determine the angular distribution of scattered light, and angle resolved scattering measurements allow more in depth optical analysis for specific wavelngths. This measurement technique has been enhanced at Southampton University to include wavelength dependent detail, resulting in the ability to gather wavelength and angle resolved scattering (WARS) measurements. These measurements are carried out using a Fianium white light laser source together with a custom built

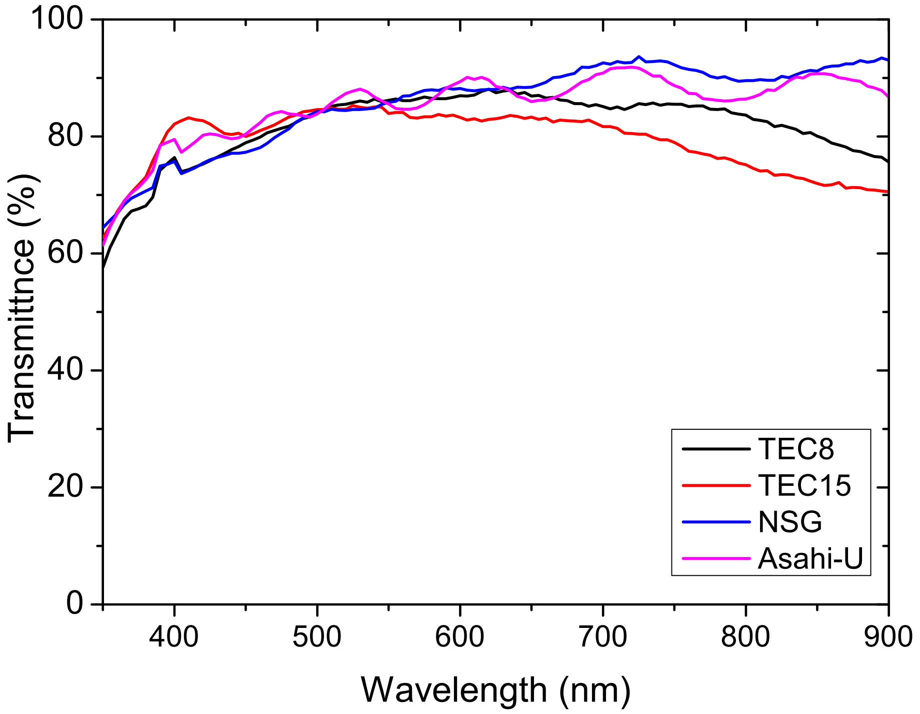

Figure 6.5: The total transmittance of four TCO film deposited on glass, using an integrating sphere

motorized goniometer system and B&WTEK spectrometer with a wavelength range of 450 nm to 900 nm[125]. . The measurement process consists of illuminating the sample at normal incidence and sweeping the detector from 85^o to 0^o, taking full spectral measurements at 1^o intervals.

The WARS results of TEC-8 and NSG TCO materials are shown in Figure 6.8 and Figure 6.9. It is observed that, in terms of optical scattering, both TCO materials are very much identical to each other. This result further confirms the conclusion made by AFM and optical transmittance. In the wavelength range of 450 nm to 600 nm, strong scattering exhibits in both TEC-8 and NSG. The most of light scattering occurs between 15^o to 50^o, while its decreases at lower and larger angles.

In the mid wavelength range from 600 nm to 750 nm, the scattering intensity decreases for all angles between 10^o to 70^o. This uniformity trend with less scattering continue at higher wavelengths from 750 nm to 900 nm. The identical diffused transmittance curve of TEC-8 and NSG match with their WARS measurement and concur with the similarity of the roughness parameters determined AFM measurement.

By analysing roughness parameters and optical transparency we have determined that TEC-15 exhibits low textured profile and would scatter incoming light very little. This low scattering behaviour is verified by WARS measurements and the data for TEC-15

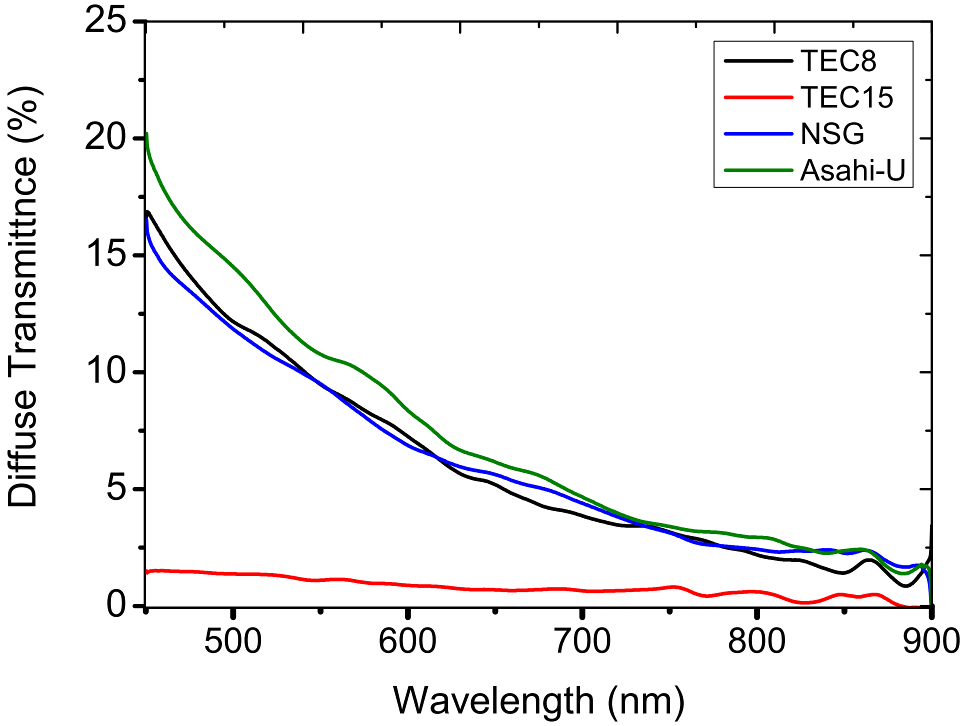

FIGURE 6.6: The diffuse transmittance of four TCO film deposited on glass, measured by an integrating sphere.

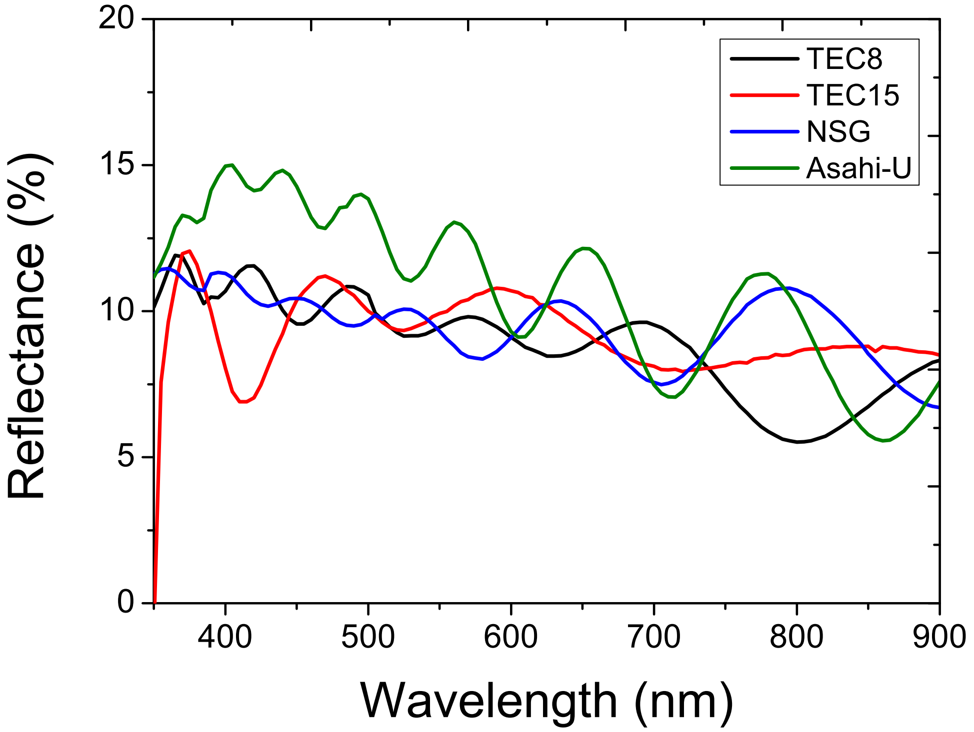

FIGURE 6.7: The reflectance spectra of four TCO substrate.

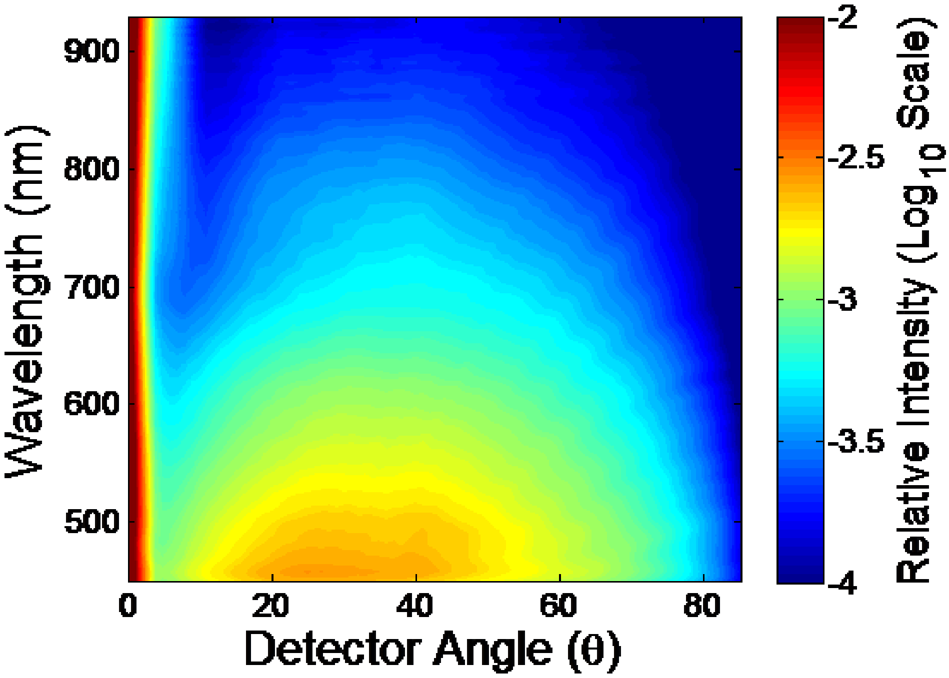

FIGURE 6.8: The WARS measurement of TEC-8, by illuminating it at normal incidence and sweeping the detector from 85^o to 0^o with wavelength range of 450 nm to 900 nm. The blue colour on left scale shows lower scattering, while red colour shows higher scattering.

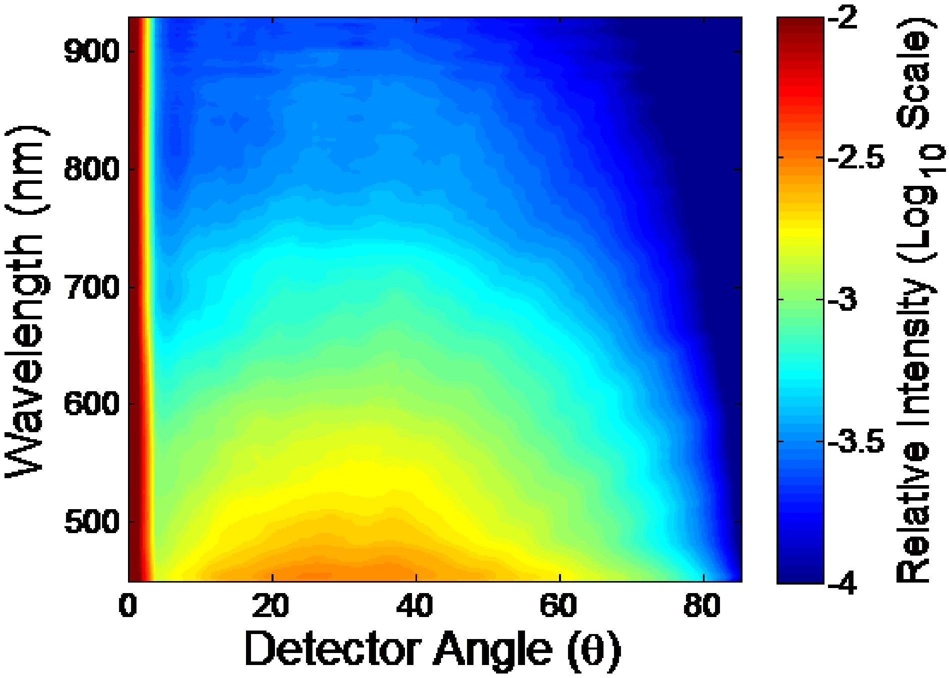

FIGURE 6.9: The WARS measurement of NSG, by illuminating it at normal incidence and sweeping the detector from 85^o to 0^o with wavelength range of 450 nm to 900 nm. The blue colour on left scale shows lower scattering, while red colour show higher scattering.

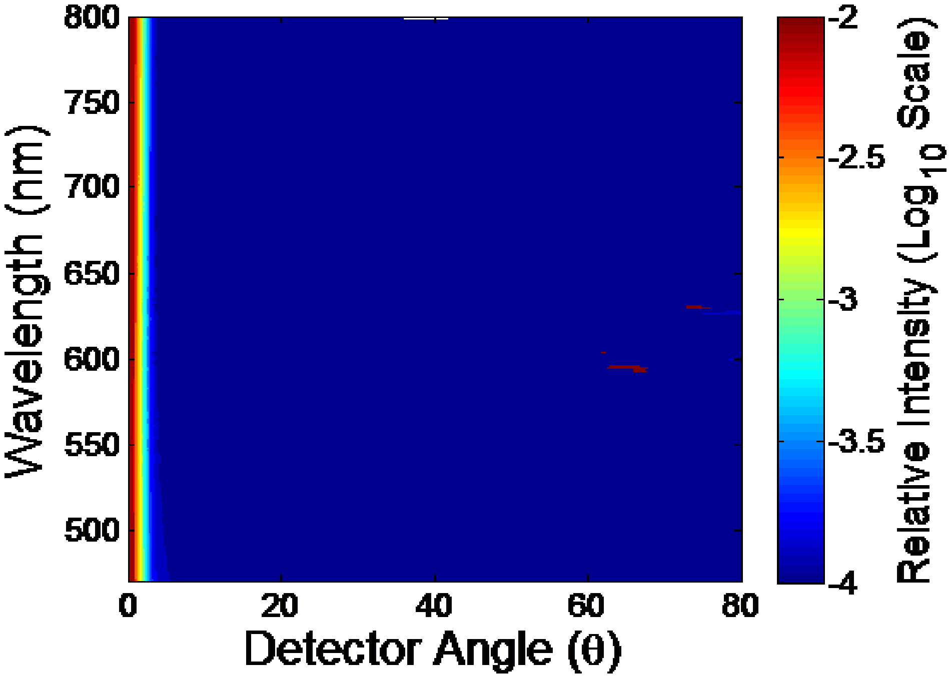

FIGURE 6.10: The WARS measurement of TEC-15, by illuminating it at normal incidence and sweeping the detector from 85^o to 0^o with wavelength range of 450 nm to 900 nm. The blue colour on left scale show lower scattering, while red colour show higher scattering.

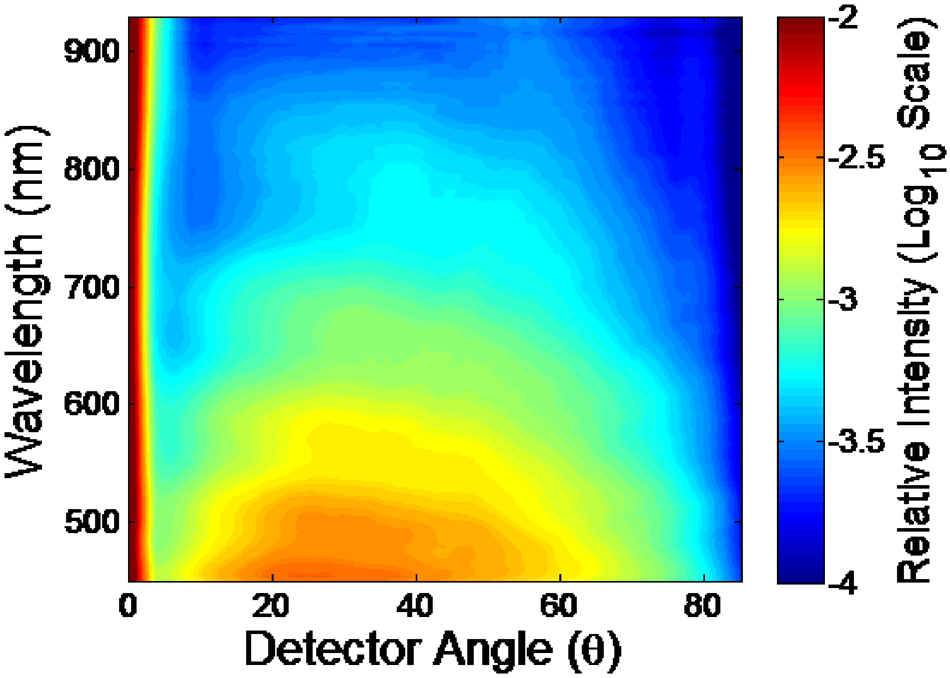

FIGURE 6.11: The WARS measurement of Asahi-U, by illuminating it at normal incidence and sweeping the detector from 85^o to 0^o with wavelength range of 450 nm to 900 nm. The blue colour on left scale show lower scattering, while red colour show higher scattering.

is shown in Figure 6.10. TEC-15 shows almost zero scatter when presented on the same scale as the other TCOs due to its much lower surface roughness. In our experiments TEC15 can be considered as a close-to planar equivalent of TEC8, thought with some antireflection properties that would not be expected of a truly planar device, it is felt that This TCO would be most suitable for experimentation with plasmonic back-reflector cell designs. The diused transmittance cure of TEC-15 matches with the TEC-15 WARS data in terms of low or zero light scattering.

Further analysis through the use of WARS measurements reveals that Asahi-U not only provides superior overall scattering intensity in comparison to the two similar TCOs, TEC-8 and NSG but also predominately scatters to slightly larger angles, particularly at wavelengths between 750nm and 780nm thus further increasing the path length of these important near bandgap wavelengths within the absorber layer. The WARS data of this excellent TCO materiel is shown in Figure 6.11. At lower wavelengths of range 450 nm to 550 nm, Asahi-U exhibits higher scattering intensity as compared identical TEC-8 and NSG materials. Moreover, this higher intensity is uniform and spread all over 10^o to 60^o under 525 nm. The diuse transmittance curve of Asahi-U shows an excellent match with the Asahi-U WARS measurement.

6.4 Single junction *pin* devices on multiple TCO substrates

After the analysis of four different commercially available TCO materials, it was decided to deposit a variety of different pin structures to investigate the effects of the different textured TCOs on the performance of a-Si:H based devices. For this purpose, four different intrinsic layers were selected with same doped layers. Each of the four devices different thicknesses were produced on each TCO material providing a set of 16 devices. The detail of individual thickness arrangements deposited on four different TCO s are shown in table (6.3).

Table 6.3: The Detail of individual thickness arrangements deposited on four different commercial TCO materials for a-Si:H based single junction *pin* devices.

TCO type	p-type layer (nm)	intrinsic layer (nm)	n-type layer (nm)
TEC-8	10	300, 350, 400, 450	45
TEC-15	10	300, 350, 400, 450	45
NSG	10	300, 350, 400, 450	45
Asahi-U	10	300, 350, 400, 450	45

All four devices for each thickness were processed simultaneously for each TCO, with each device in close proximity the differences in device properties were expected to be negligible so fair comparisons could be made

6.4.1 *at 300 nm of intrinsic layer*

The characterisation parameters of single junction *pin* devices deposited at intrinsic thickness of 300 nm on four TCO substrates are summarised in table (6.4 whereas, IV characteristic curves are shown in Figure 6.12.

Table 6.4: The characterisation parameters of a-Si:H based single junction *pin* devices deposited with 300 nm of intrinsic layer on four different commercial TCO substrates

TCOs at 300 nm	Efficiency (%)	V_{OC} (V)	FF	J_{SC} mA/cm^2
TEC-8	3.25	0.83	0.47	8.13
TEC-15	0.35	0.23	0.27	5.50
NSG	3.30	0.81	0.50	8.05
Asahi-U	4.15	0.84	0.50	9.88

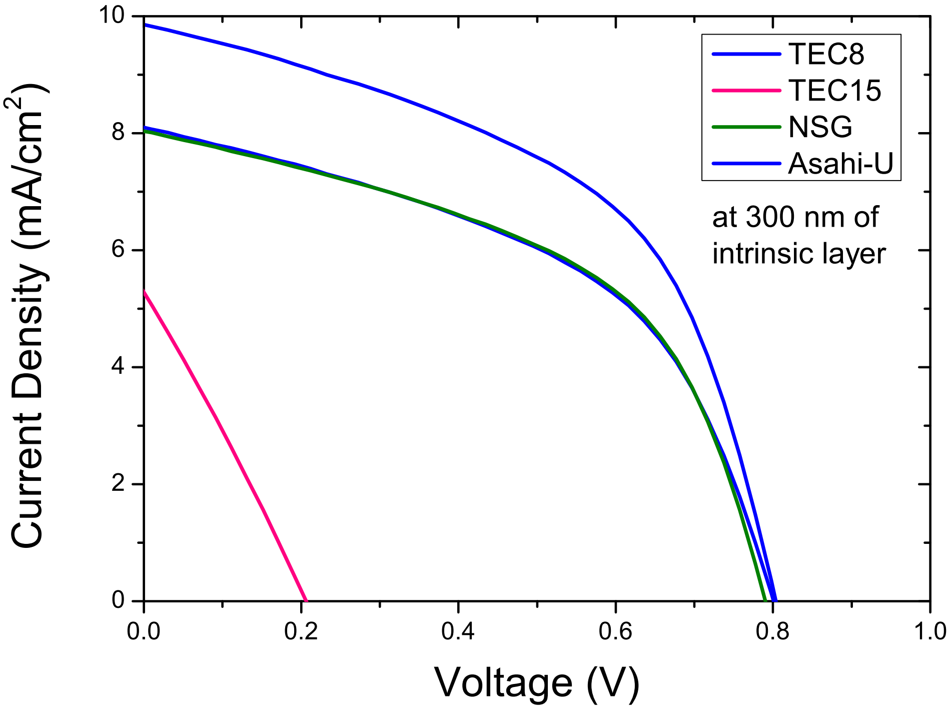

Figure 6.12: The *IV* characteristic curve of a-Si:H based single junction *pin* devices, deposited with 300 nm of intrinsic layer on four different commercial TCO substrates.

The identical performance of TEC-8 and NSG was anticipated before deposition. The performance of the Asahi-U type based device with a thin intrinsic layer is outstanding when compared to the two similar TCOs (TEC-8 and NSG), while TEC-15 shows very weak performance. The effciency of the Asahi-U type based device was found to be the highest in performance with a maximum energy conversion eciency of 4.15%, while the TEC-15 based device had the lowest effciency of 0.35%. As compared to other devices, the performance of TEC-15 is very low and the *IV* characteristic curve is unlike any other solar cell in this series of experiments. This suggests that, there is some failure in this device formation, perhaps a substrate or else localised contamination during deposition or during back contact deposition. The V_{OC} values of the other three devices are identical so there is no change in the electrical properties of these devices and the *FF* of both NSG and Asahi-U based devices are identical.

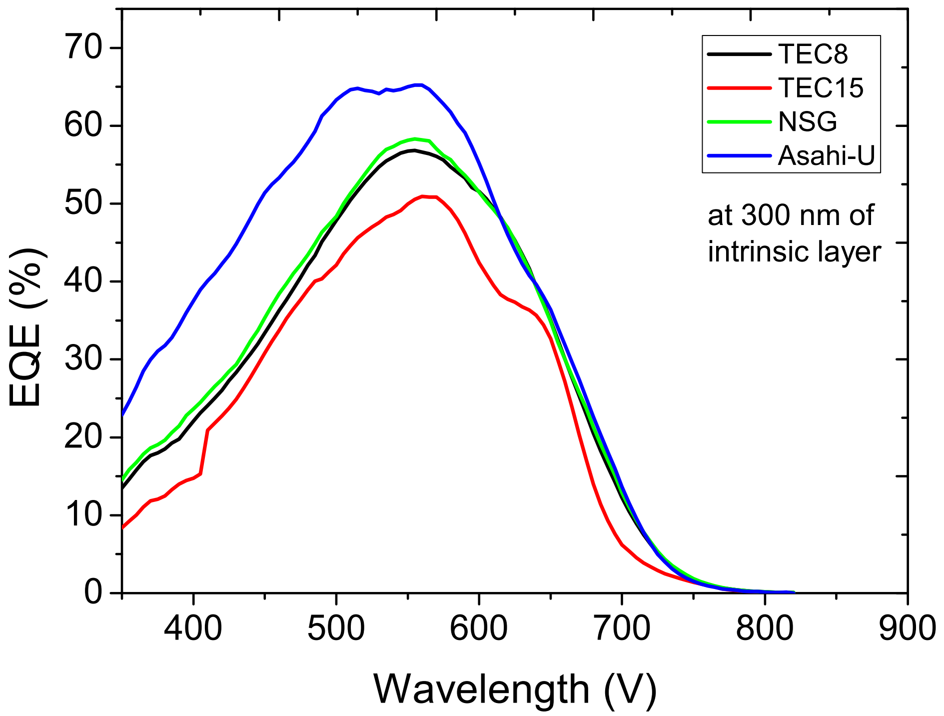

FIGURE 6.13: The external quantum efficiency curve of a-Si:H based single junction *pin* devices, deposited with 300 nm of intrinsic layer on four different commercial TCO substrates.

The external quantum efficiency (EQE) curves of all devices deposited with 300 nm of intrinsic material on four different commercial TCO substrates are illustrated in Figure 6.13. The Asahi-U based device has higher or equal quantum efficiency at all wavelengths compared to the other devices. Asahi-U also shows significantly better photon conversion at wavelengths between 380 nm and 580 nm for the thinner 300 nm intrinsic layer which is higher than 65%. Asahi-U based devices also exhibit higher EQE over all wavelength range from 350 nm to 620 nm where it is similar to TEC-8 and NSG based devices. This excellent photon conversion at lower wavelength and blue-green spectrum may be attributed to the excellent light scattering property of Asahi-U determined by WARS measurements (section 6.3). The TEC-8 and NSG based devices exhibit identical conversion efficiency and their curves overlap each other at all wavelength range which also supports the conclusions made in optical analysis of TCO materials. The conversion efficiency of TEC-15 based device is low at all wavelengths but it does come close to other devices at higher wavelength ranges, as even the relatively heavily textured TCOs have low haze values and poor light-trapping at these longer wavelengths,All four devices deposited with the thin intrinsic layer, appears to be synchronised in terms of have very similar quantum efficiency in the wavelength range from 650 nm to 800 nm. This feature illustrates that the texture of the TCO s do not make a significant contributes to scattering into the silicon layer at the higher wavelength ranges though the texture certainly contributes at the lower wavelengths and the important blue-green region of spectrum.

All four devices deposited with thin intrinsic layer, appears to be synchronised in terms of have very similar quantum efficiency in wavelength range from 650 nm to 800 nm. This feature illustrate that the texture of the TCO do not make a significant contributes to scattering into the silicon layer at the higher wavelength ranges though the texture certainly contributes at the lower wavelengths and the important blue-green region of spectrum.

6.4.2 *at 350 nm of intrinsic layer*

All four devices deposited with 350 nm of intrinsic layer more efficient as compared to the devices with the thinner intrinsic layers. The characterisation parameters of single junction *pin* devices deposited at intrinsic thickness of 350 nm on four TCO substrates are summarised in table (6.5), and the *IV* characteristic curves of those devices are assembled in Figure 6.14

TABLE 6.5: The characterisation parameters of a-Si:H based single junction *pin* devices deposited with 350 nm of intrinsic layer on four different commercial TCO substrates.

TCOs at 350 nm	Efficiency (%)	V_{OC} (V)	FF	J_{SC} mA/cm^2
TEC-8	4.69	0.75	0.50	12.17
TEC-15	4.18	0.77	0.49	10.78
NSG	4.67	0.73	0.53	11.95
Asahi-U	5.71	0.75	0.56	13.40

In this set of experiments, the three devices, TEC-8, TEC-15 and NSG demonstrate similar efficiencies between 4 and 5% while, as expected Asahi-U provides the most efficient device at 5.71%. The Asahi-U also generated the highest short-circuit current density of 13.4 mA/cm^2. The *FF* values of identical trio TEC-8, TEC-15 and NSG determined similar to each other are 0.50, 0.49 and 0.53 respectively. The V_{OC} values of all four devices are similar as illustrated in the IV -characteristics curve. The overall performance of the Asahi-U based device is higher than other three TCO based devices and TEC-15 is the least efficient device. In spite of the lowest current density the TEC-15 device provides the highest V_{OC}, this is a result of the improved device quality that can be produced on planar substrates.

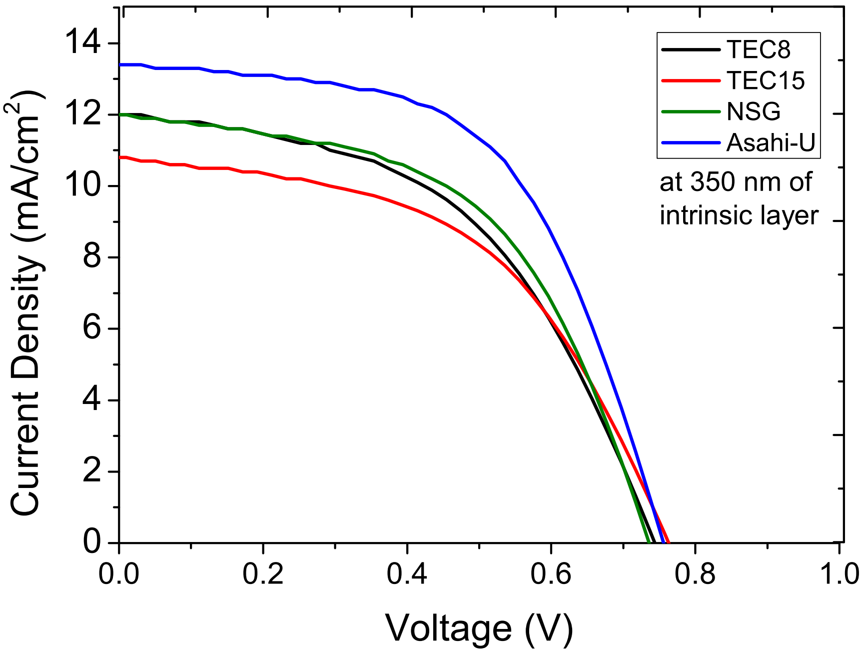

FIGURE 6.14: The *IV* characteristic curve of a-Si:H based single junction *pin* devices, deposited with 350 nm of intrinsic layer on four different commercial TCO substrates measured at room temperature under AM1.5 illumination.

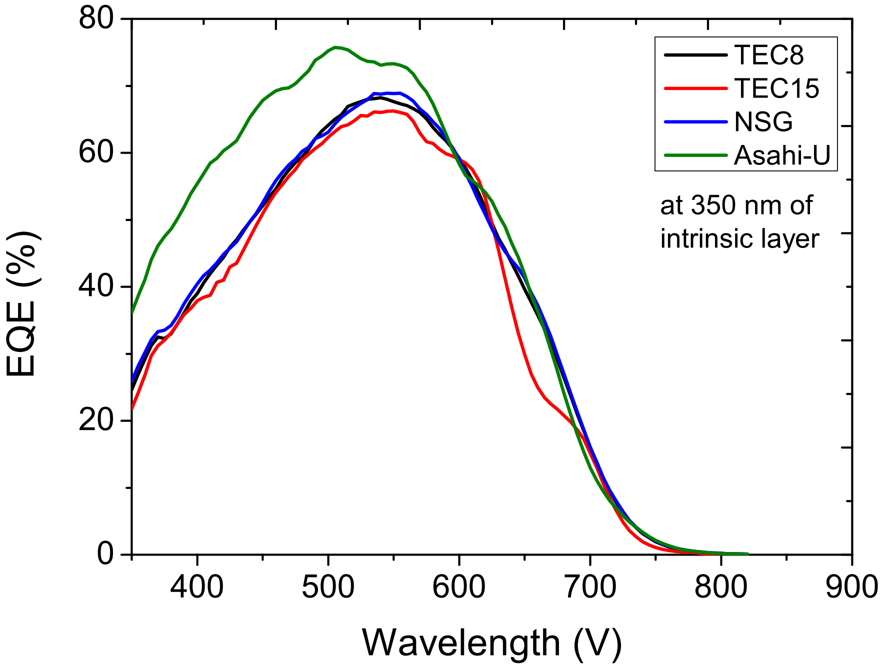

FIGURE 6.15: The quantum efficiency curve of a-Si:H based single junction *pin* devices, deposited with 350 nm of intrinsic layer on four different commercial TCO substrates.

The quantum eciency curve of a-Si:H based single junction pin devices deposited with a 350 nm intrinsic layer on the four different commercial TCO substrates are presented in Figure 6.15.

At 350 nm intrinsic thickness, the Asahi-U based device is shown to be superior to the other TCO substrates. The peak QE curve for Asahi-U lies over 70% in the important blue-green part of the spectrum between wavelength range of 500 to 600 nm. At lower wavelengths, Asahi-U based devices exhibit significantly higher QE, often 15 to 20% higher than the other TCO based devices, this we believe is as a result of reduced parasitic absorption in the TCO. The performance of all four TCO based devices once again have similar QE at wavelengths greater than 620 nm. The QE curve of TEC-8 and NSG are close over entire wavelength range whereas TEC-15 QE curve remains below the other TCOs for most of the wavelength range.

6.4.3 *at 400 nm of intrinsic layer*

In this work, fabrication with optimised growth parameters, and devices with intrinsic layers between 370 nm and 400 nm always produced the best devices. This intrinsic thickness optimization also shows that 400 nm produces the best devices. The characterisation parameters of single junction pin devices deposited at intrinsic thickness of 400 nm on each of the four TCO substrates are described in the table (6.6) we can see that all four devices have reached highest values for each and every characterization parameter. The *IV*-characteristics are presented in Figure 6.16

TABLE 6.6: The initial characterisation parameters of a-Si:H based single junction *pin* devices deposited with 400 nm of intrinsic layer on four different commercial TCO substrates.

TCOs at 400 nm	Efficiency (%)	V_{OC} (V)	FF	J_{SC} mA/cm^2
TEC-8	5.90	0.75	0.56	13.70
TEC-15	4.88	0.73	0.53	12.40
NSG	5.64	0.73	0.54	14.02
Asahi-U	5.71	0.75	0.53	14.04

The V_{OC} values for all devices are very similar to each other such that TEC-8 and Asahi-U have 0.75V, while other two TCOs TEC-15 and NSG have 0.73V. The Asahi-U based device has highest J_{SC} among all device as 14.04 mA/cm^2 but it is just behind TEC-8 in terms of efficiency as it has slightly less *FF*. The efficiencies of TEC-8, NSG, and Asahi are 5.90%, 5.64%, and 5.71% respectively which are very close to each other. The *IV*-characteristic curve of three TEC-8, NSG and Asahi based devices is more similar than for other thicknesses.

The quantum efficiency curve of a-Si:H based single junction pin devices, deposited with 400 nm of intrinsic layer on each of the four TCO substrates are illustrated in Figure 6.17.

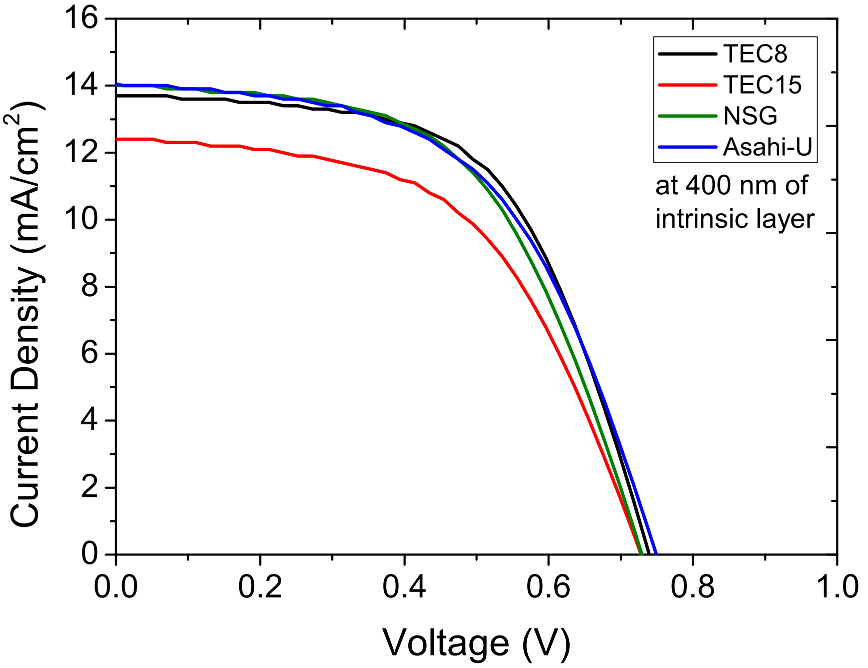

FIGURE 6.16: The initial *IV* characteristic curve of a-Si:H based single junction *pin* devices, deposited with 400 nm of intrinsic layer on four different commercial TCO substrates measured at room temperature under AM1.5 illumination.

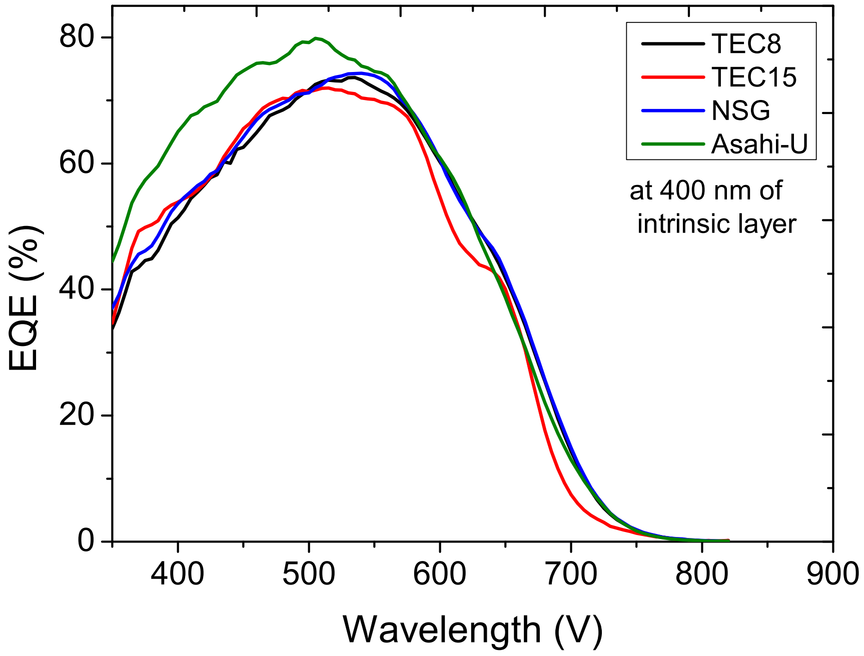

FIGURE 6.17: The initial quantum efficiency curve of a-Si:H based single junction *pin* devices, deposited with 400 nm of intrinsic layer on four different commercial TCO substrates.

At shorter wavelengths, The TEC-8, TEC-15 and NSG show a close match. At longer wavelengths, TEC-8, NSG and Asahi-U show similar QE regardless of intrinsic thickness. At 400 nm wavelength, again there is 10-15% enhancement of photon conversion for the Asahi-U based device and this enhancement is dominant up the wavelength of 580 nm where it meets with QE curves of TEC and NSG based devices.

6.4.4 *at 450 nm of intrinsic layer*

This is the final set of devices, in which 450 nm intrinsic layers are used within single junction a-Si:H based devices. This intrinsic thickness is relatively thick and all devices demonstrate reduced performance. The characterization parameters are summarised in table (6.7) and IV-characteristic measured at room temperature under AM1.5 are shown in Figure 5.18 QE curves are provided in Figure 6.18.

Table 6.7: The initial characterisation parameters of a-Si:H based single junction pin devices deposited with 450 nm of intrinsic layer on four commercial TCO substrates measured at room temperature AM1.5

TCOs at 450 nm	Efficiency (%)	V_{OC} (V)	FF	J_{SC} mA/cm^2
TEC-8	4.95	0.77	0.52	12.13
TEC-15	3.89	0.77	0.45	10.97
NSG	5.57	0.75	0.49	12.13
Asahi-U	5.12	0.79	0.48	13.34

The results obtained with the 450 nm intrinsic layers illustrate many of the same general features observation at 400 nm, though it is interesting to observe that Asahi-U appears less dominant at the increased thickness, principally as a result of the reduced FF for the Asahi device.

6.4.5 *TCO performance summary*

To summarise the performance of all four commercial TCO based solar cell devices, their eciencies and J SC values are plotted with respect to intrinsic layer thickness.

The relatively flat profile of TEC-15 TCO material has the most profound impact on the device performance as all TEC-15 devices exhibit lower photon absorption in the visible spectrum. As a result, current generation ability has been suppressed at every intrinsic thickness as illustrated in Figure 6.20. TEC-8 and Asahi-U show good performance in every device parameter, thanks to the better TCO texture. Asahi-U based devices have the highest performance, perhaps most importantly the efficiency values for 350 nm intrinsic layers are just as good as those at 400 nm, this represent a cost reduction opportunity, at least in terms of device deposition, however, Asahi-U is more expensive to produce TEC8 than NSG, so, in fact both have occupied commercial niches.

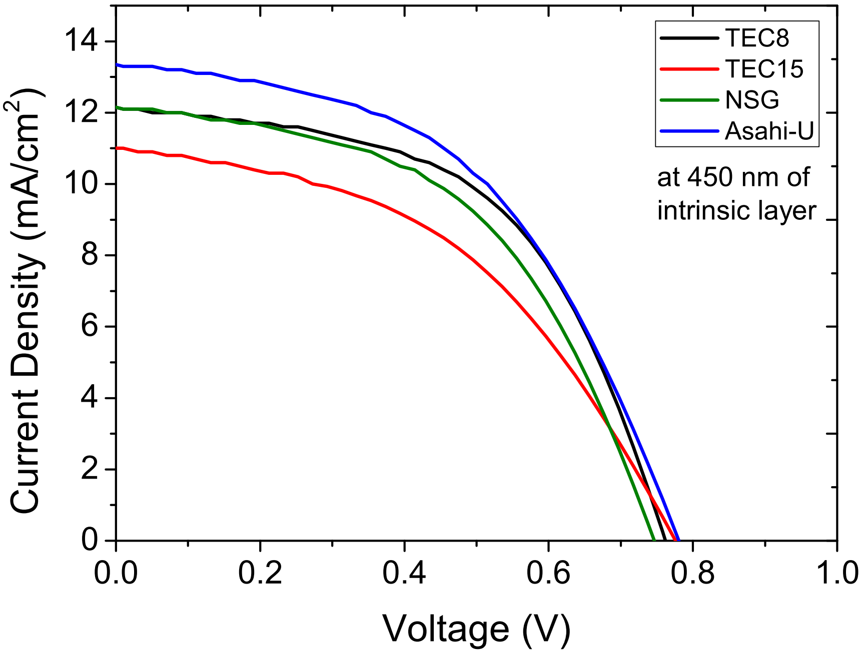

FIGURE 6.18: The initial *IV* characteristic curve of a-Si:H based single junction *pin* devices, deposited with 450 nm of intrinsic layer on four different commercial TCO substrates.

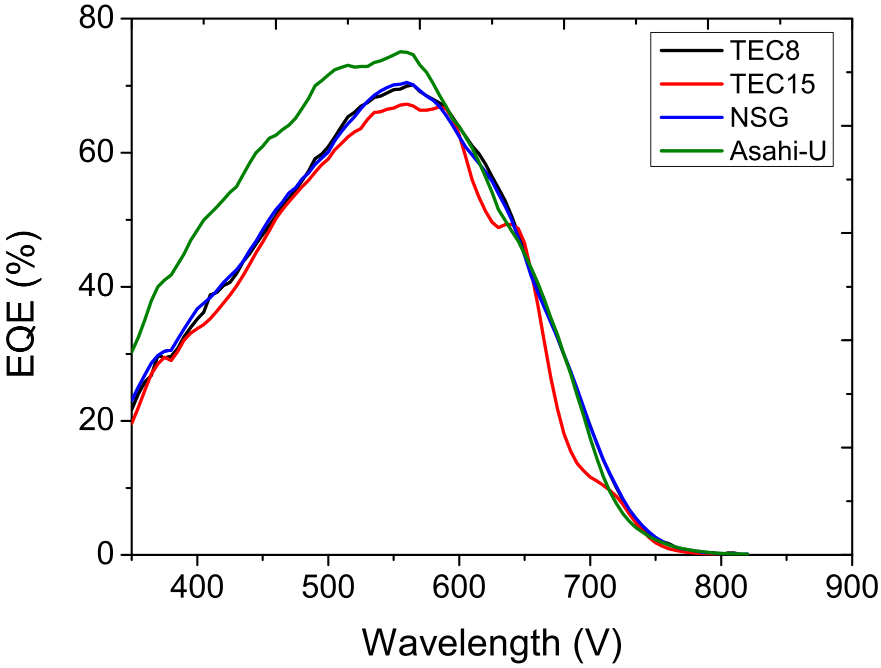

FIGURE 6.19: The quantum efficiency curve of a-Si:H based single junction *pin* devices, deposited with 450 nm of intrinsic layer on four different commercial TCO substrates.

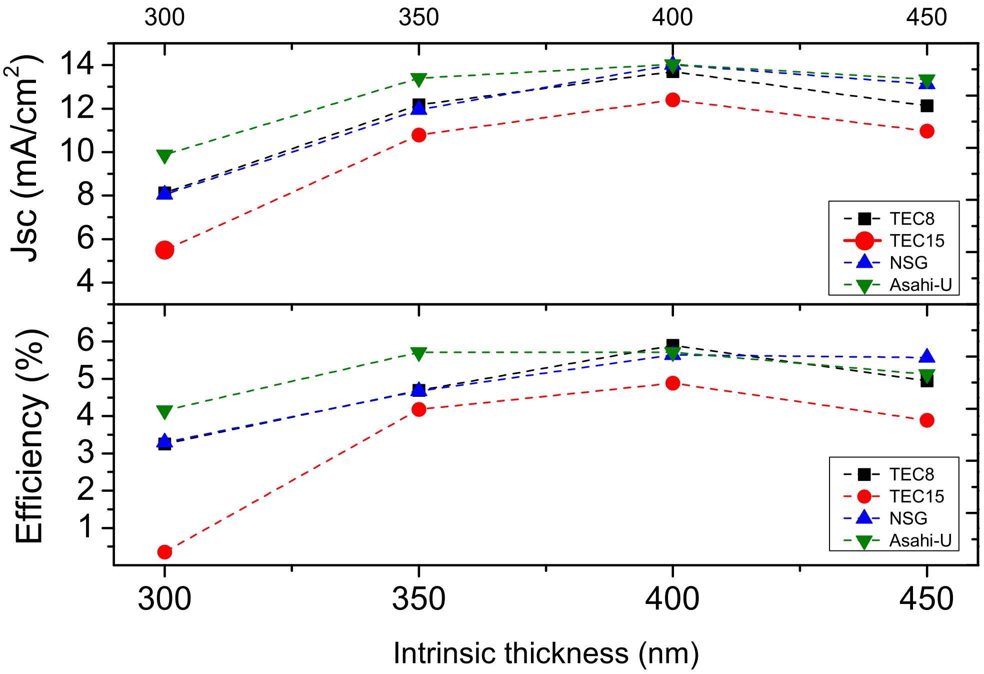

FIGURE 6.20: JSC and Efficiency of all TCO

6.5 Optical analysis of TCO based devices

In this section, the a-Si:H based single junction devices deposited with different intrinsic layers on different commercial TCO substrates are optically analysed in order to provide more insight on the efficiency of the texture based scattering and their connection to photon conversion efficiencies. From section 6.3, the quantum efficiency curves of various devices demonstrate that, photon conversion on the textured TCO based devices is very high as compared with non-textured based devices. This textured profile based photon conversion is high at short wavelengths, and at blue-green part of visible spectrum. It is further observed that photon conversion at longer wavelength no more depends on the textured profile of the device. To understand this phenomenon, textured based devices were selected and examined optically using *WARS* measurements system.

When light enters into *pin* device with back reflector, either it will be absorbed or reflected back. The light, reflected back out of the device is termed as photon loss. If the device is textured based, the light will be reflected randomly in all directions and for this case *WARS* measurements system is an ideal as it has capability to detect light between 10^o to 80^o. The *WARS* result are further simulated, in order to determine the three dimensional prospect of the randomly scattered light. The *WARS* measurement system in reflection scattering mode is illustrated in following block diagram in Figure 6.21.

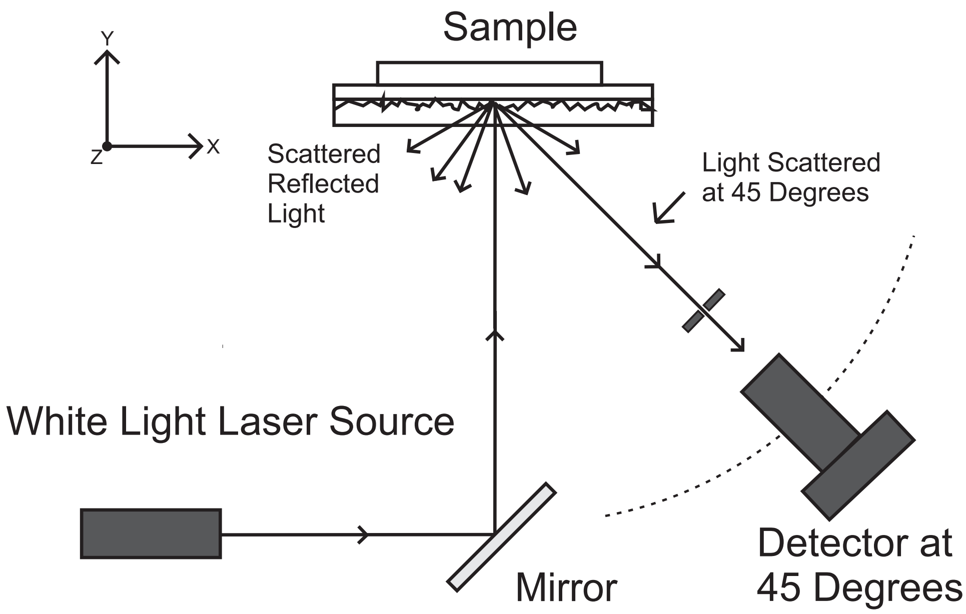

FIGURE 6.21: The *WARS* measurement system in reflection scattering mode. The white light laser source is deflected on sample via mirror and reflected scattered light is measured at detector which can sweep from 0^o to 80^o on source plane

For this optical analysis, two set of devices with 300 nm and 400 nm of intrinsic layers were selected. In addition to *WARS* measurements, total, diffuse and specular reflectance were also carried to interpret the scattered results more effectively.

6.5.1 *Devices with 300 nm of intrinsic layer*

The reflected scattering from single junction *pin* based a-Si:H with a 300 nm intrinsic layer deposited on Asahi-U TCO substrate is shown in top side of the Figure 6.22 whereas the bottom graph of the figure shows the total, diffuse and specular reflection at the same point of the device. The diffuse reflection curve of Asahi-U device with a 300 nm intrinsic layer has two bumps. The peak of one bump appeared at wavelength of 650 nm and other bump is broad and spread is spanned from 700 nm to 900 nm at longer wavelength region. This reflects that incoming photons have been scattered back and this effect has been verified by WARS measurement. It is observed that there is a large reflected scattering in all directions from 15^o to 75^o in longer wavelength regions between 700 nm and 950 nm and at 650 of wavelength regions. The WARS system detection of high scattering at particular wavelength range matches with diffuse reflection high points. As this scattering is in the reflected phase, it would not take part in active absorption in the device. This is actually a loss of photons which have escaped from the Asahi-U TCO device at large angles with respect normal incidence.

The reflected scattering from single junction *pin* based a-Si:H with 300 nm of on intrinsic layer deposited on the non textured TEC-15 TCO substrate is shown in the top side of Figure 6.23 whereas the bottom side graph the total, diffuse and specular reflation at

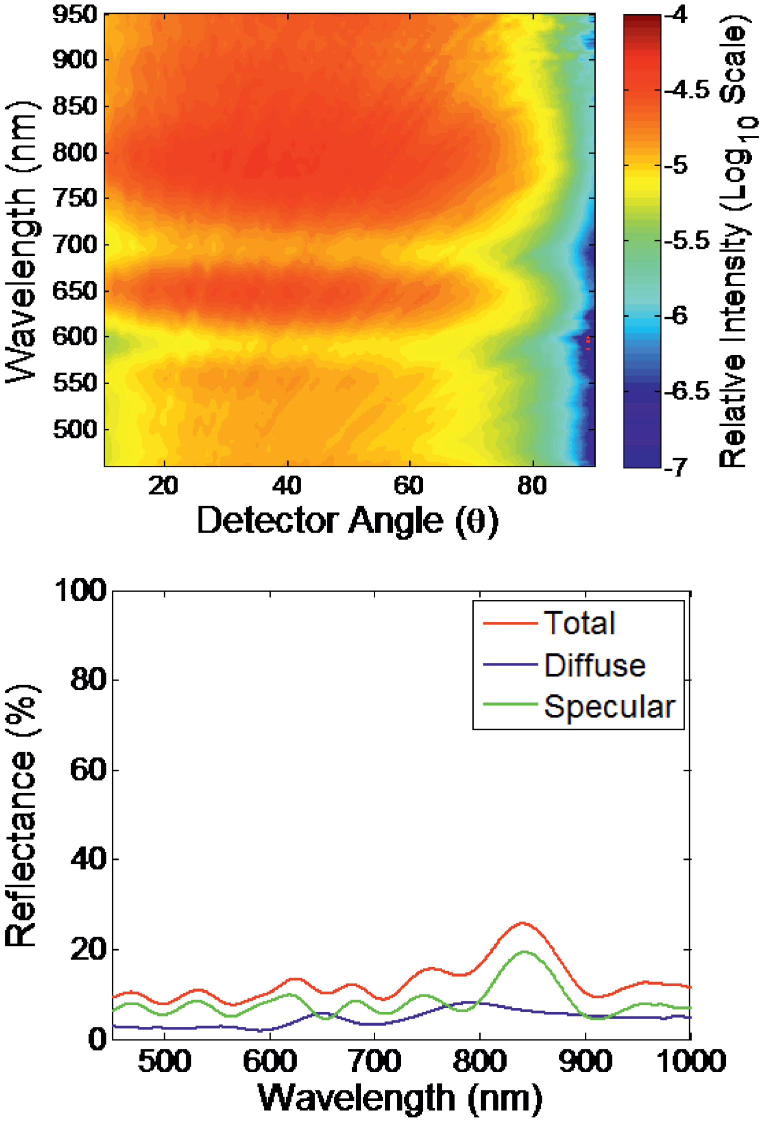

FIGURE 6.22: Amorphous based *pin* device with 300 nm of intrinsic layer deposited on Asahi-U substrate. Top: WARS reflected scattering from amorphous layer with back reflector; Bottom: Total, diffuse and specular reflection from *pin* amorphous device with back reflector.

the same point of the device. In comparison with highly textured TCO based device, TEC-15 based device has very low diffuse reflection and most light simply escapes via specular reflection. This is the reason, we don't observe any significant reflected scattering during WARS measurement. Despite limited diffuse reflection, minor scattering has been observed which appeared exactly on the same wavelength region where minor diffuse reflection has been noted. This low intense reflected scattering by is spanned over 20^o to 75^o at wavelengths of 675 nm and 800 nm.

Previously, TCO materials, The TEC-8 and the NSG which have demonstrated identical textured profile in previous device optical analysis and similar performance during device characterization, continued their matching scattering nature in post device analysis. The

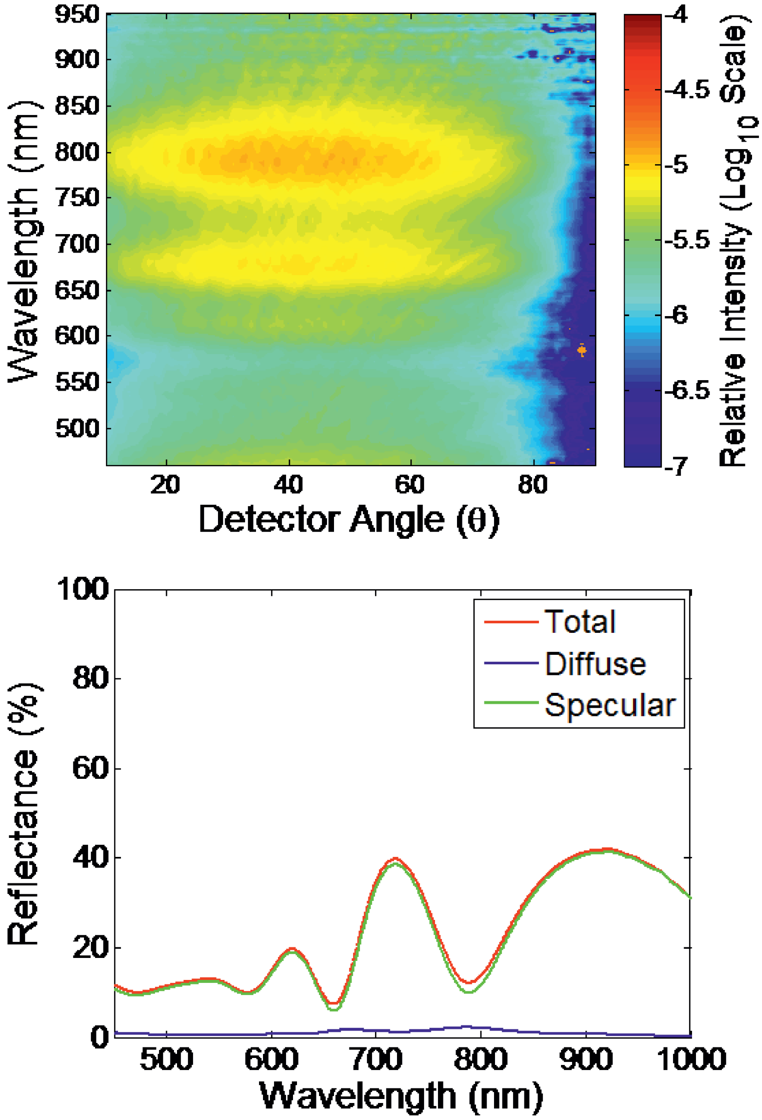

FIGURE 6.23: Amorphous based *pin* device with 300 nm of intrinsic layer deposited on TEC-15 substrate. Top: WARS reflected scattering from amorphous layer with back reflector; Bottom: Total, diffuse and specular reflection from *pin* amorphous device with back reflector.

reflected scattering from single junction *pin* based a-Si:H with 300 nm of intrinsic layer deposited on TEC-8 TCO substrate is shown in the top side of Figure 6.24 whereas lower graph of the figure illustrates the total, diffuse and specular reflection at the same point of the device. The strong reflected scattering has been observed in TEC-8 device above 650 nm which is spread at 15^o to 75^o. There is also higher reflected scattering at shorter wavelengths from 450 nm to 600 nm which is also spanned uniformly at all angles from 10^o to 70^o. This is the light which has been reflected whole *pin* device. It is also observed that TEC-8 device does not scatter back the light which reflected at large angles such as between 75^o to 80^o.

The reflected scattering from single junction *pin* based a-Si:H with 300 nm of on intrinsic

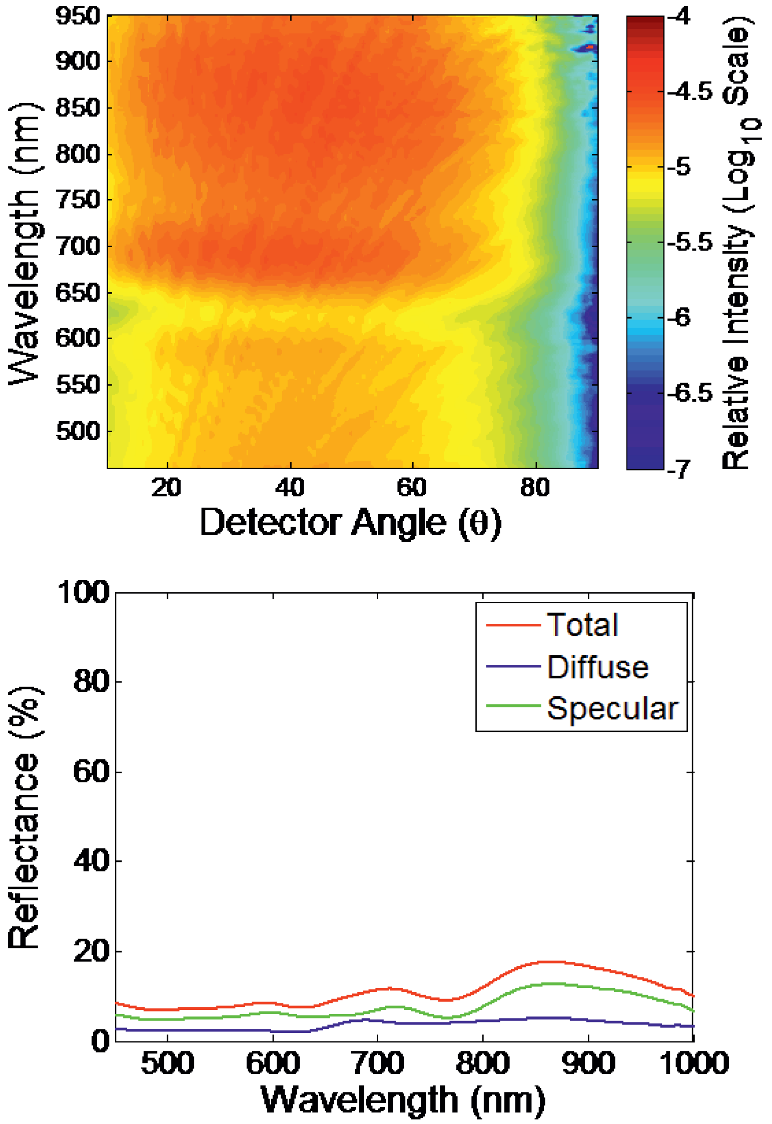

Figure 6.24: Amorphous based *pin* device with 300 nm of intrinsic layer deposited on TEC-8 substrate. Top: WARS reflected scattering from amorphous layer with back reflector; Bottom: Total, diffuse and specular reflection from *pin* amorphous device with back reflector.

layer deposited on NSG TCO substrate is shown in the top side of Figure 6.25 whereas lower graph of the figure illustrates the total, diffuse and specular reflection at the same point of the device where it can be observed that it behaves same like TEC-8 TCO device.

6.5.2 *Devices with 400 nm of intrinsic layer*

The reflected scattering from single junction *pin* based a-Si:H with 400 nm of intrinsic layer deposited on Asahi-U TCO substrate is shown in top side of the Figure 6.26 whereas

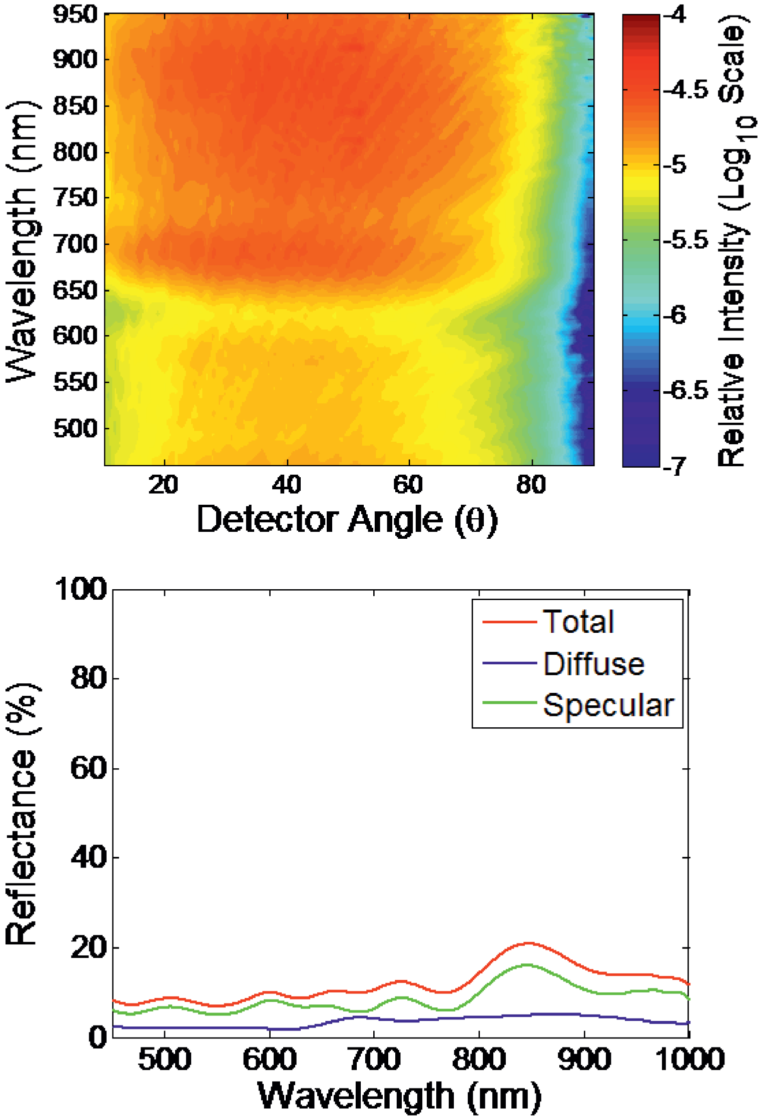

FIGURE 6.25: Amorphous based *pin* device with 300 nm of intrinsic layer deposited on NSG substrate. Top: WARS reflected scattering from amorphous layer with back reflector; Bottom: Total, diffuse and specular reflection from *pin* amorphous device with back reflector.

the lower graph of the figure shows the total, diffuse and specular reflection at the same point of the device.

In the diffuse reflection, one normal bump and one other broad bump can be observed at 675 nm and 770 nm to 900 nm respectively. These peak diffused reflection spots have been translated as high scattering regions in WARS measurement data at similar wavelengths. This is one major difference observed that intensity of this reflected scattering is lower than the scattering intensity measured in Asahi-U devices with a 300 nm intrinsic layer. This additional thickness of intrinsic layer does help to scale down the scattered photons escape. In the shorter wavelength, overall reflected scattering intensity is low and at the lowest intensity is found around the 600nm wavelength where the device

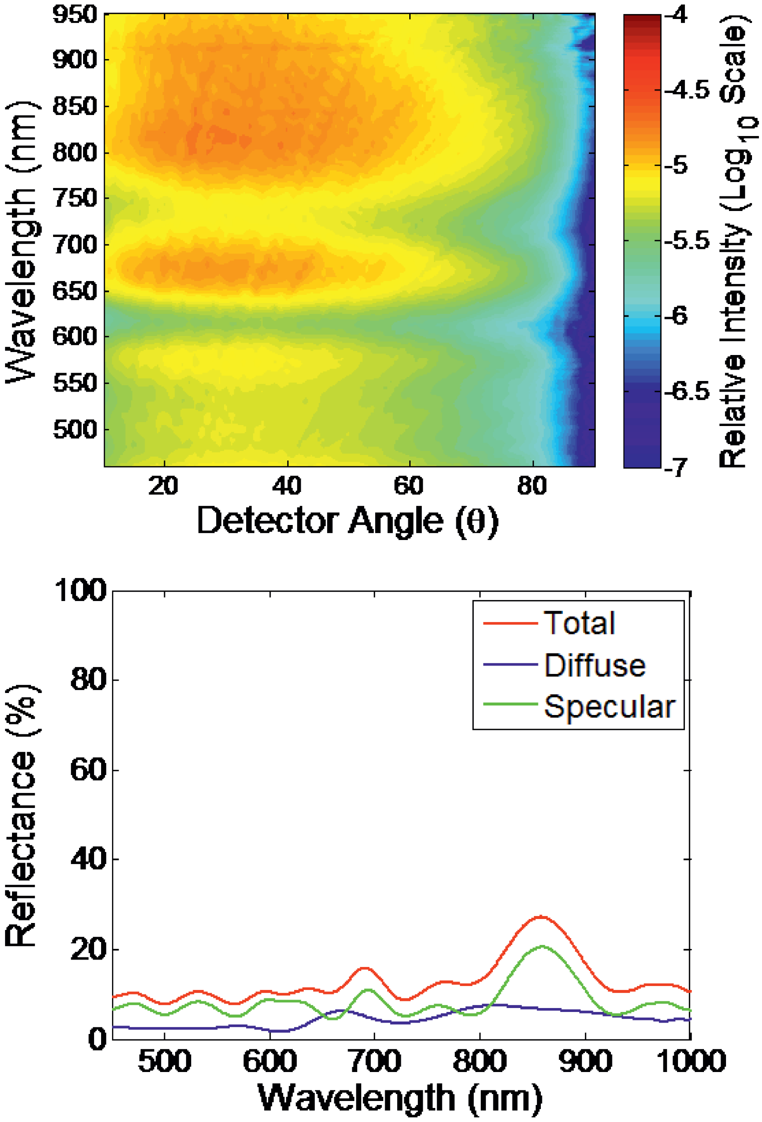

FIGURE 6.26: Amorphous based *pin* device with 400 nm of intrinsic layer deposited on Asahi-U substrate. Top: WARS measurement of reflected scattering from amorphous layer with back reflector; Bottom: Total, diffuse and specular reflection from *pin* amorphous device with back reflector.

absorbs most incoming photons. At 400 nm intrinsic layer, the Asahi-U device still has uniform scattered reflection spanned over all angles above 600 nm to long wavelength regions.

The reflected scattering from single junction *pin* based a-Si:H with a 300 nm intrinsic layer deposited on the non textured TEC-15 TCO substrate is shown in the top side of the Figure 6.23 whereas the lower graph of the same figure shows the total, diffuse and specular reflection at the same point of the device.

The diffuse reflection of TEC-15 based device with 400 nm layer has a very low a similar curve as originated with the TEC-15 device with a 300 nm intrinsic layer. The

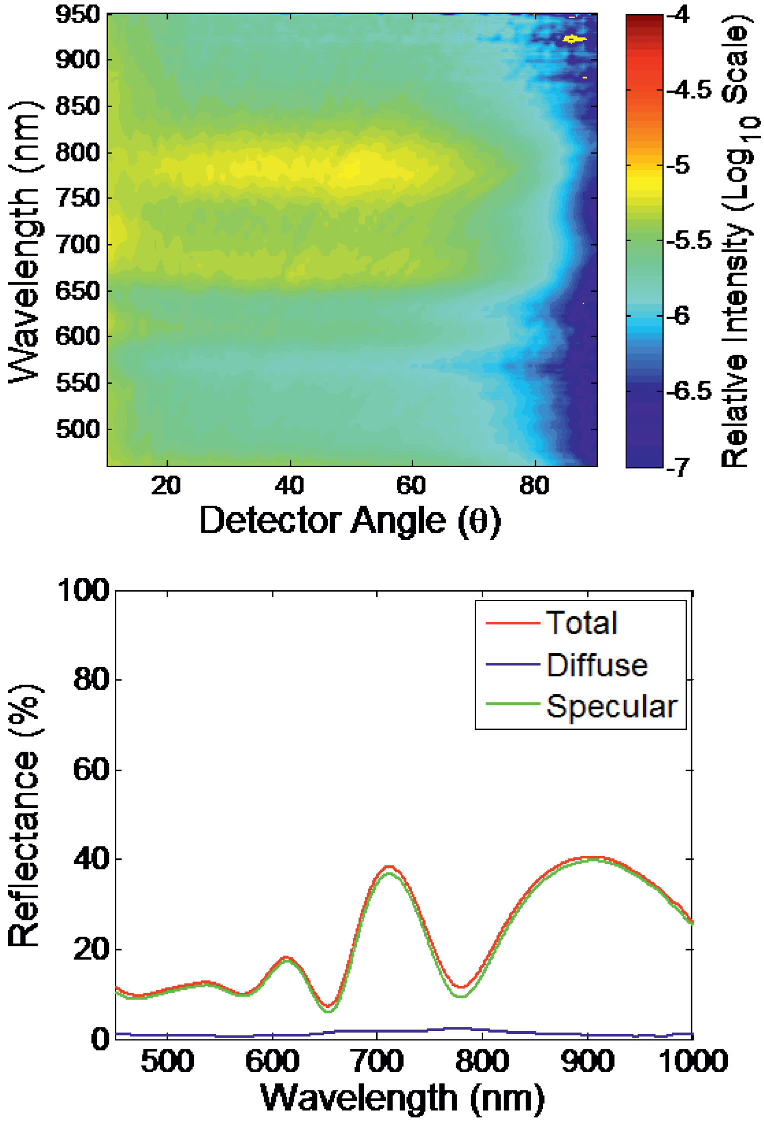

FIGURE 6.27: Amorphous based *pin* device with 400 nm of intrinsic layer deposited on TEC-15 substrate. Top: WARS reflected scattering from amorphous layer with back reflector; Bottom: Total, diffuse and specular reflection from *pin* amorphous device with back reflector.

intensity of reflected scattering is low at 400 nm intrinsic layer as compared with intensity measured at 300 nm, which again demonstrate that a thick intrinsic layer helps in preventing light escape via reflection. The TEC-15 based device has low scattering intensity at shorter wavelengths and at blue green regions of visible spectrum. The diffuse reflection of TEC-15 device has a broad hump at 650 nm to 850 nm which has been verified by *WARS* measurement with regions of high scattering intensity. The TEC-8 based device with a 400 nm intrinsic layer has lower reflected intensity in the visible spectrum as compared with the Asahi-U based device at same the thickness shown in Figure 6.28 in which, the reflected scattering from single junction *pin* based a-Si:H with a 300 nm intrinsic layer deposited on the textured TEC-8 TCO substrate

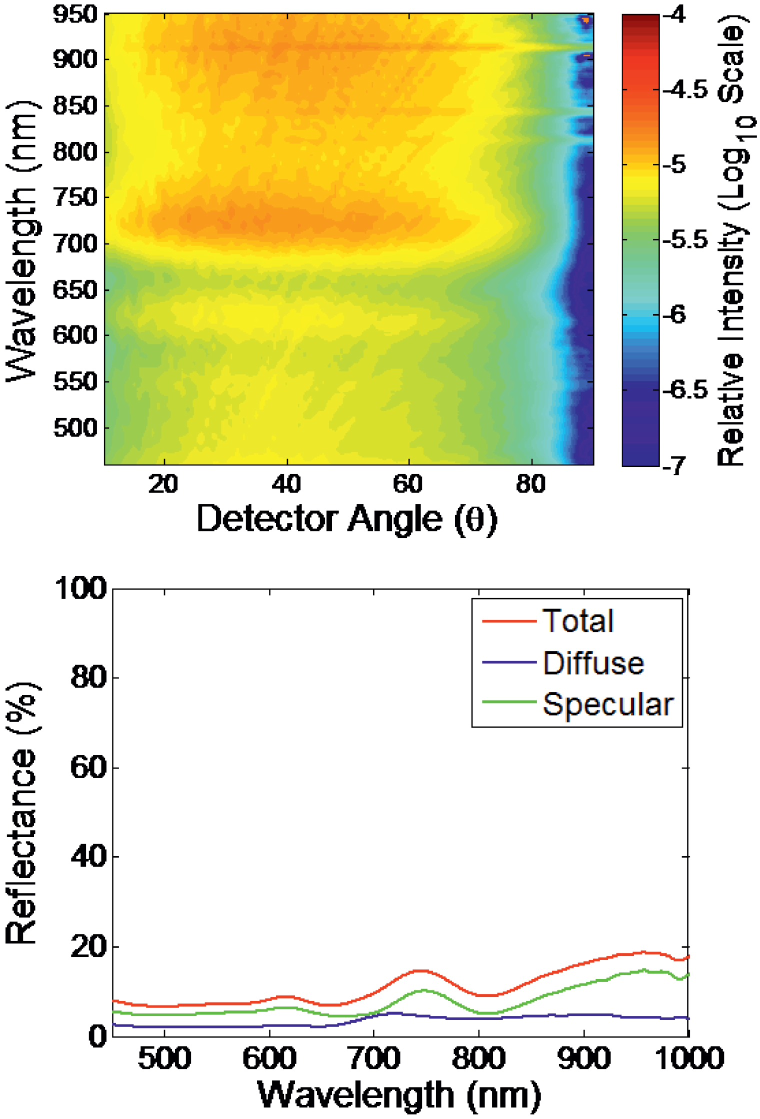

FIGURE 6.28: Amorphous based *pin* device with 400 nm of intrinsic layer deposited on TEC-8 substrate. Top: WARS reflected scattering from amorphous layer with back reflector; Bottom: Total, diffuse and specular reflection from *pin* amorphous device with back reflector.

is shown in the top side of Figure 6.23. In the same figure, the lower graph of shows the total, diffuse and specular reflection of same TEC-8 based device. After 700 nm wavelength, TEC-8 TCO devices scatter the light uniformly but this has lower intensity as compared with same TCO device with a thinner intrinsic layer. The bump in diffuse reflection curve at 720 nm has been verified by *WARS* measurement at same wavelength all over angles.

The NSG based TCO device has similar scattering profile to TEC-8 which is shown in Figure 6.29. It has low reflected scattering in short wavelength regions and strong scattering in long wavelength region. The peak value of diffuse reflectance by the NSG device has high scattering at 720 nm of wavelength.

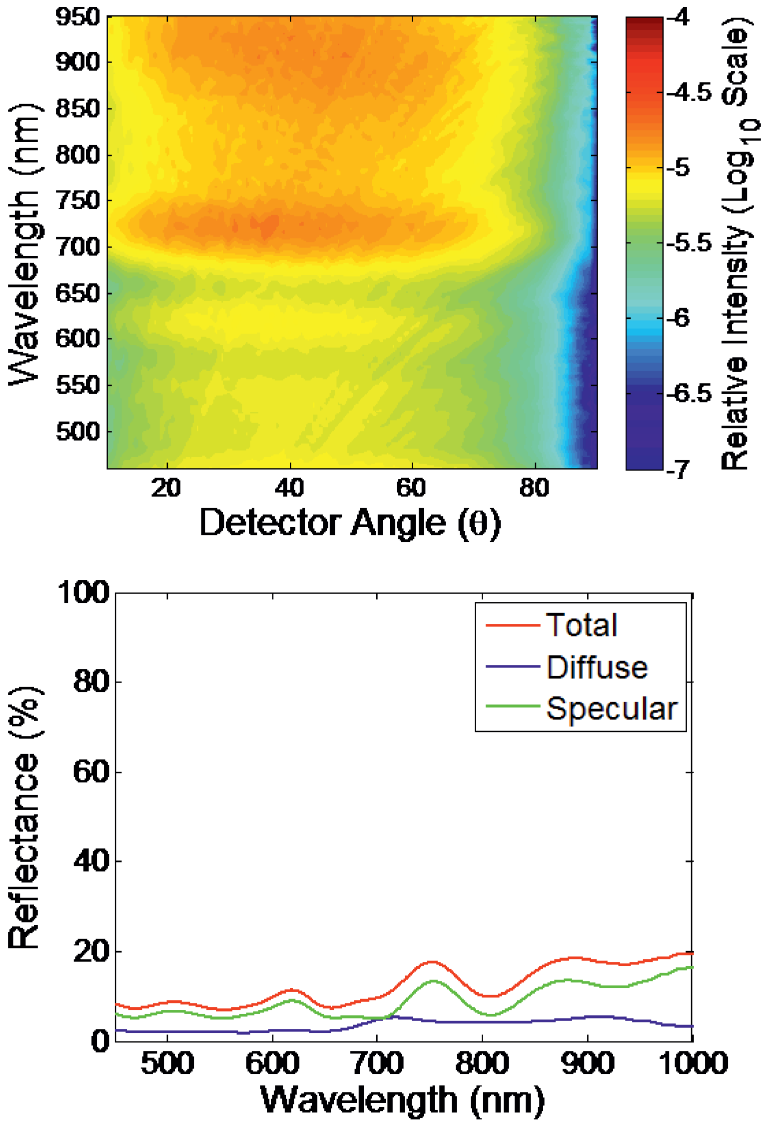

Figure 6.29: Amorphous based *pin* device with 300 nm of intrinsic layer deposited on NSG substrate. Top: WARS reflected scattering from amorphous layer with back reflector; Bottom: Total, diffuse and specular reflection from *pin* amorphous device with back reflector.

So far we have observed that all textured based devices such as Asahi-U, TEC-8 and NSG with 300 nm of intrinsic layer show strong reflected scattering at 600 nm wavelength. This scattering is uniformly spanned over all angles and continues up to long wavelengths of the incoming spectrum. The same scattering pattern has been repeated by devices with 400 nm of intrinsic thickness deposited on these textured TCO materials, but intensity of reflected scattering is over all low as compared with intensity of lower intrinsic thickness. This reflection based scattering at mid and long wavelength regions are actually caused by those photons which are not absorbed by the device and have escaped at various angles. This is the reason all these textured based TCO TEC8, NSG, and Asahi-U devices behave similar in quantum efficiency curves after 620 nm of

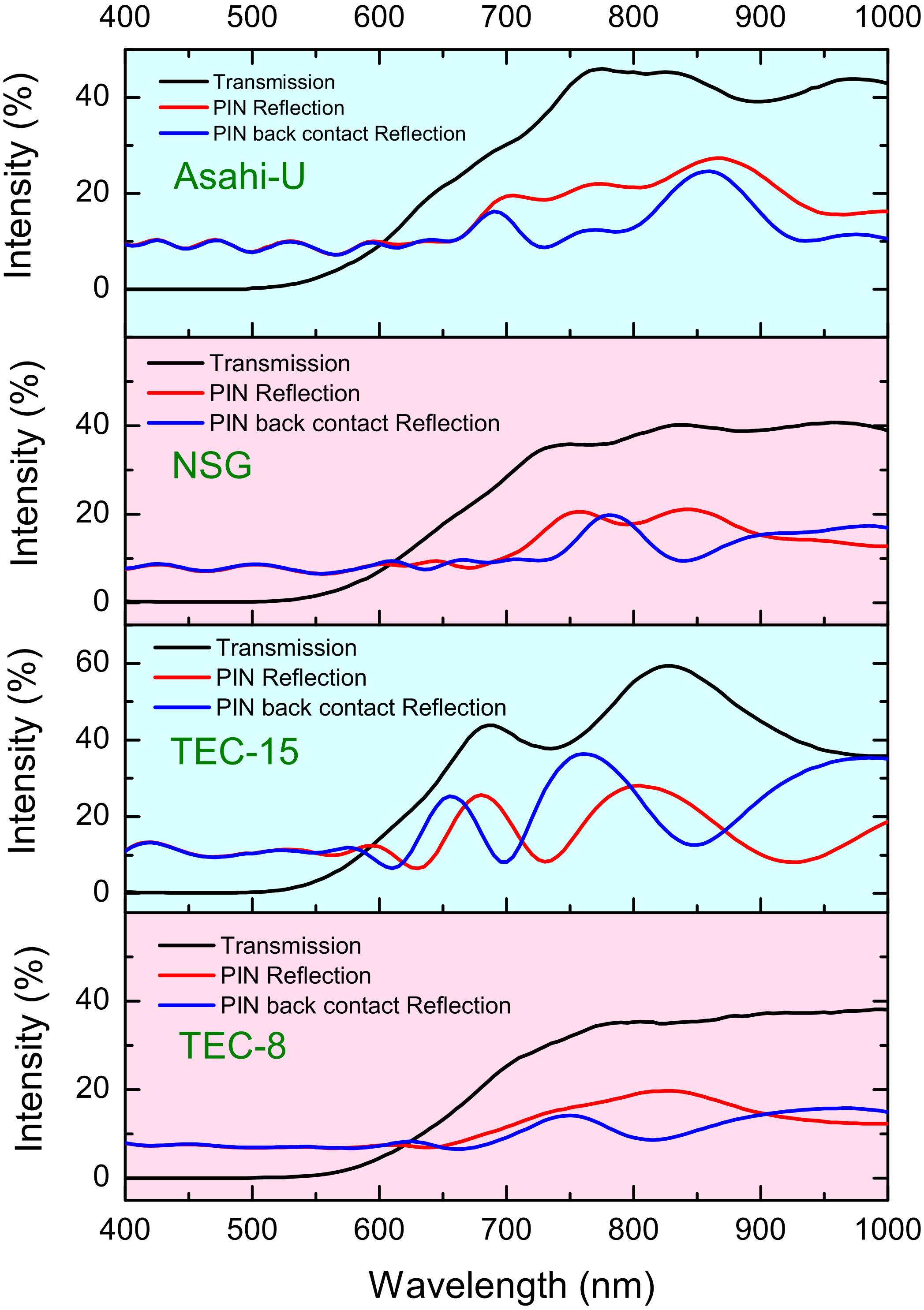

FIGURE 6.30: The transmittance and reflectance curve from *pin* and the reflection curve from *pin* back reflector from all commercial TCO material used in this report, deposited with 400 nm of intrinsic layer.

the wavelengths as shown in Figure 6.13 and Figure 6.17.

6.6 Optimised textured TCO for application in single junction a-Si:H cell

From the above discussion, we have seen that textured profile on a TCO film is crucial to improve optical absorption, especially at longer wavelengths. Now question arises, using *WARS* data with AFM analysis, can an optimized textured TCO be predicted for single junction a-Si:H based solar cells? In this chapter, four different TCO analysis already presented which are, AFM TCO analysis, *WARS* TCO analysis, *PIN* device *WARS* analysis and PIN optical reflection analysis are reviewed in order to try and predict the optimum TCO film morphology.

In a-Si:H based solar cells optical absorption is low in the near infrared region therefore use of textured TCO is essential which not only reduce the reflection but also scatter the light, thereby enhancing the optical path lengths and light trapping. The TCO light scattering can be measured by the one parameter called *Haze* which is given by

$$H_T = \frac{T_{diff}(\lambda)}{T_{tot}(\lambda)} \tag{6.1}$$

Where $Ttot(\lambda)$ is the sum of the specular transmittance and the diffuse transmittance. Using the data presented in Figure 6.5 and Figure 6.6, the haze of four TCO used in this study is plotted in Figure 6.31 and haze values for 550 nm and 800 nm are listed in Table .

Table 6.8: Haze of TCO/Glass films at 550 nm and 850 nm.

TCO	TEC-15	TEC-8	NSG	Asahi-U
Haze at 550 nm (%)	1.9	19.9	18.8	22.1
Haze at 800 nm (%)	1.7	15.6	13.8	17.1

We can observe that scattering of the light has been reduced at longer wavelengths and all TCO scatter strongly in short wavelengths. For optimized TCO, one of the main goal is to get high haze value at longer wavelengths in addition to compulsory small angle scattering at short wavelengths in order to be well suited for a-Si:H applications. From Table 6.8 data of TEC-8 (Figure 6.8) and Asahi-U (Figure 6.11), one can see that maximum light scattering takes place at 20^o to 30^o. A close comparison between the two also indicates that Asahi-U has higher angle scattering as compared to TEC-8 which suggests that higher angle scattering may give rise to longer optical paths. Therefore Asahi-U would be expected to significantly improve the performance of an a-Si:H solar

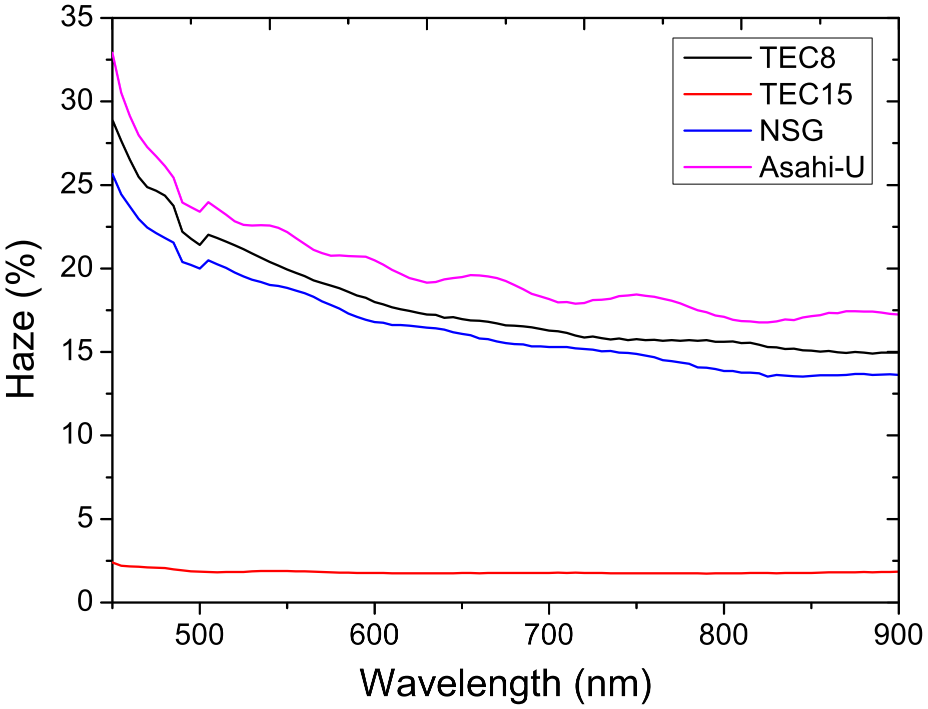

Figure 6.31: Haze of four commercially available glass/TCO films as a function of wavelength.

cell with a thin absorber layer. AFM analysis tells that among all textured TCOs, Asahi-U has lower statistical roughness parameters (Table 6.2) suggested that higher roughness do not necessarily enhance the light scattering and this has been confirmed by a study on morphological effects in a-Si:H devices[98]. It was found that large roughness of TCO film enhances the diffuse transmission in weakly absorbed region (700 nm) in a-Si:H devices and if large TCO roughness is achieved by the increasing the TCO film thickness, it may likely increases the optical absorption in TCO which is not beneficial in overall device performance. This is also suggested that the ratio of the texture feature size to the light wavelength in the material is a critical factor influencing its light scattering ability and the grain size depends on film thickness[126]. In this view we can suggest that optimized TCO film thickness should be be between 400 nm to 900 nm which is concluded optical data present in this chapter.

The topological morphology analysis of Asahi-U and TEC-8 along with scattering data from **WARS** measurement suggest that medium order grain size enhance the scattering over 500 nm of wavelength and also scatter weakly in longer wavelengths above 700 nm. The improved scattering performance of a TCO can also be demonstrated from the reflection measurement as shown in Figure 6.30 where transmittance and reflectance have been measured from *pin* device along with similar measurements from *pin* with back reflector with a-Si:H cell with 400 nm of intrinsic layer. Increased reflectance from

PIN and back reflector would indicates poorer light trapping within the cell. At short wavelengths, all textured TCO posses similar reflectance but they behave different in longer wavelengths. Asahi-U reflect more light in longer wavelengths as compared with TEC-8 or NSG. This behaviour may have been attributed to grain size morphology indicated in AFM analysis. In conclusion, for single junction a-Si:H solar cells, the textured TCO optimisation depends on its optical and morphological properties (apart from electrical) such that it should have a verity of grain sizes from large to medium in order to scatter incoming light in short wavelength to long wavelengths.

6.7 Summary

As discussed earlier in sections 6.4.1 and 6.4.3 all textured based TCO devices have similar photon conversion efficiency between 600 nm and 850 nm and their QE curves overlap each other. Post device *WARS* measurements analysis suggests that textured TCOs are still scattering the incoming at large angles but these low energy photos manage to escape via reflected scattering. This understanding of devices is more comprehensible if we look at the transmittance and reflectance curves of *pin* textured TCO devices and with 400 nm of intrinsic layer which is plotted in Figure 6.30.

It is evidently noticeable that all TCO based devices have no transmittance in the wavelength range of 400 nm to 550 nm. In the wavelength range of 550 and 650, all devices have zero to 20% transmittance. The same Figure 6.30 also demonstrate that all devices have less than 10% total reflectance from 400 nm to 700 nm. We also know from TCO materials transmittance which is shown in Figure 6.5 that all device less substrates are around 80% transparent. Therefore it is suggested that photons with wavelength range of 600 nm to 700 nm reach the *pin* structure and reflected back via scattering as revealed by WARS measurements.

Chapter 7

Germanium layer and their characterisation

Germanium is a group IV material which in crystalline form has a bandgap of 0.67 eV. Germanium has been successfully used in photovoltaic devices such as in thermo-photovoltaic devices[127], as the bottom cell of tandem and multijunction devices[25,128,129]. Germanium has much higher optical absorption in the 1300 to 1550 nm wavelength range, when compared to silicon and therefore germanium-based photodetectors are promising candidates in high speed photodetectors in telecommunication[130] and in CMOS-compatible photodetectors and modulators operating in the C telecommunications band (1520 -1560 nm)[131]. Despite this higher performance, expensive germanium wafer substrates, result in overall fabrication process becoming very costly which is a major problem in rapid economic commercialization.

There are number of methods employed for the deposition of poly crystallization germanium (poly-Ge) and micro-crystalline germanium (c-Ge) thin films. These include Short Pulse Excimer Laser deposition[132], Ge-Powder Evaporation[132], Molecular Beam Epitaxy[130,133], Ultra-high vacuum CVD deposition[131], VHF-ICP deposition[26]. *For this work, it was decided to take the benefits from the PECVD deposition technique which has been already been used for a-Si:H and c-Si:H by attempting TF Ge deposition, with a particular objective of producing IR photovoltaic devices that could provide a method by which wireless sensor nodes could be powered by lasers. In a brief germanium literature survey, it was found that researchers have not widely used the PECVD deposition method for germanium thin films.*

Large area electronics devices such thin film solar cells, and thin film transistors always require lower contact resistance and higher carrier mobility. In terms of cost, highly crystallized thin film Ge, deposited at lower temperature can serve this purpose[27,127,134]. In this chapter, PECVD deposition of poly-Ge and micro-crystalline germanium (μc-Ge) thin films and their characterisation are discussed. As there were no base deposition parameters were available, μc-Si:H deposition parameters with appropriate modifications were employed.

7.1 Initial germanium deposition

For the early depositions of poly-Ge, deposition parameters were varied as shown in Table 7.1. The 250^{o}C substrate temperature, 1000 mT chamber pressure and 450 sccm of argon flow were kept constant, while RF power, germane and hydrogen flow varied to get a start point for poly-Ge layers.

The early stage deposition of poly-Ge, various deposition parameters are varied and few kept constant as shown in Table 7.1. The 250 ^{o}C substrate temperature, 1000 mT chamber pressure and 450 sccm of argon flow kept constant, while RF power, germane (GeH_4) and hydrogen flow varied to get base for poly-Ge layers.

Table 7.1: The initial deposition parameters for Ge layers deposited via PECVD with film thickness and optical bandgap. The 250 ^{o}C substrate temperature, 1000 mT chamber pressure and 450 sccm of argon flow kept constant, while RF power, germane and hydrogen flow varied. The thickness and bandgap is determined by ellipsometry.

Sample	RF Power (W)	GeH_4 flow (sccm)	H_2 flow (sccm)	Dep. Rate (Å/s)	Bandgap (eV)
ES1#A	50	5	50	0.83	0.98
ES1#B	75	05	50	0.83	1.13
ES1#C	50	50	0	2.45	1.00
ES1#D	50	03	50	0.51	0.93
ES1#E	75	05	50	0.32	0.90

The Ge layers are deposited on glass substrates and then optically characterised by ellipsometry. The thickness and bandgap information of each layer is listed in Table 7.1. The absorption coefficient of these germanium layers is calculated from the extinction coefficient which is determined by ellipsometry illustrated in Figure 7.1.

The initial data suggests that bandgap of the Ge film is varied by changes in RF power, germane and H_2 flow. The higher germane flow give rise to faster deposition but layer bandgap is relatively high. The lowest bandgap is found in sample ES1#E where higher RF is being used with lower germane flow. These parameters suppress the deposition rate but result in the layer which has the lowest bandgap. The absorption coefficient of all samples looks identical in shape except ES1#C where higher germane flow is used. Among similar shaped curves, ES1#E has higher absorption coefficient.

To examine and verify the nature of the deposited layer, samples are analysed by Raman spectroscopy. A 532 nm laser excitation wavelength is used. The output Raman curves are illustrated in Figure 7.2. The Raman data shows that 4 out of 5 samples show a

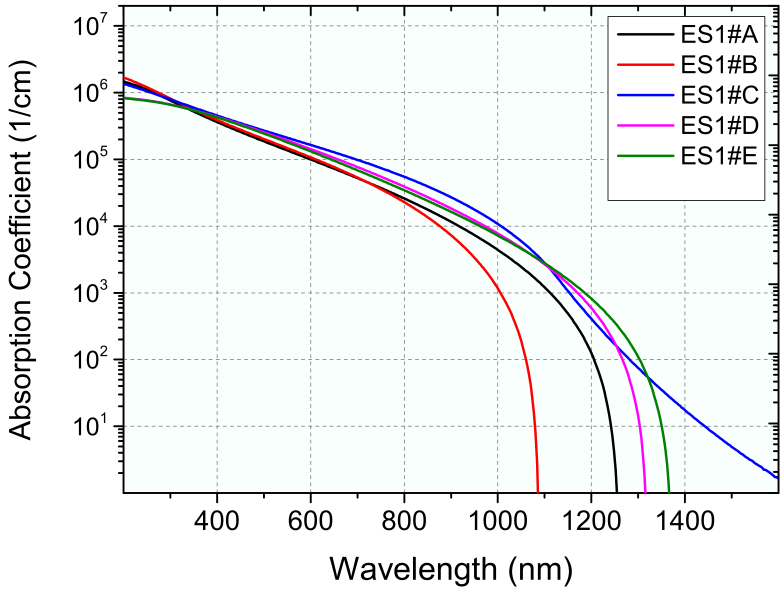

FIGURE 7.1: The absorption coefficient of PECVD grown Ge films deposited on glass samples. The absorption coefficient of these Ge layers is calculated from the extinction coefficient which is determined by ellipsometry.

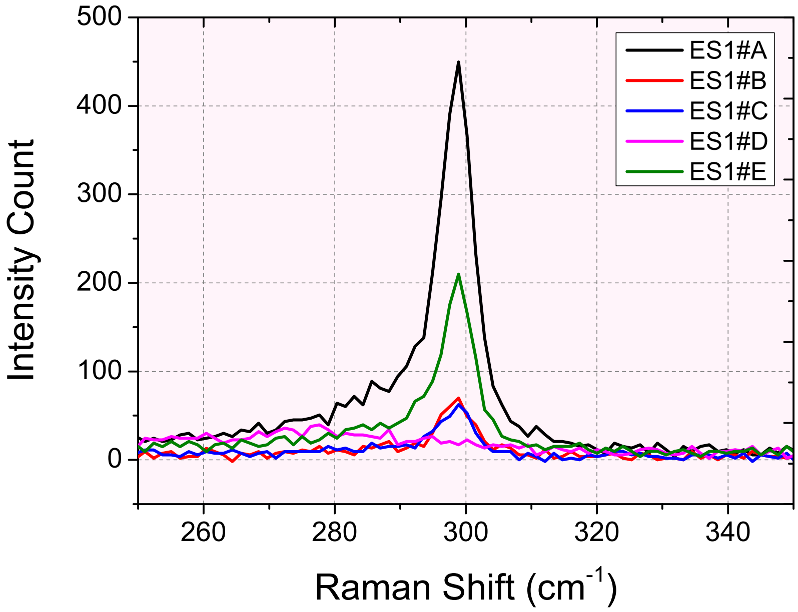

FIGURE 7.2: The Raman data of the initial Ge samples deposited on glass. These curves are generated at laser excitation wavelength of 532 nm

peak at 300 cm^{-1}, which means that these layers are either crystalline or some Ge poly-crystal phase is present in each layer. However, the intensity of crystal peaks varies with deposition parameters. The sample deposited with lower Germane to H_2 ratio has no Ge crystal peak. This sample appears amorphous in nature. The samples with 0.1 Germane to H_2 ratio shows a promising peak with variations caused by RF power. These initial depositions have at least determined the starting points for more detailed studies in the next phase both the RF power and the gas flow rates are studied.

7.2 RF Power

The deposition of Ge films with different RF power are investigated. The deposition parameters of the Ge film with RF power variations are listed in Table 7.2.

Table 7.2: The deposition parameters for Ge layers processed with different RF powers via PECVD with film thickness and optical bandgap. The 250 °C substrate temperature, 1000 mT chamber pressure and 450 sccm of argon flow kept constant, while RF power, germane and hydrogen flow varied.

RF Power (W)	GeH_4 flow (sccm)	H_2 flow (sccm)	Thickness (nm)	Bandgap (eV)
50	5	50/100	100/94	1.09/1.24
100	5	50/100	97/97	1.13/1.09
150	5	50/100	94/92	1.09/1.07
200	5	50/100	87/91	1.07/1.04

As the deposition time is same for all layers, RF power dependent thickness variations are present in film thickness. The higher RF power leads to thinner film deposition. This may be related to a high energetic plasma, in which attachment process of reactive particles to the underlying layer has been reduced as a result of high energetic collisions. With these deposition conditions, there is no significant variation in the bandgap of Ge film. This situation has repeated when H_2 flow has been increased from 50 sccm to 100 sccm.

The absorption coefficient curves of these Ge films are shown in Figure Figure 7.3 which are calculated from extinction coefficient (k), obtained from ellipsometric characterisation using the fitting oscillator model.

This data suggests that RF power has no significant effect on the absorption coefficient from 300 nm to 950 nm. However, at longer wavelengths (950 nm to 1200 nm), the absorption coefficient is narrowly higher for films deposited at higher RF power . On the other hand, H_2 variations from 50 sccm to 100 sccm do not contribute any significant changes in absorption coefficient curves.

Raman spectroscopy of Ge films deposited under various RF powers has been performed and spectra are shown in Figure 7.5. For both 50 sccm and 100 sccm of H_2flow, a

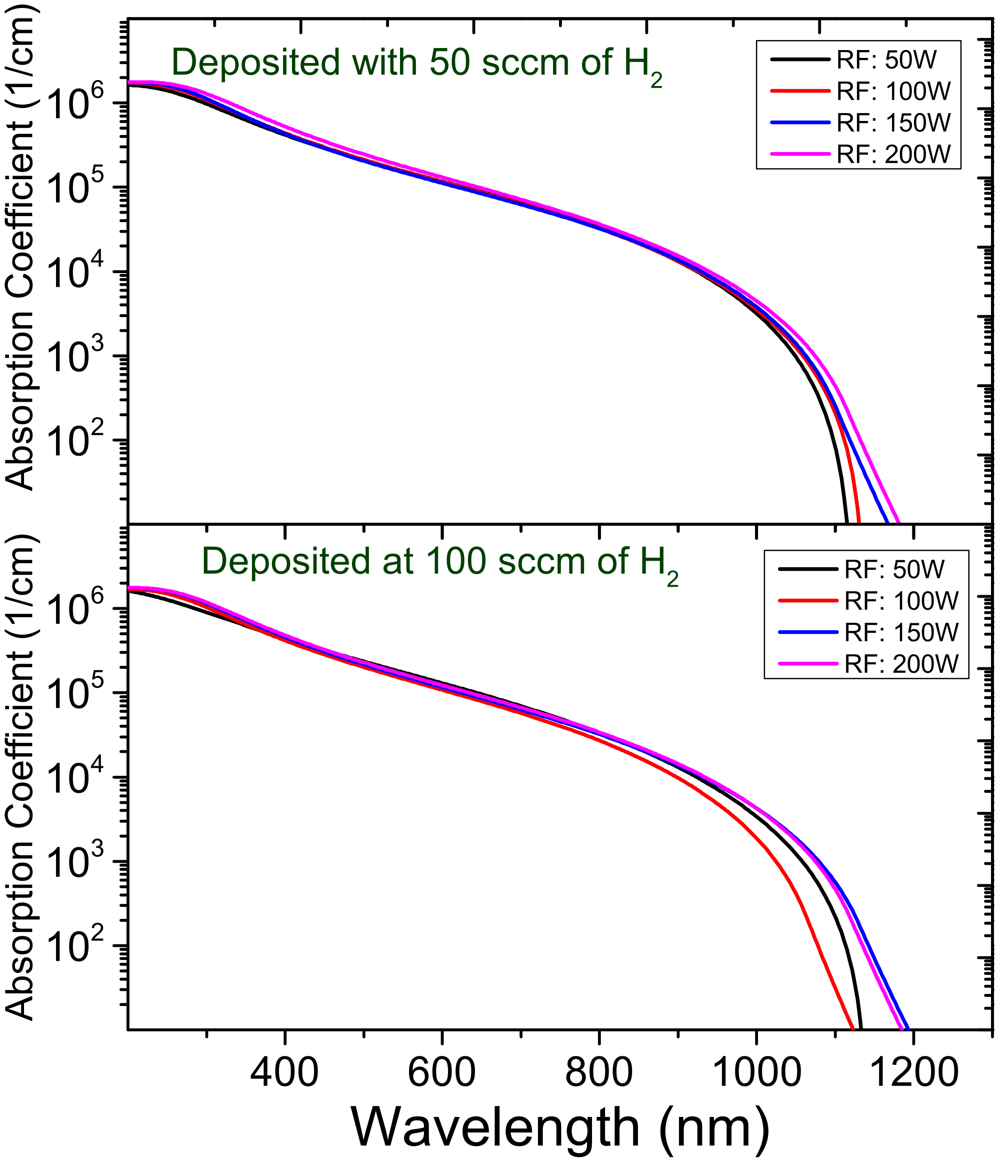

FIGURE 7.3: The absorption coefficient curves of Ge films deposited at different RF power. The curves are calculated from values of extinction coefficient (k), which are obtained from ellipsometric data.

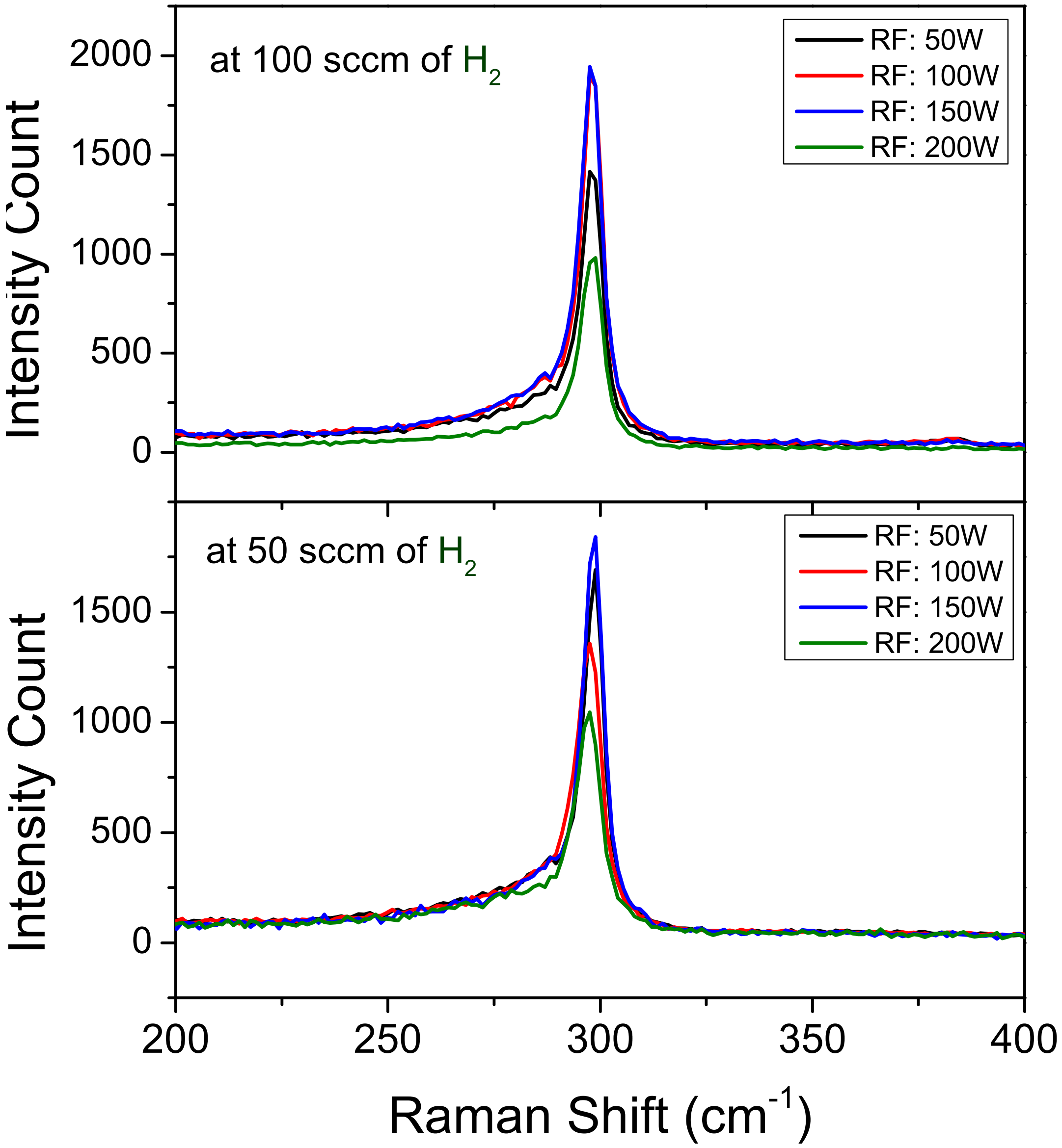

FIGURE 7.4: The Raman spectra of Ge films deposited on glass under various RF powers. The top part of figure has spectra generated from the films deposited with 100 sccm of H_2, and lower part is from films deposited with 50 sccm of H_2 flow. These curves are generated at laser excitation wavelength of 532 nm.

Raman peak emerges near 300 cm^{-1} at every value of RF power from 50 W to 200 W, which suggests that nature of deposited thin Ge films is highly crystalline. There is no indication of of a sharp peaks at a Raman shift of 280 cm^{-1}. This means that amorphous phase in the deposited Ge film is not strong [30]. However a broad curvature is present in films deposited at lower RF values. This also suggests that, the nature of Ge film can be tuned from amorphous phase to crystalline phase with the usage of higher RF power during film deposition.

The Raman spectra listed in Figure Figure 7.4 are based on as-measured, a comparison of top part and bottom part of the figure suggests that H_2 can only be determined, when comparison is made between films deposited with high flow of H_2 and no H_2 at all. The crystal nature of Ge films is also disc does not strongly contribute to formation of crystallisation in Ge film when H_2 flow changes from 50 sccm to 100 sccm. This also suggests that the effect of H_2 can only be determined, when comparison is made between films deposited with high flow of H_2 and no H_2 at all. The crystal nature of Ge films is also discussed in details later in this chapter.

7.3 Argon Dilution

In PECVD, for Ge deposition, a high dilution of source gas with H_2 flow, enhances the density of atomic H_2 which provides the surface diffusion of film precursors to find energetically favourable sites for the formation of crystalline phase[135,136]. Similarly Argon dilution also plays an important role in the growth of Ge film and its transformation to being crystalline in nature. In this section, two sets of layers are discussed which are grown under various conditions with and without argon Table (7.3)

Table 7.3: The deposition parameters for Ge layers processed with different RF powers with film thickness and optical bandgap. The 250 50 ^{o}C substrate temperature, 1000 mT chamber pressure and H_2 flow are kept constant, while RF power, germane and argon flow varied in two sets of experiments.

RF Power (W)	GeH_4 flow (sccm)	H_2 flow (sccm)	Ar flow (sccm)	Thickness (nm)	Bandgap (eV)
50	5	100	450/0	93/100	1.09/0.94
100	5	100	450/0	91/118	0.98/0.92
150	5	100	450/0	99/137	0.94/0.89
200	5	100	450/0	92/174	1.02/0.86

The table 7.3 shows that, when Ar is present in the chamber, the deposition rate of the film does not change with high RF power, but by removing Ar, the deposition rate increases with high RF power. This shift can be attributed to presence of Ar when the RF power is consumed by Ar itself for the excitation to higher states[137]. The other major impact of Ar on Ge film is the bandgap. It is seems that the bandgap of Ge film can be tuned by RF power in the absence of Ar during deposition. The absorption coefficient curves are calculated from values of extinction coefficient (k), which are obtained from ellipsometric data

Raman spectroscopy reveals that these specific Ge films deposited with Ar have a higher crystalline nature as compared with Ge film deposited with no Ar. But on the other hand it is seems that the absorption coefficients of Ge films deposited without Ar are higher in the longer wavelength region. The Raman spectra of these Ge films are listed in Figure Figure 7.6. Apart from the strong Raman shift peak near 300 ($1/\text{cm}^{-1}$), there are no apparent peaks in the other regions, which suggest that these films are high purity Ge in composition. As-measured intensity count in Raman data suggests that Ar usage during Ge film does give strong peak detection as compared with data of Ge film deposited with no Ar.

7.4 The Thickness of Germanium and Textured Substrate Effect

In this work, optical analysis of the deposited Ge films was carried out by means of spectroscopic ellipsometry whose brief detail is already mentioned in chapter 3. The thickness, bandgap and refractive index were determined by the Cody-Lorentz model[38,138] as discussed in Section 3.2.

In literature, it is found that when Ge films are in amorphous phase, their bandgap decreases with increase in film thickness[138,139] and this thickness dependent bandgap may have been attributed to the influence of the Urbach band tails arising from the amorphous effect[140]. It is also been observed that along with thickness, by tuning medium range order amorphous network structure could vary bandgap of Ge film[139,141,142].

Figure 7.7 shows a modified Mott-Davis model of Ge film for the determination of bandgap[139] In this figure shaded area indicates the region of localized states. E_0 is the gap between the localized states tail of the conduction band and the localized states tail of the valence band, E_{g1} is the gap between extended states of the conduction band and the localized states tail of the valence band. E_{g2} is the gap between extended states of the valence band and the localized states tail of the conduction band, and E_g is the gap between extended states of the conduction and valence band, and this gap actually is the mobility gap while optical band gap is equal to E_{g1} (or E_{g2})[143,144].

It is suggested that E_{g1} and E_{g2} tend to have same value and the normal transitions between localized states are ignored due to their insignificance and it is also concluded that the band gap narrows down with the increment of film thickness in some special thickness region and related to continuous random network of the amorphous film[139,145].

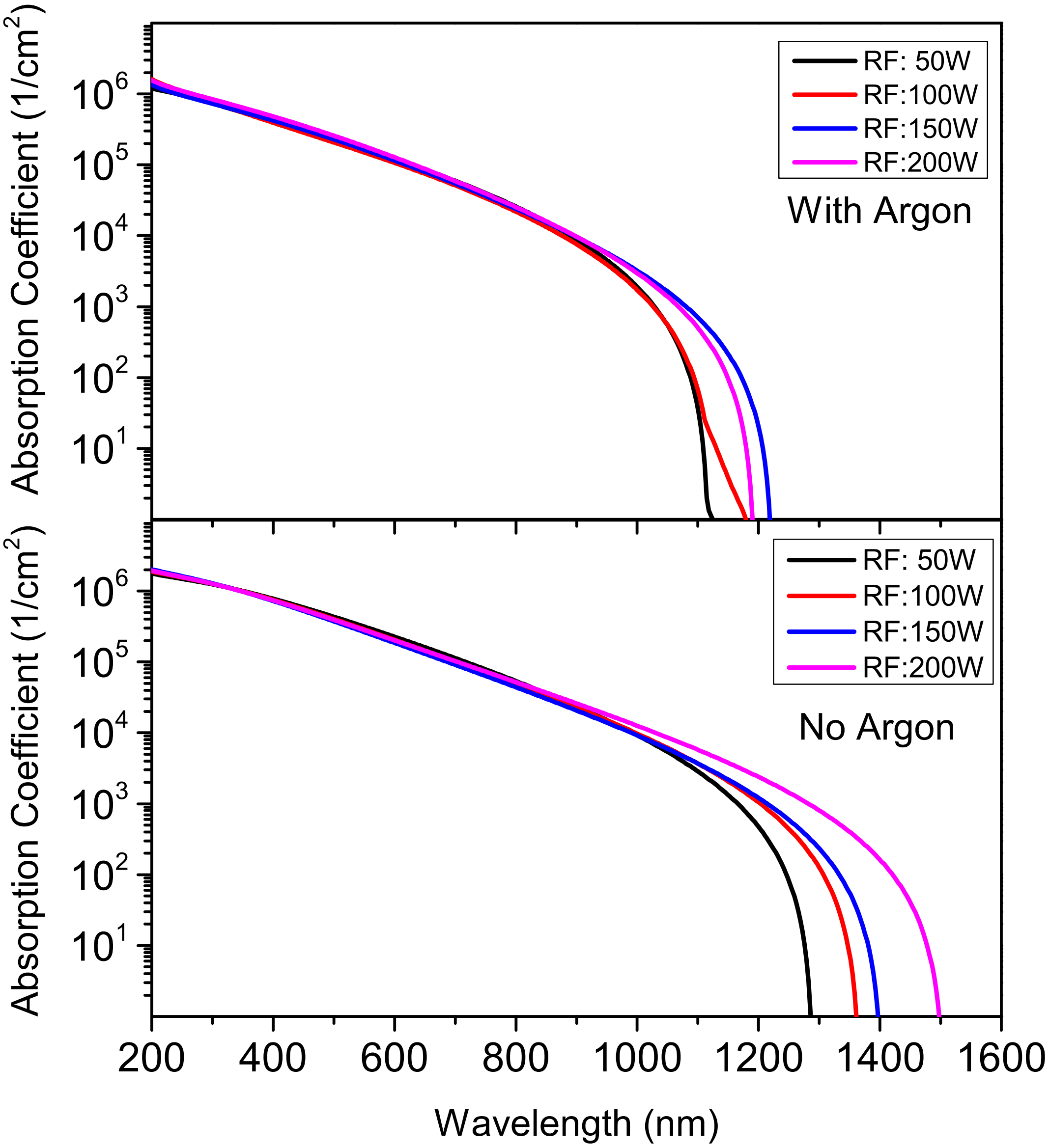

FIGURE 7.5: The absorption coefficient curves of Ge film deposited with RF power variations. The top part of the figure shows the Ge films deposited with Ar and lower bottom part the figure show Ge film deposited with no Ar. The curves are calculated from values of extinction coefficient (k), which are obtained from ellipsometric data.

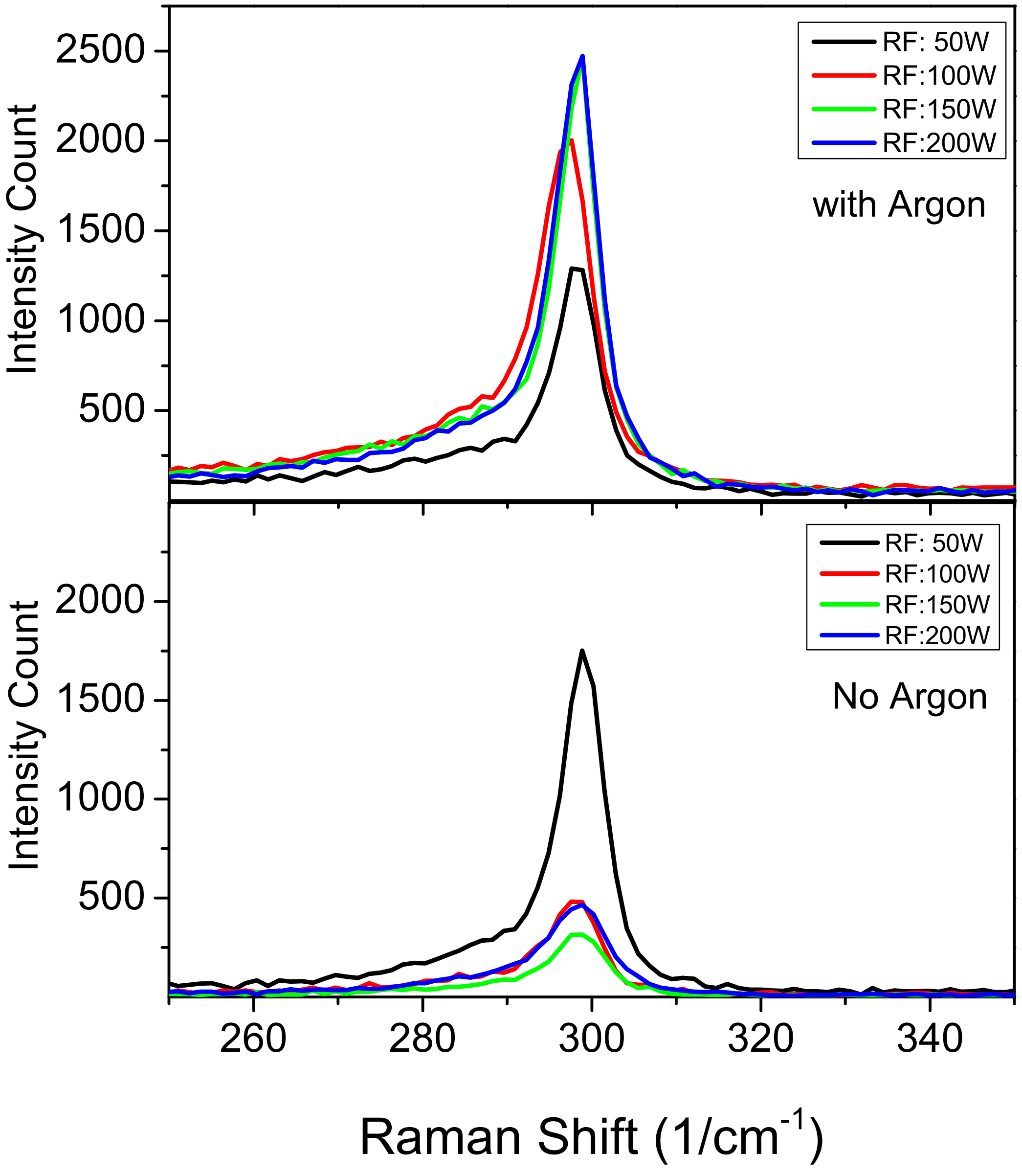

Figure 7.6: The Raman spectra of Ge films deposited on glass under various RF powers. The top part of figure has spectra generated from the films deposited with 450 sccm of Ar, and lower part is from films deposited in no Ar. These curves are generated at laser excitation wavelength of 532 nm.

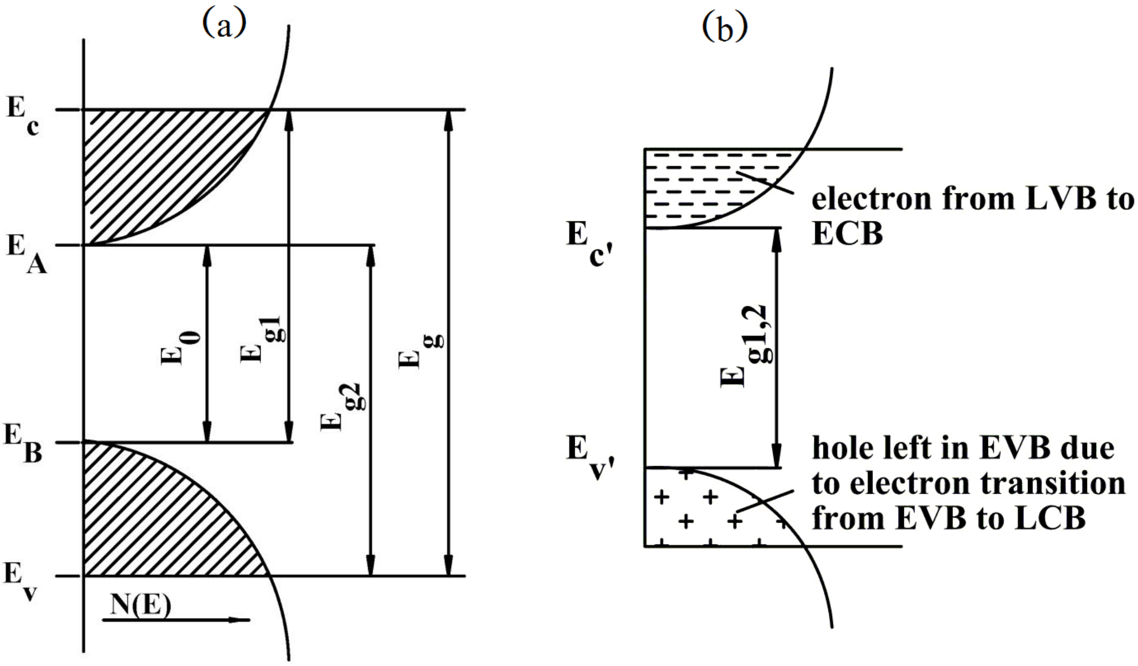

Figure 7.7: (a) Density of states function for amorphous Ge film, (b) Conduction mechanism of amorphous Ge at room temperature
These sketches are reproduced from Mott-Davis models[139].

The Figure 7.7(b) represent that electrons in localized states of the valence band (LVB) can transfer to extended states of the conduction band (ECB) by thermal activation, and electrons in extended states of the valence band (EVB) can transfer to localized states of the conduction band (LCB) by thermal activation[139]. The electrons in ECB and holes in EVB contribute most to the conduction of a-Ge films and the contribution of holes in LVB and electrons in LCB to the electrical conduction is ignored due to their very low mobilities[146].

The optical data obtained from the spectroscopic ellipsometry characterisation verify the thickness dependent bandgap in amorphous phase of the film as mentioned above and this is plotted in Figure 7.8. Table 7.4 shows the deposition parameters and bandgap of Ge films deposited with number of different thicknesses and with and without Ar usage. In the first set, a thin layer of Ge film of 97 nm and another of 650 nm are deposited in the presence of 450 sccm of Ar in the PECVD chamber. The H_2 flow and other parameters are the same. It is found that bandgap of the thin film is higher than the thicker film. Then same set of experiments are repeated without Ar and similar results are found in terms of the bandgap of the film.

A clear trend in terms of the bandgap of Ge in the film thickness has been verified in the presence or absence of Ar gas during deposition. For thin Ge films, Raman spectroscopy suggests that deposited films are purely Ge in nature. It is possible that structural nature of thin films are somehow different from thick films regardless of same deposition parameters. This data also suggests that, in order to obtain optimum Ge with the

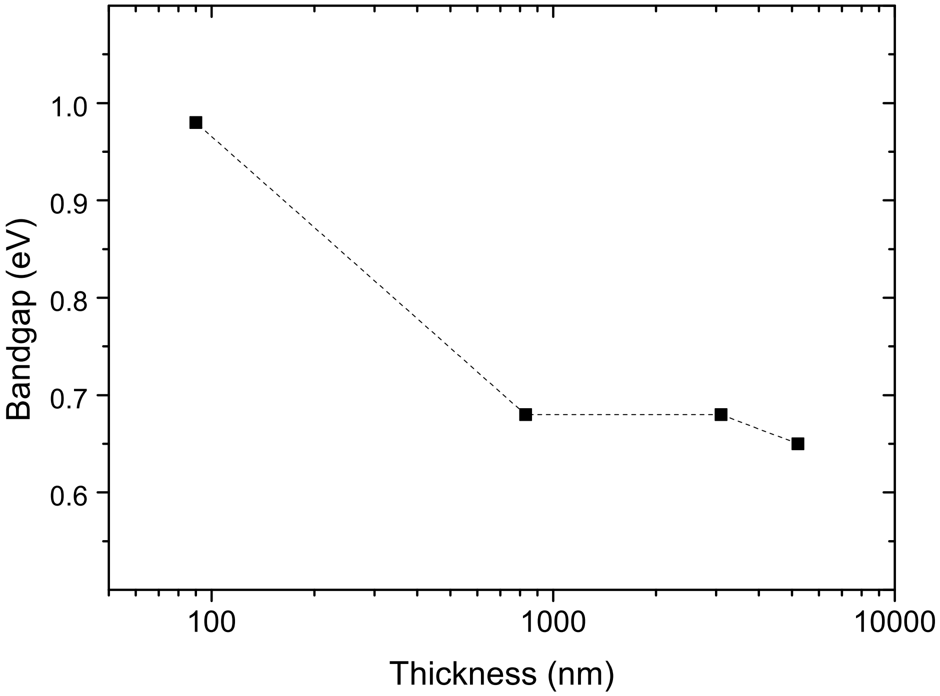

FIGURE 7.8: Band gaps of the Ge layers deposited with PECVD with various thicknesses obtained from spectroscopic ellipsometry.

TABLE 7.4: The deposition parameters for Ge layers deposited by PECVD with film different thickness and optical bandgap. Some layers are deposited without Ar and some with 450 sccm of Ar. The other fixed deposition parameters are, 250 ^{o}C substrate temperature, 500 mT chamber pressure. The RF power, germane and hydrogen flow varied and listed accordingly.

	Thickness (nm)	**RF Power** (W)	**GeH$_4$ flow** (sccm)	**H$_2$ flow** (sccm)	**Bandgap** (eV)
With Argon	97 650	100 100	5 5	100 100	1.09 0.75
No Argon	91 833	100 100	5 5	100 100	0.98 0.68
Thick layer	3100	100	5	100	0.69
Very Thick layer	5200	100	5	100	0.65
High RF	640	150	5	100	0.67

optimum bandgap, it is necessary to deposit a film at least in the range of couple of hundreds of nm in terms of thickness.

The absorption coefficient curves of these Ge films with different thicknesses are shown in Figure 7.9. One can immediately notice that the absorption coefficient for thick film is significantly higher than thin films in both cases. The other major difference is the improvement on absorption coefficient of Ge film when deposited without Ar gas. It seems that Ar gas may be beneficial in terms of getting higher deposition rates and good crystal structure, but somehow Ar also reduces the optical absorption capability in the Ge film.

The absorption coefficient curves of these Ge films with different thicknesses are shown in Figure 7.9 in which the top part of the figure shows the Ge films deposited with 97 nm and 650 nm of thickness in the presence of 450 sccm of Ar. The bottom part of the figure shows Ge films deposited with 91 nm and 833 nm thickness with no Ar presence in the chamber. One can immediately notice that the absorption coefficient for thick film is significantly higher than thin films in both cases. The other major difference is the improvement on absorption coefficient of Ge film when deposited without Ar gas. Its seems that Ar gas may be beneficial in terms of getting higher deposition rates and good crystal structure, but somehow Ar also reduces the optical absorption capability in the Ge film.

When the deposition time and thickness of Ge film increases from 800 nm to 3100 nm or to 5500 nm, there is no apparent change in the bandgap of the material as shown in table (7.4). The absorption coefficient of Ge film also seems to be least varying during film thickness change as shown in Figure Figure 7.10. In accordance with our earlier observation, one can conclude that after reaching the minimal film thickness, the absorption coefficient of Ge films remains unchanged with film thickness increases provided that other deposition parameters remained unchanged. The optical characterisation of Ge films shows that minimal film thickness lie between 100 nm and 500 nm.

As seen in chapter 6 the optical absorption in thin films can be enhanced by using a textured TCO. Ge films have also show a similar response as shown in Figure 7.11. The planar glass, a medium textured Asahi-U and highly textured ZnO substrates deposited with 3100 nm and 5200 nm Ge films are produced with identical process parameters. Optical absorption curves have been calculated from transmittance and reflectance intensities.

The lower part of the Figure 7.11 shows 3100 nm Ge film, in which strong interference in optical absorption in the longer wavelength region can be noticed. The Ge film deposited on a higher textured ZnO surface shows virtually zero interference and strong absorption, as a direct result of the textured TCO. When the thickness of Ge film is increased to over 5000 nm, the textured substrate effect becomes less significant as shown in top part of Figure 7.11. This suggests that textured substrate effect is only beneficial within

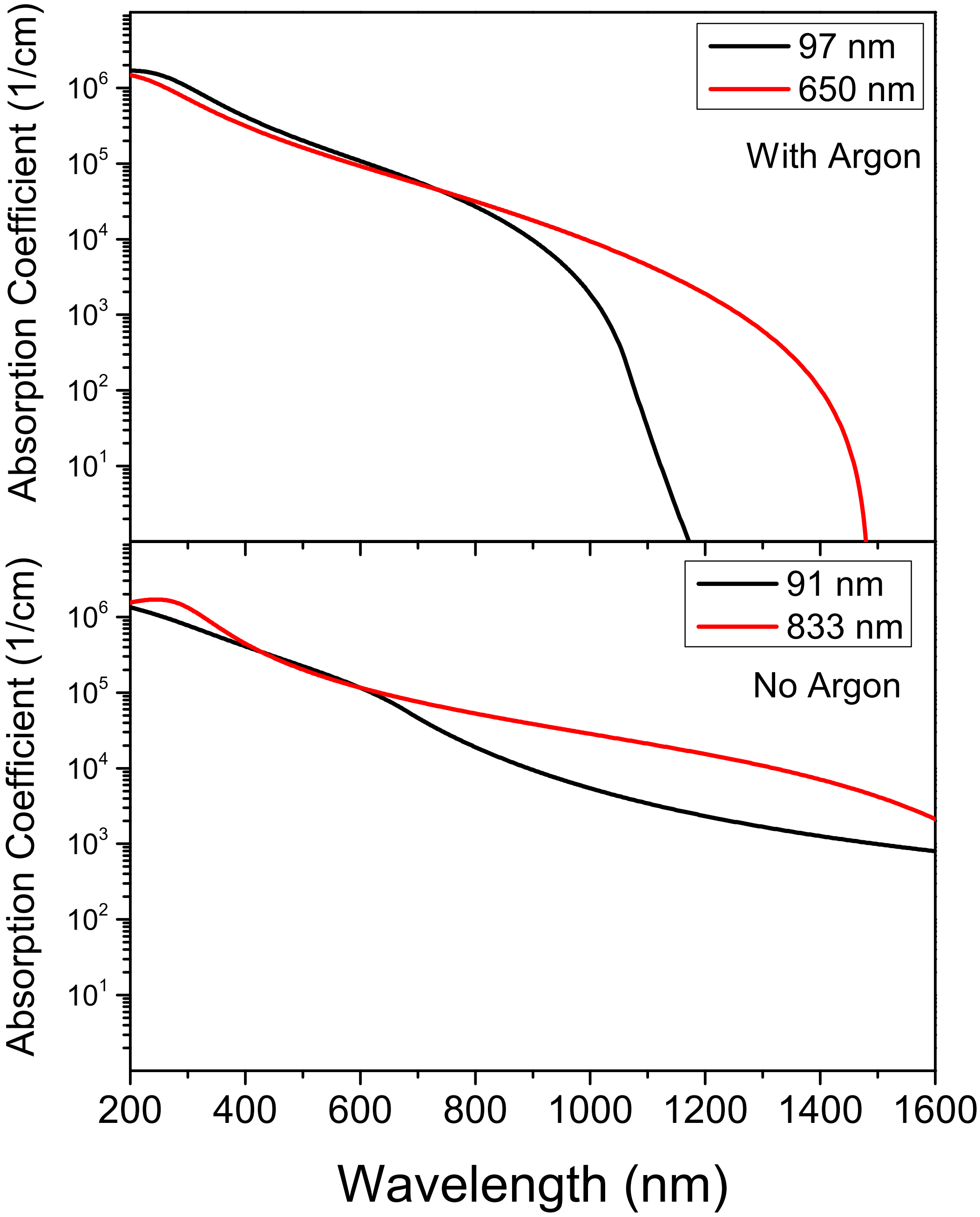

FIGURE 7.9: The absorption coefficients of Ge films with different thickness with and without Ar. These data are calculated from values of extinction coefficient (k), which are obtained from ellipsometric data.

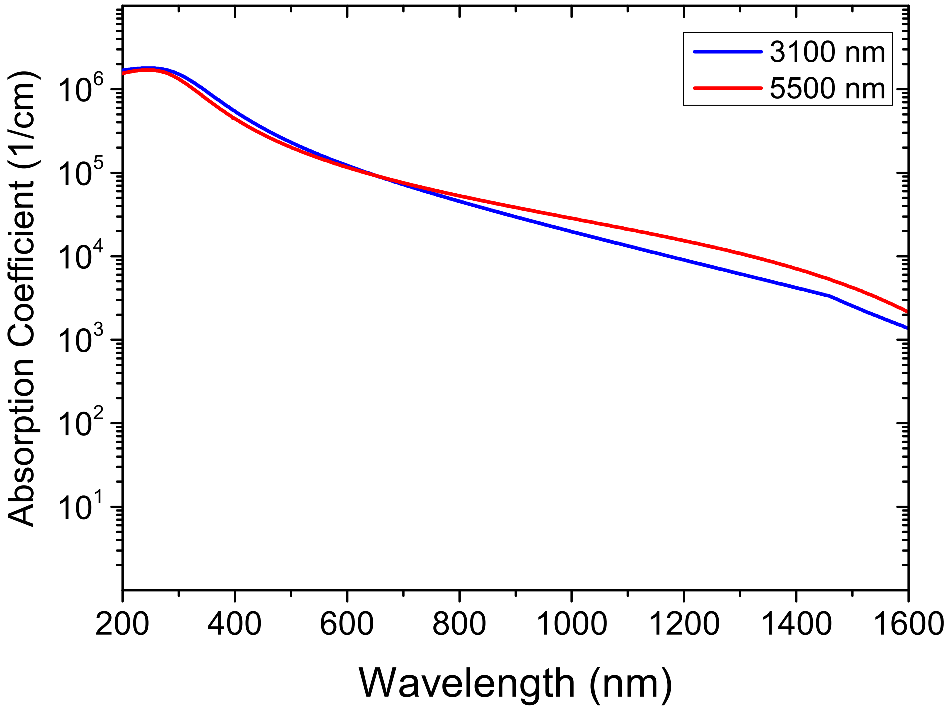

Figure 7.10: The absorption coefficient of Ge films with two different thicknesses. These curves are calculated from values of extinction coefficient (k), which are obtained from ellipsometric data.

certain range of film thickness. When Ge film is in the medium thickness range, a highly textured surface can enhance the optical absorption up to 30% or more. Similar optical absorption in two entirely different Ge films in terms of thickness suggests that textured surface is very beneficial in terms of cost and energy as PECVD deposition of Ge layer is very slow. Thus similar performance can be obtained by using half of thickness just by using highly textured surface.

7.5 Crystallinity in Germanium

The crystal fraction in the Ge films is determined from Raman spectra. As we have seen in this chapter that every Raman data has a sharp peak at determined near 300 cm^{-1} Raman shift indicates the strongest presence of microcrystalline Ge[132,147]. In addition to this, we have also observed that there is no separate sharp Raman peak for the amorphous phase of the Ge at 280 cm^{1} Raman shift, which indicates that deposited Ge films are highly crystalline in nature or in mixed crystal phase. There is no indication of the presence of pure amorphous phase as detected by Raman spectroscopy. To determine the crystal percentage in the Ge film, a representative set of Raman spectra are fitted with Gaussian fitting method near 300 cm^{-1} and 290 cm^{-1}[137,148,149].

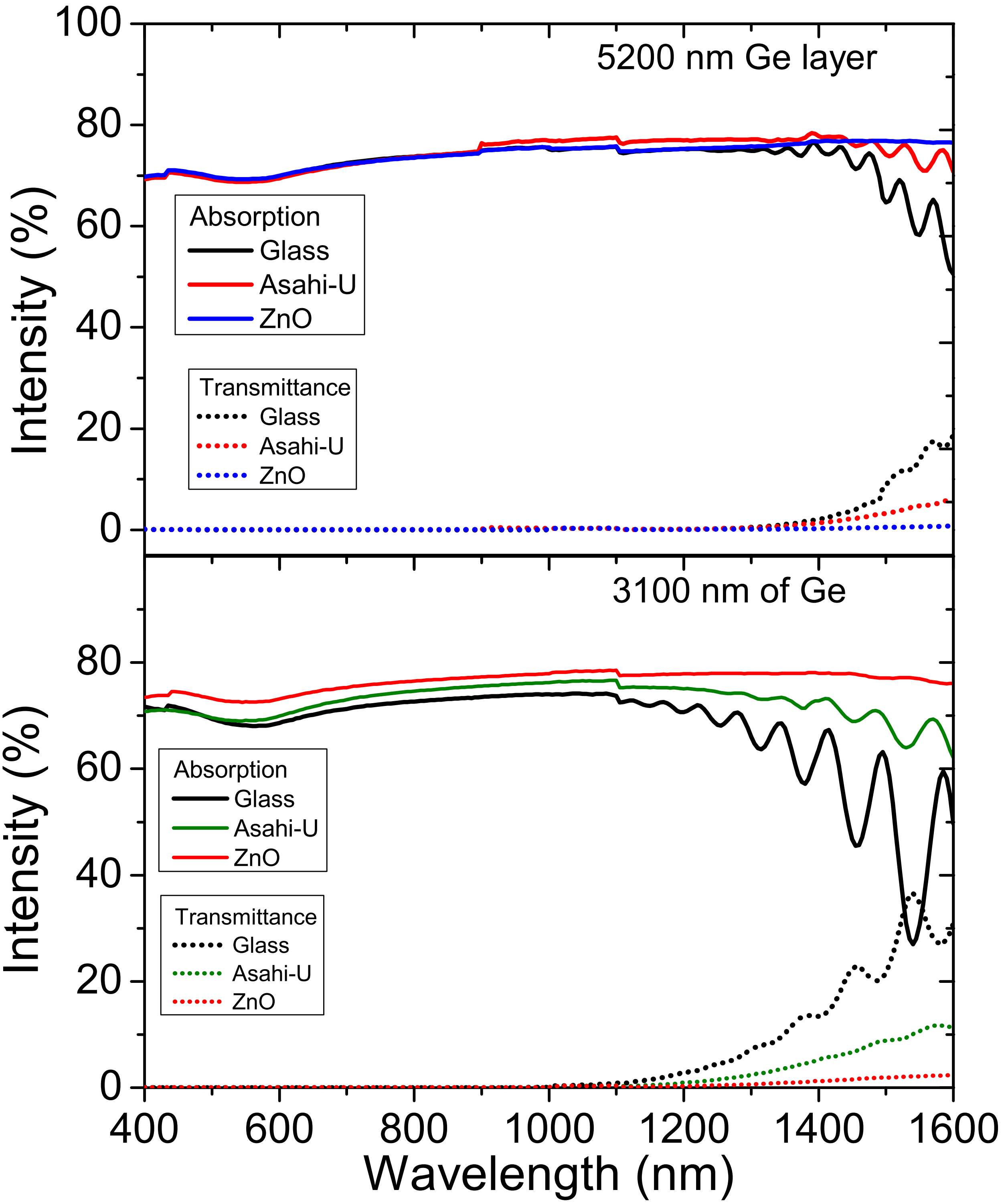

FIGURE 7.11: The optical absorption and transmittance intensity of Ge films deposited on plane glass, and textured substrates Asahi-U and ZnO with two different thicknesses.

To determine crystal fraction, one pair of films deposited at RF power of 150W are selected which is mentioned in Figure 7.4 fitted with Gaussian method shown in Figure 7.12. The top part of the figure has Ge film deposited with 50 sccm of H_2 and bottom part of the figure is Ge film deposited with 100 sccm of H_2. In both cases, Peak 1 is fitted at 298 cm^{-1} for pure crystal fraction, Peak 2 is fitted 291 cm^{-1} for mixed poly crystal fraction and Peak 3 is fitted at 240 cm^{-1} to explain the ion damage by source gases.

The degree of crystallinity in the Ge film is estimated by the crystal volume fraction (X_c) from the Raman spectra using the equation 7.1[115]

$$X_c = \frac{I_c}{(I_c + I_a)} \tag{7.1}$$

Where I_c is the combined area of sharp peaks at 298 cm^{-1} and 291 cm^{-1} and I_a is the area of broad peak at cm^{-1}. By using this formula, the crystal volume fraction of 46.54% is found in the Ge film deposited with 50 sccm H_2 and 46.63% in the Ge film deposited with 100 sccm H_2. This identical crystal volume fraction on both Ge films verify our earlier understanding that properties of Ge do not change when process flow of H_2 is changed from 50 sccm to 100 sccm.

To investigate the effect of Ar on the crystallinity of Ge film, one pair of films are selected from the experimental set listed in Figure 7.6. One of the Ge film deposited with Ar at RF power of 50 W and other deposited with Ar at 50 W. The Gaussian fitting method has been fitted at Peak 1 on 298 cm^{-1} for pure crystal fraction, Peak 2 is fitted 291 cm^{-1} for mixed poly crystal fraction and Peak 3 is fitted at 240 cm^{-1} to explain the ion damage by source gases as shown in Figure 7.13. The crystal volume fraction in Ge film deposited with Ar is found at 44% while in Ge film deposited without Ar is found 57.64%. This big change in crystal fraction with Ar flow actually verifies our understanding described in section 7.3. The strong presence of Ar during Ge film deposition actually prevents Ge becoming more crystalline in nature. This may be due to fact that in the presence of Ar, most of RF power is consumed by Ar itself for the excitation to higher states and this could influence the environment of H2 bonging as well as ionic radicals[137].

The Gaussian fitting method is also fitted on thick Ge film. The Raman spectra of two thick Ge films Figure 7.14. One Ge film is with 3100 nm and other is 5500 nm. As the Raman peak is very strong in 3100 nm film, this spectra is fitted with Gaussian fitting, which is present in the top part of the Figure 7.14. One interesting thing in Gaussian fitting with this Ge film is that, it is fitted in two peaks instead of three as done previously. This time fitting is only done on 298 cm^{-1} for pure crystal fraction, Peak 2 is fitted 291 cm^{-1} for mixed poly crystal fraction. This means that when thickness of Ge tends to increase in couple of thousands of nm, the whole film transformed into

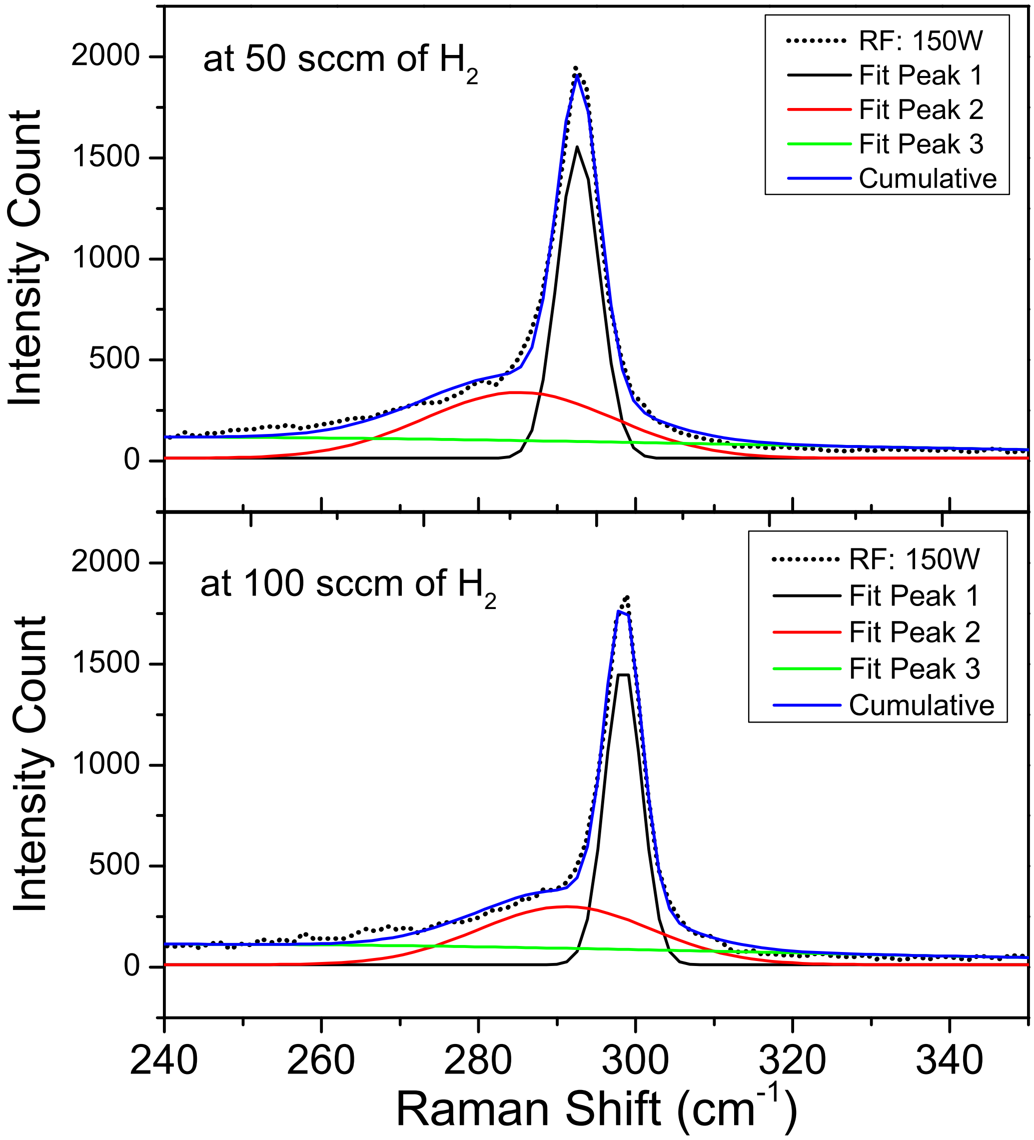

FIGURE 7.12: The Gaussian fitting of Raman spectra of Ge films deposited at 50 sccm of H_2 (top) and 100 sccm of H_2 (bottom). Peak 1 is fitted at 298 cm^{-1} for pure crystal fraction, Peak 2 is fitted 291 cm^{-1} for mixed poly crystal fraction and Peak 3 is fitted at 240 cm^{-1} to explain the ion damage by source gases.

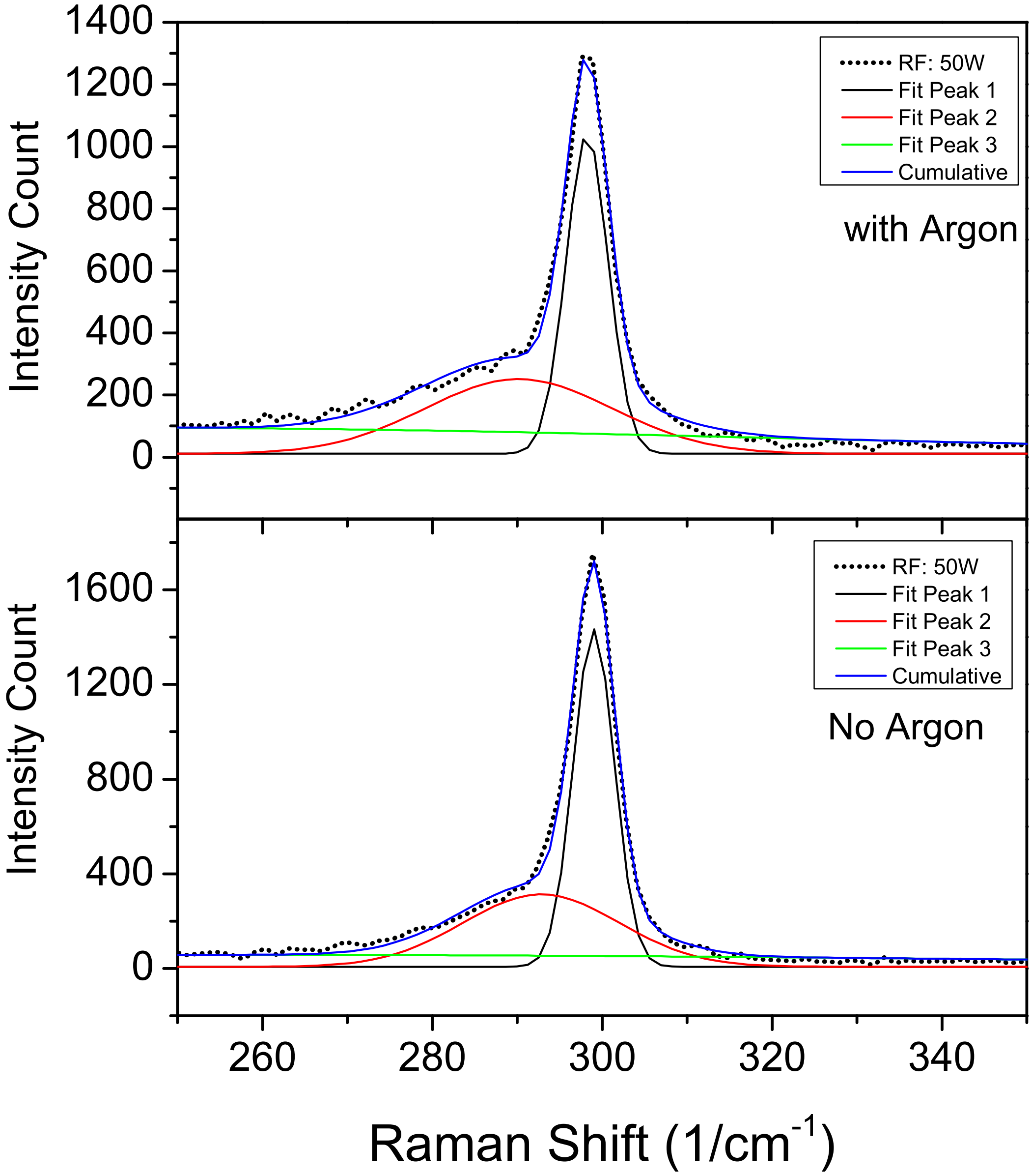

FIGURE 7.13: The Gaussian fitting of Raman spectra of Ge films deposited at 450 sccm of argon (top) and no argon (bottom). Peak 1 is fitted at 298 cm^{-1} for pure crystal fraction, Peak 2 is fitted 291 cm^{-1} for mixed poly crystal fraction and Peak 3 is fitted at 240 cm^{-1} to explain the ion damage by source gases.

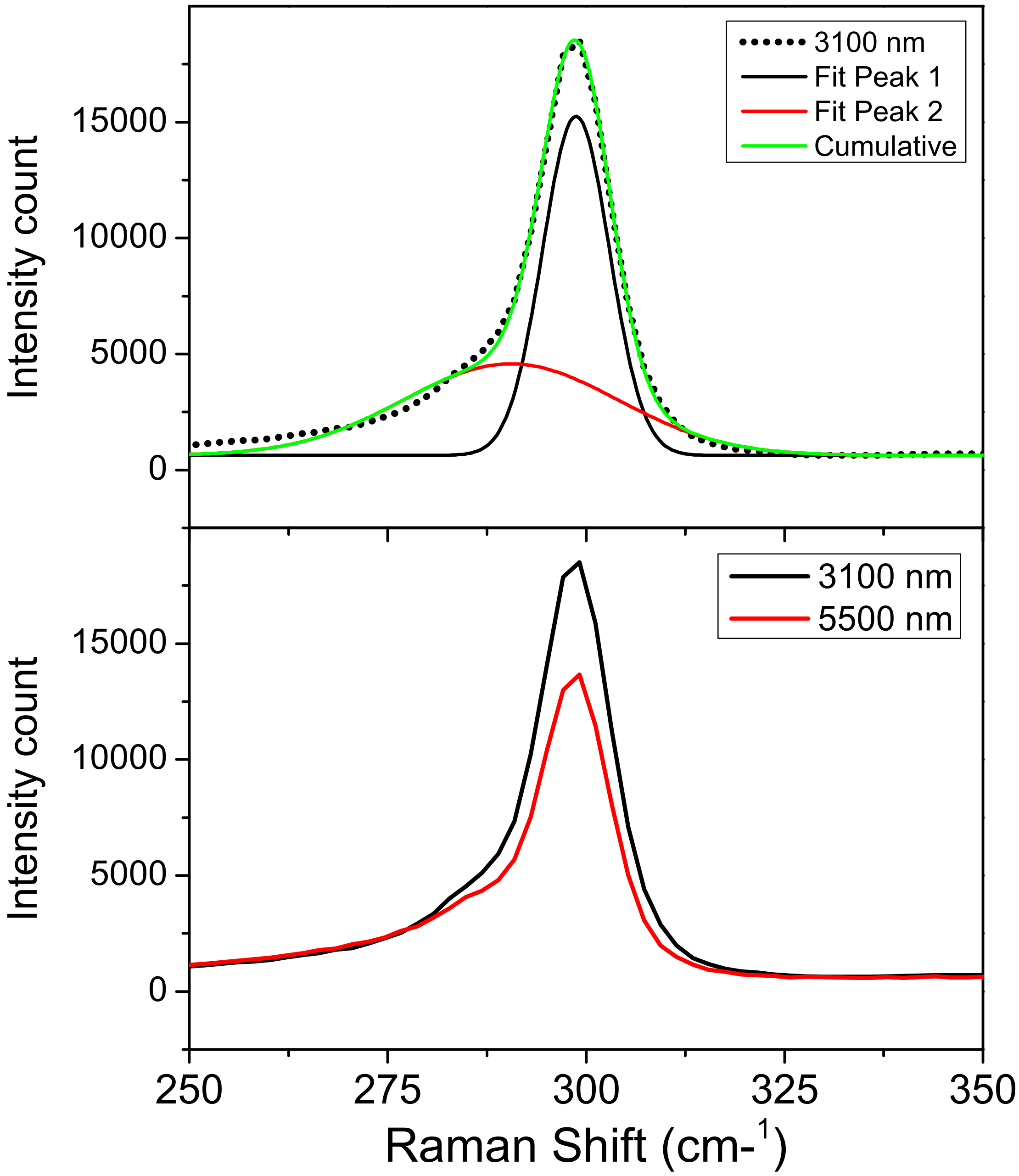

FIGURE 7.14: The bottom part of the figure show the Raman spectra of two Ge film with thickness of 3100 nm and 5500 nm. In the top side of the figure, the Raman spectra of Ge film with 3100 nm thickness is fitted with Gaussian fitting method to determine the crystal volume fraction in the film. Peak 1 is fitted at 298 cm^{-1} for pure crystal fraction, Peak 2 is fitted 291 cm^{-1} for mixed poly crystal fraction

a predominantly poly or microcrystalline phase. We have also seen this thickness effect on the bandgap of Ge film. When Ge film is thin and under 100 nm, the Ge material behaves more like amorphous film in nature. When, Ge film is thicker, its bandgap decreases toward crystalline phase. By using equation 7.1, The volume crystal fraction in 3100 nm thick film is found at 53%. The rest of volume fraction in this Ge film is not amorphous but semi or poly crystal.

Thus we have found that thickness of the Ge film plays vital role in crystal formation along with the absence of Ar. One drawback of not using Ar process gas is the slow deposition of the film which is also a positive point for the commercialization of this economical alternate of poly crystalline Ge deposition.

7.6 Ohmic Contact

Low resistivity Ohmic contacts for n-type and p-type germanium are required for most Ge based devices. The poor solubility and activation of dopant, large diffusion coefficients and the presence of unstable native oxides are the main challenges in Ge contact fabrication[29,150]. In this work, nickel (Ni) has been developed as a basic n-type Ge contact and also tried on p-type Ge film as well. The reason for the selection of Ni is that it possesses a low sheet resistance ,it is also stable at elevated temperatures and it does not easily oxidise, and has electrical resistivity phases that have comparable electrical values to nickel silicides[151,152]. The direct deposition of the Ni has been achieved by high vacuum evaporation at room temperature. In order to determine the appropriate doping concentration, Ge films with a range of different doping profiles have been used for both p-type and n-type Ge. To get the sense of lowest doping profile, one intrinsic Ge film has also been produced. The table 7.5 shows the Ge films onto which 100 nm of Ni has been deposited as Ohmic contact. In these Ge films, sample 1 is un-doped, while the rest of films are doped with phosphine or diborane with three different dopant flow rate.

Table 7.5: The list of the variable deposition parameters for intrinsic and doped Ge film deposited on glass used for Ohmic contact. The constant parameters used are RF power of 100 W, Chamber pressure of 500 mT, Temperature of 250 ^{o}C

Sample	GeH_4 flow (W)	PH_2 flow (sccm)	B_2H_6 flow (sccm)	Thickness (nm)	Film Type
1	05	-	-	50	i
2	05	01	-	47	n
3	05	05	-	49	n
4	05	08	-	49	n
5	05	-	01	34	p
6	05	-	05	52	p
7	05	-	08	60	p

The doping profile of the Ge films have been characterised by room temperature conductivity measurements and the results are listed in table 7.6.

Table 7.6: Room temperature conductivity measurements, and doping concentration of Ge film being used for Ohmic contact characterisation.

Sample	Film Type	Photoconductivity (1/Ω-cm)	Dark Conductivity (1/Ω-cm)
1	i	1.16×10^{-3}	8.79×10^{-4}
2	n	4.0×10^{-1}	3.85×10^{-1}
3	n	1.01	9.85×10^{-1}
4	n	8.48×10^{-1}	8.18×10^{-1}
5	p	9.41×10^{-2}	9.28×10^{-2}
6	p	2.02×10^{-2}	2.02×10^{-2}
7	p	6.75×10^{-4}	6.73×10^{-4}

The undoped sample is here for reference purposes to see the dopant effects both in n-type and p-type. The bulk concentration of undoped Ge film suggests that it is slightly n-type in nature perhaps due to due to oxygen incorporation that commonly occurs in PECVD film deposition[153]. For doped Ge films, three different dopant flows were used:1, 5 and 8 sccm, the effect is rapidly seen in carrier concentration and conductivity values. For n-type Ge, the highest suitable conductivities are found in films deposited with 5 sccm of phosphine, whereas, suitable p-type doping occurred at 1 sccm diborane. The conductivities of undoped, and doped Ge films are plotted in Figure 7.15.

It is observed that saturation in n-type Ge conductivities occurs at between 5 sccm and 8 sccm of phosphine flow. However, in the range tested no saturation of conductivity is observed for the p-type Ge film. When diborane flow increased, there is a reduction in carrier concentration. The photoconductivity and dark conductivity of Ge with heavily doped Ge is very much similar to an undoped sample. This effect may be attributed to the observation that excess boron incorporation degrade the crystallinity of Ge films and leads to general trend of reduction in mobility of free carriers[153,154]. Thus, in terms of conductivity, we have found that two suitable dopant flow ranges for both n-type and p-type Ge films.

To determine the contact resistance between metal and semiconductor as well the sheet resistance of semiconductor Ge film, Transmission Line Measurements (TLM)[155] have been used. For this purpose 5mm x25 mm strips of 100 nm of Ni are deposited on the Ge films as described in table 7.5, in the configuration shown in Figure Figure 7.16.

For TLM measurement, a negative to positive bias is applied to each Ge sample in dark conditions by a Keithley 2400 series source-meter with increasing distance of Ni strips. The output current-voltage curves for each Ge samples are listed in Figure 7.17. It is observed that all IV curves for Ge films are straight lines and each line extrapolates through the origin, which suggests that all Ni contacts are Ohmic in nature.

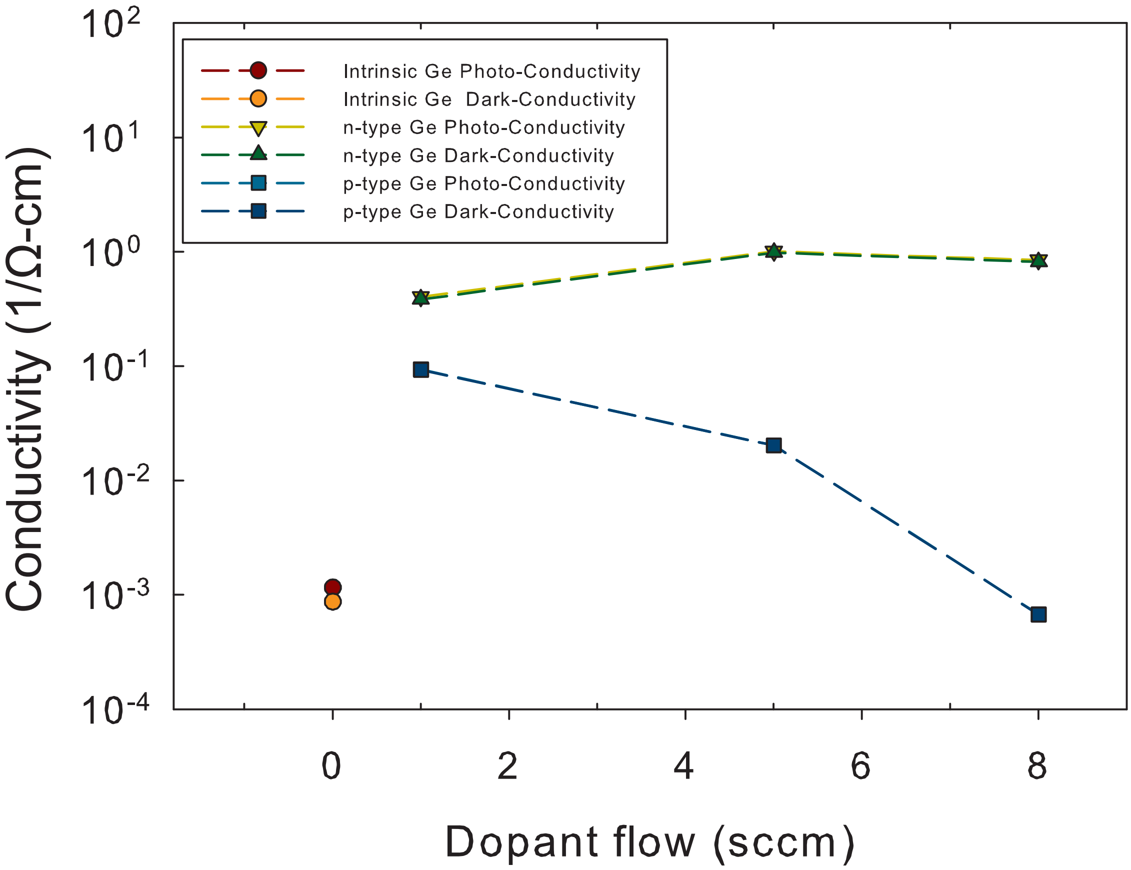

FIGURE 7.15: The room temperature photo and dark conductivities of undoped and Doped Ge film plotted as a function of dopant flow rate.

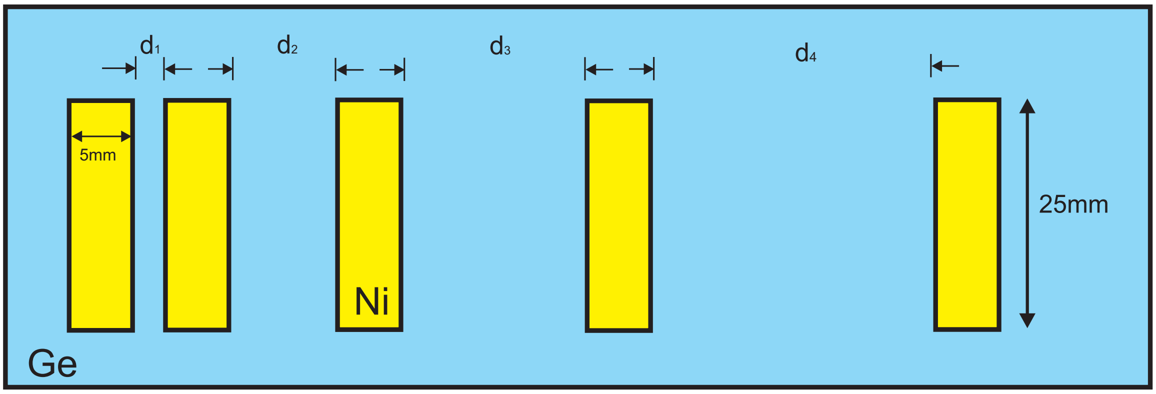

FIGURE 7.16: The schematic sketch of the sample used for Transmission Line Measurement (TLM)

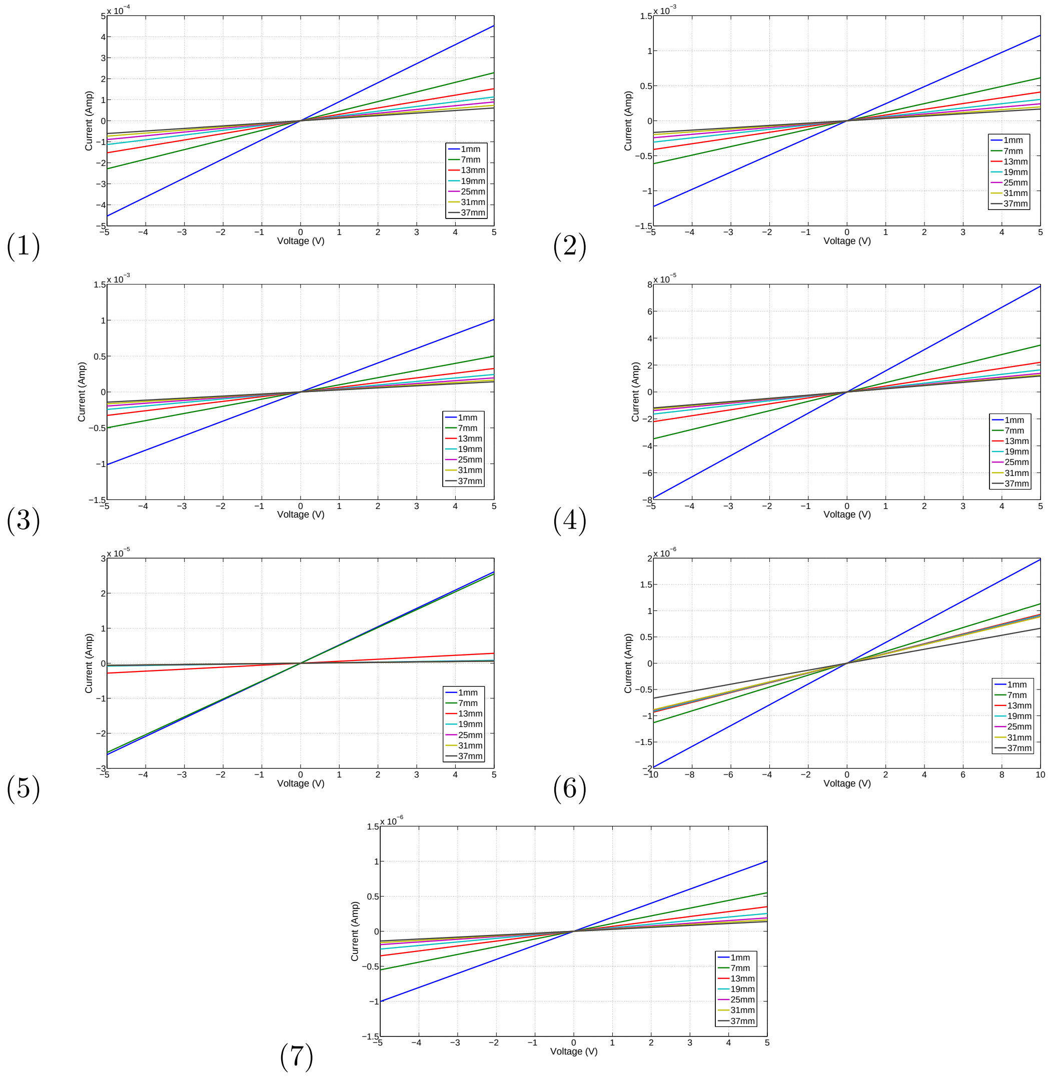

(1) (2) (3) (4) (5) (6) (7)

FIGURE 7.17: The current voltage curves of Ge film to determine the resistance. The figure numbers (1-7) indicate the Ge samples listed in table7.5.

For each Ge film, the reciprocal of the slope of the straight line has been calculated and plotted against each Ni contact strip separation distance where *IV* curve has been generated in order to determine contact resistance Figure 7.18. The sheet resistance (R$_S$ of the Ge material has been determined by the following equation,

$$R_S = \frac{R_C\ W}{L_T} \tag{7.2}$$

Where R$_C$ is contact resistance and L$_T$ is transfer length. Both R$_C$ and L$_T$ are determined from Figure 7.18. To determine the R$_C$ and L$_T$, a trend line has been applied on data points of Figure 7.18. The intersection of trend line with vertical axis will give the value of 2R$_C$ and intersection of the trend line with horizontal axis would give the value of 2L$_T$.

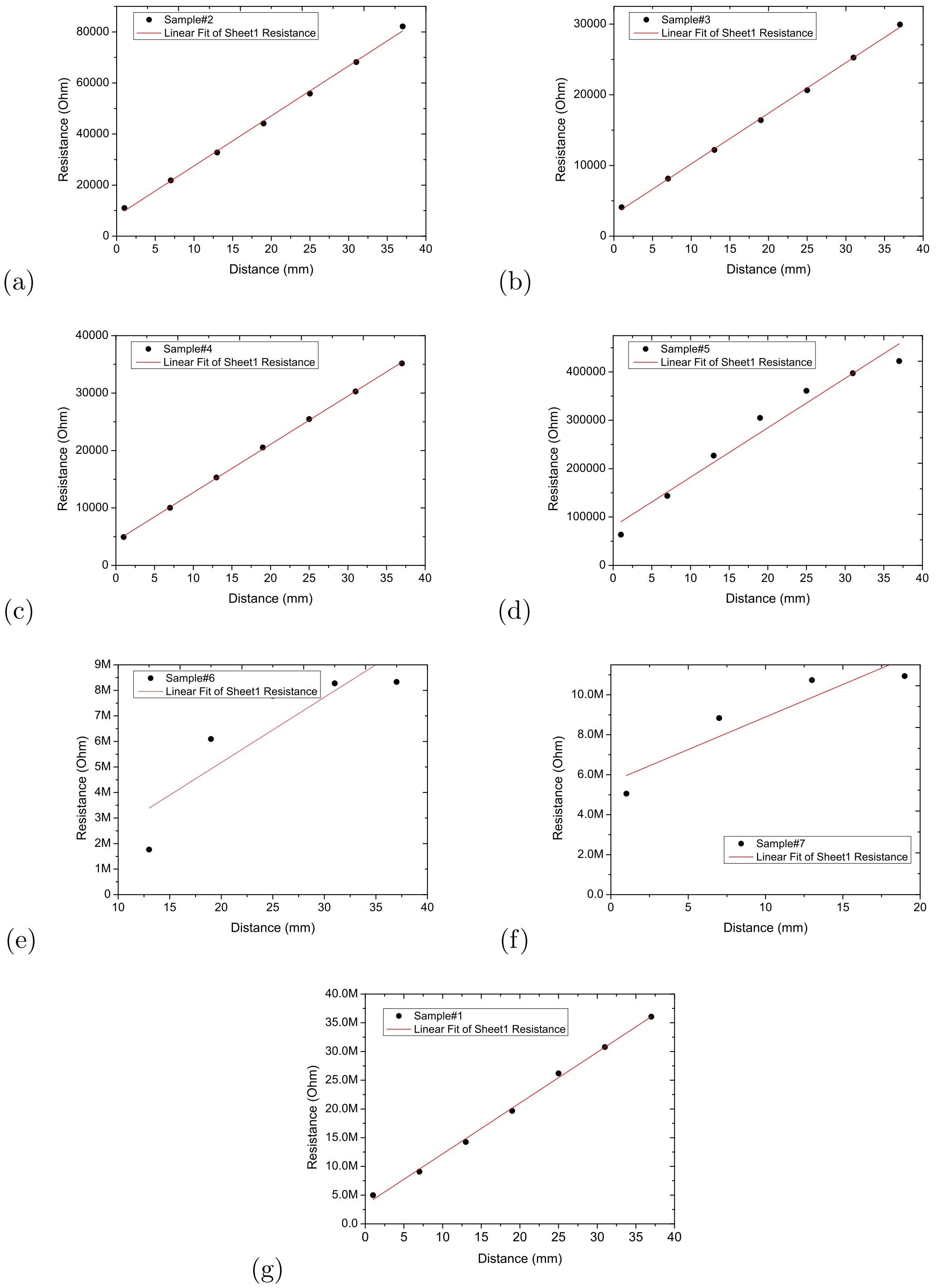

Figure 7.18: The contact resistance of each Ge film plotted against contact separation points, A trend line has applied in order to determine the values of R_C and L_T which are intersection point of trend line at vertical axis and horizontal axis divided by 2 respectively.

The specific contact resistivity (ρ_c) and bulk resistivity (ρ) of Ge-Ni contacts have been determined by the following equations respectively,

$$\rho_c = R_S\ L_T^2 \tag{7.3}$$

$$\rho = R_S\ W \tag{7.4}$$

Where W is Ge film thickness.

Table 7.7: The Ohmic contact parameters of Ge film and Ni layer including sheet resistance (R_S), specific contact resistivity (ρ_c) and bulk resistivity (ρ) listed as pre-annealed and post annealed. The sample were heated at 300 ^{o}C for 60 seconds

	Pre-Anneal			Post Anneal		
Sample	R_S ($\Omega/\Box$)	ρ_c (Ω-cm^2)	ρ (Ω-cm)	R_S ($\Omega/\Box$)	ρ_c (Ω-cm^2)	ρ (Ω-cm)
1	22113475	635924	110	12072175	1164868	60
2	48975	2008	0.2301	37668	2048	0.1770
3	17888	826	0.0876	15294	933	0.0749
4	21025	1352	0.1030	18088	1006	0.0886
5	255575	39198	0.89	296975	23906	1.00971
6	6940575	1139	36	10558575	14630	54.904
7	5260575	10692747	31	7661900	3262898	45.971

With help of figures 7.17, 7.18 and equations 7.2, 7.3 and 7.4, as deposited and measured (pre-annealed) contact properties of Ni-Ge interface are listed in table 7.7. As very thick Ge films have been used for the characterisation of the Ohmic contact, the sheet resistance of the material is expected to be high. For the undoped Ge, layer, the bulk resistivity of the Ni layer is 110 Ω-cm which is low for such thin layer. When 1 sccm of phosphine has been introduced in the layer, the bulk resistivity decreases drastically to 0.23 Ω-cm which is a huge drop in resistance. Further usage of phosphine with 5 sccm flow rate, cause more reduction in bulk resistivity to 0.09 Ω-cm. This is the lowest resistivity, which has been achieved in this group of n-type Ge layer films as more flow of phosphine give rise to increased resistivity. This may have been attributed to the earlier described observation that heavy doping gives rise to deterioration of crystal nature of the film and introduces heavy defects[153,156].

The characterisation of *p*-type Ge films with Ni interface with different doping concentration reveals that relatively good contacts have been formed at lower diborane flow rates of 1 sccm but it is far away from Ohmic contact.. The *n*-type Ge and Ni contact interface parameters (Table 7.7) are found in agreement with conductivity and carrier concentration data (Table 7.6). Its seems that a Ohmic contact with *p*-type Ge can only be achieved if low diborane flows are used during film deposition as excess boron incorporation decreases the mobility and creates more defects in the layers. This also indicates that Ni does not form a good Ohmic contact for p-type Ge films as the trend line on Figure 7.18 (d), (e) and (f) are not straight lines.

This set of 7 Ge films have been annealed at 300 ^{o}C for 60 seconds to check the heat treatment effects on Ge-Ni interface. The results of annealing of n-type Ge films have been plotted in Figure 7.19 and all parameters are also listed in table 7.7.

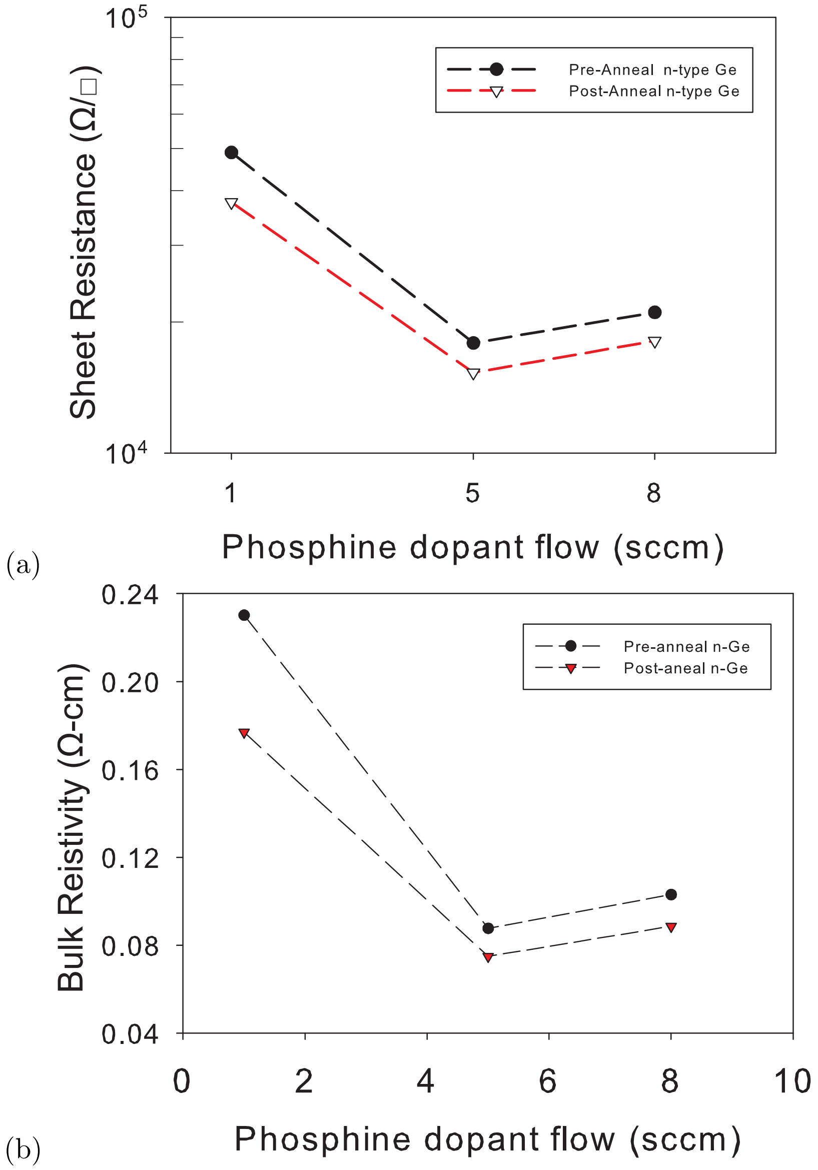

FIGURE 7.19: The sheet resistance (a) and the bulk resistivity (b) of n-type Ge films before anneal and after 60 seconds anneal at 300 ^{o}C.

It has been observed that short annealing of Ge at lower temperature has positive effects on the n-Ge-Ni surface and the sheet resistance and the bulk resistivity have been reported as low after the anneal. The trend of data points for sheet resistance and bulk resistivity before and after anneal are very similar, and this reflects that the anneal is applicable to all ranges of phosphine doping concentration.

TABLE 7.8: The Ohmic contact parameters including Sheet resistance (R_S), specific contact resistivity (ρ_c) and bulk resistivity (ρ) of both n-type and p-type Ge films, with 200 nm of Ni layer deposited and annealed at different temperatures for 60 seconds.

	n-type Ge			p-type Ge		
Sample	R_S ($\Omega/\Box$)	ρ_c (Ω-cm^2)	ρ (Ω-cm)	R_S ($\Omega/\Box$)	ρ_c (Ω-cm^2)	ρ (Ω-cm)
250	3.66×10^3	2.30×10^2	0.03	2.56×10^6	4.55×10^4	36.84
300	3.16×10^3	2.19×10^2	0.03	1.21×10^3	1.60×10^5	0.17
340	3.36×10^3	2.87×10^2	0.03	1.40×10^6	3.26×10^5	20.18
380	1.22×10^4	8.78×10^2	0.11	4.22×10^4	1.08×10^3	0.60

As we know from doping concentration and conductivity measurements n-type Ge deposited at 5 sccm of diborane provides a better n-Ge-Ni interface with lower sheet resistance and bulk resistivity, this layer was chosen to see the further temperature effects. For this purpose, four more n-type Ge layers were deposited with 5 sccm of diborane and annealed at four different temperatures (250 ^{o}C, 300 ^{o}C, 340 ^{o}C and 380 ^{o}C) for 60 seconds. The resistance parameters for n-type Ge are listed in table 7.8. The Ohmic contact parameters; sheet resistance (R_S), specific contact resistivity (ρ_c) and bulk resistivity (ρ) for n-type Ge film with 100 nm Ni are plotted as a function annealed temperature in Figure 7.20.

The temperature based anneal of n-type Ge-Ni interface for Ohmic contact suggests that every contact resistance parameter does change with the anneal temperature and a good Ohmic contact has been found at anneal temperature of 300 ^{o}C. At this point bulk resistivity is 0.03 Ω-cm which is the lowest for any n-Ge film in this work. When n-type Ge-Ni interface is annealed at an elevated temperature for a short time, a new composite material Ni-germanide (NiGe) forms and different temperatures give rise to different orientations of Ge-Ni[157]. The literature suggest that Ni-Ge offers the possibility of a low resistive contact on n-type Ge with low barrier heights[158,159]. In this report, the contact resistance tends to increase with temperature. This may be due to the fact that, in this report only thin layers of n-Ge have been used and in the case of ohmic contact formation there isnt sufficient Ge to form alternative orientations of the Ge-Ni regions.

When the p-type Ge-Ni interface is subjected to 60 seconds of annealing at 300 ^{o}C, the contact resistance parameters increase as compared to the pre-annealed samples. These parameters are listed in table 7.7, while the sheet resistance (R_S) and bulk resistivity (ρ) are plotted in Figure 7.21. The bulk resistivity of p-type Ge-Ni contact has been increased from 0.9 to 1.0 Ω-cm for a Ge film which earlier showed lower resistivity before anneal.

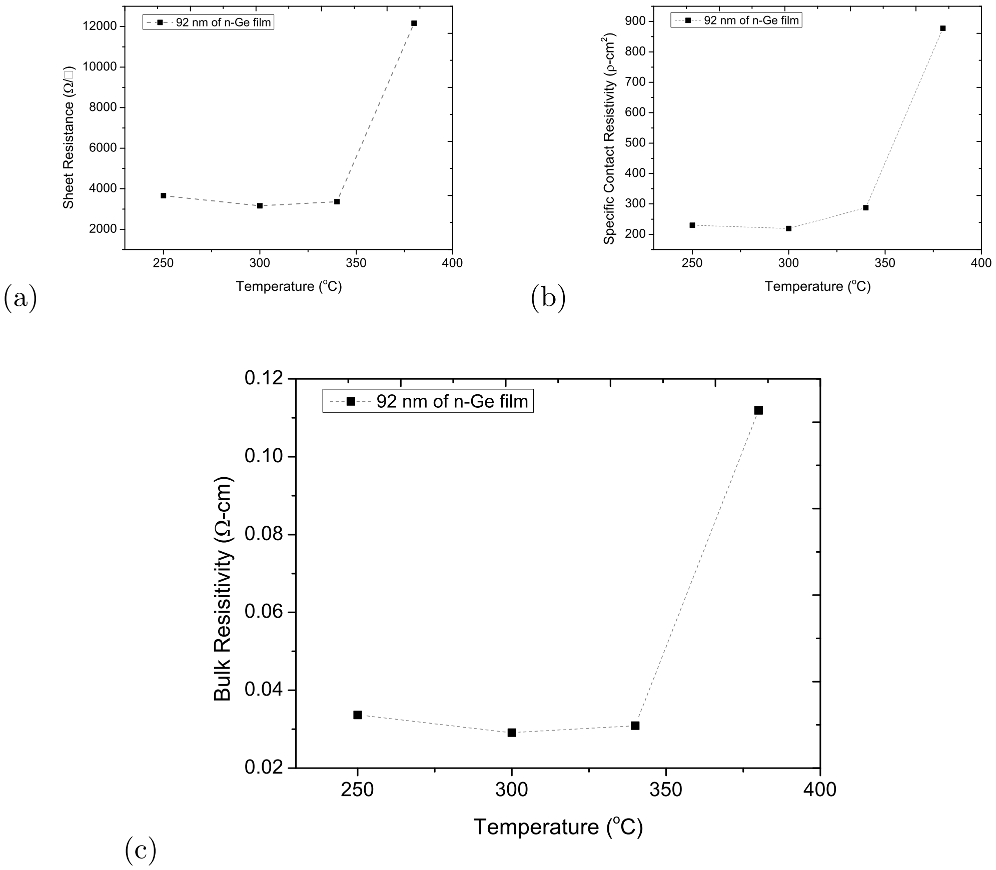

Figure 7.20: [a] The sheet resistance (R_S), [b] specific contact resistivity (ρ_c) and [c] bulk resistivity (ρ) for n-type Ge film with 200 nm Ni plotted as a function anneal temperature.

To fully understand the annealing effect on the p-Ge/Ni interface, four p-type Ge films with 114nm thickness were deposited at 2 sccm of diborane flow using PECVD. High vacuum, electron beam evaporation of Ni metal was carried out after the deposition and then these films were annealed at different temperatures for 60 seconds. The results for all contact parameters are listed in 7.8. Similarly, the sheet resistance (R_S), specific contact resistivity (ρ_c) and bulk resistivity (ρ) for p-type Ge film with 100 nm Ni are plotted as a function annealed temperature in Figure 7.22. It is observed that resistance parameters do vary with anneal temperatures.

Unlike n-Ge-Ni interface, there exist no definite trends in sheet resistance, specific contact resistivity or bulk resistivity p-Ge-Ni. These parameters vary randomly. However in one case, the p-Ge layer annealed at 300^{o}C showed similar contact resistance a found in non-annealed p-Ge sample. P-type Ge-Ni interfaces have similar contact resistance when not annealed or annealed at 300^{o}C. All other annealing at different temperature ranges give rise to increased contact parameters but overall the p-Ge/Ni interface does not behave Ohmic in nature.

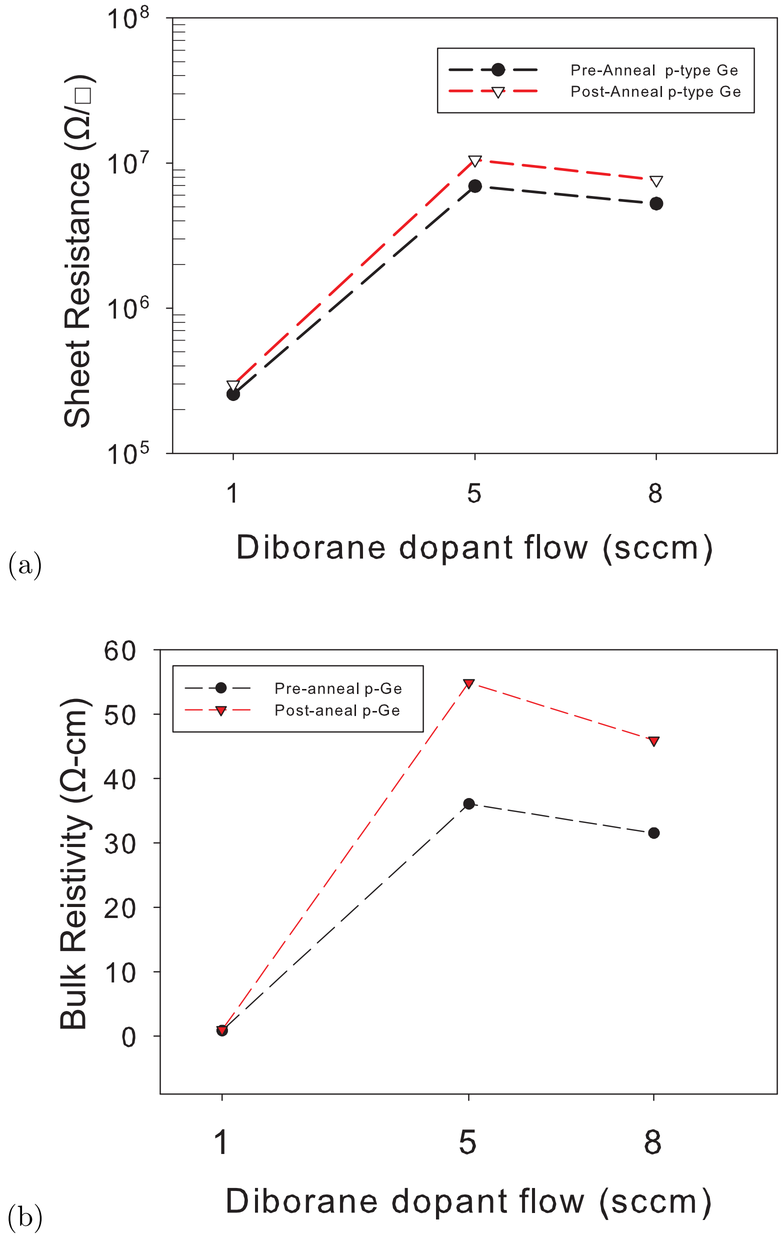

FIGURE 7.21: The sheet resistance (a) and the bulk resistivity (b) of p-type Ge films before anneal and after 60 seconds anneal at 300 ^{o}C.

This annealing behaviour of p-Ge/Ni interface suggest that, when Ni metal is used as p-type Ge Ohmic contact, an annealing step in not beneficial as is was in the n-Ge/Ni case. This observation has also been seen in p-type Ge wafers when subjected to metal contacts as p-Ge/Ni are always Ohmic in nature[28,31,160].

In semiconductor theory, Ohmic contacts or low resistive metal-semiconductor interfaces are based on a general rule of selecting a low work function metal for n-type semiconductors and high work function metal for p-type semiconductors to establish a low barrier

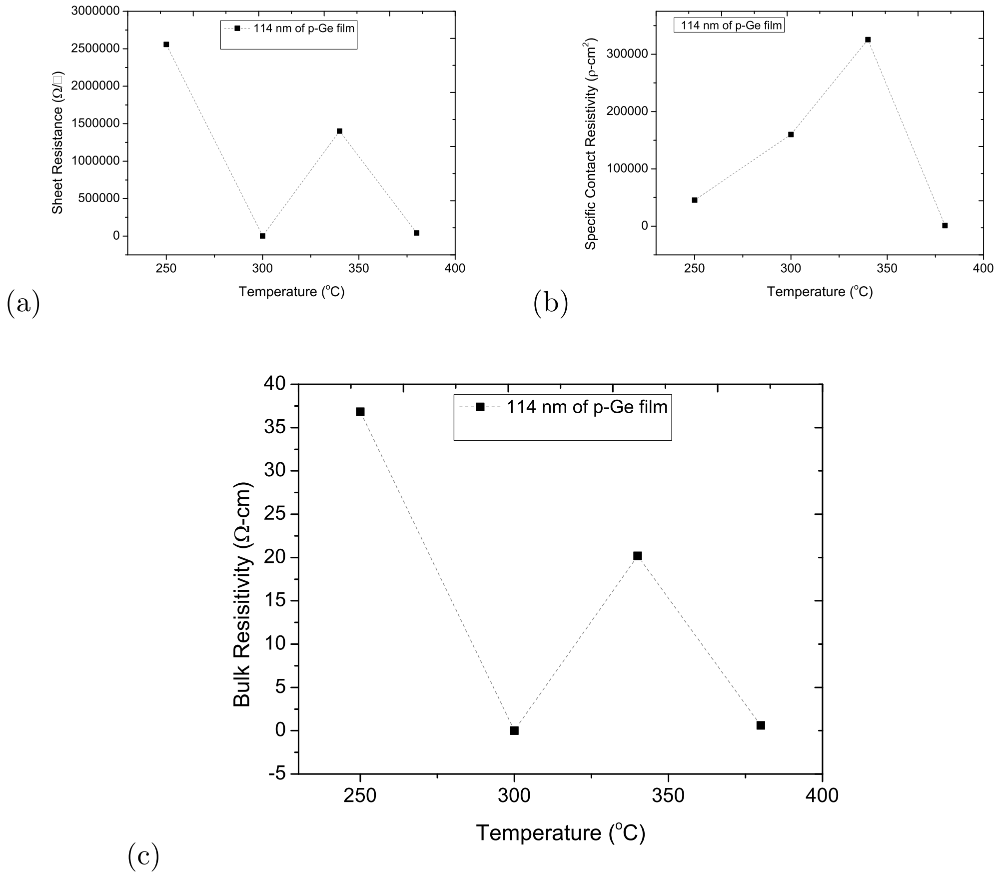

(a) (b) (c)

FIGURE 7.22: [a] The sheet resistance (R_S), [b] specific contact resistivity (ρ_c) and [c] bulk resistivity (ρ) for p-type Ge film with 200 nm Ni plotted as a function of anneal temperature. Scattered data points in each figure are linearly fitted, in order to determine the overall trend of anneal effect, although the samples set are too small to draw strong conclusion.

heights[158]. As we have seen the n-Ge/Ni possesses large contact resistance in its pre-anneal state, which is attributed Fermi level pinning by the interface near the valence band by creating a large Schottky barrier heights which are independents of metal work functions[158,161].

As we noticed above resistivity in metal contact has been reduced by annealing of the n- Ge/Ni interface, which is due to the formation of NiGe film which offers a lower resistivity due to the favourable stoichiometry of nickel germanide[162]. For p-type Ge, the Fermi level pinning of the interface state works the opposite to n-type Ge[158]. Those may be the reason that after annealing of the *p*-Ge/Ni interface, the possible formation of NiGe does not work well with nickel. As a result the pre-annealed state of the *p*-Ge/Ni interface provides the most favourable contact resistance.

Bulk resistivity values listed in Table 7.8 and Table 7.7 can be used to estimate the doping concentration present in Ge films. For this purpose, a mathematical relation is used which was calculated by D. B. Cuttriss[10] which is

$$\rho = \frac{1}{B} N^{-\alpha} \tag{7.5}$$

Where ρ is resistivity, N is impurity concentration, B and α are numerical approximation constant whose values are list in paper[10]. Using this approximation, Concentration in n-type Ge film was calculated and listed in table. These values are only approximation and real values may be larger if calculated directly. This bulk concentration values also depends on goodness of Ohmic contact.

Table 7.9: Bulk concentration values of Ge film derived from constant and approximation values used in D. B. Cuttriss, Bell System Technical Journal[10]

Sample	Resistivity (Ω-cm)	Concentration (cm-3)
1	110	out of range
2	0.23	8.06e15
3	0.08	2.88e16
4	0.10	1.80e15
5	0.89	3.95e15
6	36	4.07e13
7	31	4.73e13

In summary, a new alternate deposition method of microcrystalline germanium has been proposed with the support of experimental results. It has been possible to tune the bandgap of μc-Ge by the variation of deposition parameters such as RF power and gas flow rate. A crystalline Ge film with optical absorption of more than 70% in the 400 to 1600 nm region has been achieved. As the PECVD method is slow for Ge deposition, it takes a longer time to deposit 4 microns of film on glass. The use of a textured substrate has shown promising results of high absorption using thin layers. The doping of the Ge films to fabricate p-type and n-type layers are demonstrated to achieve bulk concentration of 10^{19} cm^{-3}. The successful fabrication of Ohmic contacts on both p-type and n-type Ge have been achieved. The lowest resistivity of 0.0291 Ω-cm for n-type and 0.17 Ω-cm for p-type Ge with the usage of Ni have been achieved.

Although there was insufficient time in this study, we now have all the component processes required to form a Ge-pin photovoltaic cell or photocell with excellent absorption in the communications band.

Chapter 8

Summary of Progress and Suggestions for Future Work

The aim of this work was to explore the capabilities of the OPT plasma 100 RF plasma enhanced chemical vapour deposition (RF-PECVD) system to fabricate device grade layers and devices for thin film photovoltaics and related semiconductor applications. Tuneable intrinsic and doped a-Si:H layers, intrinsic μc-Si:H layers, and microcrystalline Ge layers with intrinsic and n and p-type doping have been successfully fabricated. The deposition process of a-Si:H in this work showed promising deposition rate and excellent uniformity (section4.1.2). The overall film thickness uniformity on substrates such as 5×5 cm, or 100 mm wafer is excellent albeit with some edge effects. The industrial requirement for a-Si:H is for rapid deposition rates ($5\AA/s$)[6], and in this work we have successfully achieved high deposition rate for device grade layers. The controlled deposition parameters makes it possible to fabricate tuneable a-Si:H film with choice of bandgap and refractive index which opens a window for applications in active photonics devices[163].

The optical absorption is also tested for chamber pressure and substrate temperature variations in order to obtain optimised control parameters. The absorption spectra confirmed that intrinsic layers can absorb 90% of the incoming visible spectrum. The room temperature conductivity measurement verified that deposited intrinsic layers are device grade and photoresponse is found in the order 10^3 - 10^4 at different deposition conditions. The dark conductivity of deposited intrinsic layers measured in ranges which have less than $\times\ 10^{-10}\ \Omega^{-1}\text{cm}^{-1}$ requirement. Similarly photoconductivity of deposited intrinsic layer showed range $1 \times 10^{-4}\ \Omega^{-1}\text{cm}^{-1}$ which is higher than the required $1 \times 10^{-5}\ \Omega^{-1}\text{cm}^{-1}$. The p-type and n-type a-Si:H films are found highly doped such as 10^{21} atoms/cm^3 and 10^{22} atoms/cm^3 respectively which are in excellent agreement required for device grade doped layer. The thickness of the doped layers are thin and are cross verified and showed effective control which is essential for device fabrication.

One of the main goal of this work was to fabricate a highly efficient single junction device with respectable efficiency. In this work, maximum efficiency of 8.22% has been achieved and most devices reached more than 5%. Technically it is a reasonable efficiency baseline in terms of simplicity and from there new areas of research can be addressed. The use of plasmonics at different parts of a single junction device require such moderate efficiency so that their effects can be verified and this is also applicable to the use of anti-reflection engineering[164,165].

As we know that light trapping is essential in a-Si:H based solar cells whose main aim is to absorb as much as light as possible and prevent it from escaping from the device. In light trapping, the transparent conducting oxides (TCOs) play a vital role in both super-state and substrate configuration of a-Si:H based devices. In this work, the function of textured TCOs and textured devices have been analysed in detail to find out their working mechanism. This is done by a new technique known as wavelength and angle resolved scattering (WARS) measurements. Along with this, TCO materials and devices are also analysed with Atomic Force Microscopy and optical characterisation to support this new method. We have found wavelength regions where different commercially available textured TCOs offer strong scattering when used in single junction devices.

The baseline deposition parameters of a-Si:H have been extended to deposit μc-Si:H film which has a complex microstructure. The lower bandgap (1.1- 1.2 eV) of c-Si:H makes it possible to use this layer to absorb incoming infrared wavelength spectrum which again open new windows for more applications. As the crystallinity in μc-Si:H depends on the deposition parameters, 34% crystallinity has been achieved which is beneficial for a reduction in light induced degradation.

One of important finding of this work is to use the PECVD tool to its limits to fabricate device grade microcrystalline germanium. As discussed in Chapter 7, Ge is very important group IV material which has a narrow bandgap of 0.67 eV. It has been successfully used in photovoltaic application, photonics and telecommunication. In this work, a new alternate deposition method of microcrystalline germanium as has been proposed with the support of experimental results. It has been possible to tune the bandgap of μc-Ge by the variation of deposition parameters such as RF power and gas flow rates. A crystalline germanium film with optical absorption of more than 70% has been achieved in the 400 to 1600 nm wavelength range. As the PECVD method is slow for germanium deposition, its takes a longer time to deposit 4 micron of film on glass substrates. The use of a textured substrate has shown promising results of high absorption using thin layers. The doping germanium thin film to fabricate p-type and n-type layers demonstrated to achieve bulk concentration of 10^{19} 1/cm^3.

A key challenge in Ge-based industry is the formation of low resistance Ohmic contacts. This is one of the challenging fields of research in current germanium research. In this

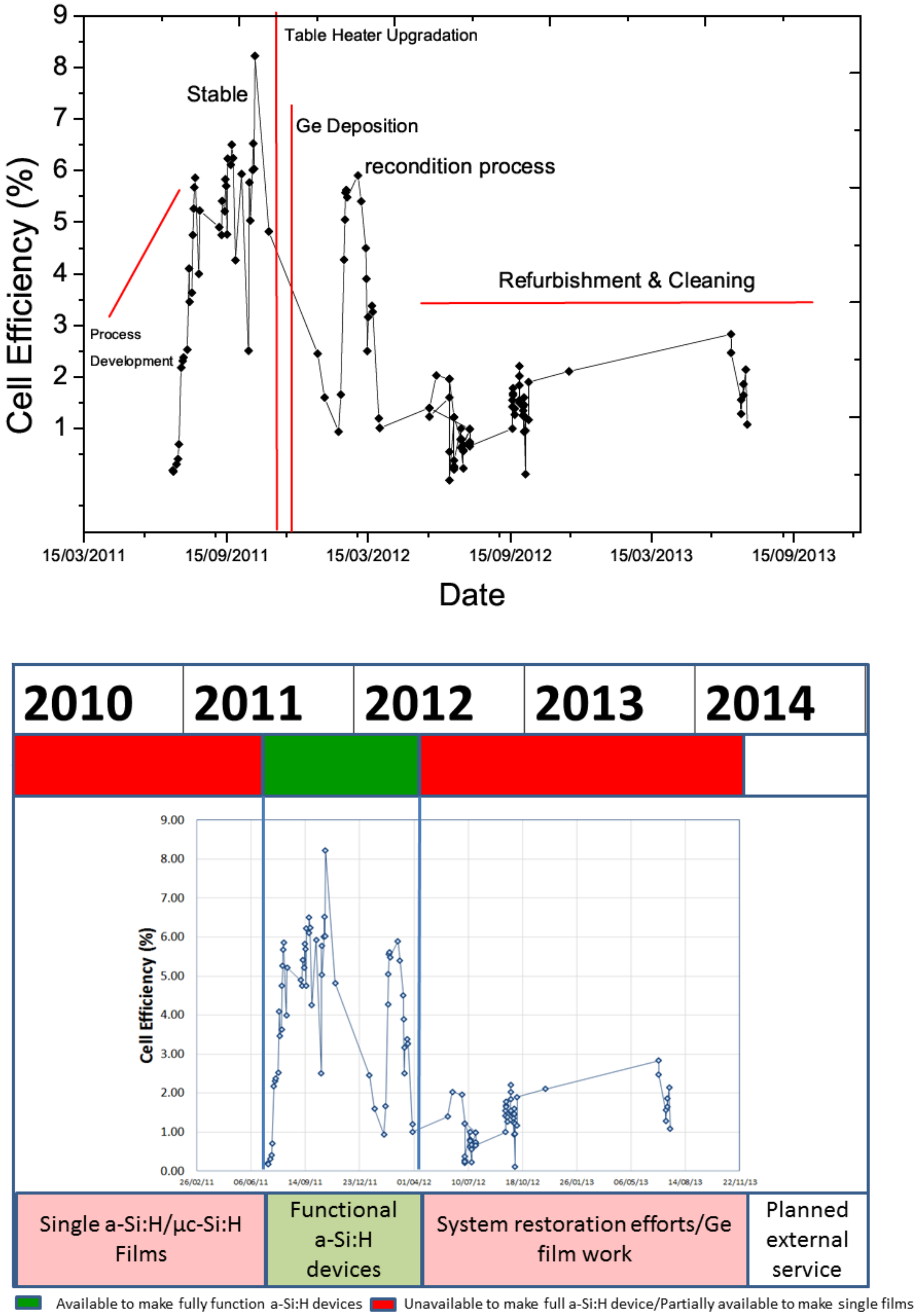

Figure 8.1: Top: Time-line of the efficiency of some selected a-Si:H based single junction devices fabricated via PECVD. Bottom: Project time line with Efficiency time line expressing availability of the tool for the deposition functional a-Si:H solar cells.

regard successful attempts on the fabrication of Ohmic contacts on both p-type and n-type Ge have been done. The lowest resistivity of Ω-cm for *n*-type and 0.17 Ω-cm for *p*-type germanium with the usage of Ni have been achieved.

With these all points, the PECVD system is also loaded with many issues which became a hindrance in this work to explore new ideas. One main issue in the PECVD system is the repeatability of certain deposition works and devices. For example, in many cases, it was very difficult to repeat measured efficiencies after few runs. This can be best explained in the selected device efficiency time-line listed in Figure 8.1

As one can see in top Figure 8.1, after reaching at high point in efficiency, there are some drops and at the end there is a continuous state of lower efficiency. After spending considerable time and effort, it is found that there is contamination issue in the system. The bottom part of same figure shows the availability of PECVD tool to deposit a functional solar cell with good device efficiency. In typical 4 years project time, this PECVD system was only available for 15% of the time which is 8 months including one Christmas break and heater replacement work. Every functional a-Si:H device work reported in this work was processed during this green duration of the time line mentioned in Figure 8.1.

Generally, a PEVCD system is designed as multi-purpose system in which one can deposit intrinsic and doped amorphous silicon, microcrystalline silicon, poly and micro-crystalline germanium or alloying by varying deposition conditions gas mixtures. As in this work, we almost worked on every aspect of fabrication, sadly to report that Oxford plasma system is unable to maintain repeatability when the system is being used from amorphous silicon to germanium due to built-in faults in the design. We have encountered serious contamination after Ge deposition. It was very difficult to repeat good efficiency levels in a-Si:H devices.

The degradation in solar cell performance and before and after heater change/Ge deposition is further explained in terms of solar cell device parameters in Table 8.1. As it is shown, *FF* and current density of solar cell has been reduced halfway. There is no apparent change in V_{OC} which indicate that actual problem of device degradation emerged from intrinsic layer which confirmed by conductivity the measurement whose

Table 8.1: Solar cell characterisation parameters of solar cells before and after heater change deposited under identical deposition parameters. Deposition parameters are: temperature 250 ^{o}C, pressure 350 mTorr, Silane and hydrogen each flow 50 sccm, p-layer thickness 10 nm, i-layer thickness 370 nm, n-layer thickness 45 nm. Similar dopant gases are used for both solar cells which are 10 sccm of boron and 6 sccm of phosphine.

Parameter	Before contamination	After contamination
Efficiency (%)	6.5	2.729
V_{OC} (V)	0.81	0.81
FF	0.62	0.47
J_{SC} (mA/cm^2)	12.81	6.99

result is listed in Table 8.2. The dark conductivity value for intrinsic layer is lower for layers fabricated in contaminated chamber which lower the dark to photoconductivity ratio which is higher for layers deposited before contamination.

Table 8.2: Photoconductivity and dark conductivity values for intrinsic thin films deposited under identical condition before and after chamber contamination . Deposition parameters are: temperature 250 °C, pressure 350 mTorr, Silane and hydrogen flow each 50 sccm.

Chamber status	Photoconductivity (1/Ω-cm)	Dark conductivity (1/Ω-cm)	Dark to Photo Ratio -
Before contamination	6.99×10^{-6}	4.83×10^{-9}	1479
After contamination	4.47×10^{-6}	3.57×10^{-8}	125

When the manufacturer (Oxford Instruments) upgraded the heating table of the PECVD tool, supporting ceramic table clips created heavy chamber contamination. Usually PECVD systems are designed to work with a high RF power environment but in the Oxford system, higher RF usage created problems when the system was reconditioned to lower power usage. It seems that current Oxford Plasma system design is only suitable for more simple applications than photovoltaics maintaining carrier lifetimes is not possible, especially when the tool has multiple purposes. It is suggested that before any film deposition chamber contamination should be removed either by changing chamber cascade or by strong chamber clean.

For future work suggestions, this work can easily be extended to many areas The baseline of amorphous based single junction devices has been achieved which can be used to investigate plasmonic light-trapping as a demonstrator structure suitable for many PV technologies. This work has shown that there is an enormous potential of Ge deposition. This is very economical as compared to wafer based research. In this method crystal microstructure and bandgap can be tuned to a desirable requirement of research. Results indicate that Ge based photovoltaic devices could be developed for remote laser-powered systems. Optimisation of Ohmic contact to microcrystalline Ge is an active area and this can be achieved very easily, as successful attempts have been made in this work. This would open a window of opportunity to use germanium film in many semiconductor research areas such as telecommunication, photonics and in microelectronics as an alternate to c-Si.

Appendix A

Publications

M Akhtar Rind*, Owain D. Clark and Darren M. Bagnall. Amorphous and Microcrystalline Silicon Films for Thin Film Solar Cells. In PVSAT-7, Heriot-Watt University, 1-3 April 2011

M.A. Rind*, D .N.R. Payne and D.M. Bagnall Thin Film Amorphous Silicon Solar Cells on Different Textured Transparent Conducting Oxides. In PVSAT-8, Northumbria University, 2-4 April 2012

L. J. Crudgington , M. A. Rind , D. N. R. Payne , D. M. Bagnall. The Effects of Varied Deposition Conditions, Including the Use of Argon, on Thin-Film Silicon Solar Cells Prepared Using PECVD. In Molecular Crystals and Liquid Crystals Feb 14, 2014

Bibliography

1. Arnulf Jäger-Waldau. PV Status Report 2011. Technical report, European Commission, DG Joint Research Centre, Institute for Energy, Renewable Energy Unit, 2011.

2. J Meier. Potential of amorphous and microcrystalline silicon solar cells. *Thin Solid Films*, 451-452:518–524, March 2004. ISSN 00406090. doi: 10.1016/j.tsf.2003.11.014.

3. Miro Zeman. *Thin film solar cells : fabrication, characterization and applications.* Wiley series in materials for electronic and optoelectronic applications. Wiley, Chichester, England; Hoboken, NJ, 2007.

4. C. R Wronski and D. E. Carlson. *Clean electricity from photovoltaics.* Series on photoconversion of solar energy, v. 1. Imperial College Press, London, 2001.

5. X. M. Deng, X. B. Liao, S. J. Han, H. Povolny, and P. Agarwal. Amorphous silicon and silicon germanium materials for high-efficiency triple-junction solar cells. *Solar Energy Materials and Solar Cells*, 62(1-2):89–95, 2000.

6. Eric A Schiff, Hegedus Steven, and Xunming Deng. Handbook of photovoltaic science and engineering. chapter Amorphous. Wiley, Hoboken NJ, 2. ed. edition, 2011.

7. a. V. Shah, H. Schade, M. Vanecek, J. Meier, E. Vallat-Sauvain, N. Wyrsch, U. Kroll, C. Droz, and J. Bailat. Thin-film silicon solar cell technology. *Progress in Photovoltaics: Research and Applications*, 12(23):113–142, March 2004. ISSN 1062-7995. doi: 10.1002/pip.533.

8. A. Shah, J. Dutta, N. Wyrsch, K. Prasad, H. Curtins, F. Finger, A. Howling, and C. Hollenstein. VHF plasma deposition: A comparative overview. *Amorphous Silicon Technology - 1992, Symposium*, pages 15–26—xxv+1198, 1992.

9. Evelyne Vallat-Sauvain and Arvind Shah. *Amorphous and microcrystalline silicon solar cells : modeling, materials, and device technology.* Kluwer Academic, Boston, 1998.

10. D. B. Cuttriss. Relation Between Surface Concentration and Average Conductivity in Diffused Layers in Germanium. *Bell System Technical Journal*, 40(2):509–521, March 1961. ISSN 00058580. doi: 10.1002/j.1538-7305.1961.tb01627.x. URL `http://ieeexplore.ieee.org/lpdocs/epic03/wrapper.htm?arnumber=6771840`.

11. John J. Conti. International Energy Outlook, 2010. URL `www.eia.gov/oiaf/ieo/index.html.`

12. Charles E. Fritts. New form of selenium cell, with some remarkable electrical discoveries made by its use. *Proceedings of the American Association for the Advancement of Science*, 33(97):128–129, 1883.

13. T. W. Case. "thalofide cell"- a new photo-electric substance. *Physical Review*, 15 (4):289, 1920.

14. L. O. Grondahl. The copper-cuprous-oxide rectifier and photoelectric cell. *Reviews of Modern Physics*, 5(2):141, 1933.

15. D. M. Chapin, C. S. Fuller, and G. L. Pearson. A new silicon p-n junction photocell for converting solar radiation into electrical power. *Journal of Applied Physics*, 25 (5):676–677, 1954.

16. Dieter Bonnet. *The CdTe thin film solar cell.* Harwood Academic, Chur, Switzerland, 1992.

17. Y M Soro, S A Filonovich, P Alpuim, and L Rebouta. Hydrogenated amorphous and nanocrystalline silicon solar cells deposited by HWCVD and RF-PECVD on plastic substrates at 150 C. *Journal of Non-Crystalline Solids*, 354:2376–2380, 2008.

18. Sheila Bailey and Ryne Raffaelle. Handbook of photovoltaic science and engineering. chapter Space Sola. Wiley, Chichester, 2011. ISBN 9780470721698.

19. Olga Malinkiewicz, Aswani Yella, Yong Hui Lee, Guillermo Mínguez Espallargas, Michael Graetzel, Mohammad K. Nazeeruddin, and Henk J. Bolink. Perovskite solar cells employing organic charge-transport layers. *Nature Photonics*, (December): 1–5, December 2013. ISSN 1749-4885.

20. R Street. *Hydrogenated amorphous silicon.* Cambridge University Press, Cambridge, 2005.

21. M.A. Green, Keith Emery, Yoshihiro Hishikawa, and Wilhelm Warta. Solar cell efficiency tables (version 37). *Progress in Photovoltaics: Research and Applications*, 19(1):84–92, 2011. ISSN 1099-159X. doi: 10.1002/pip.

22. Miroslav Zeman. ThinFilm Silicon PV Technology. *Journal of ELECTRICAL ENGINEERING*, 61(5):271–276, 2010.

23. D Fischer, S Dubail, J.A. Anna Selvan, and N Pellation Vaucher. The micrograph solar cell: Extending a-Si:H technology towards thin film crystalline silicon. In *Proceedings of 25th IEEE PVSC*, page 1053, ,Washington, DC, 1996.

24. J Yang, BJ Yan, GZ Yue, and S Guha. Comparison of hydrogenated amorphous silicon germanium and nanocrystalline silicon for multijunction solar cells - Pros, cons, and status. In *31st IEEE Photovoltaic Specialists Conference*, Lake Buena Vista, 2005.

25. Chao-Yang Tsao, Jürgen W. Weber, Patrick Campbell, Gavin Conibeer, Dengyuan Song, and Martin a. Green. In situ low temperature growth of poly-crystalline germanium thin film on glass by RF magnetron sputtering. *Solar Energy Materials and Solar Cells*, 94(9):1501–1505, September 2010. ISSN 09270248. doi: 10.1016/j.solmat.2010.02.035.

26. T. Sakata, K. Makihara, H. Murakami, S. Higashi, and S. Miyazaki. Growth of crystallized Ge films from VHF inductively-coupled plasma of H2-diluted GeH4. *Thin Solid Films*, 515(12):4971–4974, April 2007. ISSN 00406090. doi: 10.1016/j.tsf.2006.10.048.

27. Y. Okamoto, K. Makihara, S. Higashi, and S. Miyazaki. Formation of microcrystalline germanium (μc-Ge:H) films from inductively coupled plasma CVD. *Applied Surface Science*, 244(1-4):12–15, May 2005. ISSN 01694332.

28. V. Pavan Kishore, Prashanth Paramahans, Sunny Sadana, Udayan Ganguly, and Saurabh Lodha. Nanocrystal-based Ohmic contacts on n and p-type germanium. *Applied Physics Letters*, 100(14):142107, 2012. ISSN 00036951.

29. DR Gajula, D McNeill, and M Armstrong. Characterization of Nickel Germanide Schottky Contacts for the Fabrication of Ge p-MOSFETs. *The Electrochemical Society Characterization*, 3344(2001):113706, 2011.

30. M. Moreno, N. Delgadillo, A. Torres, R. Ambrosio, P. Rosales, A. Kosarev, C. Reyes-Betanzo, J. de la Hidalga-Wade, C. Zuniga, and W. Calleja. Boron doping compensation of hydrogenated amorphous and polymorphous germanium thin films for infrared detection applications. *Thin Solid Films*, 548:533–538, December 2013. ISSN 00406090.

31. a. Dimoulas, P. Tsipas, A. Sotiropoulos, and E. K. Evangelou. Fermi-level pinning and charge neutrality level in germanium. *Applied Physics Letters*, 89(25):252110, 2006. ISSN 00036951.

32. Richard C. Neville. *Solar Energy Conversion : the Solar Cell.* Elsevier Scientific Pub, New York, 1978.

33. Jenny Nelson. *The physics of solar cells.* Imperial College Press, London, 2003.

34. Alan L Fahrenbruch and Richard H Bube. *Fundamentals of solar cells : photovoltaic solar energy conversion.* New York : Academic Press, New York, 1983.

35. M. H. Brodsky, M. A. Frisch, J. F. Ziegler, and W. A. Lanford. Quantitative analysis of hydrogen in glow discharge amorphous silicon. *Applied Physics Letters*, 30(11):561, June 1977. ISSN 00036951.

36. Robert A. Street. *Hydrogenated amorphous silicon.* Cambridge solid state science series. Cambridge Univ. Press, 1991.

37. N Mott. *Conduction in non-crystalline materials.* Clarendon Press ;;Oxford University Press, Oxford ;New York, 1987.

38. A. S. Ferlauto, G. M. Ferreira, J. M. Pearce, C. R. Wronski, R. W. Collins, Xunming Deng, and Gautam Ganguly. Analytical model for the optical functions of amorphous semiconductors from the near-infrared to ultraviolet: Applications in thin film photovoltaics. *Journal of Applied Physics*, 92(5):2424, September 2002. ISSN 00218979.

39. G. E. Jellison and F. A. Modine. Parameterization of the optical functions of amorphous materials in the interband region. *Applied Physics Letters*, 69(3):371, July 1996. ISSN 00036951.

40. Richard Bube. Photovoltaic materials, 1998.

41. D. E. Carlson. *Solar cells : materials, manufacture and operation.* Elsevier Advanced Technology, Oxford, 2005.

42. Mary D. Archer and R. Hill. *Clean electricity from photovoltaics.* Series on photoconversion of solar energy, v. 1. Imperial College Press, London, 2001.

43. D. L. Staebler and C. R. Wronski. Reversible conductivity changes in discharge-produced amorphous si. *Applied Physics Letters*, 31(4):292–294, 1977.

44. H. R. Park, J. Z. Liu, and S. Wagner. Saturation of the light-induced defect density in hydrogenated amorphous-silicon. *Applied Physics Letters*, 55(25):2658–2660, 1989.

45. C. R. Wronski and D. E. Carlson. Amorphous Silicon Solar Cells. In M.D. Archer and R Hill, editors, *Clean electricity from photovoltaics*, chapter 5, page 199242. Imperial College Press,, London :, 2001. ISBN 9781848161504.

46. E a Schiff. Drift-mobility measurements and mobility edges in disordered silicons. *Journal of Physics: Condensed Matter*, 16(44):5265–5275, November 2004. ISSN 0953-8984.

47. Harvey Scher, Michael F. Shlesinger, and John T. Bendler. Time-Scale Invariance in Transport and Relaxation. *Physics Today*, 44(1):26, 1991. ISSN 00319228.

48. E.a Schiff. Low-mobility solar cells: a device physics primer with application to amorphous silicon. *Solar Energy Materials and Solar Cells*, 78(1-4):567–595, July 2003. ISSN 09270248.

49. Joohyun Koh, Yeeheng Lee, H. Fujiwara, C. R. Wronski, and R. W. Collins. Optimization of hydrogenated amorphous silicon pin solar cells with two-step i layers guided by real-time spectroscopic ellipsometry. *Applied Physics Letters*, 73(11): 1526, 1998. ISSN 00036951.

50. H. Sakai, T. Yoshida, S. Fujikake, T. Hama, and Y. Ichikawa. Effect of p/i interface layer on dark J-V characteristics and Voc in p-i-n a-Si solar cells. *Journal of Applied Physics*, 67(7):3494, 1990. ISSN 00218979.

51. H.F. Sterling Swann and R.C.G. Chemical vapour deposition promoted by r.f. discharge. *Solid State Electron*, 8, 1965.

52. R. C. Chittick, Alexande.Jh, and H. F. Sterling. Preparation and properties of amorphous silicon. *Journal of the Electrochemical Society*, 116(1):77, 1969.

53. D. E. Carlson and C. R. Wronski. Amorphous silicon solar-cell. *Applied Physics Letters*, 28(11):671–673, 1976.

54. Ruud E. I. Schropp and Miro Zeman. *Amorphous and microcrystalline silicon solar cells : modeling, materials, and device technology.* Kluwer Academic, Boston, 1998.

55. S.K. Soni, Anup Phatak, and R.O. Dusane. High deposition rate device quality a-Si:H films at low substrate temperature by HWCVD technique. *Solar Energy Materials and Solar Cells*, 94(9):1512–1515, September 2010. ISSN 09270248. doi: 10.1016/j.solmat.2010.01.027.

56. Akihisa Matsuda. Thin-film silicon – growth process and solar cell applications. *Japanese Journal of Applied Physicsi*, 43:7909–7920, 2004.

57. A Matsuda. Thin-Film Silicon: Growth Process and Solar Cell Application. *Japanese journal of applied physics*, 43(12):7909–7920, 2004.

58. A Matsuda, K Nomoto, Y Takeuchi, A Suzuki, A Yuuki, and J Perrin. Temperature-dependence of the sticking and loss probabilities of silyl radicals on hydrogenated amorphous silicon. *SURFACE SCIENCE*, 227(1-2):50–56, 1990.

59. T. Takagi, R. Hayashi, G. Ganguly, M. Kondo, and A. Matsuda. Gas-phase diagnosis and high-rate growth of stable a-si : H. *Thin Solid Films*, 345(1):75–79.

60. Antonio Luque Hegedus and Steveb. Handbook of photovoltaic science and engineering, 2003.

61. H. Curtins, N. Wyrsch, and A. V. Shah. High-rate deposition of amorphous hydrogenated silicon - effect of plasma excitation-frequency. *Electronics Letters*, 23 (5):228–230, 1987.

62. H. Meiling and R. E. I. Schropp. Stable amorphous-silicon thin-film transistors. *Applied Physics Letters*, 70(20):2681, May 1997. ISSN 00036951.

63. A. H. Mahan, Y. Xu, B. P. Nelson, R. S. Crandall, J. D. Cohen, K. C. Palinginis, and A. C. Gallagher. Saturated defect densities of hydrogenated amorphous silicon grown by hot-wire chemical vapor deposition at rates up to 150 /s. *Applied Physics Letters*, 78(24):3788, June 2001. ISSN 00036951.

64. J.-E. Bourée, A.H. Mahan, H. Matsumura, B. Schröder, R.E.I. Schropp, M.B. Schubert, S. Osono, M. Kitazoe, H. Tsuboi, S. Asari, and K. Saito. Development of catalytic chemical vapor deposition apparatus for large size substrates. *Thin Solid Films*, 501(1):61–64, 2006.

65. I. Kato, S. Wakana, S. Hara, and H. Kezuka. Microwave plasma cvd system for the fabrication of thin solid films. *Japanese Journal of Applied Physics Part 2-Letters*, 21(8), 1982.

66. J.W. Metselaar B.A.Korevaar, C. Smit, R.A.C.M.M. van Swaaij, A.H.M. Smets, W.M.M.Kessels, D.C. Schram, and M.C.M. van de Sanden. Solar cells with intrinsic a-Si:H deposited at rates larger than 5 A /s by the expanding thermal plasma. In *Proceedings of the 16th European Photovoltaic Solar Energy Conference and Exhibition, Glasgow*, 2000.

67. W. M. M. Kessels, R. J. Severens, A. H. M. Smets, B. A. Korevaar, G. J. Adriaenssens, D. C. Schram, and M. C. M. van de Sanden. Hydrogenated amorphous silicon deposited at very high growth rates by an expanding ArH[sub 2]SiH[sub 4] plasma. *Journal of Applied Physics*, 89(4):2404, February 2001. ISSN 00218979.

68. A.H.M. Smets, W.M.M. Kessels, and M.C.M. van de Sanden. External rf substrate biasing during a-Si:H film growth using the expanding thermal plasma technique. *MRS Proceedings*, 808:A9.21, March 2004. ISSN 1946-4274.

69. a. Banerjee and S. Guha. Study of back reflectors for amorphous silicon alloy solar cell application. *Journal of Applied Physics*, 69(2):1030, 1991. ISSN 00218979.

70. EA Schiff. Diffusion-controlled bimolecular recombination of electrons and holes in a-Si: H. *Journal of non-crystalline solids*, 190:1–8, 1995.

71. Y. Hamakawa, H. Okamoto, and Y. Nitta. A new type of amorphous silicon photovoltaic cell generating more than 2.0 V. *Applied Physics Letters*, 35(2):187, 1979. ISSN 00036951.

72. T. Yoshida, K. Maruyama, O. Nabeta, Y. Ichikawa, and H. Sakai. High efficiency a-Si:H two stacked tandem solar cell. In *Proceedings of the 19th IEEE Photovoltaic Specialists Conference*, pages 1095–1100, New York, 1987.

73. Arvind V Shah, Milan Vaněček, and Johannes Meier. Basic efficiency limits, recent experimental results and novel light-trapping schemes in a-Si:H, μc-Si:H and 'micromorph tandem' solar cells. *Journal of Non-Crystalline Solids*, 338-340:639–645, June 2004. ISSN 00223093.

74. Timothy J. Coutts, Keith a. Emery, and J. Scott Ward. Modeled performance of polycrystalline thin-film tandem solar cells. *Progress in Photovoltaics: Research and Applications*, 10(3):195–203, May 2002. ISSN 1062-7995. doi: 10.1002/pip.419.

75. N.P. Fischer, D; Dubail, S. ; Anna Selvan, J.A. ; Vaucher. The micromorph solar cell: extending a-Si:H technology towards thin film crystalline silicon. In *Photovoltaic Specialists Conference, 1996., Conference Record of the Twenty Fifth IEEE*, pages 1053 – 1056, Washington, DC, 1996.

76. MA Green and Keith Emery. Solar cell efficiency tables (version 43). *Progress in . . .*, (version 43):1–9, 2012.

77. J Yang, B Yan, G Yue, and S Guha. Comparison of hydrogenated amorphous silicon germanium and nanocrystalline silicon for multijunction solar cells: pros, cons, and status. *. . . Record of the Thirty-first IEEE*, pages 1359–1364, 2005.

78. N. Beck, N. Wyrsch, C. Hof, and A. Shah. Mobility lifetime product- a tool for correlating a-Si:H film properties and solar cell performances. *Journal of Applied Physics*, 79:9361–9368, 1996.

79. V. Daudrix, C. Droz, N. Wyrsch, Y. Ziegler, X Niquille, and A. Shah. Developments of more stable amorphous silicon thin film solar cells deposited at 'moderately' high temperature. In *proceedings of 162th European Photovoltaic Solar energy Conference*, pages 385–388, Glasgow, 2000.

80. C. Droz, M. Goerlitzer, N. Wyrsch, and A. Shah. Electron tranposrt in hydrogenated microcrystalline silicon: simililarities with amorphous silicon. *Journal of Non-Crystalline Solids*, 266-269:319–324, 2000.

81. C. Droz, E. Vallat-Sauvain, J. Bailat, L. Feitknencht, J. Meier, X. Niquille, and A. Shah. Electrical and microstructal charachterisation of microcrystalline silicon layers and solar cells. In *Proceedings of the 3rd World Conference on PVSEC*, 2003.

82. J. Merten, J.M. Asensi, C. Voz, A.V. Shah, R. Platz, and J. Andreu. Improved equivalent circuit and analytical model for amorphous silicon solar cells and modules. *IEEE Transactions on Electron Devices*, 45(2):423–429, 1998. ISSN 00189383.

83. N. Wyrsch, N. Beck, J. Meier, P. Torres, and A. Shah. Electric field profile in uc-Si:H p-i-n devices. In *Proceedings of Material Research Society Symposium*, pages 181–186, 1998.

84. N. Wyrsch, D. Fischer, and A Shah. Determination of internal electric field profile in a-Si:H p-i-n devices. In *Proceedings of 12th European Photovoltaic Solar energy Conference*, pages 73–76, 1994.

85. M. B. Von Der Linden, R. E. I. Schropp, J. G. F. Stammeijer, and W. F. Van Der Weg. Evaluation of the Dice Method as A Tool For Amorphous Silicon Solar Cell Optimization. *MRS Proceedings*, 258:935, February 2011. ISSN 1946-4274.

86. C.R. Wronski, T. Tiedje, and G. D. Cody. Recombination centers in phosphorus-doped hydrogenated amorphous silicon. *Solid State Communications*, 44:1423–1426, 1982.

87. F. Demichelis, F. Giorgis, C.F. Pirri, E. Tresso, G. Amato, and U. Coscia. Density of gap states in a-SiC:H films by means of photoconductive and photothermal spectroscopies. *Physica B: Condensed Matter*, 205(2):169–174, February 1995. ISSN 09214526.

88. J.K. Rath and R. E. I. Schropp. Incorporatio pf p-type microcrystalline silicon films in amorphous silicon based solar cells in a superstrate structure. *Solar Energy Materials and Solar Cells*, 53:189–203, 1998.

89. W Ma, H. Aoyama, H. Okamoto, and Y. Hamakawa. A study of interface properties in a-Si:H solar cell with uc-Si(C). *Solar Energy Materials and Solar Cells*, 41/42 (453-463), 1996.

90. Ping-Kuan Chang, Po-Tsung Hsieh, Chun-Hsiung Lu, Chih-Hung Yeh, and Mau-Phon Houng. Development of high efficiency pin amorphous silicon solar cells with the p-μc-Si:H/p-a-SiC:H double window layer. *Solar Energy Materials and Solar Cells*, 95(9):2659–2663, September 2011. ISSN 09270248.

91. B. Rech and H. Wagner. Improvement in stabilized efficiency of a-Si:H solar cells through optimized p/i interface layers. *Solar Energy Materials and Solar Cells*, 41: 475–483, 1996.

92. Miro Zeman. Advances in Microcrystalline Silicon Solar Cell Technologies. In Jef Poortmans; Vladimir Arkhipov, editor, *Thin film solar cells : fabrication, characterization and applications*, chapter 5. Chichester, England ; Hoboken, NJ : Wiley, 2007.

93. J. Springer. Absorption loss at nanorough silver back reflector of thin-film silicon solar cells. *Journal of Applied Physics*, 95(3):1427, February 2004. ISSN 00218979.

94. Wilfried Sark. Physics and technology of amorphous-crystalline heterostructure silicon solar cells, 2012.

95. C. Agashe. Efforts to improve carrier mobility in radio frequency sputtered aluminum doped zinc oxide films. *Journal of Applied Physics*, 95(4):1911, 2004. ISSN 00218979.

96. K Sato, Y Matsui, and K Adachi. Hydrogen plasma treatment of ZnO-coated TCO films. In *23rd Photovoltaic Specialists Conference*, pages 855 – 859, 1993. ISBN 0780312201.

97. I.A. Rauf. Low resistivity and high mobility tin-doped indium oxide films. *Materials Letters*, 18(3):123–127, December 1993. ISSN 0167577X.

98. RG Gordon, James Proscia, FB Ellis Jr, and AE Delahoy. tin oxide films produced by atmospheric pressure chemical vapor deposition from tetramethyltin and their usefulness in producing light trapping in thin film amorphous. *Solar energy materials*, 18:263–281, 1989.

99. Dekker T, Metselaar J, Schlatmann R, Stannowski B, van Swaaij R, and Zeman M. Correlation between surface-textured tin and zinc oxide substrates and curren enhancement in amorphous silicon solar cells. In *20th European Photovoltaic Solar Energy Conference*, page 1517, 2005.

100. Xunming Deng and Eric A Schiff. *Handbook of photovoltaic science and engineering*. Wiley, 2003.

101. Toshio Hama, H Okamoto, Yoshihiro Hamakawa, and Takeo Matsubara. Hydrogen content dependence of the optical energy gap in a-Si:H. *Journal of Non-Crystalline Solids*, 59-60:333–336, 1983.

102. Masao Shima, Masaki; Isomura. Investigation of Hydrogenated Amorphous Silicon Germanium Fabricated under High Hydrogen Dilution and Low Deposition Temperature Conditions for Stable Solar Cells. *Japanese Journal of Applied Physics*, 37(12A):6322–6327, 1998.

103. Mario Tucci. Optimization of n-doping in n-type a-SI : H / p-type textured c-Si heterojunction for photovoltaic applications. *Solar Energy Materials*, 57:249–257, 1999.

104. R.C. Reedy, Q. Wang, H. Moutinho, E. Iwaniczko, and A.H. Mahan. SIMS Characterization of Amorphous-Silicon Solar Cells Grown by Hot-Wire Chemical Vapor Deposition on Stainless Steel. Technical report, NREL, Denver Colorado, 2000.

105. O. Vetterl, F. Finger, R. Carius, P. Hapke, L. Houben, O. Kluth, A. Lambertz, A. Muck, B. Rech, and H. Wagner. Intrinsic microcrystalline silicon: A new material for photovoltaics. *Solar Energy Materials and Solar Cells*, 62(1-2):97–108, 2000.

106. Michio Kondo. An approach to device grade amorphous and microcrystalline silicon thin films fabricated at higher deposition rates. *Current Opinion in Solid State and Materials Science*, 6(5):445–453, October 2002. ISSN 13590286. doi: 10.1016/S1359-0286(02)00113-4.

107. a Abramov, D Daineka, Y Djeridane, and P Rocaicabarrocas. Detailed study of surface and interface properties of μc-Si films. *Journal of Non-Crystalline Solids*, 354(19-25):2218–2222, May 2008. ISSN 00223093. doi: 10.1016/j.jnoncrysol.2007.10.099.

108. a Matsuda. Growth mechanism of microcrystalline silicon obtained from reactive plasmas. *Thin Solid Films*, 337(1-2):1–6, January 1999. ISSN 00406090. doi: 10.1016/S0040-6090(98)01165-1.

109. A Matsuda. Formation kinetics and control of microcrystallite in micro- c-Si: H from glow discharge plasma. *Journal of non-crystalline Solids*, 59:767–774, 1983. ISSN 0022-3093.

110. Y. Tawada and H Okamoto. aSiC: H/aSi: H heterojunction solar cell having more than 7.1% conversion efficiency. *Applied Physics Letters*, 39:237, 2009. ISSN 00036951. doi: 10.1063/1.92692.

111. C.C. Tsaia, G.B. Andersona, R. Thompsona, and B. Wacker. Control of silicon network structure in plasma deposition. *Journal of Non-Crystalline Solids*, 114: 151–153, 1989.

112. K Nakamura, K Yoshino, S Takeoka, and I Shimizu. Roles of Atomic Hydrogen in Chemical Annealing. *Japan Journal of Applied Physics*, 34, 1995.

113. Jhuma Gope, Sushil Kumar, a. Parashar, P.N. Dixit, C.M.S. Rauthan, O.S. Panwar, D.N. Patel, and S.C. Agarwal. Amorphous and nanocrystalline silicon made by varying deposition pressure in PECVD process. *Journal of Non-Crystalline Solids*, 355(45-47):2228–2232, November 2009. ISSN 00223093. doi: 10.1016/j.jnoncrysol.2009.07.013.

114. D Gracin, a Gajovic, K Juraic, M Ceh, Z Remes, a Poruba, and M Vanecek. Spectral response of amorphousnano-crystalline silicon thin films. *Journal of Non-Crystalline Solids*, 354(19-25):2286–2290, May 2008. ISSN 00223093. doi: 10.1016/j.jnoncrysol.2007.10.076.

115. R. Tsu. Critical volume fraction of crystallinity for conductivity percolation in phosphorus-doped Si:F:H alloys. *Applied Physics Letters*, 40(6):534, 1982. ISSN 00036951. doi: 10.1063/1.93133.

116. Jordi Sancho-Parramon, Davor Gracin, Mircea Modreanu, and Andreja Gajović. Optical spectroscopy study of nc-Si-based pin solar cells. *Solar Energy Materials*

and Solar Cells, 93(10):1768–1772, October 2009. ISSN 09270248. doi: 10.1016/j.solmat.2009.06.008.

117. T Takagi, R Hayashi, G Ganguly, M Kondo, and A Matsuda. Gas-phase diagnosis and high-rate growth of stable a-Si : H. *Thin Solid Films*, 345:75–79, 1999.

118. S , Y Hishikawa, and S Tsuda. New interpretation of the effect of hydrogen dilution of silane on glow-discharged hydrogenated amorphous silicon for stable solar cells. *Jpn. J. Appi. Phys. Vol*, 1996.

119. Lin Zhang, Junhua Gao, Jinquan Xiao, Lishi Wen, Jun Gong, and Chao Sun. Effect of argon on the structure of hydrogenated nanocrystalline silicon deposited from tetrachlorosilane/hydrogen/argon plasma. *Physica Status Solidi (a)*, 209(6): 1080–1084, June 2012. ISSN 18626300.

120. R Collins. Evolution of microstructure and phase in amorphous, protocrystalline, and microcrystalline silicon studied by real time spectroscopic ellipsometry. *Solar Energy Materials and Solar Cells*, 78(1-4):143–180, July 2003. ISSN 09270248.

121. a. S. Ferlauto, R. J. Koval, C. R. Wronski, and R. W. Collins. Extended phase diagrams for guiding plasma-enhanced chemical vapor deposition of silicon thin films for photovoltaics applications. *Applied Physics Letters*, 80(15):2666, 2002. ISSN 00036951.

122. Akihisa Matsuda. Plasma and surface reactions for obtaining low defect density amorphous silicon at high growth rates. *Journal of Vacuum Science & Technology A: Vacuum, Surfaces, and Films*, 16(1):365, January 1998. ISSN 07342101.

123. Noboru Nakamura, Tsuyoshi Takahama, Masao Isomura, Masato Nishikuni, Kazuhiro Yoshida, Shinya Tsuda, Shoichi Nakano, Michitoshi Ohnishi, and Yukinori Kuwano. The Influence of the Si-H 2 Bond on the Light-Induced Effect in a-Si Films and a-Si Solar Cells. *Japanese Journal of Applied Physics*, 28(Part 1, No. 10):1762–1768, October 1989. ISSN 0021-4922.

124. Hsueh-Ling Yu and Chin-Chai Hsaio. Comparison of different measurement methods for transmittance haze. *Metrologia*, 46(4):S233–S237, August 2009. ISSN 0026-1394.

125. David N. R. Payne, Stuart a. Boden, Owain D. Clark, Alan E. Delahoy, and Darren M. Bagnall. Characterization of experimental textured ZnO:Al films for thin film solar cell applications and comparison with commercial and plasmonic alternatives. *2010 35th IEEE Photovoltaic Specialists Conference*, pages 001560–001564, June 2010.

126. S. Faÿ, L. Feitknecht, R. Schlüchter, U. Kroll, E. Vallat-Sauvain, and A. Shah. Rough ZnO layers by LP-CVD process and their effect in improving performances

of amorphous and microcrystalline silicon solar cells. *Solar Energy Materials and Solar Cells*, 90(18-19):2960–2967, November 2006. ISSN 09270248.

127. Tomonori Nagashima and Kenichi Okumura. A germanium back-contact type cell for thermophotovoltaic applications. *. . . 2003. Proceedings of . . .*, pages 200–203, 2003.

128. R. R. King, D. C. Law, K. M. Edmondson, C. M. Fetzer, G. S. Kinsey, H. Yoon, R. A. Sherif, and N. H. Karam. 40% efficient metamorphic GaInPGaInAsGe multijunction solar cells. *Applied Physics Letters*, 90(18):183516, May 2007. ISSN 00036951.

129. Yu Cao, Jianjun Zhang, Tianwei Li, Zhenhua Huang, Jun Ma, Xu Yang, Jian Ni, Xinhua Geng, and Ying Zhao. Effects of seed layer on the performance of microcrystalline silicon germanium solar cells. *Journal of Semiconductors*, 34(3): 034008, March 2013. ISSN 1674-4926.

130. Jian Wang and Sungjoo Lee. Ge-photodetectors for Si-based optoelectronic integration. *Sensors (Basel, Switzerland)*, 11(1):696–718, January 2011. ISSN 1424-8220.

131. KA McComber and Jifeng Liu. Low-temperature germanium ultra-high vacuum chemical vapor deposition for back-end photonic integration. *Group IV Photonics, . . .*, 2009.

132. Chil-Chyuan Kuo. Characterization of polycrystalline Ge thin films fabricated by short-pulse XeF excimer laser crystallization. *Journal of Russian Laser Research*, 29(2):167–175, June 2008. ISSN 1071-2836. doi: 10.1007/s10946-008-9008-3.

133. J. Liu, H. J. Kim, O. Hulko, Y. H. Xie, S. Sahni, P. Bandaru, and E. Yablonovitch. Ge films grown on Si substrates by molecular-beam epitaxy below 450 C. *Journal of Applied Physics*, 96(1):916, 2004. ISSN 00218979.

134. C Niikura, SY Kim, B Drevillon, and Y Poissant. Growth mechanisms and structural properties of microcrystalline silicon films deposited by catalytic CVD. *Thin solid films*, 395:178–183, 2001.

135. Jhuma Gope, Sushil Kumar, S. Sudhakar, Kalpana Lodhi, C.M.S. Rauthan, and P.C. Srivastava. Influence of argon dilution on the growth of amorphous to ultra nanocrystalline silicon films using VHF PECVD process. *Journal of Alloys and Compounds*, 577:710–716, November 2013. ISSN 09258388.

136. A. Matsuda. Formation kinetics and control of microcrystallite in μc-Si:H from glow discharge plasma. *Journal of Non-Crystalline Solids*, 59:767–774, 1983.

137. Rui Xu, Wei Li, Jian He, Yan Sun, and Ya-Dong Jiang. Investigation of nanocrystallization of a-Si1xGex:H thin films diluted with argon in the PECVD system. *Journal of Non-Crystalline Solids*, 365:37–41, April 2013. ISSN 00223093.

138. LJ Pilione, K Vedam, and JE Yehoda. Thickness dependence of optical gap and void fraction for sputtered amorphous germanium. *Physical Review B*, 35(17): 9368–9371, 1987.

139. Xiao-Dong Wang, Hai-Feng Wang, Bo Chen, Yun-Peng Li, and Yue-Ying Ma. A model for thickness effect on the band gap of amorphous germanium film. *Applied Physics Letters*, 102(20):202102, 2013. ISSN 00036951.

140. Eunice S. M. Goh, T. P. Chen, C. Q. Sun, and Y. C. Liu. Thickness effect on the band gap and optical properties of germanium thin films. *Journal of Applied Physics*, 107(2):024305, 2010. ISSN 00218979.

141. J. M. Gibson, M. M. J. Treacy, T. Sun, and N. J. Zaluzec. Substantial Crystalline Topology in Amorphous Silicon. *Physical Review Letters*, 105(12):125504, September 2010. ISSN 0031-9007.

142. J Murray Gibson. Materials science. Solving amorphous structures–two pairs beat one. *Science (New York, N.Y.)*, 335(6071):929–30, February 2012. ISSN 1095-9203.

143. SG Tomlin. The optical properties of amorphous and crystalline germanium. *Journal of Physics C: Solid ...*, 4335, 1976.

144. GKM Thutupalli and SG Tomlin. The optical properties of amorphous and crystalline silicon. *Journal of Physics C: Solid State ...*, 467, 1977.

145. G. Barkema and Normand Mousseau. High-quality continuous random networks. *Physical Review B*, 62(8):4985–4990, August 2000. ISSN 0163-1829.

146. Sir N F Mott. *Conduction in non-crystalline materials.* Clarendon Press, Oxford University Press, New York, 1987.

147. N. Yoshida, Y. Hatano, and M. Isomura. Microcrystalline germanium thin films prepared by reactive RF sputtering. *Solar Energy Materials and Solar Cells*, 95 (1):175–178, January 2011. ISSN 09270248. doi: 10.1016/j.solmat.2010.04.031.

148. Y. Ide, K. Asakusa, Y. Zhao, A. Yamada, and M. Konagai. Amorphous and microcrystalline silicon films deposited by hot wire cell method: application to silicon based thin film solar cells. *Conference Record of the Twenty-Ninth IEEE Photovoltaic Specialists Conference, 2002.*, pages 1162–1165.

149. Jhuma Gope, Sushil Kumar, A. Parashar, P.N. Dixit, C.M.S. Rauthan, O.S. Panwar, D.N. Patel, and S.C. Agarwal. Amorphous and nanocrystalline silicon made by varying deposition pressure in PECVD process. *Journal of Non-Crystalline Solids*, 355(45-47):2228–2232, November 2009. ISSN 00223093.

150. K. Gallacher, P. Velha, D. J. Paul, I. MacLaren, M. Myronov, and D. R. Leadley. Ohmic contacts to n-type germanium with low specific contact resistivity. *Applied Physics Letters*, 100(2):022113, 2012. ISSN 00036951.

151. S. Gaudet, C. Detavernier, A. J. Kellock, P. Desjardins, and C. Lavoie. Thin film reaction of transition metals with germanium. *Journal of Vacuum Science & Technology A: Vacuum, Surfaces, and Films*, 24(3):474, April 2006. ISSN 07342101.

152. K Gallacher, P Velha, D J Paul, I Maclaren, M Myronov, and D R Leadley. Ohmic contacts to n-type germanium with low specific contact resistivity Ohmic contacts to n-type germanium with low specific contact resistivity. 022113(May):1–4, 2012.

153. Chao-Yang Tsao, Jialiang Huang, Xiaojing Hao, Patrick Campbell, and Martin a. Green. Formation of heavily boron-doped hydrogenated polycrystalline germanium thin films by co-sputtering for developing p+ emitters of bottom cells. *Solar Energy Materials and Solar Cells*, 95(3):981–985, March 2011. ISSN 09270248. doi: 10.1016/j.solmat.2010.12.003.

154. Horng-Chih Lin, Hsiao-Yi Lin, Chun-Yen Chang, Tz-Gwei Jung, P. J. Wang, Ray-Chern Deng, and Jandel Lin. Effect of boron doping on the structural properties of polycrystalline silicon films grown at reduced pressures. *Journal of Applied Physics*, 76(3):1572, 1994. ISSN 00218979.

155. H.H. Berger. Models for contacts to planar devices. *Solid-State Electronics*, 15(2):145–158, 1972.

156. R. Street. Doping and the Fermi Energy in Amorphous Silicon. *Physical Review Letters*, 49(16):1187–1190, October 1982. ISSN 0031-9007.

157. Dedong Han, Yi Wang, Dayu Tian, Wei Wang, Xiaoyan Liu, Jinfeng Kang, and Ruqi Han. Studies of Ti- and Ni-germanide Schottky contacts on n-Ge(100) substrates. *Microelectronic Engineering*, 82(2):93–98, October 2005. ISSN 01679317.

158. R. R. Lieten, S. Degroote, M. Kuijk, and G. Borghs. Ohmic contact formation on n-type Ge. *Applied Physics Letters*, 92(2):022106, 2008. ISSN 00036951.

159. K. Gallacher, P. Velha, D. J. Paul, I. MacLaren, M. Myronov, and D. R. Leadley. Ohmic contacts to n-type germanium with low specific contact resistivity. *Applied Physics Letters*, 100(2):022113, January 2012. ISSN 00036951.

160. Tomonori Nishimura, Koji Kita, and Akira Toriumi. Evidence for strong Fermi-level pinning due to metal-induced gap states at metal/germanium interface. *Applied Physics Letters*, 91(12):123123, 2007. ISSN 00036951.

161. John F. Wager and John Robertson. Metal-induced gap states modeling of metal-Ge contacts with and without a silicon nitride ultrathin interfacial layer. *Journal of Applied Physics*, 109(9):094501, 2011. ISSN 00218979.

162. John Y Spann, Student Member, Robert A Anderson, Trevor J Thornton, Gari Harris, Shawn G Thomas, Clarence Tracy, and A Sample Preparation. Characterization of Nickel Germanide Thin Films for Use as Contacts to p-Channel Germanium MOSFETs. 26(3):2004–2006, 2005.

163. Francesco Giuseppe Della Corte and Sandro Rao. Use of amorphous silicon for active photonic devices. *IEEE Transactions on Electron Devices*, 60(5):1495–1505, May 2013. ISSN 0018-9383.

164. S.A. Boden and D.M. Bagnall. Bio-mimetic subwavelength surfaces for near-zero reflection sunrise to sunset. *..., Conference Record of the 2006 IEEE ...*, pages 1358–1361, 2006.

165. Baohua Jia, Xi Chen, Jhantu Kumar Saha, Qi Qiao, Yongqian Wang, Zhengrong Shi, and Min Gu. Concept to devices: from plasmonic light trapping to upscaled plasmonic solar modules. *Photonics Research*, 1(1):22, June 2013. ISSN 2327-9125.